Computational Modeling of the FeTi Hydrogenation:

Scale-bridging atoms and microstructure

Ebert Daniel Macedo Alvares

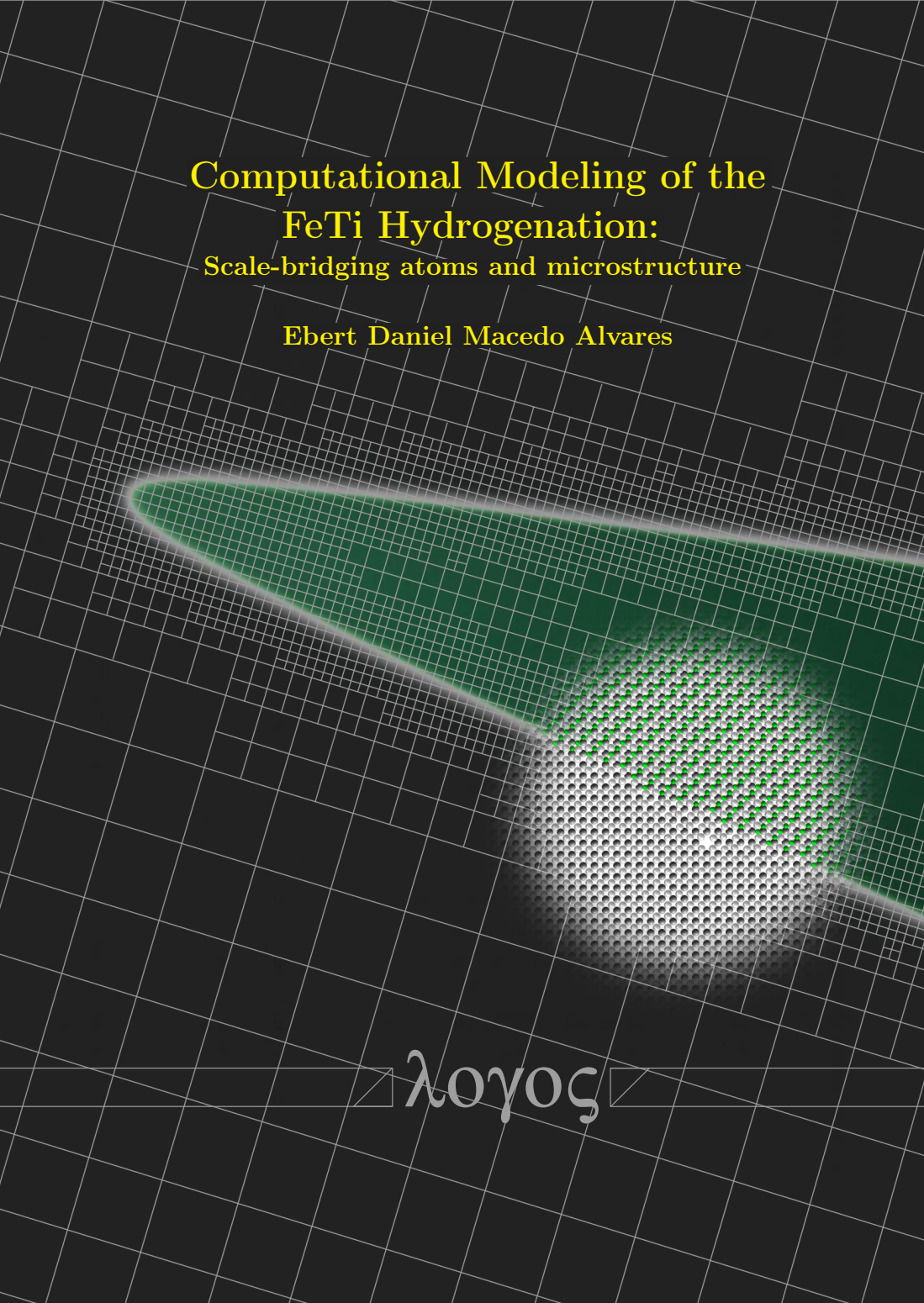

λογος

Computermodellierung der FeTi-Hydrierung

Ebert Daniel Macedo Alvares

Computermodellierung der FeTi-Hydrierung

Skalenüberbrückung von Atomen und Mikrostruktur

Logos Verlag Berlin

Bibliografische Information der Deutschen Nationalbibliothek
Die Deutsche Nationalbibliothek verzeichnet diese Publikation in der Deutschen Nationalbibliografie; detaillierte bibliografische Daten sind im Internet über http://dnb.d-nb.de abrufbar.

Logos Verlag Berlin GmbH 2026

ISBN 978-3-8325-6050-8
DOI: https://doi.org/10.30819/6050

Logos Verlag Berlin GmbH
Georg-Knorr-Str. 4, Geb. 10,
D-12681 Berlin
Germany

Tel.: +49 (0)30 / 42 85 10 90
Fax: +49 (0)30 / 42 85 10 92
http://www.logos-verlag.de

Contents

List of Figures

List of Tables

1 Introduction

1.1 Motivation and aims of the work

1.1.1 The hydrogen energy transition

The worldwide effort to limit the increase in global average temperature to well below 2 °C above pre-industrial levels [1] requires the development of a climate-neutral economy. To address this challenge, the European Green Deal has set ambitious targets: reducing greenhouse gas emissions by at least 55 % by 2030 and transforming Europe into the first climate neutral continent by 2050 [2]. Achieving these goals will require a fundamental transformation of energy production systems to reduce emissions.

A key component of this transition is the establishment of an energy production chain based on emission-free technologies. However, a significant challenge lies in the intermittent nature of current renewable energy sources, such as solar and wind. These sources are variable, producing excess energy under favorable conditions but insufficient energy when conditions are poor. This variability makes managing wasted energy an important task in the pursuit of a sustainable energy system.

In this context, hydrogen production powered by renewable energy, so-called "green hydrogen" offers a promising solution. Green hydrogen acts as an energy vector, capturing surplus energy during periods of high renewable production. This stored energy can then be used when renewable energy generation is low, helping to balance energy supply and demand. Thus, green hydrogen can play a vital role in the transition to a sustainable energy system [3].

Green hydrogen is particularly attractive because it is a renewable energy carrier that releases only water as a by-product when used [4, 5], closing its life cycle in a sustainable manner. This makes it an ideal candidate for reducing emissions across high-impact sectors, including transportation, industrial heating, chemical production, and steel manufacturing [6]. However, in order to fully integrate hydrogen into these sectors, advanced and reliable methods for hydrogen storage and delivery are essential.

Among the strategies being explored, stationary hydrogen storage systems

have gained significant attention. Acting as a buffer, these systems enable better control of energy production by storing the excess during periods of high renewable generation and releasing it when needed. This capability promotes a more efficient and resilient renewable energy infrastructure.

However, hydrogen storage presents its own challenges, as advanced technologies are required to ensure safe, efficient, and cost-effective storage. This need for improvement justifies the importance of ongoing research and technological development in hydrogen storage solutions to fully realize the potential of hydrogen as a reliable energy carrier in the transition to a climate-neutral economy. In the following sections, various hydrogen storage methods will be presented, along with a brief analysis of their advantages and drawbacks, highlighting the importance of a deeper phenomenological understanding of hydrogen's interaction with materials.

1.1.2 Hydrogen storage in molecular state

At first sight, the use of hydrogen as a fuel may appear to be an attractive strategy, as its elemental form is the lightest among all elements in the periodic table, and the combustion of hydrogen gas has the highest specific energy density, reaching $120\,\mathrm{MJ\,kg^{-1}}$ under ambient conditions [7]. This specific energy density is more than double that of conventional fossil fuels; for example, methane, gasoline, and diesel have 55.6, 46.4, and $45.6\,\mathrm{MJ\,kg^{-1}}$, respectively. However, under standard conditions, hydrogen is stable as a gas, resulting in a poor volumetric energy density of $0.003\,\mathrm{kW\,h\,L^{-1}}$ [8], which represents just a small fraction of that of, for example, methane, propane, and gasoline, 4.2, 7.1, and $9.0\,\mathrm{kW\,h\,L^{-1}}$ [9, 10].

Until the current technological stage, hydrogen has been stored mainly in its molecular form, as a compressed gas [11] or as a condensed liquid [12]. However, storing hydrogen in its molecular form presents intrinsic energetic disadvantages. This is because, to reach a volumetric energy density that is adequate, these molecular storage methods require additional work and heat to compress or liquefy the gas, which ultimately decreases the efficiency of using hydrogen as an energy carrier.

Figure 1.1 shows the comparison between the volumetric density of hydrogen in its molecular state as a function of pressure.

In theory, compressing hydrogen gas to 700 bar requires about 13 % to 18 % of its lower heating value (LHV) [14], while the work for liquefaction corresponds roughly to 10 % of the calorific content of hydrogen. In practice, however, efficiencies for liquefaction approach 30 %, elevating the energy required for these processes to increase to about 20 % to 30 % of the energy content of hydrogen [14, 15].

Further complications arise from a technological perspective. For example, gas cylinders are too heavy, and compressed hydrogen is therefore usually stored in lightweight carbon-fiber-reinforced composite tanks. These tanks, although lighter, are expensive due to their difficult manufacturing process, which imposes further complications for recycling. Moreover, even though

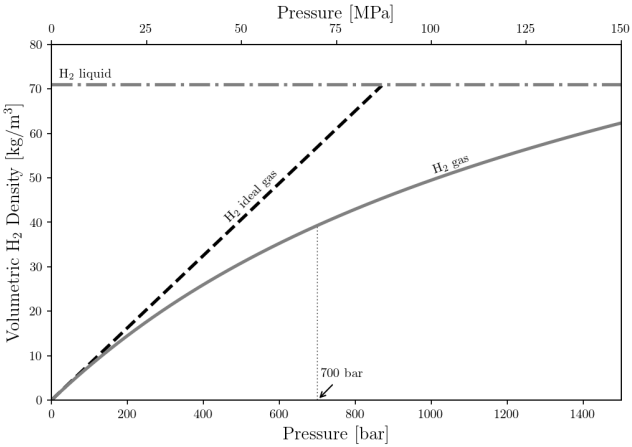

Figure 1.1: Comparison of volumetric hydrogen densities of liquefied, ideal and real gaseous hydrogen. The real hydrogen gas is plotted using Joubert's model [13] at 298.15 K.

they are stored in lightweight tanks, the energy density of hydrogen at 7×10^7 Pa (700 bar) is $5.6\,\mathrm{MJ\,L^{-1}}$, which is six times lower than that of the commonly used gasoline, which has a density of $32.0\,\mathrm{MJ\,L^{-1}}$.

In the same direction, hydrogen gas liquefaction requires a theoretical power input of $29.2\,\mathrm{kJ\,mol^{-1}}$, and since this involves additional mechanical work, the equivalent heat can be expected to be around 2.5 times higher. The heat of combustion of H_2 to liquid H_2O has a value of $285.93\,\mathrm{kJ\,mol^{-1}}$. In comparison, liquefying hydrogen gas represents 25 % of ideal efficiency [16].

Moreover, keeping the temperatures low necessitates additional components, which decrease the overall equipment volumetric and gravimetric storage capabilities. A further hurdle to molecular storage is the control of the boil-off. This phenomenon implies an estimated cost of 1 to 2 % daily hydrogen loss from the tank in mobile applications [7], which also creates problems in terms of fuel refueling frequency, cost, and safety [14].

1.1.3 Hydrogen storage as metal-hydrides

The possibility of storing a high volume of hydrogen in metals has been the subject of study since 1866, when Thomas Graham reported that palladium could massively absorb (at that time referred to as "occlude") 935 times its own volume of H_2 [17]. However, only in the 1960s, after almost a century, did metals begin to be investigated for hydrogen storage purposes [18]. Metal hydrides as solid-state hydrogen storage materials have several ad-

vantages over other classes of hydrogen storage media, owing to their high volumetric capacity and great hydrogen retention characteristics, allowing for nearly loss-free hydrogen storage during dormancy [19, 20]. In addition, metal hydrides are often considered safer storage solutions for applications where safety is a concern, since their (de)hydrogenation cycles can operate under mild conditions compared to compressed gas-based storage, which requires extremely high pressures [21, 22]. Their exceptional properties are a manifestation of the thermodynamics of the phase transformations governing the hydrogenation of these materials in the presence of hydrogen activity, which are explored in the following sections.

Fundamentals of the thermodynamics of *binary* metal-hydrides

Hydrogen reacts with many different elements to form various compounds and is usually classified by chemical bond type. Metallic hydrides, by the nature of metallic bonding, commonly exist over extended ranges of nonstoichiometric compositions and can be called interstitial alloys since hydrogen usually occupies interstitial sites of the metallic lattice [23].

The absorption of hydrogen in metals generally proceeds through several stages. First, physisorption occurs, where hydrogen is stabilized on the metal's surface by van der Waals forces. Next, in chemisorption, molecular hydrogen dissociates into atomic hydrogen (H) on the surface of the host material, forming metal-hydrogen chemical bonds. Following this, hydrogen atoms diffuse into the metal's bulk and generate a solid solution of hydrogen within the interstitial sites of the metallic lattice [24].

As the partial pressure of hydrogen increases, the solid solution can transition into a hydride phase, commonly referred to as the α- to β-phase transformation. This transformation continues until the α phase is fully converted to the β phase, provided that external thermodynamic conditions favor the stability of the hydride phase (β) over the solid solution phase (α).

In some materials, the metallic structures of the hydrogen solid solution and the hydride are quite similar. At higher temperatures, even under high pressure, hydrogen atoms tend to be randomly distributed within the lattice, making phase boundaries indistinct. However, at lower temperatures, hydrogen atoms may adopt a more ordered distribution within interstitial sites. This arrangement of hydrogen distribution can be interpreted as a spinodal decomposition if the crystal structure is significantly similar, as well as the formation of a completely new phase, depending on how substantial the changes in the crystal structure are for establishing distinct phase boundaries. The origin of phase separation arises from the interactions among dissolved hydrogen atoms, which incorporates both elastic and electronic contributions.

The structural changes associated with the transition from solid solution to hydride, particularly at low temperatures, can give rise to unique material properties. Often, after the completion of hydride formation, the hydride

itself undergoes additional structural adjustments to accommodate a larger number of hydrogen atoms within its interstitial sites.

Because of these combined structural and thermodynamic effects, the storage of hydrogen as a metal hydride offers several technical advantages. First, the volumetric hydrogen density can reach higher values in the hydride form because hydrogen atoms are more densely packed within the metal-hydride lattice compared to the liquid or compressed gas states. Second, metal hydrides can enhance safety since their decomposition is typically an endothermic process, requiring a change in external conditions and additional input energy to release hydrogen. This energetic input requirement reduces the risk of explosive reactions, providing an inherent safety mechanism.

Yet, the stability of the hydride should be considered for technical applications. If the forming compound with hydrogen is too stable or too unstable, it may not be worth reversing the reactions, as it then requires higher energy levels and other technical complications to make the process cyclic [16]. Investigating the stability of hydrides is therefore a necessary step when assessing the potential applications of metal hydrides. Their stability analysis involves understanding the thermodynamics of the hydrogenation process, which is generally characterized by evaluating their pressure-composition isotherm (PCI) curves [24].

In an ideal scenario for a *binary* metal-hydrogen system, the complete equilibrium between the bulk α, β solid phases and the hydrogen gas occurs in a defined pair of pressure (P) and temperature (T), at which all phases should present equal values of thermodynamic potentials. At this condition, the material system presents a flat plateau in the PCI curve. With increasing temperature, the pressure at which the plateau occurs increases, while the composition range of the plateau shrinks. Above a certain critical temperature (T_c), the plateau vanishes and the α-β transformation becomes a second-order thermodynamic transition, and the formation of the hydride becomes a continuous structural transformation upon pressure increase, from which phase separation is diffuse and unclear.

Below T_c, the hydride phase, or β-phase, is clearly distinct from the solid solution and grows when the hydrogen chemical potential, or hydrogen partial pressure, surpasses that of the plateau at a constant temperature. The formation of the hydride in this case involves nucleation and growth from the hydrogen supersaturation within the interstitial sites of the α phase.

The schematic representation of the properties of PCI curves over temperature and their associated description of a van't Hoff plot, together with a schematic illustration of the α-β structural transformation, is shown in Figure 1.2.

In general terms, the formation of the hydride can be seen as being controlled by concurrent thermodynamic factors, namely the enthalpy (ΔH_r) and the entropy (ΔS_r) of the reaction. These thermodynamic parameters characterize the variation in enthalpy and entropy of the hydride in relation to the metal plus the hydrogen gas states.

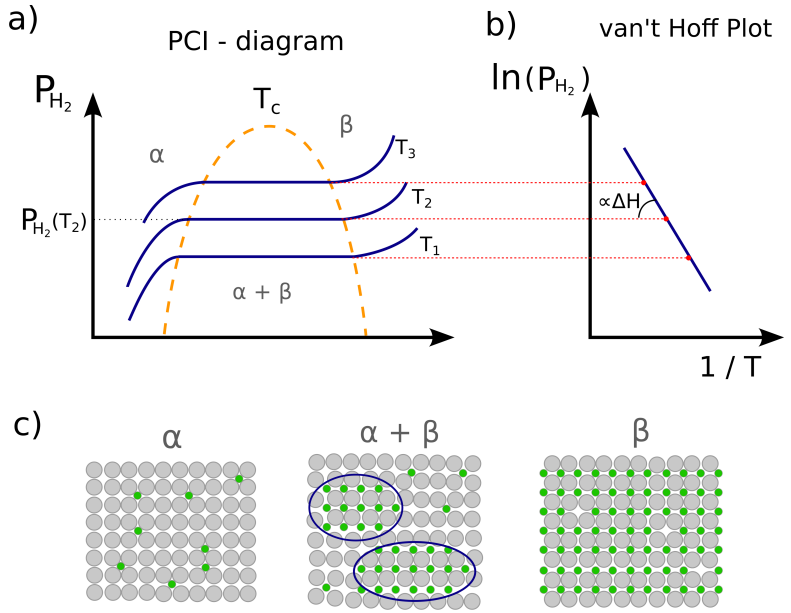

Figure 1.2: Schematic diagram of structural and thermodynamics of hydride formation. a) General behavior of PCI curves over temperature, with $T_1 < T_2 < T_3$. b) The associated van't Hoff Plot of curves shown in (a); c) Schematic illustration of the structural transformation of α-β transformation. The schematic diagram is an adaptation from the work of M. Dornheim [24].

As the main contribution to the entropy of the reaction comes from the change in entropy between hydrogen in gas form and its crystalline state within the interstitial site of the crystal, the reaction enthalpy can be considered the primary engineering parameter for materials design, which is introduced in the next subsection 1.1.3.

From the assumption of the equilibrium condition, i.e., the same hydrogen chemical potential (μ_H), the enthalpy and entropy over the constant pressure region of the phase diagram can be described by applying the isothermal Gibbs energy to the van't Hoff equation to derive its linear form (Equation 1.1) [24]:

$$\frac{1}{2}\ln\left(\frac{P_{eq}}{P_0}\right) = \frac{\Delta H_r}{RT} - \frac{\Delta S_r}{R}, \tag{1.1}$$

where P_{eq} represents the equilibrium or plateau pressure; P_0 is the standard pressure (101 325 Pa), and T is the varying temperature. Consequently, values of ΔH_r and ΔS_r are obtained, respectively, by the slope and the y-intercept, as shown in Figure 1.2b).

The thermodynamics of hydrogen adsorption/desorption govern their temperature and pressure range of applicability and can be analyzed through Equation 1.1 by performing a linear regression on the plot of the logarithm of the plateau pressure as a function of the inverse of isotherm temperatures (illustrated in Figure 1.2*b*)).

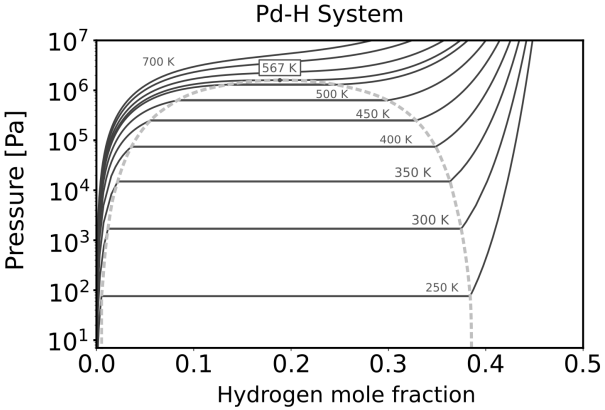

Figure 1.3: Calculated PCI curves for the Pd-H system over different temperatures. The plot shows the variation of plateau range for first-order phase transition up to its critical temperature. The PCI curves were calculated for 250 K to 700 K with steps of 50 K, including the calculation at the critical temperature 567 K. The calculations are performed with CALPHAD model provided by Joubert and Thiébaut [25].

The palladium-hydrogen system is a typical example used to discuss the thermodynamic properties introduced here. The hydride formed from the palladium metal has the same basic structure as the metal. The volume change of the solid-solution α-phase is negligible. In contrast, the β-phase has a volumetric expansion of approximately 11 % relative to the pure metal. At lower temperatures (below T_c =566 K) the α-β transformation is a first-order thermodynamic transition, and the plateau pressure of the PCI is clearly defined. Figure 1.3 illustrates the calculated PCI curves for the Pd-H system based on the model of Joubert and Thiébaut [25], which is adjusted to experimental data.

The plateau pressure represented in red in Figure 1.3 is an invariant of the pressure-composition phase diagrams for a constant temperature. They represent the unique set of thermodynamic potentials that equalize the hydrogen

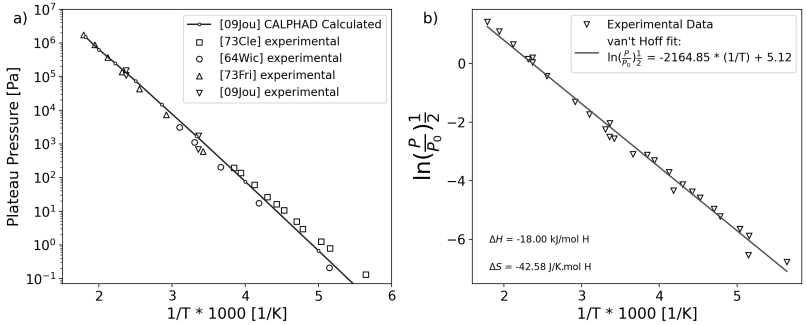

Figure 1.4: Equilibrium pressure over temperature. a) Calculated and experimental data of PCI curves of the Pd-H system with superimposed experimental data. The calculations are performed with CALPHAD model provided by Joubert and Thiébaut [25], and experimental data from 73Cle [26], 64Wic [27], 73Fri [28], and 09Jou [25]. b) Linear regression of the van't Hoff equation for the same experimental data from a).

chemical potential of the hydrogen solid-solution (α-phase), the hydride (β-phase), and the H_2 gas. By fixing these conditions within the thermodynamic model, i.e., requiring that these phases are in equilibrium, the temperature and pressure pair that satisfy such constraints can be calculated. The results of such calculations are shown in Figure 1.4*a*).

Note that by applying the proposed technique of the van't Hoff plot combined with the linear regression of the experimental data presented in Figure 1.4*b*), the values of reaction enthalpy and entropy can be determined. Using the CALPHAD model, these values are obtained by calculating the difference in enthalpy and entropy between the final and initial states of the system. From an experimental perspective, the thermodynamic aspects of metal hydride systems are straightforward but are sometimes limited to evaluating logarithmic plateau pressures against $1/T$. However, there are many other aspects of the thermodynamics of these systems.

Beyond the thermodynamics of bulk *binary* metal-metal hydride systems

One important aspect beyond the van't Hoff equation is the difference in experimental plateau pressure when measuring absorption or desorption curves, known as hysteresis. In fact, the equilibrium pressure-composition isotherm represents the state that would be observed if there were no boundaries between the solid-solution and the hydride phase. In reality, during absorption, the pressure must exceed that of the bulk equilibrium to begin transformation; during desorption, the pressure must drop below that to decompose

the hydride. The enthalpy derived from high-precision calorimetry measurements of binary hydrides confirms this. For example, the data measured for Pd-H have the same absolute value of ΔH_r for desorption and absorption [29], which confirms that the reversible α-β phase transition should be exact reverses of each other.

To understand the difference between PCI and calorimetric results, Flanagan and Oates [30] suggested that an ideal bulk thermodynamic equilibrium between the three phases should occur at a pressure level between the measured absorption and desorption plateau pressures. The conclusion is based on thermodynamic principles, as they demonstrated that these reactions would not generate entropy otherwise. In addition, they proposed that the evolved driving force, manifesting as heat from overcoming activation barriers, is partially the reason for the hysteresis.

An important aspect to note is that plateau pressures are invariant points (Gibbs phase rule) only in *binary* metal hydride systems; however, metal hydrides are often generated from intermetallic compounds or alloys. In substitutional alloys, for example, the Pd-Pt-H system, the complete equilibrium between the α, β, and gas phase implies a different metallic composition between the metallic solid solution and the hydride, and a "sloping plateau" is expected.

For metallic systems of higher than unary complexity, the thermodynamics of hydrogenation is often a phenomenon not in complete equilibrium. Instead, a paraequilibrium state governs the hydrogenation process. In this case, the metallic elements behave as a unique species due to their much lower mobility in comparison to the rapid diffusivity of hydrogen in the interstitial lattice and resemble a "frozen" metal situation. The system in this case can be referred to as pseudobinary hydrides. Under para-equilibrium conditions, only the chemical potential of the fast diffusing species, in this case hydrogen, is equal across all phases. The alloy composition, however, remains constant due to the slow mobility of metallic species, which maintain their chemical potential gradient through the different condensed phases [31, 30]. The concept of paraequilibrium will be explored further in Chapter 3 and Section 3.2.1.

Despite being different from what occurs in the bulk, in multicomponent metallic systems, even at paraequilibrium, a local equilibrium among the metals at the interface may exist. If this is the case, there is an induced compositional variation at the interface relative to the bulk, which may also influence the aspect of the PCI curve, e.g., inducing a sloped plateau [31, 30].

Furthermore, the variation of specific volume and composition between metal and hydride phases generates misfit strains and perturbed chemical bonds at the metal-hydride interface. Therefore, during the metal-metal hydride phase transformation, macroscopic energy barriers are induced, which have different natures during the hydrogenation and dehydrogenation processes. These differences partially explain the observed hysteresis [32, 33, 34].

These effects beyond bulk equilibrium have a substantial impact on hydrogenation properties. Since hydride formation often follows nucleation and

growth mechanisms, the characteristics of the interface between solid phases become critical. The interphase boundary energy includes a chemical component, arising from perturbed atomic bonds at the interface, which adds an energetic contribution to the system's total free energy. This chemical contribution scales with the area of the interphase boundary. Additionally, the lattice mismatch between the metallic and hydride phases introduces elastic strain energy within the boundary region, a mechanical contribution that scales with the volume of the forming phase.

The interplay between these chemical and mechanical contributions, along with bulk thermodynamic effects, is key to understanding hydrogenation mechanisms. In order to minimize the total free energy of the system, these contributions are balanced and dynamically adjusted against each other, thus driving the evolution of phase morphology and influencing the microstructure and kinetics of hydrogenation. These effects are further discussed in Chapter 4 and Chapter 5.

The interest of alloying and intermetallics as hydrogen storage media

Among metal hydrides, those based on binary intermetallic compounds with the general formula AB_n exhibit the thermodynamic and kinetic properties envisaged for hydrogen storage purposes. Elemental hydrides of early (A) and late (B) transition metals generally possess high negative and positive formation enthalpies (ΔH_f), meaning that they form very stable and very unstable hydrides under standard conditions, respectively [35]. In Figure 1.5, a periodic table of elements is illustrated that shows the data compiled from the formation enthalpy in Table 6.6.1 of Griessen and Riesterer [36] and Table 1 from Griessen and Driessen [37] for most binary metal hydrides of interest. For some elements, where only the heat at infinite dilution ($\Delta\overline{H}_\infty$) was available, this value was used to estimate the formation enthalpy of the corresponding monohydride.

It is often observed that combining elements A and B in specific ratios (e.g. $n = 1, 2, 3, 5$) promotes the formation of stoichiometric intermetallic compounds, ABn, which is accompanied by a reduction in the absolute value of the formation enthalpy, ΔH_f, of their corresponding ternary hydrides [38]. This reduction leads to the formation of ternary hydrides with intermediate stability, which enhances the reversibility of hydrogenation under conditions close to ambient temperature and pressure. This provides a safer hydrogen storage medium compared to molecular hydrogen tanks, which require either extremely high pressures or very low temperatures [35, 38].

Operating near ambient conditions is particularly advantageous when these materials are intended for use in residential or domestic areas. Furthermore, these intermetallics exhibit considerable variability in hydrogenation thermodynamics and kinetics when their base components are partially substituted with other suitable metals. This suggests a promising avenue for

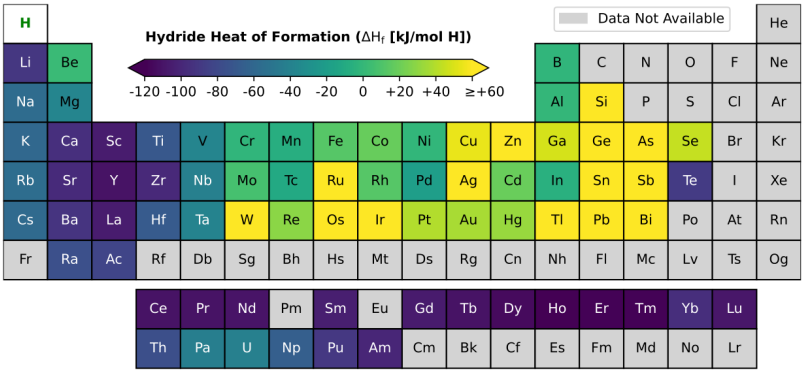

Figure 1.5: Enthalpy of formation of binary hydrides. Compiled data from experimental [36] and theoretical [37] results. For elements to which only the enthalpy of infinite dilution was available, it was used to estimate the enthalpy of formation.

tailoring these compounds to optimize performance for specific applications [38].

For vehicular applications, for example, the optimum operating pressure-temperature window for proton exchange membrane (PEM) fuel cells is in the range of 1×10^5 to 1×10^6 Pa (1 to 10 atm) and 298 to 393 K (25 to 120 °C), which represents the hydrogen delivery pressure required by the fuel cell and the temperature of waste heat available from the fuel cell for use by the storage system for hydrogen release [14]. The commercial $LaNi_5$ intermetallic metal-hydride is an example of a material capable of reversibly storing hydrogen under such operating conditions. It suffers, however, from poor gravimetric capacity. Another example, which is lighter and possesses similar operating properties, is the FeTi intermetallic. Even though the weight-related capacity of these materials is poor for mobile applications, research on how to benefit from alloying thermodynamics to modify their chemical composition with lightweight materials while fine-tuning their thermodynamic properties to preserve or enhance their reversible storage capacity is an active field of research [39, 40].

1.1.4 FeTi as solid-state hydrogen storage material

Among intermetallic compounds that reversibly store hydrogen [41], FeTi is recognized as a key material due to the possibility of large-scale production, owing to its relatively low cost compared to other intermetallic compounds. Besides, its application as a solid-state hydrogen storage material potentially poses no significant complications for reuse. FeTi has a gravimetric

and volumetric capacity of 1.87 wt% H_2 and 105 kg H_2/m^3 [35], respectively, and combines good sorption kinetics and reversibility within operating regime ranges near room temperature and atmospheric pressure. Figure 1.6 schematically compares the molecular and FeTi hydride hydrogen storage methods from an atomistic perspective. The reversible volumetric capacity of FeTi (83.7 kg H_2/m^3) [21], as well as many other metal-hydrides (MHs), even surpasses cryogenically liquefied hydrogen (71.42 kg H_2/m^3 at 20 K) [22].

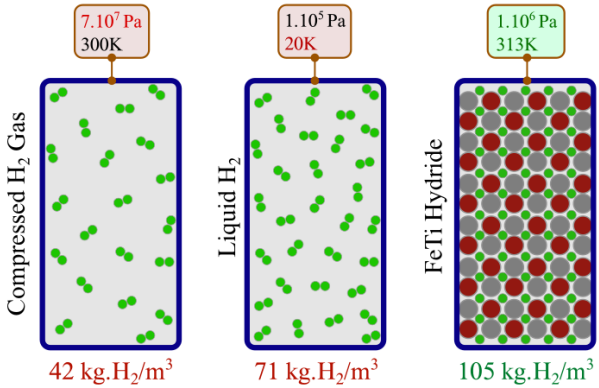

Figure 1.6: Illustration of the difference between molecular and FeTi metal-hydride hydrogen storage methods [21, 22, 35].

Furthermore, the high hydrogen storage capacity near ambient conditions is economically advantageous, as the energy-intensive processes of compression to elevate pressures and cryogenic cooling can be avoided. Moreover, hydrides present the additional benefit of offering a safer alternative for system integration. The necessity of altering their thermodynamic conditions to release hydrogen inherently mitigates potential explosive reactions. Therefore, FeTi-based materials represent an excellent storage option when the weight of the system is not a concern, e.g. hydrogen supply for residential environments, emergency power supply, and heavy-weight means of transportation like trains, ships, long-haul trucks, etc. [42, 43].

It is worth noting that previous extensive studies have focused primarily on the processing and alloying of FeTi to improve the performance of hydrogen storage [44, 39]. Relevant computational efforts have centered on atomic-level DFT calculations of bulk properties or reaction barriers to hydrogenation [45, 46, 47, 48, 49], as well as hydrogen interactions with surface oxide layers in terms of initial activation [50].

1.1.5 The use of computational methods for solid-state hydrogen storage: aims of this work

The (de)hydrogenation of metal hydrides is a complex, multistage process involving surface reactions, hydrogen diffusion, and phase transformations, all of which drive the nucleation and growth between metal and hydride phases. Understanding these processes requires unraveling both the thermodynamics and kinetics of phase transformations and the resulting microstructural evolution in the storage materials. In this context, computational modeling and simulation methods offer valuable insights by allowing researchers to identify the rate-limiting mechanisms and critical driving factors that govern hydrogen storage performance and reversibility.

To address the multiscale nature of these complex chemical, physical, and material processes, integrating computational methods that can operate effectively across different lengths and timescales is essential. For instance, a successful approach may involve combining atomic-scale simulations (e.g., first-principles calculations) with thermodynamic modeling (e.g., CALPHAD) or mesoscopic kinetic modeling (e.g., phase-field modeling). Combining these methods has the potential to provide a deeper understanding of how atomic and microscopic phenomena influence the macroscopic properties and behavior of storage materials, including the thermodynamics of intermediate and product phase formations.

In particular, three key computational capabilities are the central aim of this work: calculation of atomic structural properties, thermodynamic calculations, and a phase-field modeling and simulation method. The thermodynamic method predicts the tendancy of the bulk phase fractions of intermediate and product phases based on minimizing the system's total free energy under specified conditions. The thermodynamics are enhanced by introducing effects beyond the bulk properties, for example by accounting for effects of interface and surface energies. All these properties can be derived from first-principles methods through density functional theory (DFT). These methods provide critical insights into how storage materials behave under varying conditions, such as different hydrogen pressures, temperatures, and particle sizes, which are crucial for optimizing storage performance. The phase-field modeling (PFM) approach, on the other hand, employs a continuum description of non-equilibrium kinetics to simulate the evolution of microstructures over broad time and length scales. Its flexibility in describing complex microstructural configurations makes PFM an exceptionally powerful tool for modeling the kinetic processes of phase transformations, particularly under conditions that closely resemble those in practical hydrogen storage applications.

This thesis focuses on the FeTi alloy as a case study to develop a quantitative, multi-physics computational model that bridges various theoretical levels of analysis. By integrating atomistic and mesoscale computational methods, this work aims to develop a model to accurately simulate the (de)hydrogenation processes in FeTi, enabling more precise predictions of its hydrogen storage properties. Importantly, the larger-scale simulations

rely on atomistic parameters to characterize essential physical and chemical features, thus underscoring the importance of accurate atomic-scale data in achieving reliable, higher-level predictions.

The novelty of this approach lies in the link between a detailed multi-scale modeling and simulation framework, which incorporates advances in thermodynamic assessments, interphase boundary modeling, and phase-field modeling and simulations to handle compositional, structural, and elastic inhomogeneities within the hydrogenation processes of the FeTi hydrogen storage material. By accounting for these complexities at the atomic level, the model provides a more realistic and quantified representation of mass transport and phase transformations of the material.

By applying cross-scale fundamental properties for the development of the model proposed in this work, the phenomenological and thermodynamic properties of the system should emerge as inherent characteristics during simulations. Ultimately, this work aims to enhance the predictive capabilities of computational tools for hydrogen storage in FeTi, offering a more robust platform for further development of this material, allowing for predictive simulations and the inclusion of new elements and other microstructural features, thereby enabling the discovery of better processing routes, improved material performance, and enhanced reversibility.

1.2 Outline of the work

Chapter 2 presents the methodology, architecture, and theoretical foundations used in this doctoral thesis. The chapter is divided into three sections that present an introduction to the fundamentals of first-principles quantum mechanical analysis, followed by a description of computational thermodynamics with a focus on the CALPHAD method and the thermodynamic models utilized. The last section describes the concept and coupled phase-field equations employed for the FeTi hydrogenation simulations.

Chapter 3 begins with a detailed review of the thermodynamics of the stability of the phases involved in the hydrogenation processes of the Fe-Ti-H system. Subsequently, it presents an in-depth and step-by-step approach to combining theoretical calculations and experimental information to perform a CALPHAD-based thermodynamic assessment of the FeTi-H system. Furthermore, the capability of the resulting model and its usefulness for accurately calculating the equilibrium properties within the FeTi-H system are demonstrated, showing that it can serve as a basis for the development of the subsequent phase-field model.

Chapter 4 presents a versatile method for investigating the surface and interface characteristics of interstitial metal-hydrides. This method is then used to determine these characteristics for the FeTi, FeTiH, and H_2 gas. At the beginning of this chapter, the quantification of the surface energy of the most relevant surfaces is calculated. In the following, a new method for decoupling the chemical contribution to the interfacial energy between metals

and their corresponding interstitial metal-hydrides is demonstrated from different approaches. To conclude the chapter, these chemical contributions are used within a micromechanical analysis that reveals the preferential morphological evolution of the hydride phase with excellent agreement to Transmission Electron Microscopy (TEM) micrographs of the hydride morphology.

Chapter 5 concludes this work's discussion by demonstrating the implementation of the many physical quantities acquired in the previous chapters into a phase-field model for the quantitative simulation of FeTi hydrogenation. The capabilities of the developed model are demonstrated through phase-field simulations, which were conducted to validate the implementation and assess the model's quantitative accuracy in reproducing standard and expected outcomes. This demonstrates the model's potential for use in more advanced simulations aimed at revealing mechanisms and evaluating the performance of the alloy under operating conditions.

Chapter 6 summarizes the findings of the present work and provides an outlook, leading the path for future implementations and the expansion of the model with proposals to further analyze AB alloys for hydrogen storage.

2 Theoretical Foundations

This chapter introduces the methodology and the theoretical foundations discussed in this doctoral thesis. The methods are introduced based on their length scale and the relevant cascade propagation of the calculated properties. Therefore, the reader can expect that the chapters will have some level of dependency on the quantities discussed in the previous chapters. In general, the methodology is divided into three different levels: *atomistic level*, *thermodynamic level*, and *mesoscale level*.

2.1 Methodology overview

Fundamentally, the methodology presented in this thesis represents an integrative approach that interconnects three primary computational techniques in materials science to model the hydrogenation process. Conceptually, the developed framework is extensible to the simulation of various interstitial metal-hydride systems and, with minor adaptations, is applicable to other material classes. Figure 2.1 illustrates the comprehensive framework for the development of this thesis, as well as the major supporting software packages along with their functionalities relevant to the proposed methodology.

From the *atomistic level*, first-principles quantum mechanical calculations are used to acquire the equilibrium crystal structure of the compounds of interest. The capability of calculating the total energy of these compounds, their relationships, response to strain, and chemical interactions is analyzed. These analyzes provide essential properties, e.g., formation and reaction enthalpies, elasticity, and equilibrium lattice parameters, that are key pieces of information to inform higher-level models, as well as to derive mechanical properties that are hard or practically impossible to measure experimentally.

In the *thermodynamic level*, the thermochemical properties obtained from quantum mechanical calculations are subsequently used to support the assessments of the thermodynamic models. Computational thermodynamic techniques are essential for describing the equilibrium composition and the fraction of each phase in the system. Fundamentally, any diffusion-driven kinetic model relies on driving forces derived from the hypersurface energy densities of material systems. Therefore, the models obtained in this phase

of the methodology can be regarded as the backbone of the entire process, guiding the intensity and direction of the involved phenomena.

At the *mesoscale level*, the interfacial energies, elastic energies, diffusion barrier, and bulk energy densities derived from quantum mechanical calculations are combined with the optimized computational thermodynamic model to develop a quantitative-based mesoscale phase-field model capable of accurately simulating phase transformations under different external conditions.

Software packages

For first-principles quantum mechanical calculations, version 6.2.1 of the Vienna Ab-initio Simulation Package (VASP) was employed [51, 52, 53, 54]. Thermodynamic equilibrium calculations and the optimization of thermodynamic model parameters were performed using version 6.25 of the OpenCalphad software [55], along with version 10.2 of PyCalphad [56] and version 8.9 of ESPEI [57] software packages. Phase field simulations were performed by resolving the system of partial differential equations using the finite element method (FEM) as implemented in the MOOSE framework [58].

2.2 Introduction to First-Principles calculations

This section introduces the basis for the first-principles calculation methods that are employed in this thesis to quantify the fundamental material properties needed to upscale the simulations. The following sections provide an overview of the theoretical background. For further information, the reader is referred to the following textbooks and overview articles [59].

2.2.1 Quantum mechanics calculations and its use for thermodynamic modeling

The strong link between thermodynamic state functions and the crystallography of compounds becomes apparent when electronic structure is considered. At zero Kelvin ($T = 0$) and constant pressure, the crystal structure of an atomic system is determined by minimizing the enthalpy ($H = U + PV$), where P is the pressure, V is the volume, and U is the internal energy. This demonstrates how the crystal structure that minimizes the enthalpy corresponds to the thermodynamically stable phase.

As will be presented in subsequent sections, the internal energy U, often called E_{total}, can enhance thermodynamic evaluations due to its intrinsic connection to fundamental quantities, e.g., pressure ($P = -\left(\frac{\partial U}{\partial V}\right)$) and bulk modulus ($\kappa = -V\left(\frac{\partial^2 U}{\partial V^2}\right)$). Ultimately, the possibility of accurately calculating the internal energy and exploring the interconnection between thermodynamic fundamentals are highly useful for modeling thermodynamic kinetic properties in scales far beyond the atomic level.

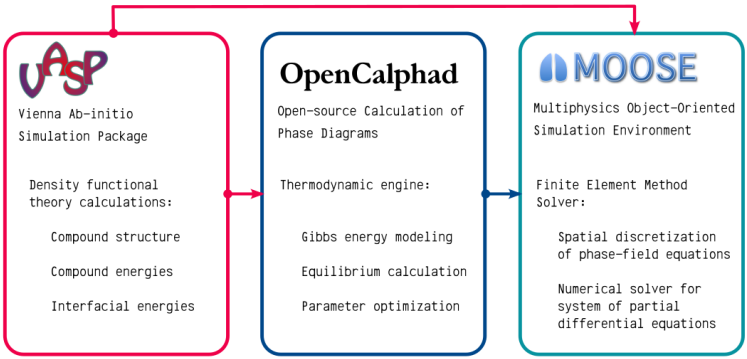

Figure 2.1: Overview of the methodology and major software packages employed for this thesis work.

In this context, quantum mechanical computations serve as a pivotal tool for determining the energies of compounds and consequently for elucidating their theoretical thermochemical properties. This capability is of paramount significance because certain properties, integral to thermodynamic modeling, pertain to compound structures that are mechanically or chemically unstable under actual thermodynamic conditions. Such instabilities render empirical measurement of these properties either impractical or exceedingly challenging with conventional experimental methodology. Fortunately, quantum mechanics allows for the calculation of these properties, and by integrating these computed properties into thermodynamic models, whether partially or completely, the precision in the evaluation of material systems can be significantly enhanced.

Validating the calculations is an important step when employing quantum mechanics calculations. One way of doing it is to find the minimum of U, or the conditions where $P = 0$, for a crystal system, and derive properties such as the equilibrium volume V_0 and the bulk modulus. As these quantities are measurable, it is possible to validate the calculation by comparing them with the extrapolated measured quantities to 0 K.

The ability to calculate the total energy of a given ground state crystal structure opens up a venue for the use of thermophysical fundamentals to handle these calculated quantities to obtain many other interesting properties; most of them are unachievable or hard to acquire by any other methods. The use of these calculations and their relations to obtain key parameters for computational thermodynamics and mesoscale simulations will be presented throughout this thesis.

2.2.2 Schödinger equation and the many-body problem

Quantum mechanical treatment requires solving the Schödinger equation (Equation 2.1) for each atom in the system, meaning that to find the ground state ψ, and its corresponding energy E, the kinetic and potential energies (Hamiltonian, or Hamilton operator, $\hat{H}$) for all species in the system should be calculated.

$$\hat{H}|\psi\rangle = E|\psi\rangle. \tag{2.1}$$

The Hamiltonian of the system, $\hat{H} = \hat{T}+\hat{V}$, can be represented as the sum of the kinetic and potential operators for each species (such as electrons and atomic core, denoted as $\hat{T}_e$ and $\hat{T}_c$, respectively) in the system, along with the sum of various operators for the Coulomb energy interactions between the charged particles (electron-electron ($\hat{V}_{e-e}$), electron-core ($\hat{V}_{e-c}$), and core-core ($\hat{V}_{c-c}$) interactions).

$$\hat{H} = \hat{T}_e + \hat{T}_c + \hat{V}_{e-e} + \hat{V}_{e-c} + \hat{V}_{c-c} \tag{2.2}$$

The number of atoms in real systems is on the order of Avogadro's number, rendering the problem virtually intractable. Furthermore, the particles are coupled, which implies that the interactions between electrons and between electrons and cores exert a mutual influence on the entire system, which reciprocally affects the individual species. This phenomenon is referred to as the many-body problem.

Born-Oppenheimer approximation

The so-called *Born-Oppenheimer approximation* was a first simplification to address the many-body problem. It consists of treating the dynamics of the electrons as decoupled from the dynamics of the nuclei. Given that atomic cores typically move more slowly and possess much lower kinetic energy compared to electrons due to their substantial mass difference, one can fix the positions of the cores and solve the electronic component independently to determine the energy gradient, which can then be used to adjust the core positions iteratively until a relaxed structure is created. By excluding the atom core kinetic energy operator ($\hat{T}_c$) and the core-core interaction potential energy operator ($\hat{V}_{c-c}$) from the Hamiltonian, the electronic Schrödinger equation is then given by

$$(\hat{T}_e + \hat{V}_{e-e} + \hat{V}_{e-c})|\psi\rangle = E_e|\psi\rangle. \tag{2.3}$$

However, this approximation alone does not solve the problem because, for a system larger than one Helium atom, the many-body problem persists due to the electrons being a set of many moving and interacting particles. Knowing that a single electron $|\psi_i\rangle$ possesses a three-dimensional spatial function in addition to a spin function, for each electron i sampled in the

problem, a set of four coordinates (three spatial plus one spin function) is added to the total wavefunction $|\psi\rangle$. With just a few data points in each spatial dimension, an atom with a half dozen electrons requires a data storage capacity that far exceeds the sum of the entire world's computational infrastructure capacity.

2.2.3 The density-functional theory (DFT) and its approximations

The many-body problem makes the analytical calculation of the internal energy via electronic structure theory, including electron correlation effects, an impossible task even for a simple crystal. It was only made treatable with the advent of density-functional theory (DFT), for which the 1998 Nobel Prize was awarded. The theoretical framework was pioneered in the 1960s by Pierre Hohenberg, Walter Kohn, and Lu Jeu Sham [60, 61]. The key feature of DFT is that fundamental system properties, like energy or structure, are not calculated via the wave function but rather the electron density as the central quantity. This reduces the complexity of the problem because now, instead of $4N_i$ coordinates for each electron i (three coordinates plus one spin function), only four are required to describe the system. They demonstrated its applicability through the formulation of two fundamental theorems.

The Hohenberg–Kohn theorems

The first theorem postulates that the electron density in the ground-state ($\rho_0(\vec{r})$) uniquely determines the Hamiltonian (except for a constant ($V_{c-c}[\rho]$)) and that, consequently, the ground state energy is a unique functional of $\rho(\vec{r})$, where $\vec{r}$ denotes a spatial vector.

$$E_0 = E[\rho_0(\vec{r})]. \tag{2.4}$$

The second theorem asserts that the exact ground state energy is the global minimum for a given external potential $V_{\text{ext}}(\vec{r})$ (coming from the atomic core), and the $\rho(\vec{r})$ electron density that minimizes the functional is the exact ground-state density.

$$E[\rho(\vec{r})] > E_0[\rho_0(\vec{r})]. \tag{2.5}$$

Although the description of the system based on the electron density simplifies solving the static Schrödinger equation, the Hamiltonian must now be represented as a functional of $\rho(\vec{r})$. No analytical functional for this purpose is known, but the so-called Kohn-Sham equations have shown an effective method to approximate this elusive functional.

The Kohn-Sham equations

Based on their theorems, Kohn and Sham introduced a set of equations capable of transforming the many-body problem into a set of single-particle equations. They simplified the problem by introducing an effective Hamiltonian for non-interacting electrons (expressed as a functional $\rho(\vec{r})$), which was assumed to possess the same density as the real system. The Kohn-Sham equations are Schrödinger-like equations derived by introducing a set of non-interacting reference single-particle orbitals that reproduce the same $\rho(\vec{r})$ as the fully interacting system.

The derivation of the Kohn-Sham equations commences with the postulation that an indeterminate exchange-correlation functional, $E_{xc}[\rho]$, encapsulates all non-classical electron interactions. Specifically, this encompasses the exchange-correlation energy contributions that persist beyond the *classical* kinetic energy functional ($T_e[\rho]$), the Hartree density functional, $V_H[\rho]$ (representing the classical Coulomb repulsion functional), which constitutes a component of the electron-electron interaction functional ($V_{e-e}[\rho]$), and the electron-core interaction functional ($V_{e-c}[\rho]$), which, in this context, corresponds to the external potential $V_{ext}[\rho]$. From this concept, the expression for the exchange-correlation functional is part of the total energy, allowing to recast the energy functional as:

$$E_e[\rho] = T_e[\rho] + V_H[\rho] + V_{e-c}[\rho] + E_{xc}[\rho]. \tag{2.6}$$

where the introduced $E_{xc}[\rho]$ is given by

$$E_{xc}[\rho] = (T[\rho] - T_e[\rho]) + (V_{e-e}[\rho] - V_H[\rho]). \tag{2.7}$$

Kohn and Sham used the variational principle applied to the whole electron energy density functional with respect to the orbitals to derive the equations that determine the single-particle wavefunctions, yielding:

$$\left[-\frac{\hbar}{2m_e}\nabla^2 + v_{\text{eff}}(\vec{r})\right]\psi_i(\vec{r}) = \epsilon_i\psi_i(\vec{r}), \tag{2.8}$$

where $\psi_i(\vec{r})$ are the Kohn-Sham orbitals, ϵ_i are the corresponding eigenvalues, $\hbar$ is the reduced Planck constant, and m_e is the electron mass. The effective potential, v_{eff}, in Equation 2.8 is therefore expressed by:

$$v_{\text{eff}} = v_c(\vec{r}) + v_H(\vec{r}) + v_{xc}(\vec{r}). \tag{2.9}$$

As can be inferred, the Kohn-Sham equations are much simpler to solve because the effective potential depends on the coordinates of only one electron.

Each of the terms that compose Equation 2.9 are derived from their corresponding functionals. For example, the first term $v_c(\vec{r})$ is the Coulomb potential created by the atomic cores, which is expressed within the functional $V_{e-c}[\rho]$, representing the interaction between the electrons and the atomic cores:

$$V_{e-c}[\rho] = \langle \psi \mid \hat{V}_{e-c} \mid \psi \rangle = \int v_c(\vec{r})\rho(\vec{r})\mathrm{d}\vec{r}. \tag{2.10}$$

The Coulomb potential ($v_c(\vec{r})$) is considered an effect caused by the atomic cores, which are treated as point charges, and is classically represented by:

$$v_c(\vec{r}) = -\frac{e^2}{4\pi\varepsilon_0} \sum_{i=1}^{M} \frac{Z_i}{\mid \vec{r} - \vec{R} \mid}. \tag{2.11}$$

Here e is the elemental charge, ε_0 is the dielectric constant, and Z_i is the atomic number of the core i at position $\vec{R}_i$.

Since the $V_{e-c}[\rho]$ functional is the only one described as a function of the position of atomic cores, the remaining functionals for the electron-electron interactions should be general for any possible electron densities.

The kinetic energy ($T_e[\rho]$) is calculated based on the concept of a single electron interacting with the charge density of all electrons. In this case, it is expressed as the sum of the kinetic energies of each electron particle, thus calculated from the single-particle wavefunctions $\psi_i(\vec{r})$ iterating over all N occupied states of the system i, through:

$$T_e[\rho] = \langle \psi \mid \hat{T}_e \mid \psi \rangle = -\frac{\hbar^2}{2m_e} \sum_{i}^{N} \int \psi_i^*(\vec{r})\nabla^2\psi_i(\vec{r})\mathrm{d}\vec{r}, \tag{2.12}$$

Where $\psi_i^*(\vec{r})$ is the complex conjugate of the single-particle wavefunction.

Although each single-particle wavefunction is a density functional defined as

$$\rho(\vec{r}) = \sum_{i}^{N} |\psi_i(\vec{r})|^2, \tag{2.13}$$

an analytical solution to express it as a function of ρ does not exist. In contrast, the density functional for the classical Coulomb energy (or the Hartree $V_H[\rho]$ for the direct electron-electron interaction) of the charge density can be analytically expressed as

$$V_H[\rho] = \frac{1}{2}\frac{e^2}{4\pi\varepsilon_0}\int\int\frac{\rho(\vec{r})\rho(\vec{r})}{|\vec{r}-\vec{r}\,'|}\mathrm{d}\vec{r}\mathrm{d}\vec{r}\,' = \frac{1}{2}\int v_H(\vec{r})\rho(\vec{r})\mathrm{d}\vec{r}. \tag{2.14}$$

A drawback of these classical descriptions is that they account for an additional interaction of the single electron with itself, leading to the so-called self-interaction error. In addition, the non-classical interactions between electrons are not included. In particular, the non-classical phenomena omitted in these descriptions include the *exchange* of electrons, which should not alter the outcomes since electrons are indistinguishable, and the quantum effects of one electron impacting others, known as *correlation*. All these effects are consequently expressed as part of the exchange-correlation potential energy $v_{xc}(\vec{r}) = \frac{\partial E_{xc}[\rho]}{\partial\rho(\vec{r})}$, which was previously introduced in Equation 2.9.

The interdependent formulation of the effective potential, the density, and the single-particle wavefunctions enforces the solution of the Kohn-Sham equations to be solved iteratively. Figure 2.2 shows a schematic routine for this iteration.

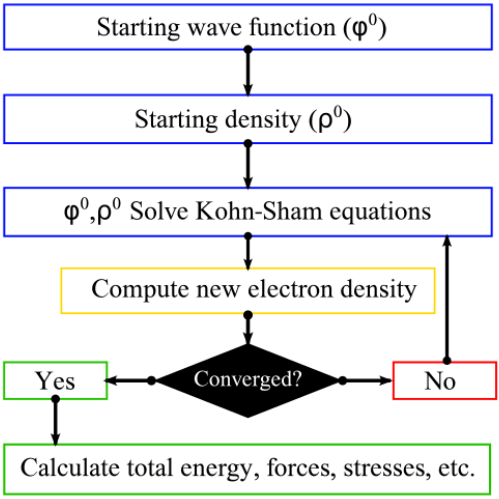

Figure 2.2: Kohn-Sham routine for solving the Schrödinger equation for one effective electron, based on the DFT method.

As illustrated in Figure 2.2, the solution generally starts with a reasonable guess of the charge density, often taken as a superposition of the atomic

charge densities. As elucidated by the second Hohenberg-Kohn theorem, the converged solution ensures a correspondence to the charge density in the ground state.

Fundamentally, the unresolved exchange-correlation functional $E_{xc}[\rho]$ represents the final component required to enable an exact calculation of the total energy and its derivatives for a specified atomic configuration.

Approximations to the Exchange-Correlation Functional

As stated previously, the exchange-correlation functional ($E_{xc}[\rho]$) is a function of the electron density that provides all the contributions of the exchange and correlation to the total energy. Although numerous approximations of $E_{xc}[\rho]$ have been developed to date, a detailed description of each is outside the scope of this thesis. Nevertheless, two of them are the most widely used and were forerunners in the DFT method. One of these is utilized throughout this thesis and is therefore introduced in this section.

The first is the Local Density Approximation (LDA). In this case, the functional $E_{xc}[\rho]$ is simply a space integral of the function that depends only on the local density at that point. The LDA considers the exchange-correlation as a function of two terms: the exchange term and the correlation term.

For the exchange term, an exact equation is calculated by assuming a non-interacting, homogeneous electron gas, which has an analytical solution. For the correlation term, there is no analytical solution. However, in 1980, Alder et al. [62] performed expensive Quantum Mont-Carlo Simulations and obtained numerical values for these correlations. This makes the XC-functional free from parameters.

$$E_{xc}^{LDA}[\rho] = \int \rho(\vec{r})\epsilon(\rho)\mathrm{d}\vec{r}. \tag{2.15}$$

While LDA provides precise geometries, such as lattice parameters for crystals, it has limitations in energy accuracy, often manifested as overestimated binding energies due to the increased delocalization of electrons [63]. This can lead to incorrect stability predictions, such as bcc Fe being unstable and germanium being metallic. To improve LDA, the XC-functional was adjusted to depend on the local variation of the density, considering both the density and its gradient ($\nabla\rho$), resulting in the creation of the Generalized Gradient Approximation (GGA) [64].

$$E_{xc}^{GGA}[\rho] = \int \rho(\vec{r})\epsilon(\rho, \nabla\rho)\mathrm{d}\vec{r}. \tag{2.16}$$

There are various approaches to consider the influence of gradients, resulting in a wide array of GGA XC-functionals with different parameterizations. The first practical GGA that could be reliably applied across a broad

spectrum of materials was presented by Perdew and Wang (PW91) [65, 66]. Among these, the most widely used for solid-state metallic structures is the functional developed by J. Perdew, K. Burke, and M. Ernzerhof (PBE) [67]. However, numerous other XC-functionals have been developed; for instance, a simpler variant of PBE is PBESol (PBE functional revised for solids), which differs from PBE in only two parameters and was created to enhance the equilibrium properties of bulk solids and their surfaces [68].

It should be acknowledged that the superior results obtained with a specific GGA or any other XC-functional do not necessarily imply their better accuracy to all cases. As already introduced in Section 2.2.1, a critical aspect of employing the DFT method involves the rigorous comparison of key calculated properties with experimentally measured properties extrapolated to 0 K. In many instances, certain approximations may yield more accurate descriptions of specific properties while being less precise for others. The scientist's role is to meticulously validate these approximations and identify the optimal compromise.

In this work, the GGA serves as the primary basis for describing the exchange-correlation functionals, and if any alternative method or theoretical level is employed in this thesis work, it will be explicitly stated and appropriately referenced.

2.2.4 Computational Solution, Plane Wave Basis Sets, and Pseudopotentials

It is not the aim of this section to provide a complete description of methods behind the solution for DFT; however, some approximations and details on how to control the accuracy of calculations should be at least introduced, as this is a key factor in guaranteeing accurate employment of the DFT method. Furthermore, the concepts introduced in this section are based on the computational methodology implemented in VASP. As it is designed for solid-state systems, the software package employs periodic boundary conditions, representing the translational symmetry of crystalline materials.

Discretization in reciprocal space

At first, it is worth mentioning that as Wavefunctions and band structure $E(\vec{k})$ are periodic in reciprocal space, i.e., they are constant for a translation of $\vec{k}$ by a reciprocal lattice vector $\vec{G}$. Single-particle Wavefunctions can be calculated for wave vectors lying in the first Brillouin zone, and the solution for the Kohn-Sham equations follows from an integration in reciprocal space.

$$\rho(\vec{r}) = \frac{1}{V_\Omega} \sum_{i=1}^{N} \int_\Omega |\psi_{i,\vec{k}}(\vec{r})|^2 \mathrm{d}\vec{k}, \tag{2.17}$$

where V_Ω is the volume of the first Brillouin zone, Ω. As the wavefunction varies slowly with respect to the wave vector, the integral presented in Equation 2.17 can be approximated by a weighted sum iterating over a discrete set of points in the reciprocal space, called **k**-points. The mesh constituted by the **k**-points can be chosen with an equally spaced mesh (`kspacing`), that are reduced based on the symmetry of the system, resulting in an irreducible **k**-points set. There is therefore a compromise between accuracy and computational demand, which should be evaluated and optimized for each system.

Plane Wave Basis Sets

Even though DFT drastically reduced the amount of data to be stored when computing quantum mechanics, three-dimensional wavefunctions must be stored for each particle. These wavefunctions are expanded into a set of orthonormal basis functions, and their related expansion coefficients are stored in the computer. The choice of basis functions depends on the modeled system's nature. For instance, atom-centered basis sets can simplify the calculations for molecules and their reactions. Conversely, for periodic systems, e.g., crystalline materials, employing a plane-wave basis set considerably reduces the complexity of the calculations. In the discussion of this thesis, since DFT is utilized to describe crystals along with their surfaces and interfaces, a plane-wave basis set is used for all computations. The use of a plane wave basis set for the expansion of a single-particle wave function is expressed by:

$$\psi_{i,\vec{k}}(\vec{r}) = \frac{1}{\sqrt{V_\Omega}} \sum_{\vec{G}} C_{\vec{G},im\vec{k}} e^{i(\vec{G}+\vec{k})\vec{r}}. \tag{2.18}$$

Where $\vec{k}$ is the wave vector, $\vec{G}$ is the reciprocal lattice vector, $i = \sqrt{-1}$. Since the summation runs over all reciprocal lattice vectors $\vec{G}$, the number of expansion coefficients $C_{\vec{G},im\vec{k}}$ is unlimited. However, it can be expected that the calculations with respect to a given property converge quickly with respect to the maximum kinetic energy of the plane waves in the basis set, and a cutoff energy E_{cut} limiting the amount of reciprocal lattice vectors can be defined with the relation.

$$|\vec{G} + \vec{k}| < \frac{\sqrt{2m_e E_{\text{cut}}}}{\hbar}. \tag{2.19}$$

With Equation 2.19, it can be expected that a higher value for E_{cut} results in more reciprocal lattice vectors, which implies higher accuracy, with the expanse of more coefficients to be stored and, consequently, higher computational cost expense. Analogous to the assessment of **k**-points, an evaluation of E_{cut} should balance precision and computational effort before determining the properties of a particular system.

Pseudopotentials

It is common to distinguish two categories of electrons of an atom. Those closer to the nucleus (core electrons) and those relatively further away from the nucleus (valence electrons). Core electrons are tightly bound to the nucleus, whereas valence electrons are more inclined to interact with near atoms, forming bonds, and participating in chemical reactions. Valence electrons usually present smoothier wavefunctions, which can be perturbed by the nuclei and the core electrons. Valence electrons can be efficiently represented by the wavefunctions expanded in the plane-wave basis set [69], even for low E_{cut}. However, limiting the kinetic energy imposes a complication in describing core electrons because they present more localized states, thus exhibiting higher oscillations in their wavefunctions. In the case of core electrons, a prohibitive number of planewaves is necessary to capture all these oscillations.

To deal with this problem, VASP, for example, assumes that localized states of core electrons are negligibly affected by the outer shell, or valence states. With this assumption, the system is decoupled from the core electron states treated beforehand by an effective potential, whereas the valence states are explicitly computed during electronic optimization vid plane-wave expansion [69, 70].

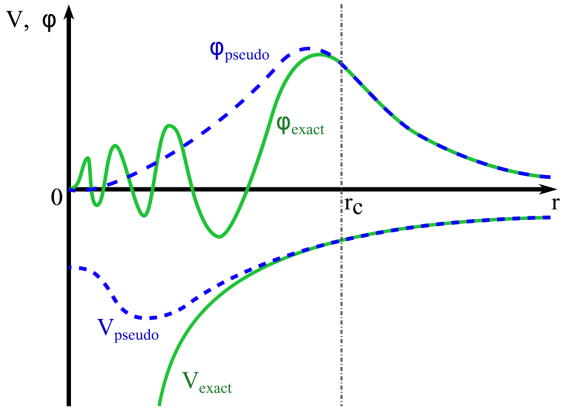

Figure 2.3: Qualitative illustration of the use of pseudopotential method. Pseudopotential (V_{pseudo}) matches the exact potential (V_{exact}), and the resulting pseudo-orbital (φ_{pseudo}) matches the exact potential (φ_{exact}), for $r > r_c$.

The technique to bypass the more complicated localized states is to replace the real potential close to the core with *pseudopotentials*. Although there are several kinds of pseudopotentials, their underlying principle re-

mains consistent: for $r > r_c$, the pseudopotential (V_{pseudo}) coincides with the true potential (V_{exact}), and the pseudo-orbital φ_{pseudo} aligns with the true orbital (φ_{exact}). This idea is depicted in Figure 2.3.

Considering the large number of core electrons in many atoms, pseudopotentials have successfully proven to be useful to accurately calculate many types of materials properties.

While this design guarantees that the wavefunction matches the exact value above r_c, altering the central part of the wavefunction results in varying eigenvalues and norms for the pseudo density. To address norm errors, Hamman, Schlüter, and Chiang proposed norm-conserving pseudopotentials [71]. Their approach ensures that the pseudopotentials maintain the same integrated charge within a distance below r_c, requiring the following condition to be met:

$$\int_0^{r_c} |\psi(r)| r^2 \mathrm{d}r = \int_0^{r_c} |\psi_{\text{pseudo}}(r)| r^2 \mathrm{d}r = Q, \tag{2.20}$$

where Q is the total charge within $r < r_c$, $\psi(r)$ is the all-electron (exact) wavefunction and $\psi_{\text{pseudo}}(r)$ is the pseudo-wavefunction. However, the solution is still limited in its accuracy.

The projector augmented wave (PAW) method increases the numerical precision by incorporating localized auxiliary functions that, through a linear transformation, are connected to the real all-electron wave functions [72]. This technique employs projections of pseudo-orbitals onto the real, precomputed all-electron orbitals to generate the eigenvalue spectrum. Due to the linearized transformation, the coefficients are derived from the inner product of the pseudo wavefunction and the orthogonally selected projection operators. Consequently, the computation is not only more accurate but also less resource-intensive, requiring fewer plane waves for the plane-wave expansion. All DFT calculations presented in this dissertation employ projector augmented wave (PAW) pseudopotentials for the systematic characterization of each atomic element.

2.3 Introduction to the Calphad Method

2.3.1 The Computational Thermodynamics Concept

Thermodynamics provide a fundamental framework for understanding the equilibrium states of systems. This foundational knowledge is essential for accurately simulating transformation processes, as systems inherently tend to reach equilibrium.

The digitization of measured thermodynamic data, along with the use of theoretically derived thermochemical data, allows for the computational determination of various parameters relevant to thermodynamic systems and their ability to predict equilibria. To accurately characterize systems and

their equilibrium states, it is essential to ensure that data from both theoretical calculations and experimental methods are carefully validated and reflective of the different levels of thermodynamic equilibrium of the system's components as a whole.

In the *Calphad method*, each phase within the system is meticulously modeled on an individual basis, with thermodynamic databases employed to systematically store detailed information on the thermodynamic model parameters pertinent to each phase. As part of the Calphad method, the *Calphad technique* outlines the methodology of selecting phase models in a manner that aligns with crystallographic data, while simultaneously facilitating extrapolations to more complex, higher-order materials systems.

In general, the overall methodology framework consists of employing available data to assess the parameters of the Gibbs energy model selected for each of the phases that are stored in thermodynamic databases that can afterwards be read by thermodynamic engines that, among other capabilities, are able to calculate the equilibrium states by performing the minimization of the total Gibbs energy of the system, constrained by a given environmental condition.

This technique, applied across a range of practical applications, is referred to as "computational thermodynamics". When thermodynamic models have been thoroughly evaluated and align well with actual conditions, computational thermodynamics can underpin kinetic models and simulations. In addition, they can be utilized to predict thermodynamic properties in non-equilibrium states and multicomponent systems, aiding in the discovery of new materials or innovative processing methods.

2.3.2 Foundation for Equilibrium Calculations

The fundamental condition for a system to reach thermodynamic equilibrium requires that all regions of a system exhibit uniform thermodynamic potentials. In practical applications, thermodynamic potentials can be classified into three primary categories: temperature, pressure, and composition. When these potentials remain uniform across the system, they indicate thermal, mechanical, and chemical equilibrium, respectively.

Systems in thermodynamic equilibrium are characterized by spatial homogeneous quantities for temperature and pressure. According to the second law of thermodynamics, this equilibrium state can be interpreted as the scenario in which a closed system achieves its maximal level of entropy.

If a closed system presents a gradient in temperature, heat flows from the hotter to the colder part. As a consequence of the second law, the entropy reduction in the hotter part is smaller than the entropy gain in the colder part, resulting in a total system entropy increase.

Equilibration of composition gradients also increases entropy in similar fashion. The same is true for the case of pressure; nonetheless, the difference in pressure inside a system can be maintained for extremely long times,

and for practical purposes, a spontaneous equilibration of pressure in solid materials is experimentally unfeasible.

However, the material can be seen as a constitution of individual closed parts surrounded by pressure barriers, and considering it as a single closed system implies that the barrier can be overcome.

An inhomogeneous system consists of many phases. In equilibrium, these phases are homogeneous within themselves.

From the perspective of internal energy (U), the equilibrium condition is reached in a closed system when the internal energy reaches its minimum value at constant entropy and volume. For experimental purposes, this definition is unpractical due to the unfeasible control of entropy at constant values for most of the systems, but on the contrary, it may be of use when performing atomistic calculations.

From the perspective of Gibbs energy, the definition of equilibrium is found more applicable because the variable constraints that define equilibria are controllable within experiments and during engineering applications. The equilibrium is then defined as the point at which the Gibbs energy of a closed system reaches its minimal value in isothermal and isobaric conditions.

2.3.3 Phase stability calculation

In the Calphad method, each phase of the system is modeled individually and thermodynamic databases are used to store information on the models and the thermodynamic parameters of the phases. These databases can be read by thermodynamic engines to minimize the total Gibbs energy of the system. In this work, OpenCalphad [55, 73, 74] and PyCalphad [56] were employed as thermodynamic engines.

The total Gibbs energy of a system (G^{tot}) is the sum of the molar Gibbs energies of the phases (G_m^{φ}) multiplied by the number of moles of the correspondent phase (m^{φ}):

$$G^{\text{tot}} = \sum_{\varphi} m^{\varphi} G_m^{\varphi}. \tag{2.21}$$

For a given set of thermodynamic potentials, the equilibrium of the system is obtained by minimizing Equation 2.21 [75].

Within the Calphad method, different types of model are employed to describe the temperature, pressure, and/or composition dependencies of the Gibbs energy of the phases in the system.

2.3.4 Gibbs Energy Models and Formalism

In this section, the thermodynamically most important Gibbs energy models and formalism used to describe this work's system and, in general, any metal-hydrogen systems will be laid out.

The Hydrogen Gas Gibbs Energy Models

When modeling metal-hydrogen systems, the proper choice of the Gibbs energy model describing the gas is of pivotal importance, especially when the Calphad method is applied for modeling hydrogenation, as the process inevitably involves the thermodynamic interaction between the metallic phase and the gas phase.

In general, the gas phase is a mixture of metallic elements in the vapor state to the most common atmospheric molecules of the Earth. However, apart from the main component of the gas phase H_2 during hydrogenation experiments, these other species are often in negligible concentration and are accurately considered to present ideal mixing properties. What contributes mainly to the Gibbs energy of the gas is consequently only the Gibbs energy of the H_2 species.

Considering that pure hydrogen is an ideal gas, its Gibbs energy expression may be acquired by the integral of the volume with respect to pressure:

$$G_{\mathrm{H_2}}^{\mathrm{gas}} = \int V \mathrm{d}P = \int \frac{RT}{P} \mathrm{d}P = {}^{0}G_{\mathrm{H_2}}^{\mathrm{gas}} + RT \ln\left(\frac{P}{P_0}\right), \tag{2.22}$$

where R is the gas constant and ${}^{0}G_{\mathrm{H_2}}^{gas}$ is the Gibbs energy reference of hydrogen at atmospheric pressure $P_0 = 1 \times 10^5$ Pa. For most practical applications, the hydrogen gas may be considered ideal, however, for some metal-hydrogen systems the hydrogenation occurs above 1×10^8 Pa, at which the ideal-model description loses accuracy [13].

A model that accounts for the shift of ideal properties at high pressures has been proposed by Joubert [13]. The model has been widely used in the Calphad community when an accurate description due to deviation of the ideal property is necessary.

Joubert introduced an equation of state expressed by a series of exponential pressure-dependent parameters and coefficients.

$$\begin{aligned} G_{\mathrm{H_2}}^{\mathrm{gas}} = {}^{0}G_{\mathrm{H_2}}^{\mathrm{gas}} &+ RT \ln\left(\frac{P}{P_0}\right) - A_1 B_1 \exp\left(-\frac{P}{B_1}\right) - A_2 B_2 \exp\left(-\frac{P}{B_2}\right) \\ &- A_3 B_3 \exp\left(-\frac{P}{B_3}\right) - A_4 B_4 \exp\left(-\frac{P}{B_4}\right) \\ &- A_5 B_5 \exp\left(-\frac{P}{B_5}\right) + CP + D \end{aligned} \tag{2.23}$$

The expression shown in Equation 2.23 approaches Equation 2.22 for low-pressure ranges ($P < 1 \times 10^7$ Pa, see Figure 5.15). The reader is referred to Joubert's publication [13] for more details about the assessment procedure of

the model's coefficients and its limitations. Nevertheless, this doctoral thesis work will recall both models when the employment of the Gibbs energy of the H_2 is necessary within the approaches proposed.

The Compound-Energy Formalism

The Compound-Energy Formalism (CEF) [76] is a generalized mathematical approach used to describe many physical models and features of different phases [75]. It can handle different cases and constituents interacting in different crystallographic sublattices. Most of the models used by the Calphad community are, in general, just special cases of the CEF. The physical meaning of the CEF parameters is dictated by the different strategies that can be employed when performing computational thermodynamics.

In general, a selection of the models for a phase should have a basis on the physical and chemical properties of the phases, reflecting their fundamental matter structure. Features that should be considered in this regard consist e.g. the crystallography, the type of bonding, possible order-disorder transitions, magnetic properties, type and range of solution, etc.

It is not the intention of this doctoral thesis to fully describe the capabilities of the CEF, however, a brief description of its general form and the basis for its application to model metal-hydrogen systems is provided in the following as a key theoretical foundation for the understanding of the thermodynamic model proposed in this work. For more details, the reader is directed to Lukas, Fries, and Sundman's book [75].

The general molar Gibbs energy of a given phase φ is expressed by:

$$G_m^{\varphi} = {}^{\text{srf}}G_m^{\varphi} + {}^{\text{phys}}G_m^{\varphi} - T \cdot {}^{\text{cnf}}S_m^{\varphi} + {}^{\text{xs}}G_m^{\varphi}. \tag{2.24}$$

The first term with superscript "srf" stands for "surface of reference" and indicates the *non-interacting* mixture of the constituents of the phase, acting as a mechanical mixture of the compounds. Any solution phase has at least two compounds limiting the solubility of the phase. These compounds are the so-called "end members". A linear interpolation of the energy of these compounds according to their composition variation will form a hyper-plane that serves as a reference from which any non-linear mixing feature may be easily identified, justifying the "srf" nomenclature.

The term prefixed with "phys" represents the contribution to the Gibbs energy due to a physical model such as magnetic transitions, and may be composition-dependent through particular physical quantities.

The pre-superscript "cnf" identifies the configurational entropy term and is based on the number of possible arrangements of the constituents in the phase.

The term with pre-superscript "xs" refers to the excess Gibbs energy related to the real Gibbs energy subtracted by the first three terms, expressing any variation not yet accounted for.

The physical origins of the Gibbs energy for the phase are attempted to be modeled only within the ${}^{\text{phys}}G_m^{\varphi}$ term, whereas the ${}^{\text{srf}}G_m^{\varphi}$ and ${}^{\text{xs}}G_m^{\varphi}$ comprise the configurational as well as vibrational, electronic, and other contributions.

In the CEF the general expressions for these terms are:

$$ {}^{\text{srf}}G_m^{\varphi} = \sum_{I_0} P_{I_0}(Y) \, {}^{\circ}G_{I_0}, \tag{2.25} $$

$$ {}^{\text{cnf}}S_m^{\varphi} = -R \sum_{s=1}^{n} a_s \sum_{i=1}^{n_s} y_i^{(s)} \ln(y_i^{(s)}), \tag{2.26} $$

$$ {}^{\text{xs}}G_m^{\varphi} = \sum_{I_1} P_{I_1}(Y) \, L_{I_1} + \sum_{I_2} P_{I_2}(Y) \, L_{I_2} + \cdots \tag{2.27} $$

The generalization of the formalism is given by introducing the constituent array denoted I. As the name suggests, it specifies one or more constituents on each sublattice, while the individual constituents are denoted i with a superscript $^{(s)}$ indicating the sublattice s. They can be of different order. The zeroth order (I_0) corresponds to the array with just one constituent on each sublattice, consequently representing the "end members" of the phase.

In Equation 2.25 the concept is applied to define the surface reference. The term $P_{I_0}(Y)$ defines the product of the constituent fractions specified by the zeroth-order constituent array. As in some cases, part of the end-member compounds defined by I_0 represent an unstable phase structure, the value of ${}^{\circ}G_{I_0}$ must be estimated. For this purpose, DFT calculations can provide excellent initial values if consistently applied, as discussed in Chapter 3.

There exists no absolute value for the Gibbs energy, and it is necessary to refer the Gibbs energy of all phases in the system to the same reference for each of the elements constituting it. The term ${}^{\circ}G_I^{\varphi}$ thus represents the Gibbs energy of formation of the constituent array I in φ from the reference states of the elements included in the constituents, which is generally a function of the temperature and pressure:

$$ {}^{\circ}G_I^{\varphi} - \sum_j b_{ij} H_j^{\text{SER}} = f(T, p), \tag{2.28} $$

where b_{ij} is the stoichiometry factor for the component j in the constituent array I and H_j^{SER} is the enthalpy of the component j in its reference state, usually taken as the value presented at room conditions (298.15 K, and 101 325 Pa).

For the configurational entropy shown in Equation 2.26, the term a_s represents the number of sites on each sublattice s and $y_i^{(s)}$ is the constituent fraction of i in the same sublattice, which are summed over each constituent in each sublattice.

The excess Gibbs energy term (${}^{\text{xs}}G_m^{\varphi}$) contains the summation of the possible interaction parameters related to the constituent's interaction within

the sublattices. A first-order constituent array represents one extra constituent in one sublattice, in the same manner a second-order constituent array represents three interacting constituents on one sublattice and also the case with two interacting constituents on two different sublattices.

As the order of the constituent array relates to the product of the fraction of the constituents, a higher than second-order constituent array expresses an increasingly small contribution for the interaction parameter and therefore is not advisable for the modeling of a phase.

The interaction parameters shown in Equation 2.27, L_{I_1}, and L_{I_2}, are named binary, and ternary interaction parameters, respectively. Binary interaction parameters express the composition dependence of constituent i and j within a sublattice. Even though many authors have proposed expressions describing these interactions the most accepted expression for binaries L_{I_1} in the Calphad community is the Redlich-Kister [77] power series, as it is symmetrical and extrapolates well to ternary and higher-order systems:

$$L_{ij} = \sum_{v=0}^{k} (x_i - x_j)^v \cdot {}^v L_{ij}, \tag{2.29}$$

where v is the order of the series terms ranging from 0 to k. Analogously to the previous constituent array series, a value of k greater than 2 is not advisable, as the product of fractions increases and an increasingly smaller contribution of higher order terms is expected. If a more complex compositional dependence is needed for modeling a phase, it should be preferred to test a new sublattice description before increasing the power series term.

Note that, because $x_i + x_j = 1$ in binary systems, only the zeroth-order (${}^0 L_{ij}$) parameters give a non-zero contribution within the middle of the system $i-j$, while the first-order parameter (${}^1 L_{ij}$) is the only asymmetric. The parameters ${}^v L_{ij}$ may exhibit temperature dependence, and usually, a linear dependence on temperature is sufficient for the accurate modeling of most systems. In cases where heat-capacity data are available, a higher order temperature dependence, often represented by $T\ln(T)$ to account for a constant excess heat-capacity, should be employed.

$${}^v L_{ij} = {}^v A_{ij} + {}^v B_{ij} T, \tag{2.30}$$

where A_{ij} and B_{ij} are constant coefficients describing the excess enthalpy and entropy, usually subject to assessment during optimization of model parameters.

The expression for the ternary excess contributions given by the second term of Equation 2.27 may be generalized by a summation over the constituents interacting in a sublattice as defined by the second-order constituent array I_2:

$${}^{\text{tern.xs}} G_m^{\varphi} = \sum_{i=1}^{n-2} \sum_{j=i+1}^{n-1} \sum_{k=j+1}^{n} x_i x_j x_k L_{ijk}. \tag{2.31}$$

For a symmetric extrapolation, the ternary interaction (L_{ijk}) parameters may take the form:

$$L_{ijk} = v_i \cdot {}^{i}L_{ijk} + v_j \cdot {}^{j}L_{ijk} + v_k \cdot {}^{k}L_{ijk}, \tag{2.32}$$

with

$$\begin{aligned} v_i &= x_i + (1 - x_i - x_j - x_k)/3 \\ v_j &= x_j + (1 - x_i - x_j - x_k)/3 \\ v_k &= x_k + (1 - x_i - x_j - x_k)/3. \end{aligned} \tag{2.33}$$

The sum of v is always unity for any order multi-component system, which guarantees the symmetrical property of the L_{ijk} parameters. This implies that if these parameters have the same value, it is equivalent to having composition-independent ternary order parameters.

It is worth noting that the approach presented here is the geometrical extrapolation first proposed by Muggianu [78]. Even though there are at least three other extrapolation methods [75], Muggianu's is arguably the preferred one due to its simplest formulation from Redlich-Kister polynomials and its capability to extrapolate to multicomponent systems.

2.4 Introduction to Phase-Field modeling

In this section, a brief introduction to the phase-field method is presented with a focus on covering the models that will be employed in this study.

2.4.1 Basic Phase-Field equations

Phase-field modeling is a powerful method capable of simulating the spatial arrangement of the microconstituents in a given system. It describes the many microstructural characteristics, for example, the different crystal structures having dissimilar compositions, different orientations of grains of phases, domains of different structural variants, and domains of different electric or magnetic polarization. The distribution, morphology, size, and intrinsic bulk phase properties of these microconstituents determine the overall properties of multicomponent and/or multiphase materials.

The phase-field method is distinguished from other approaches by the inclusion of different interface descriptions into its formalism. A given phase-field model describes the compositional and/or structural domains in a microstructure with a set of field variables that are assumed continuous across the interfacial regions of these domains.

In this regard, there are two types of field variables, conserved and non-conserved:

- Conserved – These variables evolve with time by a nonlinear diffusion equation and their value must be conserved within the simulation

domain. They are generally governed by the Cahn-Hilliard equation [79, 80], Equation 2.34.

- Non-conserved – This type of variable may have its value not conserved during the simulation and has its evolution dictated by the Allen-Cahn relaxation equation [81, 82] Equation 2.35.

These two kinetic equations combined may solve most of the common microstructural dependent materials problems and underlie many phase-field models in the literature.

The Cahn-Hilliard equation is given by:

$$\frac{\partial c_i}{\partial t} = \nabla \cdot M_i \nabla \frac{\delta F}{\delta c_i}, \tag{2.34}$$

where M_i is the diffusivity of species i, and c_i represent the conserved field variable.

The Allen-Cahn equation is given by:

$$\frac{\partial \eta_j}{\partial t} = -L_j \frac{\delta F}{\delta \eta_j}, \tag{2.35}$$

The term L_j is the mobility of the non-conserved field variable, η_j. The variable t represents the time and F is the free energy density of the system.

In essence, how F is expressed in terms of the field variables dictates the direction and destination of the evolving system, in other words, the free energy density expresses the thermodynamic, and therefore the steady state equilibrium within the system.

In contrast, the variables representing the diffusivity and mobility modulate how the system will change from its initial state to its final thermodynamic equilibrium. A quantitative description of these terms is a pivotal concern in obtaining a model capable of simulating real systems.

As mentioned above, the Cahn-Hilliard equation concerns the evolution of the conservative quantities within a system. It is assumed that the free energy density of an infinitesimal volume in a nonuniform system is dependent not only on its composition but also on how it is distinct from the nearby surrounding environment. Thus, the free energy density depends on the compositional variable, c_i, and its derivative. As the composition must be conserved in a closed system, the summation of variables c_i for a total of N species must be contained to the unit:

$$\sum_{i}^{N} c_i = 1. \tag{2.36}$$

Therefore, only one concentration and one chemical potential are independent. The free energy functional F may be dependent on both the composition and the non-conserved field variable. For a phase-field model containing N conserved variables c_i and M order parameters η_j, is described by:

$$F = \int_V \Big[f_{loc}\left(c_1, c_2, \ldots, c_N, \eta_1, \eta_2, \ldots, \eta_M\right) + f_{gr}\left(c_1, c_2, \ldots, c_N, \eta_1, \eta_2, \ldots, \eta_M\right) + E_d \Big] \, \mathrm{d}V \tag{2.37}$$

with f_{loc} defining the local free energy density as a function of all concentrations and order parameters, varying from model to model. The term E_d refers to any other term influencing the energetics within the volume, and the gradient energy density (f_{gr}) is given by:

$$f_{gr} = \sum_i^N \frac{\kappa_i}{2} |\nabla c_i|^2 + \sum_j^M \frac{\kappa_j}{2} |\nabla \eta_j|^2, \tag{2.38}$$

where κ_i and κ_j are the composition and phase gradient energy coefficients, respectively. These terms penalize the free energy density by adding an extra energy contribution for the formation of sharp interfaces. Disregarding the additional contribution to the free energy density E_d, a general equation can be written:

$$F = \int_V \left[f_{loc}(c_i, \eta_j) + \sum_i^N \frac{\kappa_i}{2} |\nabla c_i|^2 + \sum_j^M \frac{\kappa_j}{2} |\nabla \eta_j|^2 \right] \mathrm{d}V, \tag{2.39}$$

The f_{loc} is the local free energy density as a function of the conserved and non-conserved field variables. Considering a single compositional dependence with species (c_i) and a single order parameter (η_j), the partial derivatives of the free energy functional take the form:

$$\frac{\delta F}{\delta \eta_j} = \frac{\partial f_{loc}}{\partial \eta_j} - \nabla \cdot (\kappa_j \nabla \eta_j) \tag{2.40}$$

$$\frac{\delta F}{\delta c_i} = \frac{\partial f_{loc}}{\partial c_i} - \nabla \cdot (\kappa_i \nabla c_i) \tag{2.41}$$

Substituting Equation 2.40, and Equation 2.41 in Equation 2.35 and Equation 2.34, respectively, the evolution of the variables is described as:

$$\frac{\partial \eta_i}{\partial t} = -L_j \left(\frac{\partial f_{loc}}{\partial \eta_j} - \nabla \cdot (\kappa_j \nabla \eta_j) \right) \tag{2.42}$$

$$\frac{\partial c_i}{\partial t} = \nabla \cdot M_i \nabla \left(\frac{\partial f_{loc}}{\partial c_i} - \nabla \cdot (\kappa_i \nabla c_i) \right) \tag{2.43}$$

In this work, the Cahn-Hilliard equation (Equation 2.34) is split into two partial differential equations to simplify the solution of the stiff fourth-order gradient, inherent from the evolution equation governing a conserved order parameter.

The differential of the free energy with respect to the conserved order parameter of species i is defined as the chemical potential of that species (μ_i): $\mu_i = \frac{\partial f_{loc}}{\partial c_i} - \nabla \cdot (\kappa_i \nabla c_i)$.

With this approach, the fourth-order equation becomes two second-order equations at the expense of creating two coupled variables to be solved: the chemical potential μ_i, and the concentration c_i. Equation 2.43 thus becomes:

$$\frac{\partial c_i}{\partial t} = \nabla \cdot M_i \nabla \mu_i, \tag{2.44}$$

and

$$\nabla \cdot (\kappa_i \nabla c_i) = \frac{\partial f_{loc}}{\partial c_i} - \mu_i. \tag{2.45}$$

From this point, the equations are written in their weak form, and from there, the residual equations are constructed in a way to discretize the problem to be solved within the FEM. More details about this procedure can be found in the **Appendix** C.

2.4.2 The Kim-Kim-Suzuki phase-field model

The Kim-Kim-Suzuki (KKS) model is an implementation of the two-phase model presented by Kim et al.[83]. It features a single order parameter η, and introduces phase-concentrations c_α and c_β for phase α and β, respectively. The global concentration (c) is thus constrained to:

$$c = (1 - h(\eta))c_\alpha + h(\eta)c_\beta. \tag{2.46}$$

The main advantage of using KKS is that it provides the ability to choose the interfacial energy between the adjoining phases of the system independent of the interfacial width. This characteristic of the model thus allows for the simulation of the evolving system free of scale concerns. The KKS model is especially suited for systems with high heat of solution, e.g. the formation of hydrides from a metallic matrix, which in other conventional phase-field models can lead to unphysically high levels of interphase energies due to the miscibility gap contributions along the smooth interface.

For a binary two-phase system, there are only two dependent compositional field variables, one related to the chemical composition and another to the phase, c and η, respectively:

$$f_{loc}(c,\eta) = [1 - h(\eta)]\, f_\alpha(c) + h(\eta) f_\beta(c) \tag{2.47}$$

where $h(\eta)$ is the dimensionless interpolation function called "switching" function that provides a smooth sigmoidal transition from phase α to phase β by assuming the value

$$h(\eta) = \begin{cases} 0, \iff \eta = 0 \\ 1, \iff \eta = 1, \end{cases} \tag{2.48}$$

and no gradient at the minimum and maximum points.

The f_ϕ term represents the homogeneous (or bulk) free energy density of a given phase ϕ and may be derived by CALPHAD assessments of the Gibbs energy expression of the phases along with the specific volume of their unit cells.

It is worth noting that there are many other developed models and formalisms reported in the literature and that the present introduction only covers one of many that could be employed to simulate a hydrogenation process.

Within the KKS model, it is often the case that an extra function dependent on η, $g(\eta)$, is added to the equation. The $g(\eta)$ function is a double-well function with minima at $\eta = 0$ and $\eta = 1$, attributing an energy penalty for the interphase region, that can be modulated by the choice of the value of coefficient w that multiplies the function and modulates its height, creating an additional energy barrier between the phases. With this term added, the free energy density is then represented by:

$$f_{loc}(c,\eta) = [1 - h(\eta)]\, f_\alpha(c) + h(\eta) f_\beta(c) + w g(\eta). \tag{2.49}$$

The additional variables are required to be constrained to solve the model. This is obtained in KKS by the mass conservation equation (Equation 2.46) and by the pointwise equality of the phases' chemical potentials:

$$\frac{\partial f_{loc}}{\partial c} = \frac{\partial f_\alpha}{\partial c_\alpha} = \frac{\partial f_\beta}{\partial c_\beta}. \tag{2.50}$$

This constraint enforces that the chemical potential of the phases equalizes at their interface.

2.4.3 Including Micromechanics

Phase transformation in solids usually produces coherent microstructures in their early stages. In a coherent microstructure, the lattice planes and directions are continuous across the interfaces, and the lattice mismatch between

phases (or domains) is accommodated by elastic strain. The elastic energy contribution, resulting from elastic displacements, to the total free energy in a phase-field model can be introduced directly by expressing the elastic strain energy as a function of field variables or by including coupling terms between the field variables and the displacement gradients in the local free energy functions [84, 85, 86, 87].

To couple elastic deformation energy to the phase-field model, the elastic strain energy density (E^{el}) is included in the free energy density functional (F) as the additional energy term E_d shown in Equation 2.37, such that the following expression for the Allen-Cahn equation is obtained:

$$\frac{\partial \eta}{\partial t} = -L\left(\frac{\partial f_{loc}}{\partial \eta} - \kappa\nabla^2\eta - \frac{\partial E^{el}}{\partial \eta}\right). \tag{2.51}$$

The mechanical equilibrium equation is solved simultaneously by the balance of linear momentum:

$$\nabla \cdot \sigma = 0, \tag{2.52}$$

From the definition of Hooke's law, the stress-strain relation can be derived from the strain energy:

$$\sigma = \frac{\partial E^{el}}{\partial \varepsilon}, \tag{2.53}$$

and the elastic energy E^{el} as:

$$E^{el} = \frac{1}{2}\mathbb{C}_{ijkl}\left(\varepsilon_{ij} - \varepsilon^0_{ij}\right) : \left(\varepsilon_{kl} - \varepsilon^0_{kl}\right). \tag{2.54}$$

The elastic misfit strain tensor ε^0_{ij} and the stiffness tensor $\mathbb{C}_{ijkl}$ are interpolated as a function of the non-conserved order parameter η, as proposed in the Khachaturyan's scheme [88], yielding:

$$\varepsilon^0_{ij} = \epsilon^{SFTS}_{ij} h(\eta), \tag{2.55}$$

and

$$\mathbb{C}_{ijkl} = (1 - h(\eta))\mathbb{C}^{\alpha}_{ijkl} + h(\eta)\mathbb{C}^{\beta}_{ijkl}. \tag{2.56}$$

Here, the term ϵ^{SFTS}_{ij} represents the stress-free transformation strain, and $\mathbb{C}^{\phi}_{ijkl}$ is the rank four elasticity stiffness tensor of phase ϕ.

3 Thermodynamic Modeling of the FeTi Hydrogenation

3.1 Review on the thermodynamics of binary systems

3.1.1 Thermodynamics of Fe-H and Ti-H systems

For Fe and Ti, the reactivity with hydrogen is oppositely related. While both Fe and Ti metals show a temperature range in which the bcc structure is stable, the calculated enthalpy of solution in the bcc lattice of iron is $24.12\,\mathrm{kJ\,mol^{-1}}$, whereas in the bcc lattice of titanium it is $-59.82\,\mathrm{kJ\,mol^{-1}}$ [23].

On the one hand, this promotes that iron reacts poorly with hydrogen and presents negligible solubility in the solid and molten states. On the other hand, titanium presents a huge hydrogen solubility in the bcc phase as well as many distinguished hydrogen-rich hydride phases. The respective calculated phase diagrams of Ti-H and Fe-H using the thermodynamic databases assessed by Ukita [89] and Zinkevich [90], are shown in Figure 3.1 and Figure 3.2, contrasting the differences in solubility of their bcc phases.

In the Fe-H system, stable hydrides are not observed at room pressure, and iron-hydride formation is registered to occur only above 6 GPa at 523 K [90, 91], yet titanium-hydrides (TiH_2) are stable even below atmospheric pressure ($< 10^5$ Pa) at temperatures as high as 576 K [92, 93, 94].

As will be discussed in more detail in the following sections, the high stability of the titanium hydrides indicates that the near-ambient condition hydrogenation of the FeTi alloy must be a phenomenon of metastability, which strongly influences the way of dealing with most computational methods for studying this system.

3.1.2 Thermodynamics of the Fe-Ti System

At room pressure, the Fe-Ti system presents five distinguishable phases: Laves, bcc, hcp, fcc, and liquid. Much effort has been expended to describe the thermodynamics of the Fe-Ti system. The first registered trial of modeling individual phases of the system in the Calphad framework was done by Larry Kaufman and Harvey Nesor [95].

In the works that followed this first attempt, the solution phases were updated regarding the thermodynamic models employed and the incorporation of new data sets [96, 97, 98] and Dinsdale et al. [99] applied a solution model to describe solubility in the Laves phase.

Later, H. Kumar and colleagues [100] reassessed the system and updated the model for the Laves phase by describing it with three sublattices taking into account coordination numbers in the lattice positions.

In 1998, Dumitrescu and colleagues [101] compared the available assessments and recommended an evaluation of magnetic properties to further improve the thermodynamic description of the system.

The first work demonstrating the use of the ordering model to describe the bcc phase of the FeTi system was presented [102] by H. Kumar and colleagues, discussing the sharp decrease in the Gibbs energy as a result of the enthalpy of ordering Fe and Ti in the bcc lattice. This was evaluated by a parametric description of the heat capacity of the ordered phase and its difference compared to the disordered state, which was estimated using the mixing enthalpy from Miedema's work [103]. The Kumar model was widely accepted and used in many extrapolations for ternary systems [104, 105].

Later, Bo Hong and colleagues [106] revisited the system and re-adjusted the parametric models to better perform heat capacity calculations of the intermetallic phases.

More recently, Santhy and Kumar [107] applied the order-disorder model for the bcc phase from [102] and remodeled the Laves phase with two and three sublattices, with the latter closely corresponding to the crystallography of the phase. They adjusted the parameters by enhancing the models with experimental data for the stable stoichiometric compound and with first-principles calculated energies of unstable end-members. Figure 3.3 shows the calculated phase diagram proposed using the three-sublattice Laves phase model.

Following this, Kriegel et al. [108] included pressure dependency by evaluating thermodynamic models using data on the solubilities of phases under high levels of compression, between 2.3 and 2.7 GPa. Figure 3.4 compares the calculated phase diagram for ambient and high pressure.

However, the authors modeled FeTi as an individual separate phase and not as an ordered state of the bcc phase. The Laves phase was modeled with two sublattices and no magnetic contribution.

As will be seen in the next sections, the level of pressure that significantly influences the FeTi phase stability is far above the hydrogen partial pressure that induces hydrogenation of the FeTi phase near room temperature. Therefore, the pressure dependency of the solids may be neglected when the thermodynamics of FeTi hydrogenation are assessed, without losing consistency.

In particular, when Fe and Ti mix in equimolar quantities, the bcc phase undergoes ordering of elements in the bcc crystal lattice forming a CsCl-type structure, which can hydrogenate under near ambient conditions reversibly and is, therefore, the center object of study in this work.

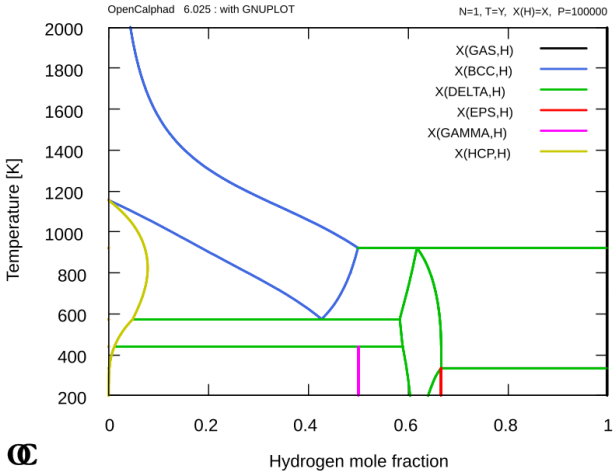

Figure 3.1: Calculated Ti-H temperature-composition equilibrium phase diagram from [89].

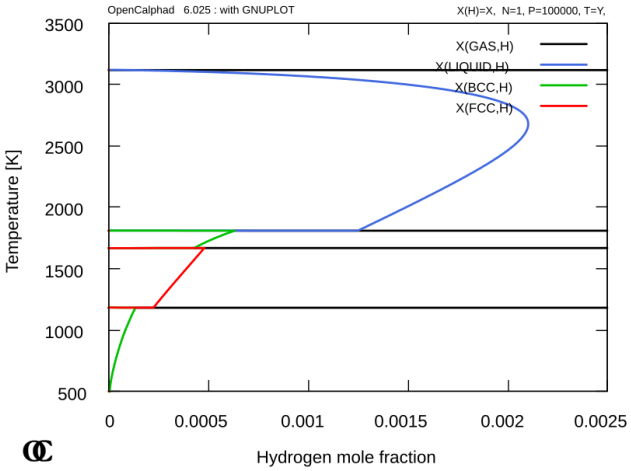

Figure 3.2: Calculated Fe-H temperature-composition equilibrium phase diagram from [90].

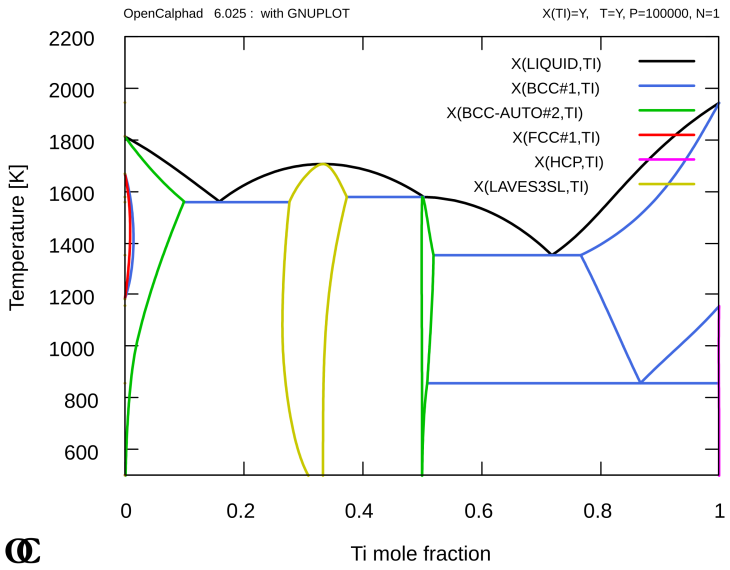

Figure 3.3: Calculated Fe-Ti phase diagram with parameters from [107].

The ordering phenomenon may appear as a second-order thermodynamic transition, as in the Al-Fe-Ni, Cu-Zn, and Fe-Si cases [75]. In these metal systems, the degree of order in the bcc lattice continuously transitions in the direction of the resulting ordered bcc (B2) phase.

Although for the FeTi system this transformation is usually discrete and considered a first-order thermodynamic transition, to ensure a better extrapolation to multicomponent systems and maintain compatibility, the most complete and widely accepted CALPHAD description of the BCC phase employs the order-disorder model. For good practice and to guarantee the fulfillment of the requirements for higher-order systems, the order-disorder model is selected to describe the FeTi phase in this work.

The model consists of describing the disordered and ordered bcc lattice as part of the same Gibbs energy expression [75]. In this work, the use of the parameters of the Kumar and Santhy order-disorder model [100, 107] was accepted, except for the parameters related to thermal vacancies in the metallic sites, which were neglected because hydrogenation of the B2 phase occurs near ambient temperature, resulting in negligible thermal vacancy fractions.

The disordered phase (bcc-A2) is thus described as a two-sublattice model

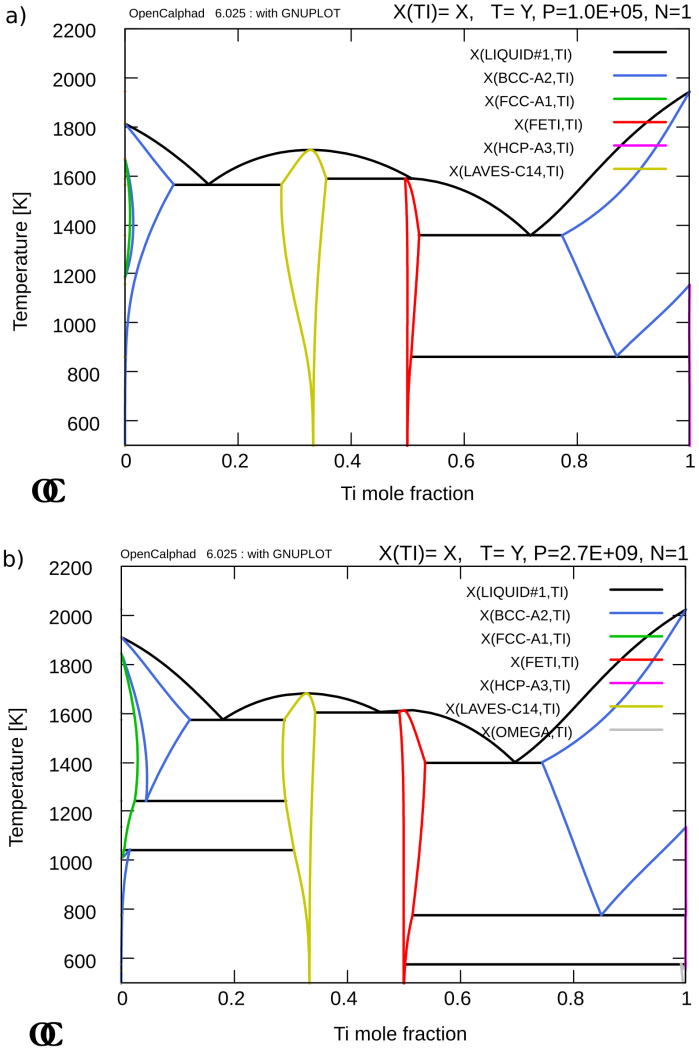

Figure 3.4: Calculated Fe-Ti phase diagram from [108] at varying pressure values. a) calculated at 1×10^5 Pa, and b) calculated at 2.7×10^9 Pa.

with formula $(\mathrm{Fe},\mathrm{Ti})_1(\mathrm{vac})_3$ and a contribution to the Gibbs energy G^{dis} expressed as:

$$\begin{aligned} G_m^{\mathrm{dis}} &= y'_{\mathrm{Fe}} G_{\mathrm{Fe:vac}} + y'_{\mathrm{Ti}} G_{\mathrm{Ti:vac}} \\ &\quad + RT\left(y'_{\mathrm{Fe}} \ln y'_{\mathrm{Fe}} + y'_{\mathrm{Ti}} \ln y'_{\mathrm{Ti}}\right) \\ &\quad + y'_{\mathrm{Fe}} y'_{\mathrm{Ti}} L^{\mathrm{A2}}_{\mathrm{Fe,Ti:vac}} \\ &\quad + G^{\mathrm{mag}}. \end{aligned} \tag{3.1}$$

The term G^{mag} is the magnetic contribution as described by the Inden-Hillert-Jarl approach [109] with the parameters of Santhy and Kumar [107]. The ordered phase (bcc-B2) is then described with a three-sublattice model with formula $(\mathrm{Fe},\mathrm{Ti})_{0.5}(\mathrm{Fe},\mathrm{Ti})_{0.5}(\mathrm{vac})_3$, and the contribution to the Gibbs energy G^{ord} expressed as:

$$\begin{aligned} G_m^{\mathrm{ord}} &= y'_{\mathrm{Fe}} y''_{\mathrm{Fe}} G_{\mathrm{Fe:Fe:vac}} + y'_{\mathrm{Ti}} y''_{\mathrm{Ti}} G_{\mathrm{Ti:Ti:vac}} \\ &\quad + y'_{\mathrm{Ti}} y''_{\mathrm{Fe}} G_{\mathrm{Ti:Fe:vac}} + y'_{\mathrm{Fe}} y''_{\mathrm{Ti}} G_{\mathrm{Fe:Ti:vac}} \\ &\quad + RT\left(\frac{1}{2}\left(y'_{\mathrm{Fe}} \ln y'_{\mathrm{Fe}} + y'_{\mathrm{Ti}} \ln y'_{\mathrm{Ti}}\right) + \frac{1}{2}\left(y''_{\mathrm{Fe}} \ln y''_{\mathrm{Fe}} + y''_{\mathrm{Ti}} \ln y''_{\mathrm{Ti}}\right)\right) \\ &\quad + y'_{\mathrm{Fe}} y'_{\mathrm{Ti}} y''_{\mathrm{Fe}} L^{\mathrm{B2}}_{\mathrm{Fe,Ti:Fe:vac}} + y'_{\mathrm{Fe}} y'_{\mathrm{Ti}} y''_{\mathrm{Ti}} L^{\mathrm{B2}}_{\mathrm{Fe,Ti:Ti:vac}} \\ &\quad + y'_{\mathrm{Fe}} y''_{\mathrm{Fe}} y''_{\mathrm{Ti}} L^{\mathrm{B2}}_{\mathrm{Fe:Fe,Ti:vac}} + y'_{\mathrm{Ti}} y''_{\mathrm{Fe}} y''_{\mathrm{Ti}} L^{\mathrm{B2}}_{\mathrm{Ti:Fe,Ti:vac}} \\ &\quad + G^{\mathrm{mag}}. \end{aligned} \tag{3.2}$$

The total Gibbs energy of the bcc phase is then written as:

$$G_m^{\mathrm{bcc}} = G_m^{\mathrm{dis}} + \Delta G_m^{\mathrm{ord}}, \tag{3.3}$$

with ΔG^{ord} given by:

$$\Delta G_m^{\mathrm{ord}} = G_m^{\mathrm{ord}}(y_i^{'}, y_j^{''}) - G_m^{\mathrm{ord}}(y_i^{'} = y_i^{''} = x_i). \tag{3.4}$$

Here, the term $G_m^{\mathrm{ord}}(y_i^{'} = y_i^{''} = x_i)$ represents the disordered state of the ordered phase BCC_B2. This is because if the species i have the same fraction in the metallic sublattices, this fraction corresponds also to the mole fraction of that species and becomes indistinguishable from a solid solution in the BCC crystal lattice. When this internal state occurs, the contribution of the ordering energy is zero ($\Delta G_m^{\mathrm{ord}} = 0$) and $G_m^{\mathrm{bcc}} = G_m^{\mathrm{dis}}$.

The order-disorder transition, as for the case of BCC_B2/BCC_A2, may therefore be described as a single Gibbs energy function. Figure 3.5 illustrates the plot of the disordered state contribution to and the total Gibbs energy of the bcc phase employing the BCC_B2/BCC_A2 order-disorder model.

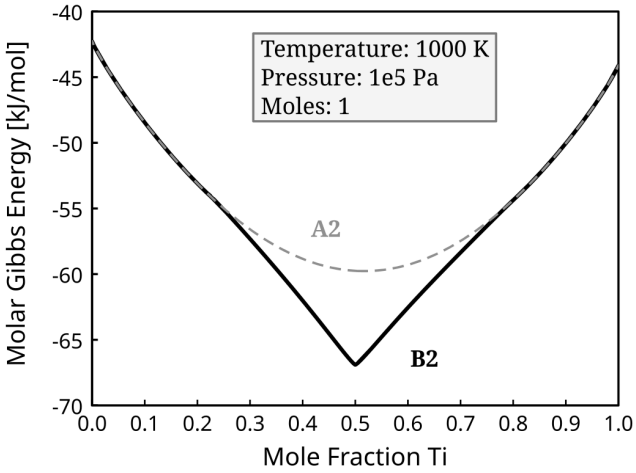

Figure 3.5: Total Gibbs energy of the FeTi bcc phase with the superimposed disordered state energy for comparison. The curves were calculated for the temperature of 1000 K using the thermodynamics parameters from [107].

One can observe that near solid solution regions, the bcc B2 occurs in a completely disordered state, and its Gibbs energy coincides with that of the bcc A2 phase. In contrast, the highest value for $\Delta G_m^{\mathrm{ord}}$ occurs in equimolar quantities of Fe and Ti when the system can create a perfectly ordered B2 phase with Fe and Ti completely separated into two distinguished metallic sublattices.

The formulated Gibbs energy may be further explored concerning its derivatives and enthalpy of mixing. Figure 3.6 shows the single phase stability analysis when applying Equation B.6, Equation B.1, and Equation B.3.

In Figure 3.6 the energetic effect of atomic ordering on the Gibbs energy of the BCC phase is observed by calculating its mixing enthalpy. At an equimolar quantity, the ordering enthalpy ($\Delta \mathrm{H}^{\mathrm{ord}}$) reaches its maximum, according to the minimum in Gibbs energy for the phase. The blue dots represent the enthalpy of many sampled internal states that the bcc phase can take. The minimization of the internal states leads to the more stable configuration for a given composition.

In equimolar composition, the internal state that minimizes the Gibbs energy of the bcc phase is given when the metallic sublattices are filled by unlike species (perfect ordering), which is annotated by "bcc B2" on Figure 3.6, correspondent to the lowest Gibbs energy of the BCC phase and indicates the highest internal state stability of the B2 phase. In contrast, when the same fractions of the opposite species are found in both metallic

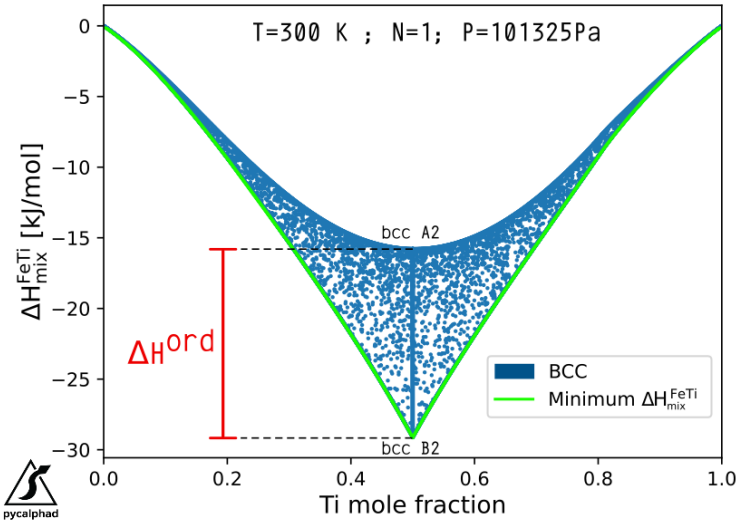

Figure 3.6: Calculated enthalpy of mixing of the bcc phase of the FeTi system at 300 K and 101 325 Pa with parameter from Santhy and Kumar [107]. The green solid line represents the minimum enthalpy of mixing for the single BCC phase configurations at a given composition.

sublattices, the Gibbs energy of the bcc phase is the highest at equimolar composition and approaches the value predicted by Miedema's model [103].

The first and second derivatives of the Gibbs energy (the chemical potential and the thermodynamic factor, respectively) are useful for quantifying the driving forces and, consequently, the tendencies of phase transformation. In Figure 3.7, the calculated chemical potentials of iron and titanium at 1500K are illustrated considering only the bcc phase.

Note that the chemical potential is constant for some regions of the curve. As in equilibrium, the chemical potential of a species is the same in the phases, and it is conclusive that the bcc phase stabilized its internal states by spontaneously decomposing into two different compositions. This is observed on both the iron-rich and titanium-rich sides of the curves, where an iron-rich or titanium-rich bcc phase would equilibrate with a bcc phase possessing near-equimolar composition.

It is also worth noting that at equimolar quantities the chemical potentials of both elements have the same value, or at least they are negligibly distinct. This similarity in chemical potential will be revisited in Section 4.1 to derive the appropriate thermodynamic model describing the chemical contribution to the interface energy between the FeTi-B2 phase and its correspondent

hydride.

In the second spatel of Figure 3.7, the thermodynamic factor is illustrated. For compositions where $\det|\Omega| = 0$ (see Equation B.3), it coincides with the two compositional sets of the bcc phase. In addition, there is a spike in the thermodynamic factor at the equimolar composition, demonstrating its high tendency to order.

Thermodynamic analysis of the internal states of the FeTi system's bcc phase is conclusive in demonstrating that the FeTi-ordered B2 phase can be considered a single compound even for metastable extrapolations. In particular, at lower temperatures, where the curves in Figure 3.7 become more distinct, this assumption becomes even more reasonable.

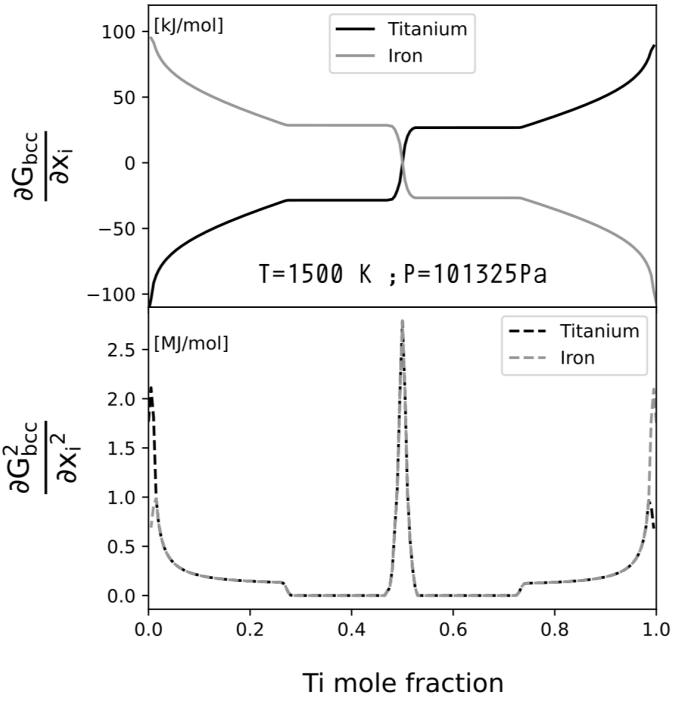

Figure 3.7: The chemical potential and the second derivative of the Gibbs energy of the bcc phase of the FeTi system calculated using parameter from Santhy and Kumar [107].

3.2 Thermodynamic modeling of the FeTi-H system

3.2.1 Introduction to the FeTi-H system

The FeTi hydrogenation

Before analyzing the hydrogen storage properties of hydride systems, the material must undergo proper activation. This process involves heat treatment under cyclic hydrogen pressure, which helps to remove any oxide layers on the surface, thereby opening up pathways for hydrogen absorption. Once activated, the *in-situ* investigation can proceed, typically through isothermal cycles of repeated hydrogen absorption and desorption. These cycles are performed by gradually equilibrating the hydrogen gas with the metallic sample in small pressure increments, using a Sieverts-type apparatus [110, 111]. The resulting pressure variations during these cycles are recorded to generate pressure-composition-isotherm (PCI) curves, which characterize the material's ability to absorb and release hydrogen at different temperatures. Figure 3.8 and Figure 3.9 show the measured absorption and desorption PCI curves of FeTi at different temperatures.

With increasing H_2 pressure, the hydrogen content in the solid system increases. Inflections of the PCI curves indicate the formation of new phases, and, in an ideal scenario, the coexistence of two solid phases results in a completely flat horizontal curve of the pressure over overall hydrogen composition within the solid material, known as plateau pressure. Such invariant reaction can be expressed with the following reaction equation (Equation 3.5):

$$\alpha\text{-FeTi} + \frac{1}{2}\mathrm{H_2} \rightarrow \beta\text{-FeTiH} + Q. \tag{3.5}$$

Where Q represents the heat of reaction. As the hydrogenation is exothermic, $Q > 0$ for absorption and $Q < 0$ for desorption.

The initial and final points of the plateau correspond to the onset and termination of the solid-phase transformations and indicate their equilibrium composition. The stability of solid phases is negligibly influenced by pressure. In practical applications, it is regarded independent, allowing a temperature-composition phase diagram for metal hydrides to align with the solubility limits derived from PCI curves. Many authors studied the hydrogenation of the FeTi intermetallic [112, 113, 114, 115]. Recently, Sujan et al. [116] reviewed FeTi hydrogenation and processing, whereas Dematteis et al. reviewed substitutional effects on the hydrogen storage properties of FeTi [35].

For FeTi, there is a consensus that hydrogenation around ambient temperatures involves at least three hydride phases, α, β, and γ. Initially, hydrogen is dissolved in the ordered B2 phase, forming the solid solution α phase. The increase in H_2 pressure quickly leads to the saturation of α after which the external thermodynamic conditions remain constant while hydrogen is absorbed, forming a new phase β. During this process, the gas phase coexists

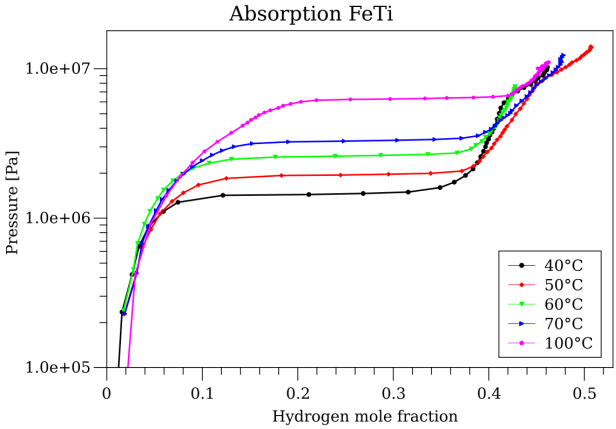

Figure 3.8: Experimentally measured absorption PCI curves at different temperatures. Raw data provided by the group colleague Dr. Yuanyuan Shang.

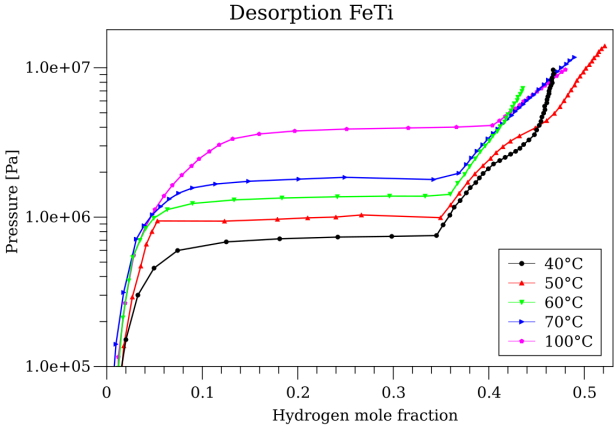

Figure 3.9: Experimentally measured desorption PCI curves at different temperatures. Raw data provided by the group colleague Dr. Yuanyuan Shang.

in equilibrium with the two solid phases. Figure 3.10 shows examples of each phase from the perspective of the bcc unit cell framework.

The completion of the transformation of $H_2 + \alpha \rightleftharpoons \beta$ accompanies the

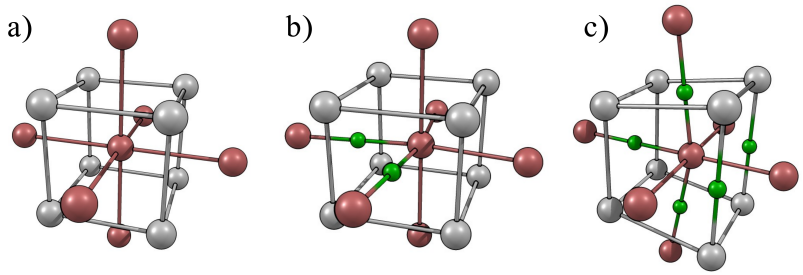

Figure 3.10: Example of crystal structures in the FeTi-H system viewed from the bcc-like unit cell framework including first neighbors Iron atoms. a) B2 (equimolar FeTi ordered bcc phase), b) β (monohydride), and c) γ (dihydride). Titanium in gray, iron in red, and hydrogen in green.

cessation of hydrogen absorption at constant pressure. At this point, with constant temperature, hydrogen is further absorbed only by externally incrementing the hydrogen partial pressure. The precise solubility range of β and the mechanisms of transformations it undergoes upon hydrogenation are not yet fully understood but seem to be highly dependent on the sample history, temperature, and sorption path [117]. Sections 3.2.3 and Section 3.2.5 will provide a plausible explanation of the underlying mechanism based on crystallographic evidence and thermodynamic analysis.

With completion of β formation at lower temperatures, the increase in hydrogen pressure results in a smooth inflection of the pressure composition curve, particularly visible in the logarithmic scale as a slopped plateau, see Figure 3.8, and Figure 3.9 for mole fraction hydrogen above 0.33. At higher temperatures, the slope increases and the inflections become less evident. Above a critical temperature, there is no clear evidence of this phenomenon, and the exact point is difficult to determine because the transition is narrow and quite gradual.

The formation of the γ phase occurs at maximal hydrogenation, and experimental evidence shows that it may be a highly stable structure in the system, whereas the formation of a second β phase named β_2 is possibly only a metastable process. This is indicated, for example, by Reidinger et al. [117] by the fact that annealing at 800 °C followed by activation facilitates the formation of γ, which could then be detected in coexistence with α at $FeTiH_{1.12}$. Another hint is the observation by Goodell et al. [118] showing that when the number of sorption cycles is increased, the second plateau fades out and a higher hydrogen pressure is required to reach the same level of hydrogen absorption. However, the first plateau pressure remains unaffected by this.

Both pieces of evidence give rise to the possibility that once γ forms, it remains in the system, blocking the formation of the intermediate β_2 phase

when a certain threshold amount of γ is present.

It should be noted that, even though the corresponding deuterides and hydrides in the FeTi-H/D systems are isomorphic [119], their lattice parameters [120] and the equilibrium pressure [121] vary slightly. For example, Fischer reported a difference in the enthalpy of reaction when using deuterium or hydrogen gas, $\Delta H_r = 3.7\,\mathrm{kJ/mol\,gas} = 31.0\,\mathrm{kJ/mol\,D_2}$ - $27.3\,\mathrm{kJ/mol\,H_2}$. This enthalpic difference led to a temperature-independent increase of less than 1×10^5 Pa in the plateau pressure of the deuteride with respect to the hydride. Regarding crystal structure variations, it is expected that the lattice parameters of β hydride are less than 0.1 Å shorter than those of the β deuteride counterpart, as shown in Schober's work [120]. Consequently, as some transition points detected in deuterides could exhibit slight shifts compared to those in corresponding hydrides, this should be considered when analysing the subsequent hypotheses.

FeTi-H paraequilibrium

As briefly introduced in Section 3.1.2, the FeTi system presents two different intermetallics: the Laves phase with approximate composition Fe_2Ti, and the B2 phase, an ordered bcc phase with approximate FeTi stoichiometry. The Laves phase negligibly absorbs hydrogen and does not form hydrides near standard conditions, while the B2 phase is responsible for providing the reversible hydrogen storage properties envisaged under ambient conditions.

Reilly and Wiswall were the first to study the hydriding properties of FeTi [113]. Although the B2 phase has relatively low solubility of hydrogen, it reversibly transforms into a monohydride at near atmospheric pressure and room temperature. This transformation can be reversed with relatively small changes in thermodynamic potentials, which provides the material with a high level of engineering control for use as a hydrogen storage material.

Special care should be taken when the thermodynamics of multicomponent metal hydrides are analyzed because such compounds are formed under hydrogenation conditions that do not promote a complete equilibrium.

This is a consequence of the significant differences between metallic atoms (M) and hydrogen atoms (H). The radii of metal atoms are generally much larger than those of hydrogen atoms and tend to establish the main lattice of the crystal structure. In contrast, H atoms enter the bulk and occupy the interstitial sites. In stark contrast to the low mobility of metal atoms, hydrogen atoms have much higher mobility at room temperature. Table 3.1 lists the diffusion coefficients (D) of Fe, Ti, and H in the B2 FeTi phase and evidences the pronounced difference in diffusivities between hydrogen and the Fe and Ti metallic species.

With diffusivities at least four orders of magnitude slower—especially at low temperatures—only H species can respond fast enough to changes in chemical potential, allowing them to quickly diffuse into interstitial sublattices and form hydrides.

Table 3.1: Diffusion coefficients (D), $D = D_0 \exp\left\{\frac{\Delta E_a}{RT}\right\}$, of Fe, Ti, and H in the B2 FeTi phase at various temperatures.

Element	Temperature [K]	D [m^2/s]	Reference
Fe	973	9.57×10^{-15}	[122]
Ti		8.12×10^{-16}	
Fe	1123	4.45×10^{-14}	
Ti		2.43×10^{-15}	
H	673	$\approx 1.0 \times 10^{-11}$	[123]

When this situation is attended, the hydrogen chemical potential equalizes in each co-existing phase, while this does not happen for the metallic elements that keep the alloy composition constant. In other words, the chemical equilibrium occurs only for hydrogen, whereas the metal elements are not necessarily in chemical equilibrium with the other species of the system. Reaching complete equilibrium is hindered by the sluggish diffusion kinetics of metallic elements, causing a metastable thermodynamic equilibrium of the phases. Such an internal meta-stable state is considered a para-equilibrium.

FeTi-H phase-diagrams

The first proposed phase diagram for the $FeTiH_x$ system [113] indicates that the solubility limit of α and the equilibrium composition of β with α would be constant at least up to 70 °C. It also shows the existence of a critical temperature between 55 °C and 70 °C above which a discrete coexistence of β and γ can no longer occur and the transformation should become continuous (indicated by dashed lines in Figure 3.11). This phenomenon was assumed based on the lack of evidence of a second plateau for the 70 °C isotherm curve and the vestigial plateau trace at 55 °C.

Later, Bowman et al. [124] extended the phase diagram by compiling higher temperature PCI sets from Reilly [113, 125] and Yamanaka [115]. Despite some uncertainties, there was good agreement with respect to α to β phase limits. Bowman's NMR study revised the $FeTiH_x$ diagram (including some uncertainty range for low temperature lines), extended the α+β phase limits to a higher temperature and showed an absence of the critical temperature for the β+γ two-phase region below 127 °C [124]. He also suggested a γ-β transformation at 117 °C either because of a critical stability temperature or due to some release of hydrogen.

In light of calorimetric and structural data in the range between 1–72 °C, Lebsanft [126] proposed a variation of the α-β solubility limit, indicating that somehow they would converge to a critical point at higher temperatures and

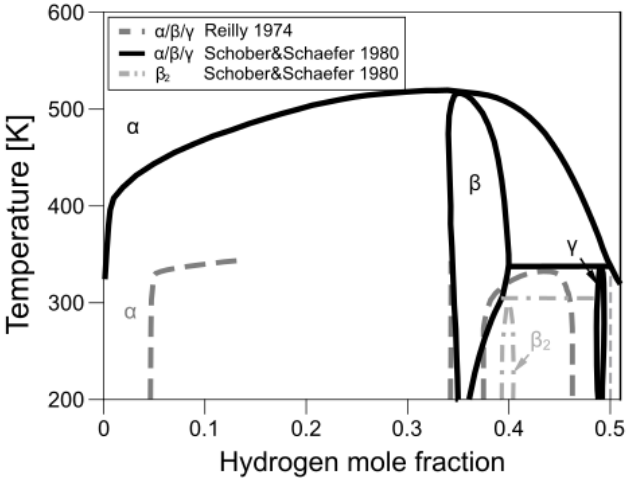

Figure 3.11: Adaptation of the schematic FeTi-H phase diagram from Schober and Schaefer [120] superimposed to the one proposed by Reilly and Wiswall [113]. See the text for more detailed explanation.

that the limit of stability of β should be much closer to $FeTiH_2$, showing that γ is possibly only stable as a quasi-stoichiometric compound. Although not mentioned by Lebsanft in his thesis, Schefer et al. [127] claimed that an additional plateau was visible in the low-temperature curves from Lebsanft and thus that the β_2 phase could be forming.

Soon after, Schober analyzed the system by Transmission Electron Microscopy (TEM) at varying temperatures. The cooling of the samples confirmed that β and γ could be kept at cryogenic temperatures, while the heating of the sample revealed a peritectoid transition $\gamma \rightleftharpoons \alpha + \beta$ above 60 °C [128]. Schober and Schäfer later detected another phenomenon when cooling below 35 °C [120]. They found that plate-like phases precipitate in hydrogen-rich β regions, in accordance with the previous evidence [127] of an existing ordered β_2 in equilibrium with β_1. Their published schematic phase diagram suggested another peritectoid reaction $\beta_2 \rightleftharpoons \gamma + \beta_1$ around 35 °C at $FeTiH_{1.33}$, as shown by dashed-dotted lines in Figure 3.11.

More recently, Endo et al. [129] used *in-situ* synchrotron radiation X-ray diffraction (SR-XRD) analysis under a severe hydrogen fluid pressure of 5 GPa at 600 °C and observed a hydrogen-induced order-disorder transition from the ordered FeTi solid solution α into a bcc hydride. Under these harsh conditions, the α-like phase presented higher hydrogen solubility and transformed into the bcc hydride, which underwent a lattice expansion of

21% at its maximal hydrogenation stage. After some time, the bcc hydride decomposed into TiH_2 and Fe_2Ti.

In conclusion, the $FeTiH_x$ phase diagram is essentially metastable since the hydrogenation of FeTi occurs under para-equilibrium conditions. Thus, there is no confirmation that the kept metallic equimolar quantity of the hydrides in the two-phase regions is in their thermodynamically most stable form. However, since the alloy maintains its composition due to the sluggish diffusion kinetics of the metal elements at lower temperatures and because the enthalpies of formation of TiH_2 and Fe_2Ti are much lower compared to those of ternary hydrides [115], the system tends to disproportionate to eventually reach complete equilibrium, as observed by Endo et al. [129].

3.2.2 Crystal structure of FeTi-based hydrides

The application of statistical thermodynamics is fundamental to the thermodynamic modeling of a system. Consequently, modeling a compound must closely align with its crystal structure, as this is a crucial factor in the statistical analysis of solid phases. Hence, the key properties of FeTi hydrides are examined in this section to aid in the proper selection of thermodynamic models for the phases.

Hydrogen absorption in metallic materials occurs through interstitial diffusion mechanisms. The B2 phase itself presents a relatively low solubility of hydrogen, and unlike most of the bcc metals, such as Fe and Ti [130, 23, 131, 132, 92, 133, 93], where hydrogen preferentially occupies tetrahedral sites, in the FeTi B2 phase, hydrogen preferentially occupies the octahedral sites. This was demonstrated by many Neutron Diffraction (ND) experiments performed on the deuterides of the FeTi system [134, 135, 136, 128, 119, 121].

Although most crystallographic characterizations are performed on deuterides instead of on the hydride itself, TEM and X-ray diffraction (XRD) experiments show that the FeTi-H system is isostructural with FeTi-D [128, 120, 119, 117]. Therefore, the isotopic effect can be assumed to be negligible.

Under room temperature conditions, hydrogenation of FeTi results in the formation of the solid solution phase, α, up to $FeTiH_{0.1}$. The monohydride phase, β, extends from $FeTiH_{1.04}$ to around $FeTiH_{1.22}$, and the dihydride phase, γ, remains stable between $FeTiH_{1.71}$ and $FeTiH_{1.93}$. In the FeTi-H system, at least three hydrides with different crystal structures are observed.

Due to the ordering of metallic elements into two sublattices, the FeTi B2 phase presents two distinguished types of octahedral interstitial sites. One of them is composed of four Ti and two Fe atoms (Ti_4Fe_2) with Fe atoms as the nearest neighbors, while the second type has four Fe and two Ti atoms (Ti_2Fe_4) with Ti atoms as the first neighbors. Considering the larger metallic atom radii of Ti with respect to Fe, which can be calculated from the bcc lattice constant of Ti $a = 3.231$ Å [89], resulting in a radius of $a\frac{\sqrt{3}}{4} = 1.399$ Å, or considering its hcp structure leading to a radius of 1.445 Å [137], while for bcc Fe the lattice constant is $a = 2.866$ Å, which leads to a metallic atomic

radius of 1.241 Å [137], resulting in the sizes of the different octahedral interstitial sites being ≈0.21 Å for the Ti_4Fe_2 and ≈0.0262 Å for the Ti_2Fe_4, which are calculated considering the smallest sphere that fits within the interstitial site. Consequently, hydrogen preferentially stabilizes in Ti_4Fe_2 sites [138].

α hydride

The α-hydride forms via random dissolution in Ti_4Fe_2 sites of the B2 phase [Figure 3.10 a)]. This is supported by DFT calculations [139], which show that hydrogen is more stable (less energetic) when located in the Ti_4Fe_2 octahedral sites than in Ti_2Fe_4 for hydrogen concentrations between 0 and 0.33 hydrogen atomic fraction. For the Ti_4Fe_2 sites, an exothermic enthalpy of reaction is calculated as $\Delta H \approx -4.3\,\mathrm{kJ/mol.H}$, whereas for Ti_2Fe_4, the reaction is endothermic with an enthalpy of $\Delta H_r \approx 19.3\,\mathrm{kJ/mol.H}$, both at 0.33 hydrogen atomic fraction. These findings align with ND experiments [136].

Fischer also observed that the degree of ordering of metallic elements in the bcc-like structure of the α-hydride is negligibly affected by hydrogenation, even after several cycles, and that the slight variation of the measured order parameter should come from surface effects [121].

The α hydride is thus analogous to the B2 phase, with a slightly larger lattice parameter at its saturation of the hydrogen solid solution ($a_\alpha = 2.979$ Å) and hydrogen atoms randomly occupying Ti_4Fe_2 octahedral sites [136, 119] to an extent of up to 0.05 hydrogen mole fraction in the crystal.

Additional hydrogen insertion in α increases the displacement of the nearest Fe neighbors of the Ti_4Fe_2 octahedral interstitial sites and induces a phase transformation of α into β.

β hydride

The β hydride has an orthorhombic structure [134] with space group $P222_1$. The β phase is indexed with lattice parameters $b_\beta \approx 4.3$ Å, which is similar to the diagonal of the ordered FeTi B2 phase, $a_\beta \approx 4.5$ Å and $c_\beta \approx 2.98$ Å. The interstitial sites are slightly deformed compared to those of the B2 phase; in particular, the Ti_4Fe_2 octahedral sites present are divided into two distinguished geometries, namely H_1 and H_2, which are partially occupied.

The occupancy of these octahedral sites gives rise to two forms of the beta phase, β_1 and β_2 [128, 117, 127]. Both have similar crystal structures except for the hydrogen distribution in these sites. Experimental investigations show an ordered hydrogen occupation in these sublattices for both forms of β [134, 127, 120]. Schäfer et al. [140] discussed neutron diffraction results if the interstitial atoms were evenly occupied, that is, H1 / H2 = 0.50 / 0.50, or distributed in a ratio of 0.90 / 0.10.

However, the most accepted analyzes of hydrogen occupancy in these interstitial sites conclude that the β_1 phase is characterized by H1/H2 =

0.88/0.12 [127, 140], while β_2 is H1 / H2 = 0.92/0.45. These sublattice occupancies correspond roughly to the FeTiH and $(FeTi)_3H_4$ formula units, respectively.

Upon hydrogenation, the volume expansion of β reaches 4.5%, and experimental evidence suggests that the phase transition $\beta_1 \rightleftharpoons \beta_2$ occurs discontinuously at room temperature. Nevertheless, the transition may also be described as a single-phase continuous process, with both sites being simultaneously enriched with hydrogen [128, 127].

γ hydride

The γ phase crystal structure is still under debate but is known to have at least 1.74 hydrogen atoms per Fe-Ti pair. The phase appears as a consequence of further hydrogenation of the β hydride during absorption. The difficulties in defining the crystallography of the γ hydride are due to the fact that its formation at room temperature requires a hydrogen partial pressure above 5 MPa, which is hard to maintain during experiments. Additionally, the γ phase is stable only within a narrow range of hydrogen compositions. The strain generated during its formation and the residual β phase in the sample can introduce noise in the diffraction signal, making it difficult to obtain precise crystallographic data.

Many authors have proposed different crystal structures for the γ phase. Based on X-ray diffraction experiments, Reilly proposed a cubic structure [113]. Fischer et al. indicated that an orthorhombic structure [121] is suggested based on ND experiments. Shortly after, ND and TEM studies correlated γ with the orthorhombic crystal structure of β [127, 135], leading to assumptions that γ is formed from the complete insertion of hydrogen at the previously observed Ti_4Fe_2 sites of β and into an additional Ti_2Fe_4 octahedral site. This would drive it towards the formation of a monoclinic P2/m structure, therefore losing orthogonality and degrees of symmetry.

Schefer observed that not only the deuteride but also the hydride compound show an analogous transformation [127]. Soon after, Schäfer et al. [119] identified an increase in monoclinic distortion of γ with decreasing temperature.

Fischer et al. [141] concluded that the Ti_2Fe_4 sites are energetically much less favorable and possibly the last to be filled with hydrogen, reaching a partial occupation of 91% at high hydrogen concentrations. It was assumed that the orthorhombic Cmmm crystal structure better suits neutron diffraction data than the monoclinic P2/m, which was later corroborated by observations from Thompson et al. [142] and DFT calculations of the fully hydrogenated γ ($FeTiH_2$).

3.2.3 First-principles calculations

The initial crystal structures of the compounds observed experimentally in the FeTi-H system, α (FeTi), β (FeTiH), and γ ($FeTiH_2$), were obtained from

those provided by the Web platform "Materials Project" [143]. Subsequently, the structures were optimized with respect to ion position, cell shape, and volume. Section A.1 from the **Appendix** A shows the evaluation procedure to obtain the optimal DFT settings employed in this work. Ultimately, the Perdew and Wang (`PW91`) [65, 66] exchange-correlation functional within the generalized gradient approximation (GGA) was selected to be employed.

Bulk structures and elastic properties

The total energy as a function of volume was fitted to the Birch-Murnaghan equation of state [144], from which the equilibrium volume, the bulk modulus and its derivative, the equilibrium lattice parameters, and the minimum energy were acquired and are listed in Table 3.2. Refer to **Appendix** A.1 for additional details concerning these calculations.

Table 3.2: This work calculated α and β phases bulk properties compared to experimental values from the literature [134, 145]

	Equilibrium volume [Å^3]	Lattice parameter [Å]	Bulk modulus [GPa]
Phase	Calc. (Exp.)	Calc. (Exp.)	Calc. (Exp.)
$\alpha-$FeTi	25.75 (26.25)	a=b=c =2.95 (2.97)	192.6 (189.0)
β-FeTiH*	56.46 (58.93)	a=4.56 (4.54) b=4.26 (4.39) c=2.90 (2.96)	185.2 (N/A)

*The experimental values for the β-phase were measured for its deuteride form [134].

Formation and reaction energies

In order to compute internal state energies, the obtained equilibrium structures were kept fixed, and hydrogen was permuted to all uniquely distinguishable octahedral sites that are experimentally observed to be occupied.

Then, the structures of the compounds were relaxed with respect to ion positions while the unit cell structure was kept constant. The ground-state formation energy of each compound ($\Delta E^{\phi}_{(\mathrm{FeTi})_\mathrm{m}\mathrm{H}_\mathrm{n}}$) was calculated in reference to its stable-element reference (SER) ground-state energy calculated using DFT, as described in Equation 3.6.

$$\Delta E^{\phi}_{(\mathrm{FeTi})_\mathrm{m}\mathrm{H}_\mathrm{n}} = E^{\phi}_{(\mathrm{FeTi})_\mathrm{m}\mathrm{H}_\mathrm{n}} - \left(\frac{m}{2}E^{\mathrm{bcc}}_{\mathrm{Fe}} + \frac{m}{2}E^{\mathrm{hcp}}_{\mathrm{Ti}} + \frac{n}{2}E^{\mathrm{molec}}_{\mathrm{H_2}}\right). \tag{3.6}$$

Note that the SER for hydrogen corresponds to its molecular gaseous form and was approximated by the calculated DFT energy of a H_2 molecule in vacuum, neglecting its entropic term. The terms $E_{\mathrm{Fe}}^{\mathrm{bcc}}$ and $E_{\mathrm{Ti}}^{\mathrm{hcp}}$ are the ground-state DFT energies of the SER, representing bcc iron and hcp titanium, respectively.

Due to symmetry, there are only two options for adding a single hydrogen to the α-phase unit cell: the Fe_2Ti_4 and the Fe_4Ti_2 octahedral sites. The permutation of distributing up to six H atoms in both octahedral sites produces 20 distinguished compounds.

The present DFT computations show that the lowest formation energy for adding a given number of H atoms into the α unit cell lattice is obtained when the H atoms are the furthest apart from each other and preferentially located in Fe_2Ti_4 sites, agreeing with the findings from Nong et al. [139].

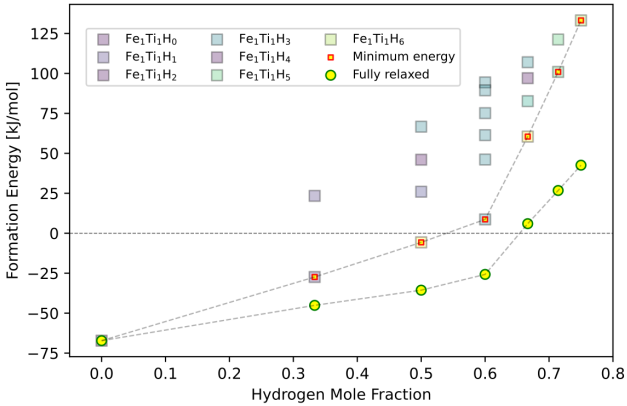

Figure 3.12: DFT ground-state formation energies of the compounds with α crystal structures obtained by hydrogen-vacancy permutations in the octahedral sites.

As an initial step in investigating internal energy variations when hydrogen enters the octahedral interstitial lattice of the β phase, hydrogen and vacancy permutations were performed within the 12 possible sites. Such an approach results in 1360 configurations (some of them possibly identical from a crystallographic perspective). These compounds were relaxed with respect to the ion positions and, subsequently, for a given composition, the minimum energy compound was fully relaxed (i.e. with respect to the ion positions, cell shape, and volume). The formation energies and reaction energies were calculated for each of these compounds. Figure 3.13 shows the calculated formation energy of the β compounds.

In Figure 3.13, it is possible to detect that both the relaxed ion-position minimum energy curve and the fully relaxed structures show inflections

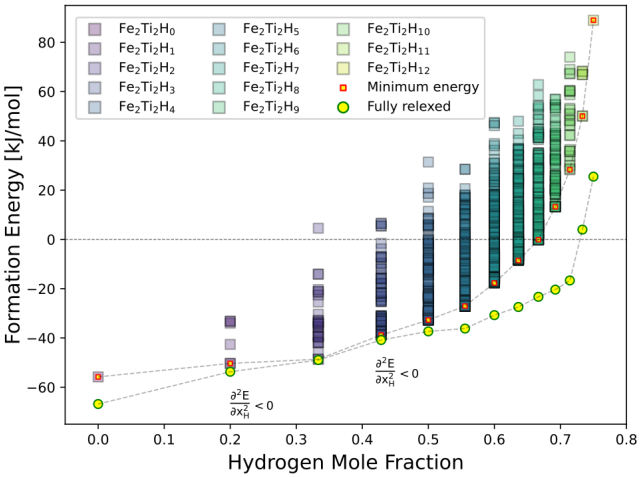

Figure 3.13: DFT ground-state formation energies of the compounds with β crystal structures obtained by hydrogen-vacancy permutations in the octahedral sites.

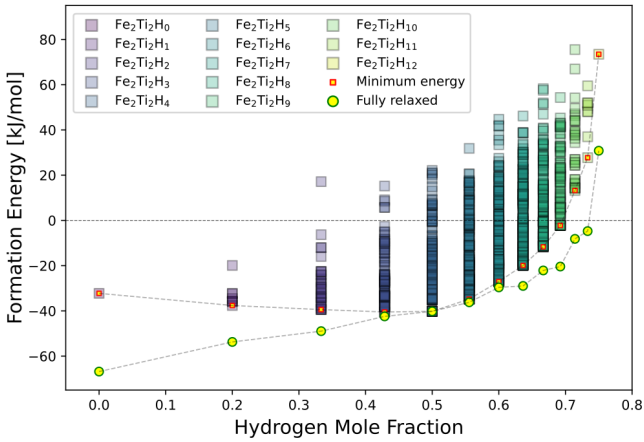

Figure 3.14: DFT ground-state formation energies of the compounds with γ crystal structures obtained by hydrogen-vacancy permutations in the octahedral sites.

with convex curves between FeTi and FeTiH, and between $FeTiH_2$ and FeTiH composition ranges, which consequently presents positive partial second derivatives of the energy curve with respect to the hydrogen mole fraction $(\partial^2 E/\partial x_H^2)$ at $x_H = 0.2$ and $x_H = 0.43$. This features the characteristic that the β phase is able to coexist with its β_2 form, which would correspond to the same orthorhombic lattice structure, but with a richer hydrogen content at the octahedral sites compared to β_1.

Analogously, Figure 3.14 presents the calculated resulting formation energies of γ compounds. For γ compounds, the convex characteristic of the relaxed minimum curve of the ion position is not observed as for the β phase, and no other local minimum energy is observed in addition to that for $x_h = 0.5$. This contributes to the conjecture that the second-order thermodynamic transition observed within the FeTi system during hydrogenation could be an expression of the internal energy minimization related to intrinsic internal configuration states of the β hydride structure.

For comparison purposes, the ion-relaxed minimal energy structures for α, β, and γ phases are superimposed in Figure 3.15.

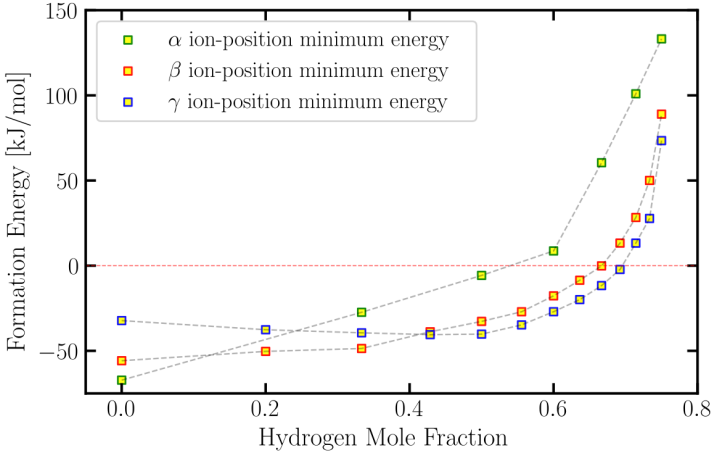

Figure 3.15: DFT ground-state formation energies of minimum energy ion-position relaxed compounds with α, β, and γ crystal structures obtained by hydrogen-vacancy permutations in the octahedral sites.

From Figure 3.15 the internal state energies of the orthorhombic β and monoclinic γ structures with respect to the amount of hydrogen in the unit cell can be compared with each other, showing that at the ground state, the β-structured compounds present lower formation energy for regions below $(FeTi)_2H_3$ than that of γ-structured compounds, which tends to be more

stable than the β phase for compounds with higher hydrogen content than that of the $(FeTi)_2H_3$ structure.

Moreover, for this composition ($x_H = 0.43$), the minimum energy ion-relaxed structure of β and the γ structures are energetically similar, and even though their crystal structure is not the same, their formation energy varies by not more than 1.6 kJ/mol. Even though the formation energy provides a general idea of the compounds stability and is one of the default quantities for energy comparison in materials sciences, an in-depth analysis can be performed via evaluation of the hydrogenation energies. These are obtained from the reaction energy of hydrogen with the precursor alloy to form a hydride. As the hydrogenation of an alloy is performed in constant hydrogen partial pressure and temperature, this quantity can be compared to the measured absorption energy. The equation for obtaining such a value is given by Equation 3.7:

$$\Delta E^{\phi}_{(\mathrm{FeTi})_\mathrm{m}\mathrm{H}_\mathrm{n}} = E^{\phi}_{(\mathrm{FeTi})_\mathrm{m}\mathrm{H}_\mathrm{n}} - (mE^{\mathrm{B2}}_{\mathrm{FeTi}} + \frac{n}{2}E^{\mathrm{molec}}_{\mathrm{H_2}}), \tag{3.7}$$

where m and n relate to the stoichiometry of the compounds.

It is noteworthy that $(FeTi)_2H_3$ stoichiometric β- and γ-phase compounds exhibit comparable formation and reaction energies in their thermodynamically favored configurations. This corroborates the hypothesis proposed by Reilly [113] that the $\beta \Leftrightarrow \gamma$ transformation may occur as a first- or second-order transition with the critical point occurring for low values of thermodynamic potentials, i.e. close to ambient temperature and atmospheric pressure.

However, as mentioned above, from the ground state analysis presented here, it is possible to infer that, even at the ground state, the $\beta_1 \rightleftharpoons \beta_2$ transformation may also occur as a first-order thermodynamic transition. These findings suggest that there may exist a competition between β_2 and γ during further hydrogenation of the β phase. Given that the formation and reaction energies of the $(FeTi)_2H_3$ compounds with the orthorhombic and monoclinic structures are very similar, a stabilization of β_2 with orthorhombic structure in a metastable state may occur depending on the path of the hydrogenation process.

Moreover, since β_2 stabilizes in this metastable state, it is possible to conjecture that the transformation process of β_2 into γ is likely to be very sensitive to external thermodynamic potentials and their variation rate. Such thermodynamic potentials could be mechanical or thermal in origin, meaning that a stiff variation in partial hydrogen pressure in the surroundings of the β phase, strain energy induced by mechanical alloying or any other kind of mechanical work, or even cooling or heating rates, could significantly influence the final microstructure and phase constitution of the hydrogenated FeTi alloy.

Employing Equation 3.7, the reaction energy (or absorption energy), for the β-FeTiH phase is found as $\Delta E^{\beta}_{\mathrm{abs}} = -24.94$ kJ/mol.H_2, and for the

γ-$FeTiH_2$ phase as $\Delta E^{\gamma}_{abs} = -26.45$ kJ/mol.H_2. These values are consistent with the reaction enthalpy for the formation of β and γ hydrides during FeTi hydrogen absorption, which are reported between -22.8 and -27.4 kJ/mol.H_2 for β (first plateau) and between -26.6 and -33.9 kJ/mol.H_2 for γ (second plateau) depending on the initial state (i.e., the preparation method) of the sample, as summarized by Dematteis et al. [35].

3.2.4 Thermodynamic modeling

In this section, the rationale for the development of the CALPHAD thermodynamic models employed in this work is presented and discussed.

Thermodynamics of the paraequilibrium description

As mentioned in Section 3.2.1, hydrogenation of the FeTi alloy takes place under para-equilibrium conditions. This limits the unrestricted optimization of model parameters in thermodynamic assessments, as the Gibbs energy minimization predicts the most stable state of the system, including the most stable state of each phase of the materials system. This complete equilibrium condition is not reached during the hydrogenation process. Instead, the hydrogenated FeTi alloy remains in a metastable state, which is only possible because of the lower mobility of the metallic species in comparison to the hydrogen mobility under hydrogenation conditions.

For example, if the binary descriptions of the BCC phase of the Fe-Ti [107], Ti-H [89], and Fe-H [146] system are combined, it is possible to extrapolate the Gibbs energy surface into ternary regions, as shown in Figure 3.16.

Figure 3.16 and Figure 3.17 show that the internal state stabilizing the BCC phase in the Fe-Ti-H system lies around TiH_2 composition. Consequently, if a hydride phase with equimolar FeTi composition is entered into the system, a near TiH_2 BCC phase will tend to equilibrate with the hydride, which is not observed during the hydrogenation of FeTi. This more stable equilibrium prevents the adjustment of model parameters necessary to describe the equilibrium between the FeTi-B2 phase with the FeTi equimolar ternary hydride. However, from the deffinition of paraequilibrium, only the mobile element equilibrate while the sluggish ones behave as a single element [147]. As mentioned previously, this situation is clearly expecteded in metal- metal hydride systems, as evidenced by their discrepant diffusivities, as shown in Table 3.1. In this case, the paraequilibrium condition enforces that the metallic composition remains constant with a ratio of one Fe species for each Ti species.

To account for such conditions, Fe and Ti are merged into a hypothetical element 'FT' in this work, so that it represents the equimolar FeTi alloy. The models must then be configured accordingly. By doing so, the isoplethal section FeTi-H of the ternary system is correlated to the pseudo-binary metal-hydrogen FT-H system. This description allows the evaluation of hydride model parameters under para-equilibrium. It also avoids including the more

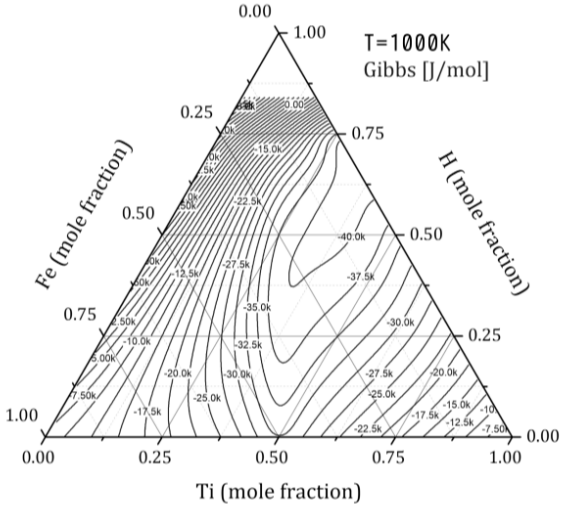

Figure 3.16: Gibbs energy projection of the BCC phase of the Fe-Ti-H ternary system calculated at 1000 K. The model parameters are taken from [107] for Fe-Ti, [89] for Ti-H, and [146] for Fe-H.

stable binary phases that compose the complete equilibrium, and instead of predicting the decomposition of the hydrides into Fe_2Ti + TiH_2, or the stabilization of the BCC phase with near TiH_2 composition, the equilibrium calculation thus describes the metastability of the equimolar ternary hydrides with the H_2 gas. In the next subsections, the phase models that follow this strategy guideline are presented.

Thermodynamic model of the α phase

Since the B2 structure has three octahedral sites per metallic atom, a two-sublattice (2SL) model (FT)(vac, H)$_3$ was used to describe the α phase accounting for a 1:3 ratio of substitutional to interstitial sites keeping consistency with most models describing bcc-like structures [75]. The first SL accounts for the metallic sites, while the second SL represents the octahedral sites where vacancies (vac) and hydrogen (H) mix. The Gibbs energy per mole of formula units is expressed as follows:

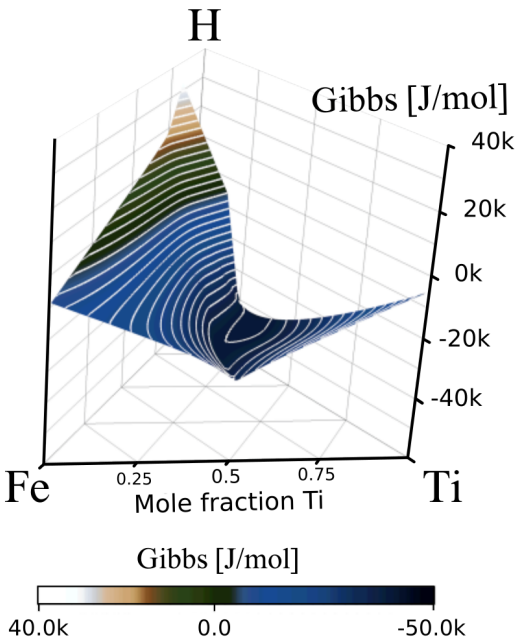

Figure 3.17: Gibbs energy surface of the BCC phase of the Fe-Ti-H ternary system calculated at 1000 K. The model parameters are taken from [107] for Fe-Ti, [89] for Ti-H, and [146] for Fe-H.

$$
\begin{aligned}
G^{\alpha} = \quad & {}^{o}y_{\mathrm{vac}}\,{}^{0}G^{\alpha}_{\mathrm{FT:vac}} \\
& + {}^{o}y_{\mathrm{H}}\,{}^{0}G^{\alpha}_{\mathrm{FT:H}} \\
& + 3RT({}^{o}y_{\mathrm{H}} \ln {}^{o}y_{\mathrm{H}} + {}^{o}y_{\mathrm{vac}} \ln {}^{o}y_{\mathrm{vac}}) \\
& + {}^{o}y_{\mathrm{vac}}\,{}^{o}y_{\mathrm{H}} \sum_{\upsilon=0}^{n} {}^{\upsilon}L^{\alpha}_{\mathrm{FT:H,vac}}({}^{o}y_{\mathrm{H}} - {}^{o}y_{\mathrm{vac}})^{\upsilon}\,. \qquad (3.8)
\end{aligned}
$$

The ${}^{o}y_i$ variables represent the fraction of species i placed in the octahedral sites. The last term of Equation 3.8 is the Redlich-Kister polynomial [77], where ${}^{\upsilon}L_{\mathrm{FT:H,vac}}$ accounts for the υ^{th}-order binary interaction between hydrogen and vacancy in the interstitial lattice. This can be expressed as ${}^{\upsilon}L^{\alpha}_{\mathrm{FT:H,vac}} = {}^{\upsilon}A^{\alpha} + {}^{\upsilon}B^{\alpha}T$, where A and B are optimized model parameters.

The Gibbs energies of the end-members of the α phase are represented by the ${}^{0}G^{\alpha}_{\mathrm{FT:vac}}$ and ${}^{0}G^{\alpha}_{\mathrm{FT:H}}$ terms. Note that if the α phase has no hydrogen in

the interstitial sites, it becomes structurally identical to the FeTi BCC_B2 phase. The Gibbs energy term ${}^{0}G^{\alpha}_{\mathrm{FT:vac}}$ is, therefore, a representation of the perfectly ordered FeTi BCC phase (G^{B2}), and the Gibbs energy expression for this end-member may be obtained by the analytical solution of the order-disorder model from Santhy and Kumar [107] when Fe and Ti are perfectly ordered in the BCC lattice.

As demonstrated in Section 3.1.2, because the ordering is generally a second-order thermodynamic transition for many metallic systems, the order-disorder description of the bcc phase enforces the treatment of the ordered and the disordered state within the same Gibbs-energy expression.

Following the description Santhy and Kumar [107], a two-sublattice model $(\mathrm{Fe, Ti})(\mathrm{vac})_3$ representing a solid solution of Fe and Ti in the BCC metallic lattice (disordered phase, or BCC_A2) and a 3SL model $(\mathrm{Fe, Ti})(\mathrm{Fe, Ti})(\mathrm{vac})_3$ to represent the partitioning of the metallic site into two different sites (ordered phase, or BCC_B2) are employed.

The disordered state of the ordered phase is given when each element fraction in each partitioned sublattice is equal to the overall mole fraction. The reduction of the Gibbs energy due to ordering is calculated by the difference between the 'ordered phase' and the 'ordered phase as disordered' [75].

The maximum ordering contribution in the FeTi BCC lattice occurs when each partitioned metallic sublattice is fully occupied by unlike metallic atoms, as shown in Figure. 3.10 a). With this condition inserted into the thermodynamic model, it assumes $(\mathrm{Fe})_{0.5}(\mathrm{Ti})_{0.5}(\mathrm{vac})_3$ or $(\mathrm{Ti})_{0.5}(\mathrm{Fe})_{0.5}(\mathrm{vac})_3$ configurations, becoming perfectly ordered.

To derive the analytical solution, any of these configurations should converge to identical results; thus, for this demonstration, the $(\mathrm{Fe})_{0.5}(\mathrm{Ti})_{0.5}(\mathrm{vac})_3$ configuration is selected. Consequently, the specified constraints are derived: $y^{'}_{\mathrm{Fe}} = 1$, $y^{'}_{\mathrm{Ti}} = 0$, $y^{''}_{\mathrm{Fe}} = 0$, $y^{''}_{\mathrm{Ti}} = 1$ and, $x_{\mathrm{Fe}} = 0.5$, $x_{\mathrm{Ti}} = 0.5$.

Moreover, because of the crystal symmetry of the BCC_B2 phase:

$$G_{\mathrm{Ti:Fe:vac}} = G_{\mathrm{Fe:Ti:vac}}, \tag{3.9}$$

$$L^{\mathrm{B2}}_{\mathrm{Ti:Fe,Ti:vac}} = L^{\mathrm{B2}}_{\mathrm{Fe,Ti:Ti:vac}}, \tag{3.10}$$

$$L^{\mathrm{B2}}_{\mathrm{Fe:Fe,Ti:vac}} = L^{\mathrm{B2}}_{\mathrm{Fe,Ti:Fe:vac}}. \tag{3.11}$$

For FeTi, the magnetic contribution can be neglected as the equimolar B2 ordered phase is not magnetic. Finally, the perfectly ordered Gibbs energy expression is given by:

$$\begin{aligned} G^{\mathrm{dis}}_{m}(x_{\mathrm{Fe}} = x_{\mathrm{Ti}} = 0.5) = {} & 0.5G_{\mathrm{Fe:vac}} + 0.5G_{\mathrm{Ti:vac}} \\ & + RT\,(0.5\ln 0.5 + 0.5\ln 0.5) \\ & + 0.25L^{\mathrm{A2}}_{\mathrm{Fe,Ti:vac}}, \end{aligned} \tag{3.12}$$

and

$$G^{\mathrm{ord}}_{m}(y^{'}_{\mathrm{Fe}} = 1,\ y^{''}_{\mathrm{Ti}} = 1) = G_{\mathrm{Fe:Ti:vac}}, \tag{3.13}$$

and

$$\begin{aligned} G_m^{\text{ord}}(y_{\text{Fe}}^{'} = y_{\text{Ti}}^{''} = 0.5) = {} & 0.5 G_{\text{Fe:Ti:vac}} \\ & + RT\,(0.5 \ln 0.5 + 0.5 \ln 0.5) \\ & + 0.25 L_{\text{Fe,Ti:Fe:vac}}^{\text{B2}} \\ & + 0.25 L_{\text{Fe,Ti:Ti:vac}}^{\text{B2}}. \end{aligned} \tag{3.14}$$

Note that, for equimolar quantities ($x_i = x_j = 0.5$), the Redlich-Kister polynomial form attributed to the interaction parameters for the case of the disordered phase and the ordered phase as disordered, i.e., $L_{\text{Fe,Ti:vac}}^{\text{A2}}$, $L_{\text{Fe,Ti:Fe:vac}}^{\text{B2}}$, and $L_{\text{Fe,Ti:Ti:vac}}^{\text{B2}}$, only the zero-th order ($\upsilon = 0$) interaction parameters take effect:

$$x_i x_j \sum_{\upsilon=0}^{n} {}^{\upsilon} L_{i,j}^{\phi} (x_i - x_j)^{\upsilon}. \tag{3.15}$$

Therefore:

$$L_{\text{Fe,Ti:vac}}^{\text{A2}} = {}^{0} L_{\text{Fe,Ti:vac}}^{\text{A2}}, \tag{3.16}$$

$$L_{\text{Fe,Ti:Fe:vac}}^{\text{B2}} = {}^{0} L_{\text{Fe,Ti:Fe:vac}}^{\text{B2}}, \tag{3.17}$$

$$L_{\text{Fe,Ti:Ti:vac}}^{\text{B2}} = {}^{0} L_{\text{Fe,Ti:Ti:vac}}^{\text{B2}}. \tag{3.18}$$

Now, applying Equation 3.3 and Equation 3.4, the energy of the perfectly ordered FeTi BCC_B2 phase becomes:

$$G^{\text{B2}} = G_m^{\text{dis}}(x_{Fe} = x_{Ti} = 0.5) \tag{3.19}$$

$$\begin{aligned} & + G_m^{\text{ord}}(y_{Fe}^{'} = 1,\ y_{Ti}^{''} = 1) - G_m^{\text{ord}}(y_{Fe}^{'} = y_{Ti}^{''} = 0.5) \\ & = 0.5 G_{\text{Fe:vac}} + 0.5 G_{\text{Ti:vac}} + 0.5 G_{\text{Fe:Ti:vac}} \\ & + 0.25\ {}^{0} L_{\text{Fe,Ti:vac}}^{\text{A2}} \\ & - 0.25 \left({}^{0} L_{\text{Fe,Ti:Fe:vac}}^{\text{B2}} + {}^{0} L_{\text{Fe,Ti:Ti:vac}}^{\text{B2}} \right) \end{aligned} \tag{3.20}$$

The parameters ${}^{0} L_{\text{Fe,Ti:vac}}^{\text{A2}}$, ${}^{0} L_{\text{Fe,Ti:Fe:vac}}^{\text{B2}}$, ${}^{0} L_{\text{Fe,Ti:Ti:vac}}^{\text{B2}}$, and $G_{\text{Fe:Ti:vac}}$ were assessed by Santhy and Kumar [107]:

$$\begin{aligned} & 2 G_{\text{Fe:Ti:vac}} = G^{\text{FeTi}} = \\ & - 76147 - 46.603 T \\ & + 8.663 T \ln(T) - 7.151.10^{-3} T^2 \\ & + 1.121169.10^{-6} T^3 \end{aligned} \tag{3.21}$$

$$ {}^{0}L^{\mathrm{A2}}_{\mathrm{Fe,Ti:vac}} = -68448 + 23.825T \tag{3.22} $$

$$ {}^{0}L^{\mathrm{B2}}_{\mathrm{Fe,Ti:Fe:vac}} = -10953 \tag{3.23} $$

$$ {}^{0}L^{\mathrm{B2}}_{\mathrm{Fe,Ti:Ti:vac}} = -6097 \tag{3.24} $$

The assessed parameters representing the pure BCC Fe and Ti are obtained by the Gibbs energy assessments from Dinsdale [148]:

$$ G_{\mathrm{Fe:vac}} = {}^{0}G^{\mathrm{SER}}_{\mathrm{Fe}} \tag{3.25} $$

$$ G_{\mathrm{Ti:vac}} = {}^{0}G^{\mathrm{BCC}}_{\mathrm{Ti}} \tag{3.26} $$

Ultimately, it is shown that the parameter representing the perfect ordered BCC_B2 phase includes the formation energy of the FeTi BCC_B2 phase referenced in the pure metals in their BCC lattice, and terms coming from the excess contributions of the equimolar 'disordered phase' and the 'ordered phase as disordered', which is attributed to the value of $G^{\alpha}_{\mathrm{FT:vac}}$.

The second term ${}^{0}G^{\alpha}_{\mathrm{FT:H}}$ may be expressed from the Gibbs energy of formation of the hypothetical compound $FeTiH_6$ with metallic B2 structure and all available octahedral sites occupied by hydrogen atoms. For simplicity, this compound is attributed the name α_6. The term ${}^{0}G^{\alpha}_{\mathrm{FT:H}}$ is thus expressed by:

$$ {}^{0}G^{\alpha}_{\mathrm{FT:H}} = {}^{0}G^{\alpha}_{\mathrm{FT:vac}} + \frac{3}{2}G^{\mathrm{SER}}_{\mathrm{H_2}} + \Delta H^{\alpha_6}_{f} + \Delta S^{\alpha_6}_{f} T\,. \tag{3.27} $$

The enthalpy and entropy of formation for the $FeTiH_6$ compound ($\Delta H^{\alpha_6}_{f}$ and $\Delta S^{\alpha_6}_{f}$, respectively) are evaluated using the experimental and DFT results obtained in the present study. The formation energy of $FeTiH_6$ in the α structure was obtained through Equation 3.6 and used to represent the experimental value of $\Delta H^{\alpha_6}_{f}$.

Thermodynamic model of the β phase

Experimental evidence shows that the β phase has at least one hydrogen per formula unit and that hydrogen occupies the first octahedral site. Thus, the model for representing the β phase was chosen as a 3-sublattice model: $(FT)_2(H)(vac, H)$, in which hydrogen is always fully occupying the second sublattice site.

The first sublattice represents the substitutional positions of the metallic sites, while the second and third sublattices represent the H1 and H2 interstitial sites, respectively. Such a model allows additional hydrogen to enter and mix with vacancies only in H2. When the H2 sites are empty or occupied by hydrogen, the model gives rise to two end-members in the frame of the β crystal lattice, with compositions FeTiH and $FeTiH_2$, which may thus be related to the β_1 and β_2 atomic configurations, respectively.

The mixing in the H2-sublattice allows the description of the miscibility gap between β_1 and β_2 and its dependence on temperature permits the reproduction of the observed critical temperature above which the transformation appears as a continuous process.

The Gibbs energy of β per mole of formula unit is given as:

$$\begin{aligned} G^{\beta} =& {}^{\mathrm{H2}}y_{\mathrm{vac}}\,{}^{0}G^{\beta}_{\mathrm{FT:H:vac}} + {}^{\mathrm{H2}}y_{\mathrm{H}}\,{}^{0}G^{\beta}_{\mathrm{FT:H:H}} \\ &+ RT({}^{\mathrm{H2}}y_{\mathrm{H}} \ln {}^{\mathrm{H2}}y_{\mathrm{H}} + {}^{\mathrm{H2}}y_{\mathrm{vac}} \ln {}^{\mathrm{H2}}y_{\mathrm{vac}}) \\ &+ {}^{\mathrm{H2}}y_{\mathrm{vac}}\,{}^{\mathrm{H2}}y_{\mathrm{H}} \sum_{\upsilon=0}^{n} {}^{\upsilon}L^{\beta}_{\mathrm{FT:H:H,vac}}({}^{\mathrm{H2}}y_{\mathrm{H}} - {}^{\mathrm{H2}}y_{\mathrm{vac}})^{\upsilon}\,, \end{aligned} \tag{3.28}$$

where ${}^{\mathrm{H2}}y_i$ represents the fraction of component i in the H2 octahedral sites.

Analogous to the α phase, the last term of Equation 3.28 is the L^{β} Redlich-Kister polynomial with ${}^{\upsilon}L^{\beta}_{\mathrm{FT:H:H,vac}} = {}^{\upsilon}\mathrm{A}^{\beta} + {}^{\upsilon}\mathrm{B}^{\beta}\mathrm{T}$.

The ${}^{0}G^{\beta}_{\mathrm{FT:H:vac}}$ and ${}^{0}G^{\beta}_{\mathrm{FT:H:H}}$ terms are, respectively, the Gibbs energies of formation of β_1-FeTiH and β_2-$FeTiH_2$ compounds referenced to the FeTi-B2 and H_2-gas phases:

$${}^{0}G^{\beta}_{\mathrm{FT:H:vac}} = 2\,{}^{0}G^{\alpha}_{\mathrm{FT:vac}} + \frac{1}{2}G^{\mathrm{SER}}_{\mathrm{H_2}} + \Delta H_f^{\beta_1} + \Delta S_f^{\beta_1} T \tag{3.29}$$

$${}^{0}G^{\beta}_{\mathrm{FT:H:H}} = 2\,{}^{0}G^{\alpha}_{\mathrm{FT:vac}} + G^{\mathrm{SER}}_{\mathrm{H_2}} + \Delta H_f^{\beta_2} + \Delta S_f^{\beta_2} T\,. \tag{3.30}$$

The terms ΔH_f^{*} and ΔS_f^{*} in Equation 3.29 and Equation 3.30 the formation enthalpy and formation entropy of the end-members of the β Gibbs energy phase model, which are evaluated during the optimization of the model parameters (see Table. 3.3 for the optimized values).

For the end-members of the β phase, the DFT formation energies were calculated referenced in the B2 phase and the H_2 molecule, as stated in Equation 3.31 and Equation 3.32:

$$\Delta E^{\beta_1}_{\mathrm{FeTiH}} = E^{\beta_1}_{\mathrm{FeTiH}} - (E^{\mathrm{B2}}_{\mathrm{FeTi}} + \frac{1}{2}E^{0K}_{\mathrm{H_2}}) \tag{3.31}$$

$$\Delta E^{\beta_2}_{\mathrm{FeTiH_2}} = E^{\beta_2}_{\mathrm{FeTiH_2}} - (E^{\mathrm{B2}}_{\mathrm{FeTi}} + E^{\mathrm{0K}}_{\mathrm{H_2}})\,. \tag{3.32}$$

Thermodynamic model of the gas phase

The gas phase was considered to have an ideal behavior within the temperature and pressure range of interest [13]. In principle, the ternary gas can contain Fe, FeH, Fe_2, H, H_2, Ti and Ti_2. In this study, only FT and H_2 were chosen to constitute the gas phase because these species are the most

likely to be encountered in the temperature regime of hydrogen storage materials. Since H_2 is much more stable in H-rich regions and because allowing a solubility of FT supports numerical convergence during the equilibrium calculations, the FT species was adopted as a constituent in the gas phase model. The total Gibbs energy of one mole of "formula unit" (FT, H_2) of the gas phase is then given by:

$$G^{\text{gas}} = \sum_i y_i [{}^0G_i^{\text{gas}} + RT \ln(P/P_0)] + RT \sum_i y_i \ln y_i \,, \tag{3.33}$$

where ${}^0G_i^{\text{gas}}$ is the standard Gibbs energy of constituent i in the gas state from the SGTE database [148], which is based on the JANAF thermochemical tables [149], P_0 stands for the atmospheric pressure of 101325 Pa, y_i is the constituent fraction of species i, and R is the universal gas constant. The vapor Fe parameters were chosen to account for the hypothetical FT species in the gas phase.

3.2.5 Thermodynamic assessment of model parameters

The optimization of the thermodynamic model parameters was carried out with the OpenCalphad software version 6.25 [55] and PyCalphad version 10.2 [56] in conjunction with ESPEI version 8.9 [57]. The data relating to solubility limits over temperature were taken from the measured PCI curves from our group. The calculated DFT ground-state formation energies of each endmember of the phase models were assumed to be a reasonable approximation to the enthalpy of formation at room temperature (298.15 K) and therefore employed as experiments during the optimization of the model parameters. The experimental data for the α phase solubility limits came from absorption curves where α is in equilibrium with the H_2 reservoir.

Neither absorption nor the desorption pressure-composition curves represent the true equilibrium [30]. Despite the high level of hysteresis, the average pressure and solubility limit between absorption and desorption plateaux pressure was used to represent the $\alpha - \beta - GAS$ phase equilibria. The solubility limits for the β phase were taken from desorption curves.

Plausible initial values for the model parameters were chosen based on experience and thermodynamic intuition and evaluated while giving selected pieces of data certain weights to achieve a satisfactory description of the system. In general, higher weights were attributed to equilibria involving three phases, and lower weights to data containing some discrepancies and inconsistencies.

The summary of all the model parameters of the assessed phases is shown in Table 3.3:

As an initial step, the model parameters for the phases were inserted into OpenCalphad [55] and the equilibrium composition of the α phase with the GAS phase was deployed as a function of pressure and temperature.

Table 3.3: Assessed thermodynamic parameters of the FeTi-H system in Joules per mole of formula units.

Model parameters	Reference
$G^{\text{xs}}_{\text{dis}} = -68448 + 23.825T$	[107] and this work
$G^{\text{xs}}_{\text{ord}} = -10953 - 6097$	[107] and this work
${}^{0}G^{\text{FeTi}} = -76147 - 46.603T + 8.663T\ln(T) - 7.151E^{-3}T^2 + 1.121169E^{-6}T^3$	[107]
${}^{0}G^{\text{B2}}_{\text{Fe:Ti:vac}} = 0.5\,{}^{0}G^{\text{FeTi}}$	[107] and this work
${}^{0}G^{\alpha}_{\text{FT;vac}} = 0.5G^{\text{SER}}_{\text{Fe}} + 0.5G^{\text{bcc}}_{\text{Ti}} + 0.25\,{}^{0}G^{\text{FeTi}} + 0.25G^{\text{xs}}_{\text{dis}} - 0.25G^{\text{xs}}_{\text{ord}}$	[107] and this work
${}^{0}G^{\alpha}_{\text{FT:H}} = {}^{0}G^{\alpha}_{\text{FT:vac}} + \frac{3}{2}G^{\text{SER}}_{\text{H}_2} + 195392 + 118T$	This work
${}^{0}G^{\beta}_{\text{FT:H:vac}} = 2\ {}^{0}G^{\alpha}_{\text{FT:vac}} + \frac{1}{2}G^{\text{SER}}_{\text{H}_2} - 11725 + 47.2T$	This work
${}^{0}G^{\beta}_{\text{FT:H:H}} = 2\ {}^{0}G^{\alpha}_{\text{FT:vac}} + G^{\text{SER}}_{\text{H}_2} - 17928 + 81.8T$	This work
${}^{0}L^{\alpha}_{\text{FT:H,vac}} = -327809$	This work
${}^{1}L^{\alpha}_{\text{FT:H,vac}} = -139278$	This work
${}^{0}L^{\beta}_{\text{FT:H,vac}} = -6629 + 35.8T$	This work
${}^{1}L^{\beta}_{\text{FT:H,vac}} = -19336 + 56.5T$	This work

Figure 3.18 shows the comparison of the solubility limit of the experimental and calculated hydrogen mole fraction in the α phase after the optimization of model parameters.

The results were satisfactory with an average Relative Standard Deviation (RSD) not greater than RSD=10^{-2}. Moreover, the optimized thermodynamic model for the α phase could reproduce the formation enthalpy, $\Delta H_f^{\alpha_6} = 42.63$ kJ/mol.at, in excellent agreement with the formation energy, $\Delta E^{\alpha}_{\text{FeTiH}_6} = 42.57$ kJ/mol.at, obtained through DFT calculations at the ground state.

In the following, the optimized model parameters for the α phase were kept fixed while the thermodynamic models of the phases were transferred and deployed into PyCalphad and ESPEI. The model parameters of the β were optimized *via* the Markov Chain Monte Carlo (MCMC) approach as implemented in ESPEI [57] to reproduce both plateaux pressure (i.e., the α-β-GAS, and β_1-β_2-GAS equilibria) and the formation energies of the β_1 and β_2 end-members (refer to Equation 3.31 and Equation 3.32). Figure 3.19 shows a qualitative view of the convergence. It is possible to claim that after around 30 iterations, the probability does not change and the parameters are unlikely to be further optimized. Therefore, the parameters can be assumed to be converged because, from this point on, the value of the parameters may change without significant improvement of the RSD. In Figure 3.20, the calculated equilibrium pressure between α, β_1, and the GAS phase as a

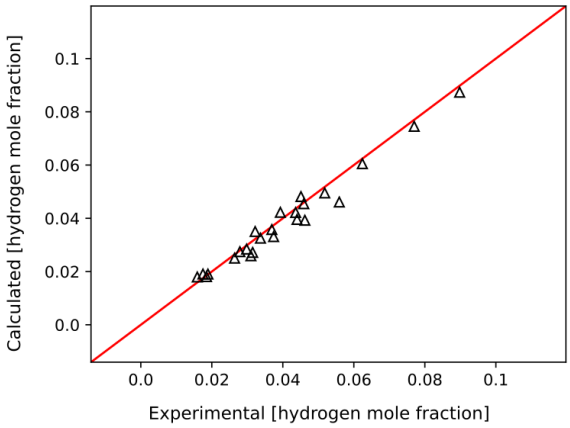

Figure 3.18: Comparison between calculated and experimental solubility limit of the α phase from this work.

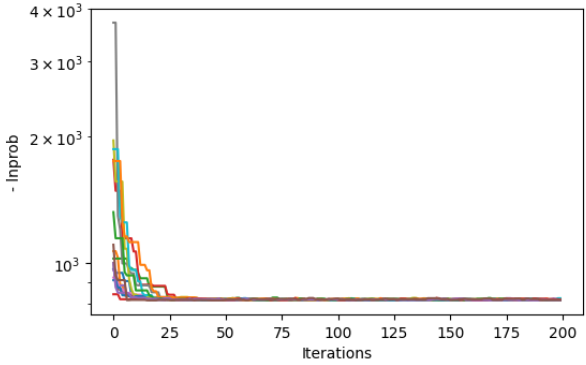

Figure 3.19: Probability changes for all of the β phase thermodynamic model parameter chains as a function of iterations, resulting from an ESPEI MCMC optimization run. Each color links to a individual parameter of one of the parameter chains.

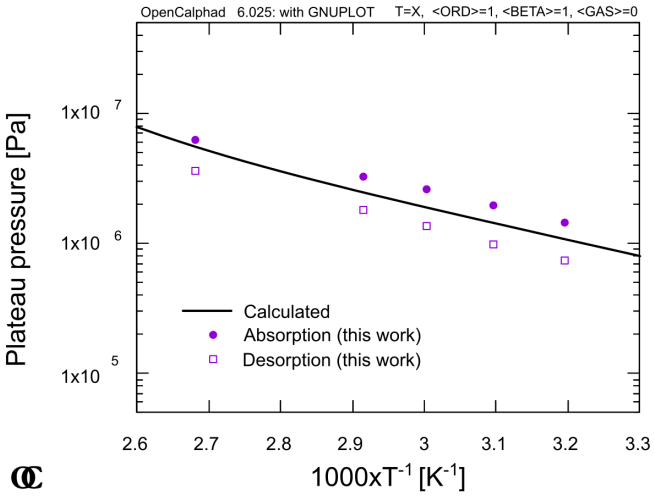

Figure 3.20: Plateau pressure calculated with the thermodynamic model from this work compared to this work's experimental data.

function of temperature is plotted together with plateaux pressure values experimentally obtained from the absorption and desorption PCI curves.

The first plateau pressure values are the most significant properties predicted by the developed thermodynamic model, as they indicate the minimum temperature and pressure capable of stabilizing the β phase and consequently enable the prediction of engineering level parameters to control the hydrogenation of the FeTi material. As discussed by Flanagan [30], the true bulk thermodynamic equilibrium pressure may lie between those measured from absorption and desorption curves, which is reproduced by the present developed model.

One of the advantages of using an MCMC approach is that it provides a set of thermodynamic model parameters that reproduce the experimental data with similar accuracy. Therefore, by calculating many equilibria through this collection of thermodynamic model parameter chains, the probability and/or the error of a given calculation can be estimated and propagated throughout the thermodynamic computations.

As an example, Figure 3.21 shows the probability of finding metal/hydride and hydrogen gas in equilibrium (i.e, finding the α and H_2 or β and H_2 equilibria) at 313 K. Figure 3.21 can be compared against the experimental data shown in Figure 3.23, which shows that the PCI curve for both absorption and desorption are found in agreement with the calculated data. Moreover, it reaffirms the accuracy of the calculated values for the first plateaux and

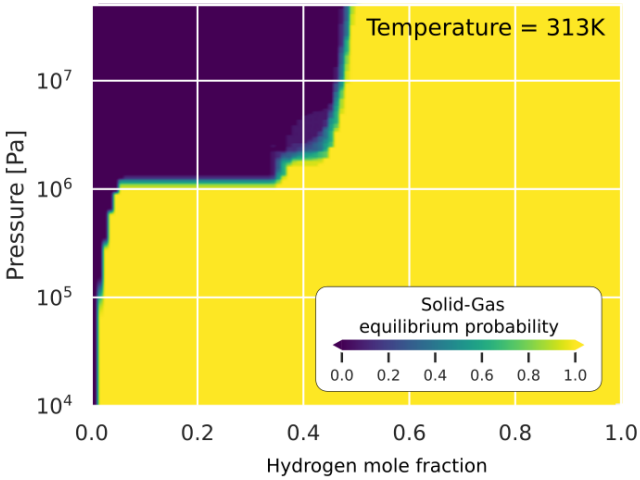

Figure 3.21: Calculated probability diagram for finding hydrogen in solid state material while in equilibrium with hydrogen gas for the FeTi-H system at 313 K.

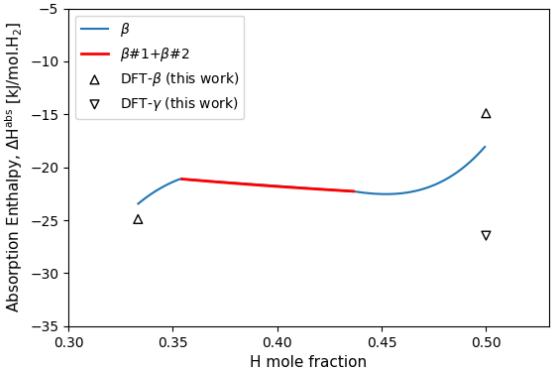

Figure 3.22: Calculated absorption enthalpy from this work's CALPHAD assessment compared with calculated DFT data from this work.

demonstrates that the hydrogenation characteristics after the formation of the β phase are less well-behaved, as characterized by the probability diagram for the stability of β being more diffuse.

From this point on, the analysis of the stability and the possible reasons

for such a huge hysteresis encountered between the absorption and desorption curves during the (de)hydrogenation of FeTi is elucidated based on the aforementioned DFT computations and the current thermodynamic assessment.

First, the calculated absorption enthalpy shown in Figure 3.22 will be analyzed. The calculated data is superimposed with that calculated through DFT in this study for comparison.

To begin with, it is worth mentioning that the absorption enthalpy within the β phase compositional range, calculated with Calphad, is in close agreement with DFT results.

Moreover, it is interesting to note that the absorption energy of the γ phase lies below β_1 and β_2, which reinforces the experimental argument that once formed, the γ phase is more stable within the hydrogenated material. As evidenced in Figure 3.15, from the ground state perspective, the energy of the $(FeTi)_2H_3$ compound with a monoclinic structure is just slightly lower in energy than that possessing the orthorhombic variant. Nevertheless, these energies refer to the perfect hypothetical infinite bulk compounds, whereas in reality, the β_1–β_2 phase transformation should be interpreted as an orthorhombic structure transforming into another similar but larger orthorhombic structure enriched in hydrogen.

This transformation, therefore, should be expected to be energetically less demanding when compared to the β_1–γ phase transformation, defined as a transformation from an orthorhombic into a monoclinic structure, which requires a higher energy barrier to be overcome due to a higher level of symmetry reduction.

From the combination of the DFT analysis with the thermodynamic assessments, it is possible to conjecture that the transformation of β_1 into β_2 may be viewed as a metastable phenomenon under the framework of paraequilibrium. Following this concept, it can be expected that the interphase boundaries between the β_1 and β_2 phases are less energetic; consequently, such a transformation could be more likely to occur during hydrogenation than the one from β_1 into γ. In addition, the micromechanical effects during the β_1–γ transformation are likely to be a crucial factor that prevents the observation of the γ phase when hydrogenating the material under mild conditions and with a low number of hydrogenation cycles. Therefore, the β_2 phase can be viewed as a metastable step from which the complete transformation to γ is facilitated by providing a reduced activation energy barrier for complete hydrogenation. The calculated pressure-composition phase diagram at 313 K, superimposed with experimental data from this work, is shown in Figure 3.23. Good agreement is also obtained in the analyzed pressure range, especially for the α solubility limits.

The higher stability of the γ phase has several implications for the reversibility of the hydrogen storage properties. Once γ is formed, it tends to remain in the materials as its reversible transformation into the metal or α phase is thermodynamically hindered by the aforementioned micromechanical factor and its more stable bulk energy in comparison to the β phase.

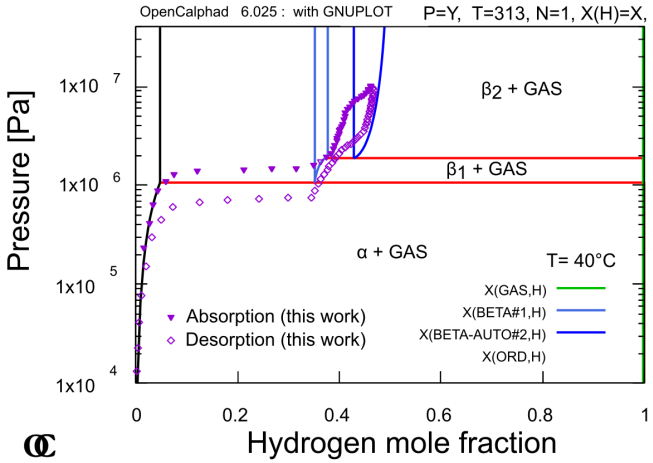

Figure 3.23: Calculated pressure-composition paraequilibrium phase diagram of the FeTi-H system compared with experimental PCI data from this work.

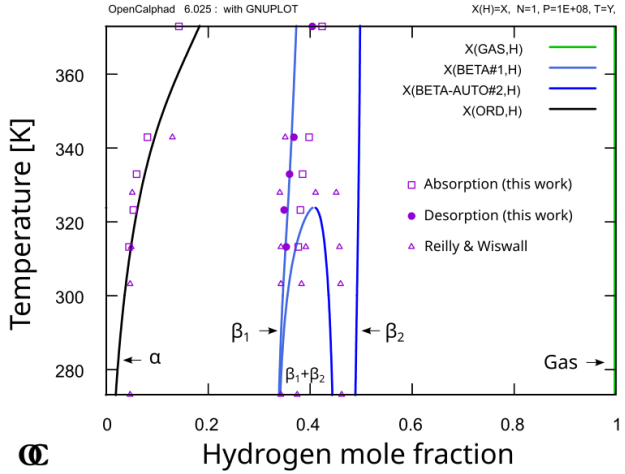

Figure 3.24: Calculated temperature-composition paraequilibrium phase diagram of the FeTi-H system compared with experimental PCI data from this work and Reilly [113]

With the model developed in this study, the limiting pressure for the formation of the γ phase can be inferred from the calculation of the second plateau pressure (i.e., the equilibrium between β_1, β_2, and the GAS phases), which is modeled with temperature dependence.

With the premise that γ is a more stable structure in the range of β_2 composition, avoiding bypassing the pressure barrier for the formation of β_2, the γ phase may be avoided. Ultimately, how to prevent the formation of the γ phase can be interpreted through a simple analysis of the temperature and pressure that β_2 may occur, which improves the control of the hydrogenation reversibility of the material in real engineering applications.

Further analysis of such a phenomenon is addressed in Chapter 5, Section 5.2.4, where a kinetic perspective is demonstrated by simulating the β phase spinodal decomposition.

The calculated para-equilibrium temperature-composition phase diagram of the FeTi-H system comparing the experimental data from this work and Reilly [113] is shown in Figure 3.24. The experimental data are in close agreement with the calculated equilibrium compositions. In particular, the solubility limits and the miscibility gap within the β phase region are calculated in agreement with the interpretation of Reilly. The estimated critical point is calculated at $x_{\mathrm{H}} = 0.41$, $T_c = 324$ K in good agreement with estimates by Reilly and Wiswall [113].

4 Interfacial Properties of FeTi Metal-Metal Hydride

In this chapter, a method for quantifying interphase boundary energies and their implication in micromechanics and interphase boundary alignment is developed and demonstrated by applying it to study the interfacial properties between metallic matrix α (FeTi) and hydride β (FeTiH).

4.1 Interphase boundary chemical energy

In this section, two distinct generalizable thermodynamic models for the quantification of the chemical contribution to the interfacial energy between a metals and their interstitial metal-hydrides are for the first time derived. These models are here named as `Grand Potential`, and `Hydrogenation Reaction` approaches. The models yield the same concluding equation, which shows how to simplify atomic models and reduce computational demand.

4.1.1 The Grand Potential approach

From a thermodynamic perspective, the hydrogenation reaction is driven by the gradient of the hydrogen chemical potential (μ_{H}) between the phases α and β. Hence, the existence of a stable interface only occurs under equilibrium conditions near the interphase boundary:

$$\mu_{\mathrm{H}} = \mu_{\mathrm{H}}^{\alpha} = \mu_{\mathrm{H}}^{\beta}. \tag{4.1}$$

However, the hydrogen chemical potential depends on the surrounding external conditions. Accordingly, this study formulates all energies that describe this equilibrium with respect to the grand potential $\Omega(V, T, \mu)$. Neglecting the vibrational contributions to the free energy of the system, the bulk potentials of the phases α and β can be defined as

$$\Omega_{\mathrm{bulk}}^{\alpha} = E_{\mathrm{FeTi}}^{\mathrm{bulk}} - \mu_{\mathrm{FeTi}} \tag{4.2}$$

and

$$\Omega_{bulk}^{\beta} = E_{\mathrm{FeTiH}}^{\mathrm{bulk}} - \mu_{\mathrm{FeTiH}}, \tag{4.3}$$

respectively.

Although alloy hydrogenation generally occurs under paraequilibrium [30], due to the structural similarity of phases and the pronounced chemical disparity between metals and hydrogen atoms, it can be assumed that the variation of the chemical potential of the metallic species in interstitial metal-hydride systems is negligible, i.e.

$$\mu_{\mathrm{Fe}}^{\alpha} \approx \mu_{\mathrm{Fe}}^{\beta} \equiv \mu_{\mathrm{Fe}} \tag{4.4}$$

$$\mu_{\mathrm{Ti}}^{\alpha} \approx \mu_{\mathrm{Ti}}^{\beta} \equiv \mu_{\mathrm{Ti}}. \tag{4.5}$$

In such an equilibrium condition, the corresponding chemical potentials μ_{FeTi} and μ_{FeTiH} are not independent, but satisfy

$$\mu_{\mathrm{FeTiH}} = \mu_{\mathrm{Fe}} + \mu_{\mathrm{Ti}} + \mu_{\mathrm{H}} \tag{4.6}$$

$$= \mu_{\mathrm{FeTi}} + \mu_{\mathrm{H}}. \tag{4.7}$$

The reaction potential of the β phase formation is then obtained based on the reaction

$$\alpha(\mathrm{FeTi}) + \frac{1}{2}\mathrm{H}_2 \rightarrow \beta(\mathrm{FeTiH}) \tag{4.8}$$

as illustrated in Figure 4.1 *via*

$$\Delta\Omega_r = E_{\mathrm{FeTiH}}^{\mathrm{bulk}} - E_{\mathrm{FeTi}}^{\mathrm{bulk}} - \mu_{\mathrm{H}}, \tag{4.9}$$

emphasizing mathematically that the hydride phase becomes more stable when the hydrogen chemical potential increases and vice versa.

A direct calculation of the chemical potential of hydrogen with atomistic simulations is computationally costly. However, one can compute the ground-state energy E_{H_2} as a reference, and then obtain the variation of the chemical potential $\Delta\mu$ from thermodynamic assessments of its Gibbs energy and/or well-established thermochemical tables:

$$\mu_{\mathrm{H}} = \frac{1}{2}\left(E_{\mathrm{H}_2} + \Delta\mu_{\mathrm{H}_2}\right). \tag{4.10}$$

In this work, both the ideal gas model and the model from J.-M. Joubert [13] (more accurate for high pressures) were employed for obtaining the chemical potential difference $\Delta\mu_{\mathrm{H}_2}$ and its relation to other thermodynamic quantities, such as temperature and pressure. Inserting Equation 4.10 into Equation 4.9 links the reaction potential $\Delta\Omega_r$ to the DFT-calculated hydrogenation energy $\Delta E_r^{\mathrm{DFT}}$ (refer to Equation 3.6):

$$\Delta\Omega_r = \Delta E_r^{\mathrm{DFT}} - \frac{1}{2}\Delta\mu_{\mathrm{H}_2}. \tag{4.11}$$

The same approach may be applied to derive the surface and interface energies and link them to the total energies calculated with DFT. Here, the

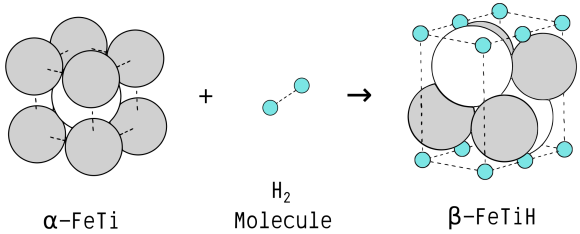

Figure 4.1: Visualization of the reaction: $\alpha(\mathrm{FeTi}) + \frac{1}{2}\mathrm{H_2} \rightarrow \beta(\mathrm{FeTiH})$. Gray: Fe atoms; white: Ti atoms; blue: H atoms.

surface energy γ_s of a phase ϕ is defined as the energy needed to create the surface ($\Delta\Omega_s^\phi$) per unit of area (A):

$$\gamma_s^\phi = \frac{\Delta\Omega_s^\phi}{A} = \frac{1}{2A}\left(\Omega_{\mathrm{slab}}^\phi - N_\phi \Omega_{\mathrm{bulk}}^\phi\right), \tag{4.12}$$

where the factor of $\frac{1}{2}$ accounts for the presence of two identical surfaces in the surface slab model, and N_ϕ is the number of bulk units of ϕ in that model. Similarly to the bulk, the grand potential can be written as $\Omega = E - \sum_j N_j \mu_j$ in thermodynamic equilibrium, with E being the DFT energy, j running over all elements and N_j being the number of atoms of element j in the structure. Inserting this into Equation 4.12 gives

$$\gamma_s^\phi = \frac{1}{2A}\left[E_{\mathrm{slab}} - N_\phi E_{\mathrm{bulk}}^\phi - \sum_j \left(N_j^{\mathrm{slab}} - N_\phi N_j^\phi\right)\mu_j\right]. \tag{4.13}$$

Thus, the surface energy can be approximated directly from the DFT energies for stoichiometric surface models, where $N_j^{\mathrm{slab}} = N_\phi N_j^\phi$ for all elements j. However, the surface stoichiometry may also change for a given surface orientation due to different possible terminations and reconstructions. If there is an excess (or deficiency) of a species compared to the bulk phase, the surface energy becomes dependent on the chemical potential of that species. In that case, it is most convenient to reference the chemical potential against the DFT ground state energy E_j similar to Equation 4.10:

$$\mu_j = E_j + \Delta\mu_j. \tag{4.14}$$

This allows to extrapolate the surface energy calculated with DFT

$$\gamma_s^{\mathrm{DFT}} = \frac{1}{2A}\left[E_{\mathrm{slab}} - N_\phi E_{\mathrm{bulk}}^\phi - \sum_j \left(N_j^{\mathrm{slab}} - N_\phi N_j^\phi\right) E_j\right] \tag{4.15}$$

to experimental conditions at any given chemical potential:

$$\gamma_s^{\phi} = \gamma_s^{\phi_{DFT}} - \frac{1}{2A} \sum_j \left(N_j^{\text{slab}} - N_{\phi} N_j^{\phi} \right) \Delta\mu_j \tag{4.16}$$

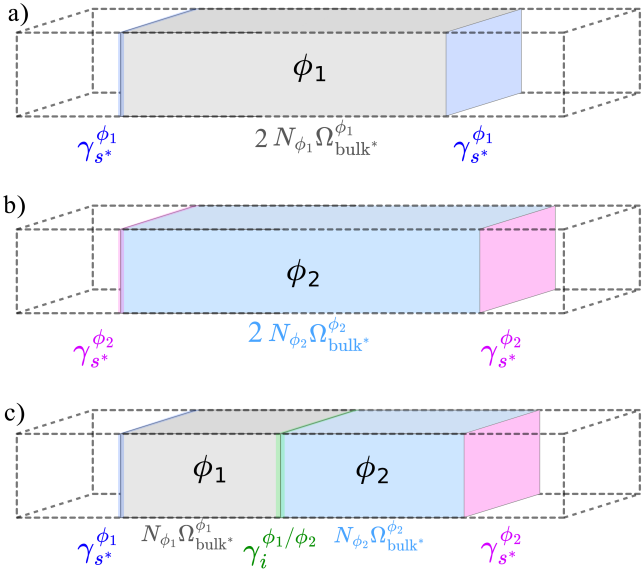

Figure 4.2: Illustration of the type of interface model adopted in this study. Strained slab of phase ϕ_1 (a), and Strained slab of phase ϕ_2 (b) commensurate to form an interface slab (c). The vacuum-exposed strained surfaces of phases ϕ_1 and ϕ_2 are represented in blue and magenta, respectively, while the interface are represented in green. Dashed lines represent the periodic boundaries of the simulation cell.

One approach for modeling interfaces involves creating a slab model that comprises two phases, each featuring distinct surfaces on either side of the slab, with an interface located in the middle, as shown in Figure 4.2c). Following the same concept as for the calculation of the surface energies, the energy balance in Equation 4.12 is adapted for this type of model to express the energy of a single interface γ_i as

$$\begin{aligned} \gamma_i^{\phi_1/\phi_2} = & \frac{1}{A_i} \left(\Omega_{\text{slab}}^{\phi_1/\phi_2} - N_{\phi_1} \Omega_{\text{bulk}^*}^{\phi_1} - N_{\phi_2} \Omega_{\text{bulk}^*}^{\phi_2} \right) \\ & - \gamma_{s^*}^{\phi_1} - \gamma_{s^*}^{\phi_2}, \end{aligned} \tag{4.17}$$

for an interface slab consisting of two phases ϕ_1 and ϕ_2 and having two surfaces with energies $\gamma_{s^*}^{\phi_1}$ and $\gamma_{s^*}^{\phi_2}$, respectively. Note that due to the common unit cell of the interface slab, the two phases must be strained to commensurate into the common section area A_i. Therefore, the reference states need to be strained accordingly, which is why these energies are marked with an asterisk (*).

Computation of interface energies in this scenario is resource-intensive because it requires the individual calculation of strained bulk systems and surface models. However, Equation 4.17 can be drastically simplified by choosing reference surface models with exactly twice as many units of each phase ($N_{\phi_i}^{(s)} = 2N_{\phi_i}$). This conceives a concept where both surface slabs (with grand potentials $\Omega_{\text{slab}^*}^{\phi_1}$ and $\Omega_{\text{slab}^*}^{\phi_2}$) are cleaved in half and these halved portions are united, forming an interface, leading to:

$$\gamma_i^{\phi_1/\phi_2} = \frac{1}{A_i}\left[\Omega_{\text{slab}}^{\phi_1/\phi_2} - \frac{1}{2}\left(\Omega_{\text{slab}^*}^{\phi_1} + \Omega_{\text{slab}^*}^{\phi_2}\right)\right]. \tag{4.18}$$

Note that, as before, there can be an excess or depletion of any species in the model, which becomes evident when incorporating the dependence on the chemical potential. For the α/β interfaces studied in this work, Equation 4.18 becomes:

$$\begin{aligned}\gamma_i^{\alpha/\beta} = \frac{1}{2A_i}\Big[\, & 2E_{\text{slab}}^{\alpha/\beta} - (E_{\text{slab}^*}^{\alpha} + E_{\text{slab}^*}^{\beta}) \\ & - (2N_{\text{Fe}}^{\alpha/\beta} - N_{\text{Fe}}^{\alpha} - N_{\text{Fe}}^{\beta})\mu_{\text{Fe}} \\ & - (2N_{\text{Ti}}^{\alpha/\beta} - N_{\text{Ti}}^{\alpha} - N_{\text{Ti}}^{\beta})\mu_{\text{Ti}} \\ & - (2N_{\text{H}}^{\alpha/\beta} - N_{\text{H}}^{\beta})\mu_{\text{H}} \,\Big].\end{aligned} \tag{4.19}$$

Since there is a freedom to choose the number of atoms in the reference models, one can pick the models of the strained surface slabs α and β with the same number of Fe and Ti atoms as that of the α/β interface model and double the number of hydrogen atoms in the surface slab β compared to that of the interface slab α/β, thus simplifying Equation 4.19 to:

$$\gamma_i^{\alpha/\beta} = \frac{1}{A_i}\left[E_{\text{slab}}^{\alpha/\beta} - \frac{1}{2}\left(E_{\text{slab}^*}^{\alpha} + E_{\text{slab}^*}^{\beta}\right)\right]. \tag{4.20}$$

In summary, the resulting Equation 4.20 demonstrates the feasibility of calculating the interface energy solely based on the DFT total energies of the α and β strained surface slabs and the α/β interface slab with the proper choice of the models. As an additional validation, the same conclusion is obtained by the derivation of the interface energy from a hydrogenation perspective, as shown in the next subsection.

The presented concept of choosing appropriate models simplifies the calculation of interface energies and can be generalized to other coherent interfaces

as well. Especially for intermetallics that form interstitial hydrides, the choice of atomic models that meet the requirements of our approach is evident and straightforward. Moreover, this approach could be useful as an additional method to streamline the elimination of contributions of elastic energy when computing the energy of the intrinsic domain wall in ferroelectric materials, as was done similarly in [150].

4.1.2 The Hydrogenation Reaction approach

In this section, the expression for calculating the interface energy of an α-β interface energy is derived based on the concept of the reaction energy of the precursor phases.

First, the hydrogenation energy per formula unit of the β phase (ΔE^b) is defined as:

$$\Delta E^b = E_\beta - \frac{n_H^b}{2} E_{\mathrm{H}_2} - n_\alpha^b E_\alpha. \tag{4.21}$$

Where E_α is the total energy of the α phase per formula unit. n_α^b and n_H^b are the numbers of formula units of α and hydrogen atoms in the bulk phase β, respectively.

The strained surface slabs of the α and β are used as the reference structure, and for conciseness, they are, respectively, called α-slab or β-slab throughout this section. Similarly, the interface slab with the same unit cell as the α- and β-slabs is called the α/β-slab.

Similarly to Equation 4.21, the hydrogenation energy of the β-slab is defined as:

$$\Delta E^s = E_{\mathrm{slab}}^\beta - \frac{n_H^s}{2} E_{\mathrm{H}_2} - E_{\mathrm{slab}}^\alpha, \tag{4.22}$$

where E_{slab}^α and E_{slab}^β are, respectively, the total energy of the α-slab and β-slab, and n_H^s is the number of hydrogen atoms in the β-slab model.

Analogously, the hydrogenation energy of the α/β-slab (ΔE^i) follows:

$$\Delta E^i = E_{\mathrm{slab}}^{\alpha/\beta} - \frac{n_H^i}{2} E_{\mathrm{H}_2} - E_{\mathrm{slab}}^\alpha, \tag{4.23}$$

where $E_{\mathrm{slab}}^{\alpha/\beta}$ is the total energy of the α/β-slab and n_H^i is the number of hydrogen atoms in the α/β-slab model.

Figure 4.3 shows the visual interpretation of Equations 4.22 and 4.23.

The dependencies of the slab energy, along with the surface and interfacial properties, can be determined. From the point of view of a hydrogenation process, the formation of the β-slab consists of the full hydrogenation of the α-slab, which forms a β-bulk interior material and two surfaces $(h\,k\,l)_\beta$ at the expense of two $(u\,v\,w)_\alpha$ surfaces, as shown in Figure 4.3 a). In terms of energy balance, it can be written as:

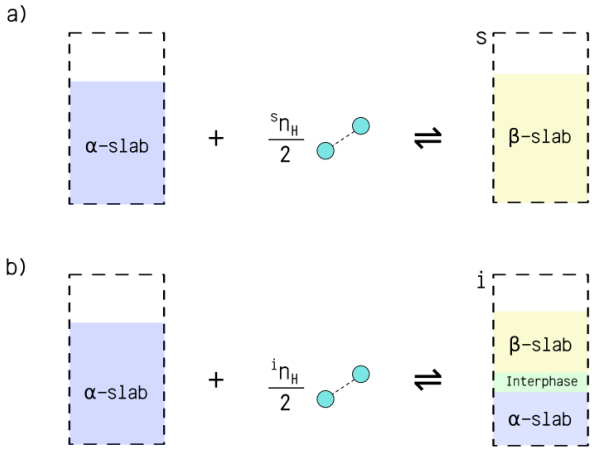

Figure 4.3: Illustration of the hydrogenation reactions of: a) the β-slab (s) and b) the α/β-slab (i) by fully or partly hydrogenating the same α-slab precursor.

$$\Delta E^s = \frac{n_H^s}{n_H^b}\Delta E^b + 2A_i\left[\gamma_s^\beta - \gamma_s^\alpha\right]. \tag{4.24}$$

Analogously, if just partial hydrogenation of the α-slab occurs, the same concept may apply to evaluate the formation energy of the α/β-slab. In this case, upon hydrogenation, there will be the creation of a β surface to the detriment of the α surface, and the emergence of an interphase region associated with an interfacial energy γ_i (see Figure 4.3 *b*)):

$$\Delta E^i = \frac{n_H^i}{n_H^b}\Delta E^b + A_i\left[\gamma_i + \gamma_s^\beta - \gamma_s^\alpha\right]. \tag{4.25}$$

By performing the operation Equation 4.25 - $\frac{1}{2}$ Equation 4.24, the dependency on surface energy is effectively eliminated, yielding a generalized expression for the interface energy. This derived expression comprehensively accommodates any conceivable type of hydrogen-terminated surface of the precursor slabs:

$$\gamma_i = \frac{1}{A_i}\left[\Delta E^i - \frac{1}{2}\Delta E^s - \left(\frac{n_H^i}{n_H^b} - \frac{1}{2}\frac{n_H^s}{n_H^b}\right)\Delta E^b\right]. \tag{4.26}$$

Choosing β-slab and α/β-slab models so that $n_H^i = \frac{1}{2}\, n_H^s$ and inserting Equation 4.22 and Equation 4.23 into Equation 4.26, eliminates the depen-

dency on the β-bulk formation energy (ΔE^b), and the expression reduces to:

$$\gamma_i = \frac{1}{A_i}\left[E^{\alpha/\beta}_{\text{slab}} - \frac{1}{2}\left(E^{\alpha}_{\text{slab}} + E^{\beta}_{\text{slab}}\right)\right]. \tag{4.27}$$

The resulting Equation 4.27 is identical to the Equation 4.20. It thus reinforces the correctness of the application of the Grand Potential approach and the feasibility of calculating the interface energy solely based on the proper choice of the α-slab, β-slab, and α/β-slab models. It should be noted that the thermodynamic approach using the grand potential is more generalizable and allows for simplifying a wider range of interface calculations, while the approach presented here is limited to systems that only change through the addition or exchange of one species.

4.1.3 Application of the models to the FeTi-H surfaces and interphase boundaries

Surface and interface modeling

In order to construct an atomistic model for the α/β interface, one must know the orientation relationship between the phases. From a geometric analysis of the crystal structure of the hydrides of the FeTi alloy, Westlake [138] suggested that the formation of the β phase from the matrix of the α phase would occur through the shared planes $(1\,1\,0)_\alpha \parallel (1\,0\,0)_\beta$, $(1\,\bar{1}\,0)_\alpha \parallel (0\,1\,0)_\beta$ and $(0\,0\,1)_\alpha \parallel (0\,0\,1)_\beta$. This simple geometric relationship was adapted and is represented by an atomistic model in Figure 4.4.

The orientation relationship shown in Figure 4.4 was used as a basis for the construction of the surface and interface slabs analyzed in this study. For the α-FeTi phase, symmetric slabs were built for the orientations $(1\,1\,0)_\alpha$ and $(0\,0\,1)_\alpha$, while for the β-FeTiH phase $(0\,1\,0)_\beta$, $(0\,0\,1)_\beta$, and $(1\,0\,0)_\beta$ slabs were created. Depending on the phase and orientation of the slab, different terminations are possible as illustrated in Figure 4.5. In the following, these terminations will be referenced with superscripts attached to the orientation. For example, $(1\,0\,0)^{\text{H}_2}_\beta$ refers to the hydrogen terminated $(1\,0\,0)$ surface of the β-FeTiH phase. For the construction of interface slabs, the α and β surface slabs were cleaved along their common plane and stacked together. A vacuum space of at least 15 Å was added to separate the interface slabs from their periodic image. The amount of vacuum and the distance between the surface and the interface were chosen concerning the convergence test performed for the calculation of the surface energy, i.e. with a minimum number of atomic layers to ensure sufficient bulk material that mitigates interaction effects between their surfaces and interface. Figure 4.6 shows the created $(1\,1\,0)^{\text{FeTi}}_\alpha \parallel (1\,0\,0)^{\text{FeTi}}_\beta$ interface slab atomic model as an example.

Due to the differences in the lattice parameters of the α and β phases, the area and geometry of their slab sections also differ. Figures. 4.7 exemplify

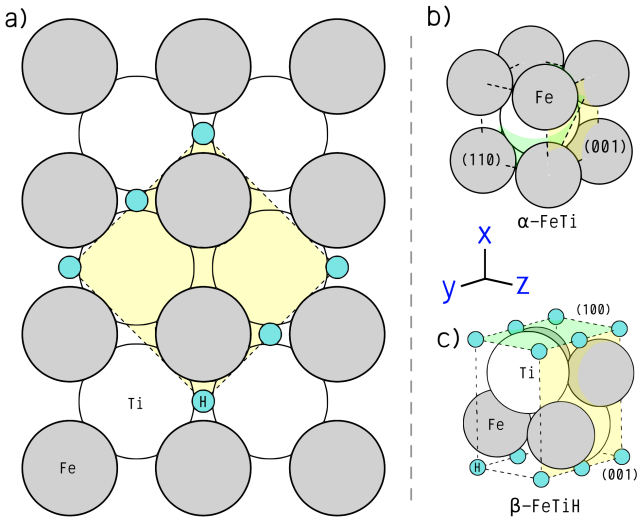

Figure 4.4: Schematic image of the β hydride formation in the α matrix. a) Indication of the orientation of the β hydride in relation to six α phase unit-cells from the viewpoint of their $(0\,0\,1)_\alpha \parallel (0\,0\,1)_\beta$ common plane (note that the representation of the β-phase unit cell as a yellow square is deformed to fit the α-matrix); b) A single unit-cell of a α-phase with indications of the interface plane $(1\,1\,0)_\alpha$ in green and the $(0\,0\,1)_\alpha$ plane in yellow; c) A single unit-cell of the β-phase and the indication of the interface plane $(1\,0\,0)_\beta$ in green and a common plane $(0\,0\,1)_\beta$ in yellow. Gray: Fe atoms; white: Ti atoms; cyan: H atoms.

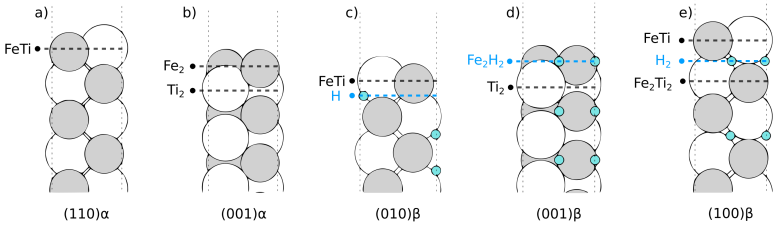

Figure 4.5: Representation of the atomic model of the surface slab terminations. Gray: Fe; white: Ti; blue: H atoms. a) $(1\,1\,0)_\alpha$, b) $(0\,0\,1)_\alpha$, c) $(0\,1\,0)_\beta$, d) $(0\,0\,1)_\beta$, and e) $(1\,0\,0)_\beta$. Horizontal dashed lines represent the transverse section cut that leads to a given termination (see the text for a detailed explanation). Terminations containing hydrogen are represented by blue text.

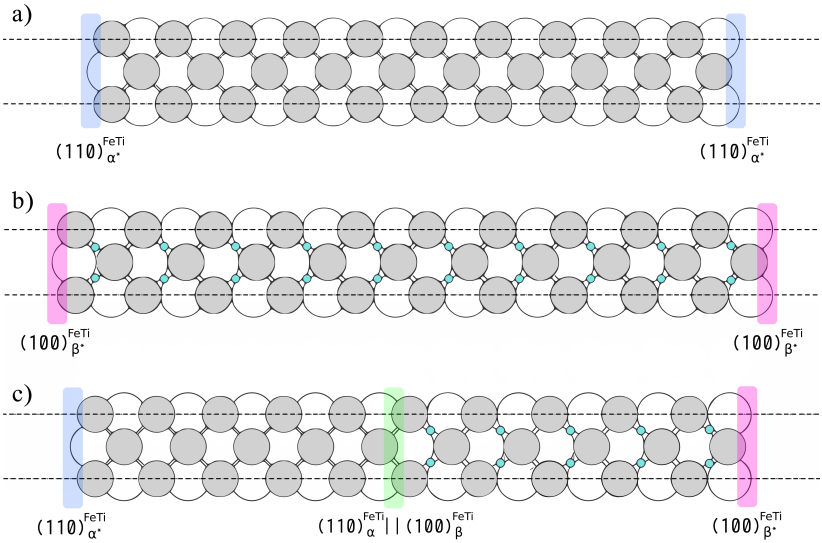

Figure 4.6: Illustration of the atomic model of the a) strained $(1\,1\,0)^{FeTi}_{\alpha^*}$ slab, b) strained $(1\,0\,0)^{FeTi}_{\beta^*}$ slab, and c) $(1\,1\,0)^{FeTi}_{\alpha} \parallel (1\,0\,0)^{FeTi}_{\beta}$ interface slab. The interface $(1\,1\,0)^{FeTi}_{\alpha} \parallel (1\,0\,0)^{FeTi}_{\beta}$, strained surface $(1\,1\,0)^{FeTi}_{\alpha}$, and strained surface $(1\,0\,0)^{FeTi}_{\beta}$ regions are represented in green, blue, and magenta. Gray: Fe atoms; white: Ti atoms; cyan: H atoms.

this for the case of the slab sections of $(1\,1\,0)_{\alpha}$, $(1\,0\,0)_{\beta}$, and $(1\,1\,0)_{\alpha} \parallel (1\,0\,0)_{\beta}$. As mentioned in Section 4.1, this disparity creates a mismatch, and the unit cell of the interface slab model must be chosen so that the α and β slabs are commensurate. Different approaches to commensurating two phases are reported in the literature, the most common being the so-called (1x1) model, where only the unit cell of one phase is used and the second is scaled to meet the two lattices composing the interface [151, 152]. However, because the calculated bulk moduli of the α and β phases are very similar to each other (see Table 3.2), the cross-section lattice parameters of the interface slabs were chosen as an average value between those of the slabs α and β.

Quantification of FeTi-H surface energies

As stated in the previous section and illustrated in Figure 4.5, for a given orientation, the slabs present different types of terminations.

Note that, unlike the $(1\,1\,0)_{\alpha}$ surface, which presents only one kind of termination, the $(0\,0\,1)_{\alpha}$ surface may present two different terminations:

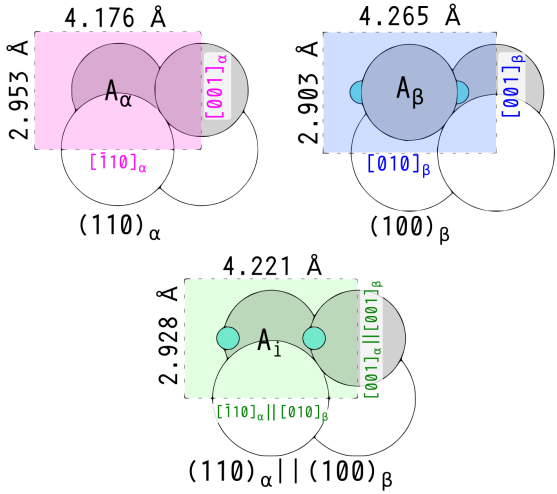

Figure 4.7: Comparison of $(1\,1\,0)_\alpha$ (magenta), $(1\,0\,0)_\beta$ (blue) and $(1\,1\,0)_\alpha \parallel (1\,0\,0)_\beta$ (green) slab sections.

$(0\,1\,0)_\alpha^{\mathrm{Fe}_2}$ and $(0\,1\,0)_\alpha^{\mathrm{Ti}_2}$. If one constructs $(0\,0\,1)_\alpha$ and $(0\,1\,0)_\beta$ slabs with the same termination on both surfaces, the slab would deviate from the $Fe_{0.5}Ti_{0.5}$ equimolar stoichiometry, and the surface energy becomes dependent on the chemical potential of Fe or Ti. The metallic elements in FeTi tend to reduce the energy of the system by a large amount via ordering in the body-centered cubic (bcc) lattice, and their variation of the chemical potential is expected to be acutely sensitive to small variations in the metallic composition. This variation is difficult to determine from an atomistic perspective, and similarly, extrapolations from thermodynamic assessments to low temperatures may be quantitatively inaccurate if only high-temperature data are used to assess thermodynamic model parameters [75].

Therefore, when calculating non-stoichiometric slab surface energies, one must choose elements that serve as a viable reference state for the chemical potential. To ensure consistency, the total energy per atom of bcc-Fe and H_2 were chosen as the reference state chemical potential for all the non-stoichiometric slabs analyzed (see Equation 4.16).

The surface energies in the ground state were calculated using Equation 4.16 with $\Delta\mu_j = E_j$, and the results are shown in Table 4.1.

As discussed by Z. Łodziana [153], the $(1\,1\,0)_\alpha$ lattice plane has the densest atomic packing and is expected to present the lowest surface energy among the surfaces of the α phase. This relation was observed, and although the calculation of surface energies is highly sensitive to the DFT

Table 4.1: Calculated ground state surface energies

Surface Slab	Chemical Formula	γ_s^{DFT} [J/m^2]
$(1\,1\,0)_{\alpha}^{\mathrm{FeTi}}$	$Fe_{20}Ti_{20}$	2.510
$(0\,0\,1)_{\alpha}^{\mathrm{Fe_2}}$	$Fe_{20}Ti_{18}$	2.828
$(0\,0\,1)_{\alpha}^{\mathrm{Ti_2}}$	$Fe_{18}Ti_{20}$	3.243
$(0\,0\,1)_{\beta}^{\mathrm{Ti_2}}$	$Fe_{18}Ti_{20}H_{18}$	3.285
$(0\,0\,1)_{\beta}^{\mathrm{Fe_2H_2}}$	$Fe_{20}Ti_{18}H_{20}$	1.623
$(0\,1\,0)_{\beta}^{\mathrm{FeTi}}$	$Fe_{20}Ti_{20}H_{19}$	2.591
$(0\,1\,0)_{\beta}^{\mathrm{H}}$	$Fe_{19}Ti_{19}H_{20}$	1.412
$(1\,0\,0)_{\beta}^{\mathrm{Fe_2Ti_2}}$	$Fe_{20}Ti_{20}H_{18}$	2.626
$(1\,0\,0)_{\beta}^{\mathrm{FeTi}}$	$Fe_{18}Ti_{18}H_{18}$	2.901
$(1\,0\,0)_{\beta}^{\mathrm{H_2}}$	$Fe_{18}Ti_{18}H_{20}$	0.153

exchange-correlation functional used [154, 155], the results of this work are qualitatively and quantitatively consistent with those of Z. Łodziana.

As mentioned previously, the variation in the chemical potential may be referenced with respect to the total energy of the H_2 molecule in the ground state, allowing for the investigation of the pressure dependence.

In this case, assuming that the slab is in contact with a hydrogen atmosphere containing the H_2 species, the hydrogen chemical potential will be correlated with external conditions, influencing the stability of the surface terminations. Therefore, the effect of pressure and temperature on the species i in the atmosphere that is in equilibrium with the surface should be considered.

If the H_2 species forms an ideal gas reservoir around the surface, the chemical potential of H_2 species can be written as:

$$\mu_{H_2}(T,P) = \mu_{H_2}(T,P_0) + \frac{1}{2}kT\ln\left(\frac{P}{P_0}\right). \tag{4.28}$$

Equation 4.28 describes the temperature and pressure dependencies of the chemical potential of H_2 species. Considering the total energy of a unit of H_2 species at the ground-state as the reference state and using the relations:

$$G = H - TS \tag{4.29}$$

and

$$\left(\frac{\partial G}{\partial N_{H_2}}\right)_{P,T} = \mu_{H_2}. \tag{4.30}$$

$\mu_{H_2}(T, P_0)$ can be written as:

$$\begin{aligned}\mu_{H_2}(T, P_0) &= E_{H_2}^{\text{total}} + \Delta G(\Delta T, P_0, N_{H_2}) \\ &= E_{H_2}^{\text{total}} + H(T, P_0, N_{H_2}) - H(0\text{ K}, P_0, N_{H_2}) \\ &\quad - T\left[S(T, P_0, N_{H_2} - S(0\text{ K}, P_0, N_{H_2})\right].\end{aligned} \tag{4.31}$$

Taking the total energy of the species i at zero temperature E_i^{total} as the reference state, the enthalpic and entropic differences referenced to the ground-state limit may be acquired from well-established thermochemical tables [149]. Combining Equation 4.28 and Equation 4.31, the chemical potential of species i may be obtained for any given temperature and pressure pair (T, p).

As follows, Equation 4.28 and Equation 4.31 were used, respectively, to describe both the ideal ($\mu_{\text{H}_2}^{id}$) and Joubert's model ($\mu_{\text{H}_2}^{\text{Joubert}}$) for the H_2 gas [13].

The effects of H_2 partial pressure on the surface stability for each surface energy, calculated as a function of hydrogen gas pressure, are shown in Figure 4.8.

From Figure 4.8, one can observe that among the surfaces studied, and within the hydrogen partial pressure conditions for FeTi hydrogenation (in the range of 0.01 to 10 MPa, as discussed in Section 3.1.2), the surfaces terminated with hydrogen are much less energetic, with the $(001)_{\beta}^{\text{H}_2}$ surface being by far the most stable. As a result, the shift in the ideal properties of the H_2 gas [13], occurring only above 2×10^8 Pa, does not influence the order of the stability ranking of surface energies. This quantitatively confirms that the hydrogenation of FeTi is also possible from the perspective of surface thermodynamics.

Moreover, under high-pressure conditions, the $(1\,0\,0)_{\beta}^{\text{H}_2}$ surface energy approaches zero. On a purely theoretical basis, a negative value for the surface energy means that the formation of such a surface would be a spontaneous thermodynamic process; however, at such pressure levels, the H_2 gas itself is expected to undergo a continuous phase transformation into a solid state [13, 5]. Furthermore, at room temperature and partial hydrogen pressures above 10^6 Pa, the β phase is expected to absorb hydrogen and transform into either β_2 or γ phase, as discussed in Section 3.1.2.

Quantification of the chemical term of FeTi-H interface energies

When the β phase is formed from the hydrogenation of the α phase, the metallic structure undergoes a volume variation of around 1.25 Å^3 per metallic atom, which represents an increase of approximately 11 % in volume. This

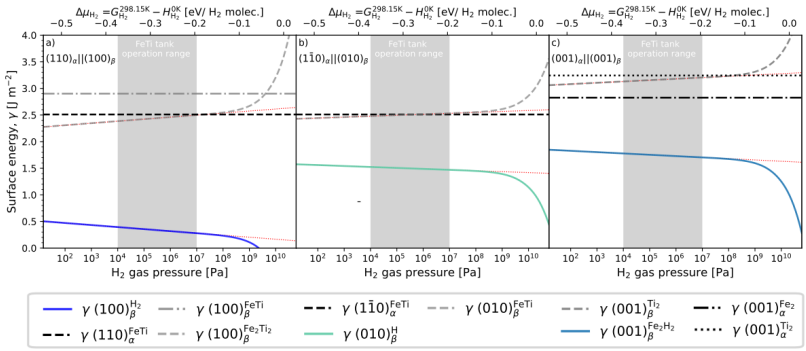

Figure 4.8: Calculated a) $(1\,1\,0)_\alpha$ and $(1\,0\,0)_\beta$ b) $(1\,\bar{1}\,0)_\alpha$ and $(0\,1\,0)_\beta$ and c) $(0\,0\,1)_\alpha$ and $(0\,0\,1)_\beta$ surface energies over pressure at 298.15 K. Note that each panel corresponds to surfaces parallel to the given interface orientation: $(1\,1\,0)_\alpha \parallel (1\,0\,0)_\beta$, $(1\,\bar{1}\,0)_\alpha \parallel (0\,1\,0)_\beta$ and $(0\,0\,1)_\alpha \parallel (0\,0\,1)_\beta$, respectively. The bottom and top horizontal axes show the relationship between hydrogen H_2 gas pressure and hydrogen chemical potential. For surfaces dependent on the hydrogen chemical potential, the Joubert Gibbs energy model for H_2 gas ($\mu_{H_2}^{\text{Joubert}}$) [13] was used. Superimposed red dotted lines represent the coincident surface energy when calculated using the ideal model for the gas H_2 ($\mu_{H_2}^{id}$).

variation is mainly related to the elongation along the a_β axis (see Figure 4.4 *c*). Among the interfaces examined in this study, the $(1\,1\,0)_\alpha \parallel (1\,0\,0)_\beta$ is consequently the least affected by this expansion and culminates in the formation of a highly coherent interface.

For the $(1\,1\,0)_\alpha \parallel (1\,0\,0)_\beta$ interface, the α region is compressed in one direction and stretched in the other, while the β region is compressed and stretched in the opposite way (see Figure 4.7). The $(1\,\bar{1}\,0)_\alpha \parallel (0\,1\,0)_\beta$ interface alternates compression and stretching along the interface plane directions, with a higher level of compression and stretching occurring along the $[1\,0\,0]_\beta$ (or $[1\,0\,1]_\alpha$) direction (see Figure 4.1). On the contrary, for $(0\,0\,1)_\alpha \parallel (0\,0\,1)_\beta$, the α region is stretched and the β region is compressed along both directions.

When these misfits are present, the formation of coherent interfaces increases the free energy of the system due to elastic strain fields that arise [156].

Thus, the energy needed to form a coherent interface is composed of two contributions, as follows:

- The chemical energy that arises as a result of a less stable atomic bonding state occurring at the interface.
- The elastic energy resulting from the strain necessary to achieve a commensurate crystal lattice.

Initially, to analyze the degree of mismatches, the misfit σ was calculated [151, 152, 157] as follows:

$$\sigma = 1 - \frac{2A_\omega}{A_\alpha + A_\beta}, \tag{4.32}$$

where A_α and A_β are the surface areas of the non-strained surface slabs α and β, respectively, and A_ω denotes their overlapping area. Figure 4.7 illustrates this concept applied to the $(1\,1\,0)_\alpha \parallel (1\,0\,0)_\beta$ interface. The calculated mismatch of each interface orientation is shown in Table 4.2.

Table 4.2: Calculated surface slabs cross-sections and their overlapping areas in Å^2 and the correspondent interface mismatches.

interface	A_α	A_β	A_ω	σ [%]
$(1\,1\,0)_\alpha \parallel (1\,0\,0)_\beta$	12.33	12.38	12.12	1.88
$(0\,0\,1)_\alpha \parallel (0\,0\,1)_\beta$	17.44	19.45	17.44	5.44
$(1\,\bar{1}\,0)_\alpha \parallel (0\,1\,0)_\beta$	12.33	13.40	12.12	5.79

The $(0\,0\,1)_\alpha \parallel (0\,0\,1)_\beta$ and $(1\,\bar{1}\,0)_\alpha \parallel (0\,1\,0)_\beta$ interfaces present a modest mismatch of around 5.44% and 5.79%, respectively, while the $(1\,1\,0)_\alpha \parallel (1\,0\,0)_\beta$ interface is highly coherent (1.88%).

This high coherence was also inferred when it was analyzed by transmission electron microscopy (TEM) by Schober [128]. The author observed the formation of coherent and semicoherent lenticular plates of the β phase, which expressed themselves oriented along the $[0\,0\,1]_\alpha$ direction. The dominant interface was observed to appear parallel to the $(1\,1\,0)_\alpha$ plane.

Table 4.3 lists the calculated chemical contributions to the interface energies of the three different orientations $(1\,1\,0)_\alpha \parallel (1\,0\,0)_\beta$, $(1\,\bar{1}\,0)_\alpha \parallel (0\,1\,0)_\beta$, and $(0\,0\,1)_\alpha \parallel (0\,0\,1)_\beta$, created based on surface slabs with different terminations.

However, the value of the interface energy was observed to be consistent and not affected by the surface termination of the precursor slabs. The difference between the interfacial energies for a given orientation with different terminations is found to be within the convergence limit of DFT, approximately 10 mJ/m^2. This validates the approach introduced in Section 4.1, since the interface energies should be independent of surface processes, which in practice occur far away from the interface. Furthermore, it simplifies interface modeling by allowing for the choice of termination and/or reconstruction by convenience. Furthermore, this approach demonstrates that it is not necessary to compute surface energies to quantify the chemical contribution to the interface energy, a presumed prerequisite [158, 159]. Moreover, by avoiding dependence on the bulk and surface energy references, this model should also improve the cancelation of errors intrinsic to the DFT total energy calculations.

Table 4.3: Calculated chemical components of the interface energies (mJ/m^2) for the interfaces created from surface slabs with different surface terminations (marked with superscript) and their corresponding chemical formulas

Interface Slab	Chemical Formula	γ_i [mJ/m^2]
$(1\,1\,0)_{\alpha}^{\mathrm{FeTi}} \parallel (1\,0\,0)_{\beta}^{\mathrm{H_2}}$	$Fe_{18}Ti_{18}H_{10}$	71.9
$(1\,1\,0)_{\alpha}^{\mathrm{FeTi}} \parallel (1\,0\,0)_{\beta}^{\mathrm{FeTi}}$	$Fe_{20}Ti_{20}H_{10}$	68.0
$(1\,1\,0)_{\alpha}^{\mathrm{FeTi}} \parallel (1\,0\,0)_{\beta}^{\mathrm{Fe_2Ti_2}}$	$Fe_{22}Ti_{22}H_{10}$	72.3
$(1\,\bar{1}\,0)_{\alpha}^{\mathrm{FeTi}} \parallel (0\,1\,0)_{\beta}^{\mathrm{FeTi}}$	$Fe_{25}Ti_{25}H_{12}$	95.3
$(1\,\bar{1}\,0)_{\alpha}^{\mathrm{FeTi}} \parallel (0\,1\,0)_{\beta}^{\mathrm{H}}$	$Fe_{25}Ti_{25}H_{13}$	100.4
$(0\,0\,1)_{\alpha}^{\mathrm{Fe_2}} \parallel (0\,0\,1)_{\beta}^{\mathrm{Fe_2H_2}}$	$Fe_{28}Ti_{26}H_{14}$	57.3
$(0\,0\,1)_{\alpha}^{\mathrm{Ti_2}} \parallel (0\,0\,1)_{\beta}^{\mathrm{Ti_2}}$	$Fe_{28}Ti_{30}H_{14}$	62.0

It is worth noting that, as explained in Section 4.1, the values of $E^{\alpha}_{\mathrm{slab}*}$ and $E^{\beta}_{\mathrm{slab}*}$ required for Equation 4.20 are calculated using strained α and β slabs having the same numbers of FeTi pairs as the interface slab. Thus, the total energy of each precursor slab contains the elastic energy associated with the strain necessary to create the coherent interface. The calculated interface energy (γ_i) is therefore a representation of the chemical contribution to the interphase boundary energy. The values obtained in the interval between 57.3 and 100.4 mJ/m^2 are consistent with the estimated value of approximately 50 mJ/m^2 [160, 161], which may reach an estimated maximum of 200 mJ/m^2 [156] for coherent interfaces.

4.2 Interphase boundary strain energy density

4.2.1 Fundamentals for microelasticity theory

The hydride phase formation gives rise to large perturbations of local volume due to significant density change upon transformation, leading to a large lattice mismatch between metal (α) and hydride (β) phases. Therefore, the micromechanical responses play a pivotal role in determining the phase stability and the transformation kinetics. More specifically, the associated interfacial coherency strain energy strongly affects the morphology of the growing hydrides, as well as their growth kinetics of the hydride phase [162]. To efficiently assess the orientation of a low-energy interphase boundary between the hydride and matrix phases, the interfacial coherency strain energy density function, $B(\vec{n})$, from Khachaturyan-Shatalov microelasticity theory (KS) [88] can be used:

$$B(\vec{n}) = \mathbb{C}_{ijkl}\varepsilon_{ij}\varepsilon_{kl} - \vec{n}_i\sigma^0_{ij}\Omega_{jk}(\vec{n})\sigma^0_{kl}\vec{n}_l \tag{4.33}$$

with,

$$\sigma^0_{ij} = \mathbb{C}_{ijkl}\varepsilon_{kl} \tag{4.34}$$

and,

$$\Omega^{-1}_{jk} = \mathbb{C}_{jilk}n_in_l, \tag{4.35}$$

where $\vec{n}$ is the unit vector that characterizes the interface normal in a three-dimensional Cartesian space. The term ε_{ij} represents the stress-free transformation strain (SFTS), which relates the uniform lattice distortion strain necessary for the parent phase to transform into a given variant of the product phase when no stress response is considered. The term $\mathbb{C}_{ijkl}$ is the elastic stiffness tensor, which is considered homogeneous (i.e., identical elastic moduli) between the product and the parent phase in KS. In addition, the theory also considers the size of the matrix to be infinite (i.e., stress-free state macroscopically), and a platelet-shape of the product phase (i.e., planar interface).

By finding $\vec{n}$ that minimizes the function $B(\vec{n})$ (i.e., $\vec{n_0}$), it is possible to identify the elastically preferable phase boundary orientation as a result of the elastic properties of phases (i.e, metal and hydride) and their crystallographic orientation relationship. This represents the normal vector of the habit plane of the forming hydride phase.

4.2.2 Micromechanical analysis

As a baseline case, the fully coherent interfaces between the β hydride phase and the α parent phase are firstly considered for the micromechanical analysis in comparison with the chemical contribution counterpart that was analyzed for the same interface types in Section 4.1.3. Following this, the possible coherency loss and its consequence to the phase boundary energy and orientations is then examined.

For convenient consideration of the lattice correspondence, the orthogonal lattice vectors and the corresponding lattice parameters of the α phase were redefined within the present micromechanical analysis. More specifically, the crystallographic orientation of the α phase was adapted in a way that it satisfies the orientation relationship with the β, as shown in Figure 4.4(a). The lattice parameters of the α phase were then newly defined on the Cartesian coordinate system for the β phase. Within this crystallographic framework, the crystal structure of the α phase can be regarded as a tetragonal structure (see Figure 4.9(a)), while the β phase counterpart is an orthorhombic structure (see Figure 4.9(b)).

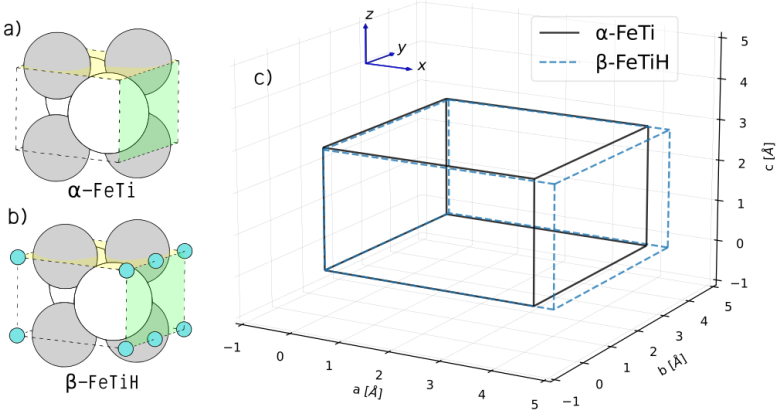

Figure 4.9: Representation of the relationship between the β hydride and the α matrix. a) The α phase within tetragonal lattice structure, b) the orthorhombic β phase, and c) superimposition of the tetrahedral α and orthorhombic β unit cells. Gray: Fe atoms; white: Ti atoms; cyan: H atoms

As illustrated in Figures 4.9(a) and (b), the unit cells of both phases include four common metallic atoms, emphasizing the specific volumetric expansion resulting from hydrogenation. Therefore, it was considered the formation of the β hydride in the α phase as a tetragonal-to-orthorhombic phase transformation involving large volume expansion, which is clearly described in Figure 4.9(c). From the lattice correspondence shown in Figure 4.9(c), the deformation gradient tensor for the α-to-β transformation is obtained as

$$F_{ij} = \begin{bmatrix} \delta^a & 0 & 0 \\ 0 & \delta^b & 0 \\ 0 & 0 & \delta^c \end{bmatrix}, \tag{4.36}$$

where $\delta^a = \frac{a_\beta - a_\alpha}{a_\alpha}$, $\delta^b = \frac{b_\beta - b_\alpha}{b_\alpha}$, $\delta^c = \frac{c_\beta - c_\alpha}{c_\alpha}$, with a_α, b_α, c_α and a_β, b_β, c_β being the lattice parameters of the α, and β phases, respectively. Based on the finite strain formalism, the SFTS is then computed by:

$$\epsilon_{ij}^{SFTS} = \varepsilon_{ij} = \frac{1}{2}\left([F_{ij}]^\intercal \cdot F_{ij} - I\right), \tag{4.37}$$

where I is the identity matrix and $[F_{ij}]^\intercal$ is the transpose of F_{ij}.

By considering equivalent symmetrical operations for the tetragonal α phase ($a_\alpha = b_\alpha$) to the orthorhombic β phase transformation, two distinct structural variants can be identified, resulting in the two corresponding SFTS

tensors (F_{ij-I}, and F_{ij-II}), that are related by a 90° rotation around the c lattice vector (i.e., z axis shown in Figure 4.9(c)). Using the lattice parameters from the first-principles calculations shown in Table 4.4, the computed SFTSs are given as the following:

$$F_{ij-I} = \begin{bmatrix} 0.092 & 0 & 0 \\ 0 & 0.021 & 0 \\ 0 & 0 & -0.017 \end{bmatrix} \tag{4.38}$$

and,

$$F_{ij-II} = \begin{bmatrix} 0.021 & 0 & 0 \\ 0 & 0.092 & 0 \\ 0 & 0 & -0.017 \end{bmatrix}. \tag{4.39}$$

To account for the homogeneous modulus assumption in the KS theory, i.e. the elastic moduli of the parent and product phases are assumed to be the same, a simple average of the elastic moduli of the α and β phases was used to construct the homogeneous elastic stiffness tensor ($\mathbb{C}_{ijkl}$) used in Equation 4.33-4.35.

Note that the lattice parameters and elastic moduli of the two phases are defined on the same Cartesian coordinate system (i.e., $x-y-z$ for the β phase in Figure 4.9(c)) for consistency within the micromechanical analysis, which are tabulated in Table 4.4. It should also be emphasized that all reference values are derived from the first-principles calculations from this work.

Figure 4.10(a) shows the plot of the computed $B(\vec{n})$ using the anisotropic elastic stiffness tensor and the SFTS derived above.

The direction that minimizes $B(\vec{n})$ (Equation 4.33), represented by the unit vectors $\vec{n}_0$, corresponds to the preferred phase boundary (i.e., habit plane) normal for the formation of the product phase. The preferred phase boundary normal $\vec{n}_0$ was identified by numerical minimization as indicated in Figure 4.10 (with arbitrary magnitude). The unit vector $\vec{n}_0$ identified is given by $[\pm 0.942, 0.000, \pm 0.335]$ in the Cartesian coordinate system, leading to $B(\vec{n}_0) = 0.093$ GPa as the minimum interfacial coherence strain energy density. Within the lattice plane system of the β phase (see Figure 4.9), the corresponding habit plane is close to the $\{3\,0\,1\}_\beta$ family of crystal planes, which is approximately equivalent to the $\{1\,2\,0\}_\alpha$ plane in the original lattice plane system for the cubic α phase (see Figure 4.4(b) for reference).

From the chemical contribution point of view, the most energetically stable interface is $(0\,0\,1)_\alpha \parallel (0\,0\,1)_\beta$ as indicated in Table 4.3. By transforming this interface notation to the coordinate system for the micromechanical analysis (see Figure 4.9 for clarity), the corresponding plane is normal to the z axis, which carries the highest strain energy density as shown in Figure 4.10 a). The discrepancy between the chemically and the mechanically stable interface orientations may indicate how the phase boundary evolves as the hydride grows. Note that the relative impact of the chemical contribution

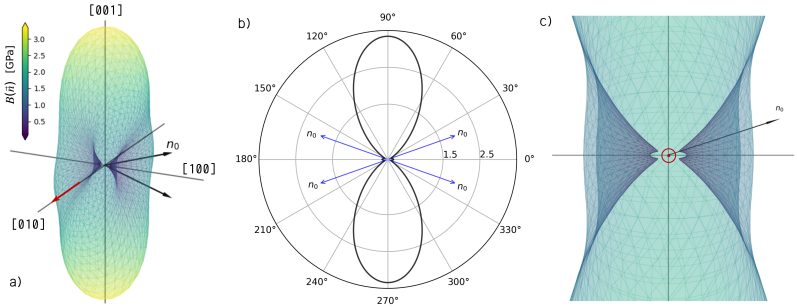

Figure 4.10: Spherical plots of $B(\vec{n})$ for a flat and coherent interface a) general three-dimensional view with gradient colors representing the values in GPa (note that some level of transparency is applied to the $B(\vec{n})$ surface to highlight the minimum values). Black arrows represent two instances of directions that minimize elastic energy $\vec{n_0}$. b) Polar plot of $B(\vec{n})$ projected on the $(0\,1\,0)_\beta$ plane with $\vec{n_0}$ represented with blue arrows. c) Same as a) but viewed from the $[0\,1\,0]_\beta$ direction (red arrows) and zoomed on the minimum points.

Table 4.4: Calculated lattice parameters (in Å) and elastic constants (in GPa) using Voigt notation.

	α-FeTi (tetragonal)	β-FeTiH (orthorhombic)
a [Å]	4.176	4.560
b [Å]	4.176	4.265
c [Å]	2.953	2.903
c_{11}	306.0	313.0
c_{22}	306.0	302.2
c_{33}	379.5	360.0
c_{44}	148.3	86.3
c_{55}	75.0	63.4
c_{66}	75.0	74.5
c_{12}	165.0	173.3
c_{13}	106.5	82.8
c_{23}	106.5	99.6

scales with d^2, while the mechanical contribution counterpart scales with d^3, where d represents the size of the growing hydride. Therefore, at the early stage of hydride phase formation in a matrix metal phase, the chemical contribution to the interface energy is dominant, of which anisotropy determines the morphological behavior of the forming phase (i.e., $(0\,0\,1)_\beta$ is preferred). On the other hand, as the hydride phase grows, the strain energy contribu-

tion commensurate with interfacial mismatch between the adjoining crystal lattice increases and becomes more dominant (i.e., $\{3\,0\,1\}_\beta$ is preferred).

So far, only fully coherent interfaces have been considered. However, as the hydride phase grows more, the accumulation of the coherency strain energy may significantly lower the phase stability due to large volume expansion. Therefore, the phase boundaries tend to lose the interfacial coherency by creating an array of misfit dislocations to accommodate the large volume expansion, which partially releases the coherency strain energy. In particular, the coherency loss is expected to occur when the energy to form the dislocations becomes lower than the energy penalty to maintain interfacial coherency, which determines the critical condition for transitioning from coherent to semi-coherent (or incoherent) interfaces [156, 161, 88].

Concerning the directional tendency of the misfit dislocation array, the formation of the array along the x and y directions is less probable than along the z direction since $(0\,0\,1)_\beta$ interface boundary incorporates the most chemically stable atomic configuration, which may have a propensity for maintaining its intrinsic defect-free atomic configuration. In addition, since the Burgers vector ($\vec{b}$) along the z axis is shorter than those along the x and y axes (refer to Table 4.4), the formation of misfit (edge) dislocation along the z axis is expected to be energetically more stable, considering that the dislocation energy is proportional to the magnitude of $\vec{b}$. Therefore, it can be assumed that the loss of coherency occurs preferentially along the $[0\,0\,1]$ direction. Following this assumption, the effect of the coherency loss along the $[0\,0\,1]$ direction on the phase boundary orientation is examined. For this purpose, a strain component ε_{33}^{def} was introduced to account for modification of the SFTS due to the formation of misfit dislocations that perturb the lattice coherency along the z axis. The value of ε_{33}^{def} may vary from 0 to $-\varepsilon_{33}^{coh}$ $(= -\delta^c)$, corresponding to a transition from a perfectly coherent to a perfectly incoherent interface (i.e., complete loss of coherency) along the $[0\,0\,1]_\beta$ axis, respectively [163], while maintaining the lattice coherency along other direction (i.e., mixed interfacial coherency). As an extreme case, the complete loss of coherency along $[0\,0\,1]$ is considered, leading to $F_{33-I}^{000} = \varepsilon_{33}^{coh} + \varepsilon_{33}^{def} = \delta^c - \delta^c = 0$ [163, 164].

Figure 4.11 compares the full coherency and the mixed coherency scenarios for the cross-section of the function $B(\vec{n})$ along the $(0\,0\,1)_\beta$ plane in polar coordinates. For the mixed coherency case (i.e., complete loss of coherency only along $[0\,0\,1]$), the family of planes that minimize $B(\vec{n})$ becomes $\{1\,0\,0\}$, while for the fully coherent case, the identified habit plane is inclined by an angle of 19.5° with respect to the planes $\{1\,0\,0\}$. Note that the $\{1\,0\,0\}$ planes correspond to the $(1\,1\,0)_\alpha \parallel (1\,0\,0)_\beta$ interface plane shown in Figure 4.4. Interestingly, as also observed by Heo et al. [163], the calculated value of $B(\vec{n}_0)$ for the mixed coherency case (0.0966 GPa) remains almost the same as that of the fully coherent counterpart (0.0931 GPa). This indicates that the phase boundary orientation varies due to coherency loss, while the corresponding strain energy contribution is almost unchanged.

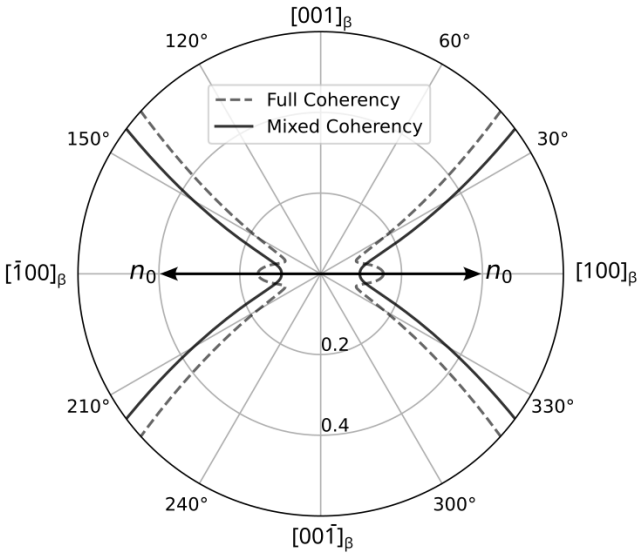

Figure 4.11: Cross-section of $B(\vec{n})$ in GPa along the $(0\,1\,0)_\beta$ plane using SFTS for the mixed coherency ($F_{33-I} = \delta^c - \delta^c = 0$, that is, complete coherency loss solely along the [0 0 1] direction) case. Superimposed in dashed lines is the full coherency case ($F_{33-I} = \delta^c$) presented again for comparison. Black arrows represent the directions that minimize the interfacial coherency strain energy density for the mixed coherency case, $\vec{n_0}$.

Importantly, the findings discussed above provide insight into possible phase boundary orientation variation during the hydride phase formation and growth from $\{0\,0\,1\}_\alpha \parallel \{1\,0\,0\}_\beta$ (chemically stable) to $\{1\,2\,0\}_\alpha \parallel \{3\,0\,1\}_\beta$ (mechanically stable with full coherency) to $\{1\,1\,0\}_\alpha \parallel \{1\,0\,0\}_\beta$ (mechanically stable with mixed coherency). This is evidenced by an experimentally characterized β hydride shape formed in FeTi reported in the literature (e.g., micrographs shown in Schober's work [128, 120]). Figure 4.12 shows an adapted micrograph presented in Figure 2 from Schober [128]. As observed in the experimental micrograph (see Figure 4.12), μm-sized lenticular plate-like particles are formed with the interphase boundaries parallel to $(1\,1\,0)_\alpha$ planes. It is interesting to note that the tips of the hydrides form closing sharp shapes with different boundary orientations inclined by $\approx 20°$ with respect to the $(1\,1\,0)_\alpha$ planes, which is close to the predicted phase boundary orientation with full coherency.

As discussed previously, for μm-sized large precipitates, it is reasonable to expect that the elastic contribution to the interphase boundary energy is

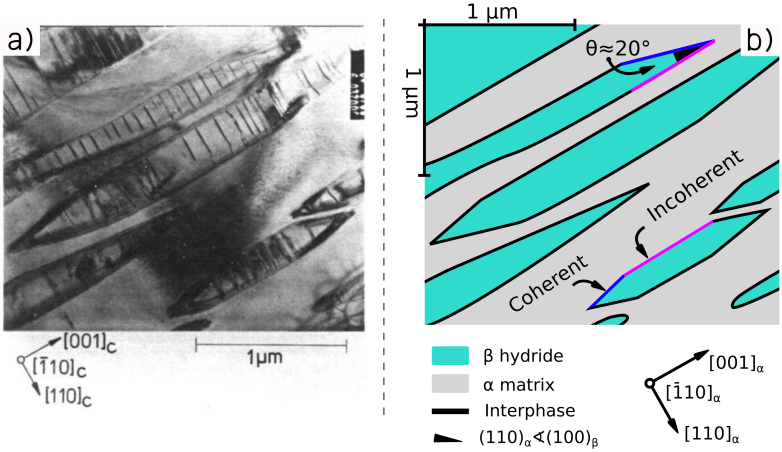

Figure 4.12: Mircrostructure of β phase precipitation on a α matrix. a) Schober's Figure 2 micrograph [128], with reproduction permission from Elsevier. b) Adaptation of Schober's micrograph, where magenta- and blue-colored lines depict examples of incoherent and coherent interfaces, respectively.

the primary driving factor influencing the morphology of the precipitates. Therefore, the phase boundary orientation is most likely to be aligned along the mechanically stable direction. Based on our analysis of the two extreme cases that may occur along the [0 0 1] direction, i.e. fully coherent and fully incoherent cases, it can be inferred that the habit plane orientations predicted by the micromechanical analysis for the two cases may bound the range of phase boundary orientations within the tip-region, which explains the dominant interphase boundary orientations observed by Schober [128]. However, as discussed by Heo et al. [163], there could be many distinct combinations of interfacial defects along different crystallographic orientations, leading to the stabilization of the same habit plane. Thus, the creation of misfit dislocation along the z axis may be only one of many possible defect combinations that stabilize the $\{1\,0\,0\}$ phase boundaries.

Critical size of a β particle before plastic relaxation

The critical size of a precipitate β (FeTiH), above which the system plastically relaxes (i.e., forms dislocations) is analyzed in this section. To assess this quantitatively, some assumptions are made. First, it is considered a constant geometry of the particle in the initial stage of precipitation (i.e., a constant aspect ratio for different particle sizes). Based on the lattice mismatch illustrated in Figure 4.9, as well as quantified in Equation 4.36,

it is possible to determine the minimum lattice parameters of β that geometrically produce an edge dislocation in each direction x, y and z, from the inversion of each value δ: $(\delta^a)^{-1} = 10.87$, $(\delta^b)^{-1} = 47.61$, $(\delta^c)^{-1} = 58.82$ (see Equation 4.36 and Equation 4.38, for reference), respectively, resulting in an estimated correspondence of $y = 5x$, and $z = 6x$ (Figure 4.13(a)). Note that the $(1\,1\,0)_\alpha \parallel (1\,0\,0)_\beta$ interface plane corresponds to the $y - z$ plane in Figure 4.13. The comparison of the estimated aspect ratio with the illustrated particle highlighted by arrows labeling coherent and incoherent interfaces in Figure 4.12b) confirms the validity of this approximation. From this assumption, it is also possible to estimate the dislocation density of the $y - z$ plane as 1 dislocation ($\perp$) per area $A_{yz}^{(\perp)} = \|47\vec{b_\beta} \times 58\vec{c_\beta}\|$ (Figure 4.13(b)).

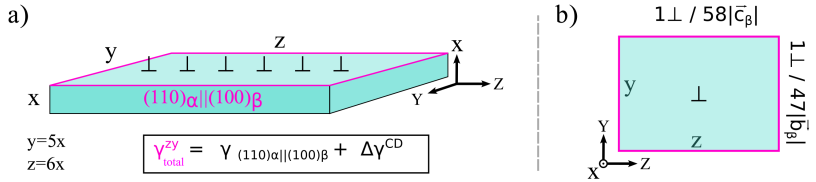

Figure 4.13: Schematically visualization of the geometrical assumption of the aspect ratio of a β particle forming in the early stages. a) Three-dimensional view, highlighting the interface plane subject to loss of coherency contoured in color magenta. b) top view of the plane indicating the assumed ideal dislocation density.

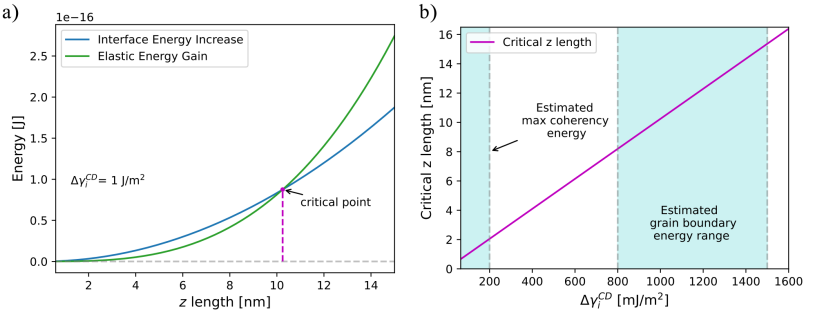

Figure 4.14: Comparison between chemical and elastic contribution for loss of coherency. a) Superimposed plot of interface energy increase and elastic energy gain. b) Critical size variation with $\Delta\gamma_i^{\mathrm{CD}}$.

Yet, there is a competition between the elastic energy penalty ($E_{\mathrm{el.}}^{\mathrm{gain}}$) to maintain coherency along the $(1\,0\,0)$ plane that scales with the volume of the

particle ($V = xyz$):

$$E_{\text{el.}}^{\text{gain}} = V \Delta B_n(\vec{n} = [1\,0\,0]), \tag{4.40}$$

where

$$\Delta B_n(\vec{n} = [1\,0\,0]) = B_n^{\text{coh.}}(\vec{n} = [1\,0\,0]) - B_n^{\text{mix}}(\vec{n} = [1\,0\,0]), \tag{4.41}$$

$B_n^{\text{coh.}}(\vec{n} = [1\,0\,0]) = 0.155\,\text{GPa}$ represents the full coherency case (i.e., $\varepsilon_{33} = \delta^c$) and $B_n^{\text{mix}} = 0.096\,\text{GPa}$ represents the mixed coherency case (i.e., $\varepsilon_{33} = 0$). The variation of the total interface energy ($\Delta\Gamma_i^{\,yz}$), resulting from the arial energy increase associated with the formation of misfit dislocations ($\Delta\gamma_i^{CD}$) is given by:

$$\Delta\Gamma_i^{\,yz} = kA_{yz}^{(\perp)}\Delta\gamma_i^{CD}, \tag{4.42}$$

which scales with arial variation of the $(1\,1\,0)_\alpha \parallel (1\,0\,0)_\beta$ interface, which is controlled by the proportionally constant k in Equation 4.42. Figure 4.14(a) shows the superimposed plots of Equation 4.40 and Equation 4.42 over the z length of the $(1\,1\,0)_\alpha \parallel (1\,0\,0)_\beta$ interface for an estimated impact of $1\,\text{J}\,\text{m}^{-2}$ increase in the interface energy when a misfit dislocation is formed in the interface. Due to competition between the elastic energy penalty and the interfacial energy variation with the change in coherence of the $(1\,1\,0)_\alpha \parallel (1\,0\,0)_\beta$ interface, the critical particle size is determined by the intersection of the two curves (calculated at $z = 10.25$ for $\Delta\gamma_i^{\text{CD}} = 1\,\text{J}\,\text{m}^{-2}$), above which coherency loss is preferred to maintaining full coherency.

Taking the lower reference limit of $200\,\text{mJ}\,\text{m}^{-2}$ [156] (estimated as the maximum of a coherent interface energy), and a higher reference limit of $800\,\text{mJ}\,\text{m}^{-2}$ (related, e.g., to the grain boundary of bcc-Fe [165, 166]), an estimative of the range of the values of $\Delta\gamma_i^{\text{CD}}$ can be inferred. Figure 4.14(b) shows the variation of the critical size as a function of $\Delta\gamma_i^{\text{CD}}$.

Based on these assumptions, it is possible to conclude that in the early stage of β particle precipitation, maintaining a full coherency state is favorable up to $150\,\text{nm}^3$.

5 Phase-Field Simulations of the FeTi Hydrogenation

5.1 Phase-Field Modeling the FeTi-H system

In this section, the basic equations governing Phase-Field simulations will be shown and discussed regarding their interconnection. Subsequently, the solution for such a system of coupled Partial Differential Equations (PDEs), using the Finite Element Method (FEM) via the Moose software package is briefly introduced and discussed regarding the applicability to solving and simulating the hydrogenation of FeTi.

The KKS formulation is employed in this study with the two-phase model describing the α-FeTi and the β-FeTiH phases. The non-conserved order parameter (η_β) is attributed to represent the local fraction of the β-FeTiH hydride phase. Thus, the Allen-Cahn equation (Equation 2.35) is given by:

$$\frac{\partial \eta_\beta}{\partial t} = -L_\beta \frac{\partial F}{\partial \eta_\beta}. \tag{5.1}$$

The conserved field variable is attributed to the global hydrogen composition of the system (x_H), and the split version of the Cahn-Hilliard equation (Equation 2.34) becomes:

$$\frac{\partial x_\mathrm{H}}{\partial t} = \nabla \cdot M_\mathrm{H} \nabla \mu_\mathrm{H}, \tag{5.2}$$

and

$$\frac{\partial f_{loc}}{\partial x_\mathrm{H}} = \nabla \cdot (k_{x_\mathrm{H}} \nabla x_\mathrm{H}) - \mu_\mathrm{H}. \tag{5.3}$$

From the KKS model description, the interface constraint yields:

$$\frac{\mathrm{d}f_\alpha}{\mathrm{d}x_\mathrm{H}^\alpha} = \frac{\mathrm{d}f_\beta}{\mathrm{d}x_\mathrm{H}^\beta}. \tag{5.4}$$

5.1.1 Modeling the free energy functional of the FeTi-H system

Because the microstructure evolves in the direction that minimizes the free energy of the material, modeling the materials system's free energy functional is considered the cornerstone of phase-field simulations. Consequently, the phase-field modeling approach can be defined as a modular framework with the main focus on the description of the free energy of the problem. In this section, the idea behind the modeling of the FeTi-H free energy functional is described in detail based on the thermodynamic model presented in Chapter 3 and the phase-field model presented in Section 2.4.

For the FeTi-H system, the local free energy density description (see Equation 2.37 for reference), incorporates the hydrogen mole fraction within the system as the conserved field variable (x_{H}) and the fraction of β-phase within the system as the non-conserved η_β. The free energy density functional is then expressed as:

$$F = \int_V \left[f_{loc}\left(x_{\mathrm{H}}, \eta_\beta\right) + f_{gr}\left(x_{\mathrm{H}}, \eta_\beta\right) \right] \mathrm{d}V. \tag{5.5}$$

The gradient energy contribution is expressed by:

$$f_{gr} = \frac{\kappa_{x_{\mathrm{H}}}}{2} |\nabla x_{\mathrm{H}}|^2 + \frac{\kappa_{\eta_\beta}}{2} |\nabla \eta_\beta|^2 \tag{5.6}$$

while the local free energy density is expressed by:

$$f_{loc} = \left(1 - h(\eta_\beta)\right) f_\alpha(x_{\mathrm{H}}^\alpha) + h(\eta_\beta) f_\beta(x_{\mathrm{H}}^\beta) + w g(\eta_\beta). \tag{5.7}$$

For this work, the switching function $h(\eta)$ was chosen as the known "high" polynomial form, expressed by:

$$h(\eta) = \eta^3(6\eta^2 - 15\eta + 10) \tag{5.8}$$

whereas the double-well energy barrier function is given by:

$$g(\eta) = \eta^2(1 - \eta)^2. \tag{5.9}$$

The terms f_α, and f_β represent the Gibbs free energy densities of the individual α and β phases. Their values can be acquired from the thermodynamic assessment introduced in Chapter 3 after performing a proper dimensional analysis to transform the thermodynamic expressions of the bulk phases from their molar Gibbs energies to their corresponding volumetric (or density) values. This dimensional analysis is demonstrated later in this section.

For convenience, in the phase-field modeling in this study, the Gibbs energy expressions of the bulk phases are used with a shift from the conventional reference state. Instead of describing the Gibbs energy of the phases referenced on the standard element reference (SER), the variation of the Gibbs energy within the FeTi-H system was described referenced at the Gibbs energy of the pure FeTi (B2) phase and the H_2 gas-phase at the current external temperature and pressure conditions.

Changing the reference state should add a value to the Gibbs energy, which is the difference between the pure element at the SER and the state defining the reference. This affects the thermodynamic modeling in their reference Gibbs energy terms and is represented by different end-members, which are identified with a *sr* superscript on the expressions below. For the α phase [Equation 3.8], the end-member expression of the Gibbs energy model then becomes:

$$ {}^{sr}G^{\alpha}_{\mathrm{FT:vac}} = {}^{0}G^{\alpha}_{\mathrm{FT:vac}} - G^{\mathrm{B2}} = 0, \tag{5.10} $$

and

$$ \begin{aligned} {}^{sr}G^{\alpha}_{\mathrm{FT:H}} &= {}^{0}G^{\alpha}_{\mathrm{FT:vac}} - G^{\mathrm{B2}} + \frac{3}{2}G^{\mathrm{SER}}_{\mathrm{H_2}} - \frac{3}{2}G^{\mathrm{gas}}_{\mathrm{H_2}} + \Delta H_f^{\alpha_6} + \Delta S_f^{\alpha_6} T \\ &= -\frac{3}{2}RT\ln\left(\frac{P}{P_0}\right) + \Delta H_f^{\alpha_6} + \Delta S_f^{\alpha_6} T. \end{aligned} \tag{5.11} $$

The same concept is applied to the β phase [Equation 3.28] and yields:

$$ \begin{aligned} {}^{sr}G^{\beta}_{\mathrm{FT:H:vac}} &= 2\,{}^{0}G^{\alpha}_{\mathrm{FT:vac}} - 2G^{\mathrm{B2}} + \frac{1}{2}G^{\mathrm{SER}}_{\mathrm{H_2}} - \frac{1}{2}G^{\mathrm{gas}}_{\mathrm{H_2}} + \Delta H_f^{\beta_1} + \Delta S_f^{\beta_1} T \\ &= -\frac{1}{2}RT\ln\left(\frac{P}{P_0}\right) + \Delta H_f^{\beta_1} + \Delta S_f^{\beta_1} T \end{aligned} \tag{5.12} $$

as well as

$$ \begin{aligned} {}^{sr}G^{\beta}_{\mathrm{FT:H:H}} &= 2\,{}^{0}G^{\alpha}_{\mathrm{FT:vac}} - 2G^{\mathrm{B2}} + G^{\mathrm{SER}}_{\mathrm{H_2}} - G^{\mathrm{gas}}_{\mathrm{H_2}} + \Delta H_f^{\beta_2} + \Delta S_f^{\beta_2} T \\ &= -RT\ln\left(\frac{P}{P_0}\right) + \Delta H_f^{\beta_2} + \Delta S_f^{\beta_2} T \end{aligned} \tag{5.13} $$

For the gas phase, the shift of reference state yields:

$$^{sr}G^{\text{gas}}_{\text{FT}} = {}^{0}G^{\text{gas}}_{\text{FT}} - G^{\text{B2}} + RT\ln(P/P_0) \tag{5.14}$$

and

$$^{sr}G^{\text{gas}}_{\text{H}_2} = {}^{0}G^{\text{gas}}_{\text{H}_2} - G^{\text{gas}}_{\text{H}_2} + RT\ln(P/P_0) = 0. \tag{5.15}$$

An isothermal energy analysis using the above shift of reference states is shown in Figure 5.1. Intentionally, these mathematical operations set the reference state of the FeTi-H system to yield zero energy at the purely metallic FeTi-B2 phase and H_2 gas. However, these transformations do not affect the relative mixing properties. As a consequence, it becomes evident that the β hydride phase is increasingly more stable with increasing hydrogen partial pressure, as shown by its Gibbs energy being reduced relative to that of the α- and gas-phase for positive variation of hydrogen partial pressure, and vice versa. Figure 5.1 illustrates the variation of pressure and its effect on the system using phase models with shift of reference states.

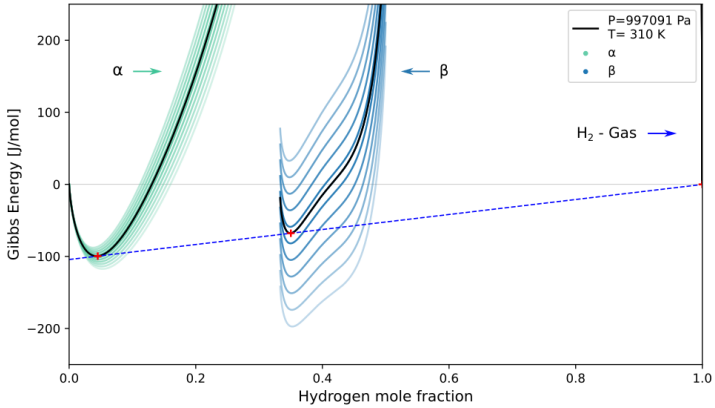

Figure 5.1: Calculated molar Gibbs energy of the phases of the FeTi-H system at 310 K. The plots are calculated for different hydrogen partial pressures ranging in a logarithmic space from 7.97×10^5 Pa to 1.39×10^6 Pa. The black solid lines represent the Gibbs energies of the phases at the unique α-β-gas equilibrium pressure at 310 K. The common tangent representing the three-phase equilibrium is superimposed as a dashed blue line with red "plus" marks identifying the equilibrium composition of the phases. An increasing level of transparency is applied proportional to how far the curves were calculated from the three-phase equilibrium.

Note that the para-equilibrium condition (illustrated in Figure 5.1 for $T = 310\,\mathrm{K}$ and $P = 997\,091\,\mathrm{Pa}$) can be represented by a common tangent line that intercepts the Gibbs energy curves. The composition of the intercepts is, therefore, the para-equilibrium composition, with the tangent line being a direct and visual representation of the phases assuming equal hydrogen chemical potential ($\mu_{\mathrm{H}}^{\alpha} = \frac{\mathrm{d}G^{\alpha}}{\mathrm{d}x_{\mathrm{H}}} = \mu_{\mathrm{H}}^{\beta} = \frac{\mathrm{d}G^{\beta}}{\mathrm{d}x_{\mathrm{H}}} = \mu_{H}^{\mathrm{Gas}} = \frac{\mathrm{d}G^{\mathrm{Gas}}}{\mathrm{d}x_{\mathrm{H}}}$).

For the molar density conversion, the equilibrium volume of both the α and β phases shown in Table 3.2 and their respective thermodynamic models presented in Section 3.2.4, that is, $(\mathrm{FT})(\mathrm{Va},\mathrm{H})_3$ and $(\mathrm{FT})_2(\mathrm{H})(\mathrm{Va},\mathrm{H})$, are taken into account. Note that there is one mole of metallic atoms (m.a) per formula unit (f.u) and two moles of metallic atoms per primitive unit cell (u.c) for the α phase, while there are two moles of metallic atoms per formula unit and four metallic atoms per primitive unit cell for the β phase (see Figure 4.4 for example). Thus, the dimensional analysis that transforms the Gibbs energies in Joules per mole of formula units into Joules per cubic meter is expressed by the following:

$$G^{\alpha}\left[\frac{\mathrm{J}}{1\cdot\cancel{\mathrm{mol\cdot f.u.}}}\right]\cdot\left[\frac{1\cdot\cancel{\mathrm{mol\cdot f.u.}}}{1\cdot\mathrm{mol}\cdot\cancel{\mathrm{m.a.}}}\right]\cdot\left[\frac{2\cdot\cancel{\mathrm{m.a.}}}{1\cdot\cancel{\mathrm{u.c.}}}\right]\cdot\left[\frac{1\cdot\cancel{\mathrm{u.c.}}}{25.75\cdot\cancel{\mathrm{\AA}^3}}\right]\cdot\left[\frac{1\cdot\cancel{\mathrm{\AA}^3}}{(10^{-10}\cdot\mathrm{m})^3}\right]$$
$$= 12895.63\cdot G^{\alpha}\left[\frac{\mathrm{J}}{\mathrm{m}^3}\right] = f^{\alpha}, \tag{5.16}$$

for the α phase, and

$$G^{\beta}\left[\frac{\mathrm{J}}{1\cdot\cancel{\mathrm{mol\cdot f.u.}}}\right]\cdot\left[\frac{1\cdot\cancel{\mathrm{mol\cdot f.u.}}}{2\cdot\mathrm{mol}\cdot\cancel{\mathrm{m.a.}}}\right]\cdot\left[\frac{4\cdot\cancel{\mathrm{m.a.}}}{1\cdot\cancel{\mathrm{u.c.}}}\right]\cdot\left[\frac{1\cdot\cancel{\mathrm{u.c.}}}{56.46\cdot\cancel{\mathrm{\AA}^3}}\right]\cdot\left[\frac{1\cdot\cancel{\mathrm{\AA}^3}}{(10^{-10}\cdot\mathrm{m})^3}\right]$$
$$= 5882.3\cdot G^{\beta}\left[\frac{\mathrm{J}}{\mathrm{m}^3}\right] = f^{\beta}, \tag{5.17}$$

for the β phase. The dimensional analysis yields an easy way to transform the molar Gibbs energy into the Gibbs energy density.

Furthermore, the Gibbs energies of the phases presented in Section 3.2.4 are expressed as functions of the interstitial lattice composition, representing the dissolution of hydrogen in the vacant sites of the bulk crystal. Therefore, computing the hydrogen mole fraction within the phases is not straightforward since vacancies cannot be considered when calculating molar quantities within the bulk phases. The Gibbs energy expressions of the bulk phases are therefore accordingly transformed as a function of the global hydrogen composition of the system. For the case of the α phase, this transformation is obtained from the following correspondence:

$$x_H^{\alpha} = \frac{3\ {}^{o}y_H}{1 + 3\ {}^{o}y_H}, \tag{5.18}$$

and

$$^{o}y_H = \frac{x_H}{3 - 3x_H} \tag{5.19}$$

while for the β phase, the correspondence is given by:

$$x_H^{\beta} = \frac{1 + {}^{H2}y_H}{3 + {}^{H2}y_H}, \tag{5.20}$$

and

$${}^{H2}y_H = \frac{x_H}{3 - 3x_H} \tag{5.21}$$

Finally, the Gibbs free energy density of the system can be constructed as a function of the conservative x_H and the non-conservative η_β field variables. Figure 5.2 plots the local free energy density in units of $\mathrm{J\,cm^{-3}}$.

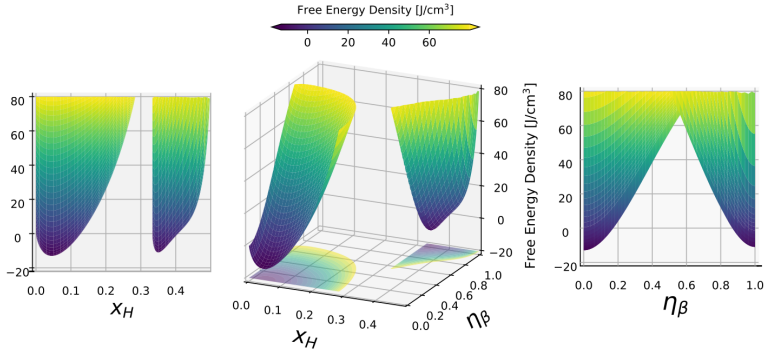

Figure 5.2: Calculated local free energy density (f_{loc}) over hydrogen mole fraction x_H and β hydride phase fraction (η_β).

Note that for the following phase-field simulations, this formulation of the free energy density was implemented into the KKS model in units of $\mathrm{nJ\,\mu m^{-3}}$ for better scaling of numerical units as will be further explained in the next sections.

5.1.2 Parametrization of the interphase energy and thickness

One advantage of the Kim-Kim-Suzuki model relies on the fact that the interfacial energy is independent of the free energy of the bulk phases. Moreover,

the interfacial energy can be found analytically through Equation 5.22 for a unidimensional equilibrated interface:

$$\gamma_{\text{int}} = \frac{\sqrt{\kappa_{\eta_\beta} w}}{3\sqrt{2}} \tag{5.22}$$

where γ_{int} represents the interfacial energy, the κ_{η_β} term is the gradient energy coefficient between the α, and β phases, and w is the height of the free energy barrier (Equation 5.9).

The analytical solution yields also the interface thickness 2λ, which is given by:

$$2\lambda = \frac{\xi\sqrt{2\kappa_{\eta_\beta}}}{\sqrt{w}}, \tag{5.23}$$

where ξ is a constant that is dependent on the definition of the interface thickness, generally taken e.g. as $\xi \cong 2.2$ when η_β changes from 0.1 to 0.9 at $-\lambda < x < \lambda$, and $\xi \cong 2.94$ when η_β changes from 0.05 to 0.95.

The resulting expression presented in Equation 5.22 and Equation 5.23 may be used to obtain an analytical solution to the parametrization of the phase-field model if the energy and thickness of the interphase are provided. As an example, Figure 5.3 shows the numerical solution for Equation 5.22 and Equation 5.23 using the values of the chemical contribution to the interphase energy (see Table 4.3 in Section 4.1.3 for reference) imposing an interphase thickness of 2 nm and 1 nm.

Note that in Figure 5.3, the solid black line represents the variation of Equation 5.22 for the fixed averaged interfacial energy of 76.0 mJ/m^2, and the green region represents the same, but in the range obtained when using the minimal and maximum calculated chemical contribution to the interphase energy of Table 4.3. Parameterized values for achieving the target interphase energy of 76.0 mJ m^{-2} with specified thicknesses of 1 and 2 nm are shown in Table 5.1.

Table 5.1: Parameterization values for achieving target interphase energy of 76.0 mJ m^{-2} with specified thicknesses.

Thickness [nm]	w [nJ/μm^3]	κ_β [nJ/μm]	Interphase Energy [mJ/m^2]
1	1.0037	$1.03636525 \times 10^{-7}$	76.0
2	0.5016	$2.07273868 \times 10^{-7}$	76.0

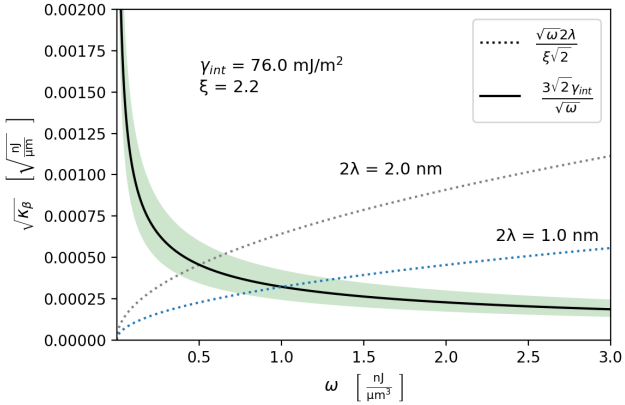

Figure 5.3: Numerical solution for the parametrization of the phase-field model interphase energy of 76.0 mJ/m^2 and interphase thickness of 2 nm (gray dotted line) and 1 nm (blue dotted line) for an unidimensional problem. Note that the green range shown represents the minimum value of 57.3 mJ/m^2 and maximum value of 100.4 mJ/m^2 given in Table 4.3, and that the units for the calculation were given in [nJ/μm^2], and [μm], for γ_{int} and λ, respectively.

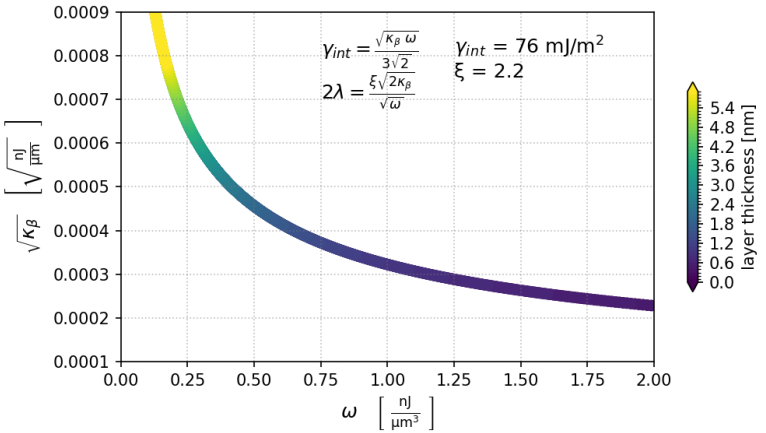

Figure 5.4: Correlation of $(w,\ \sqrt{\kappa_\beta})$ pairs that yields an interphase energy of 76.0 mJ m^{-2} together with the associated layer thickness.

A more systematic approach to identifying the possible pair (w, $\sqrt{\kappa_\beta}$) that yields a given layer thickness is shown in Figure 5.4.

For such an approach, the value of the chemical contribution to the interphase energy was kept constant while the numerical solution for the system of Equation 5.22 and Equation 5.23 was calculated. The layer thicknesses that result from these solutions are plotted as a color map in Figure 5.4, demonstrating the flexibility window for choosing the pair parameters (w, $\sqrt{\kappa_\beta}$) that result in the predicted 76.0 mJ m^{-2} interphase energy calculated from first-principles in Section 4.1.3.

5.1.3 Mobility parameters

The diffusivity and mobility of the species within the system should be considered to quantify the correct kinetic behavior of the simulations. As an initial step, hydrogen diffusion within the system was simply considered as independent of hydrogen concentration (x_H) and attributed to the same value regardless of the phase, that is, independent of the η_β order parameter, following the Boltzmann-Arrhenius equation:

$$D = D_0 \exp\left(\frac{-E_a}{RT}\right), \tag{5.24}$$

where D_0 is the temperature-independent diffusivity of hydrogen, and E_a is the activation energy for diffusion. These coefficients can be adjusted based on experimental data. The activation energy may be computed by the height of the potential energy barrier for hydrogen to migrate from interstitial sites, which can be calculated from DFT. By applying the nudged elastic band (NEB) method [167] it is possible to find the minimum energy path between a given initial and final state. In addition, the method may be coupled with a climbing image approach (CI-NEB) [168] that will search for the saddle point along the minimum energy path. These techniques were applied to find the activation energy for the hydrogen atom to diffuse from two nearest neighbors Fe_2Ti_4 octahedral sites. The calculations were performed using the optimal DFT settings defined in Section 3.2.3. The calculations were performed with a 4x4x4 FeTi-B2 supercell per hydrogen atom to avoid influence from self-interaction between periodic images. Figure 5.5 illustrates the results.

Note that Figure 5.5 a) shows a superposition of the calculated structures with a level of transparency, demonstrating the minimum energy path of the hydrogen atom (in green) along the two octahedral sites. From Figure 5.5 a) some displacements of the iron nearest neighbors are also noticeable. Figure 5.5 b) plots the energy variation over the summation of all atom displacements, usually called "reaction coordinate". The energy of the saddle point was calculated as 0.6292 eV or 60.71 kJ/mol H, which is in close agreement with the theoretical work of Kulkova et al. [169] (0.62 eV).

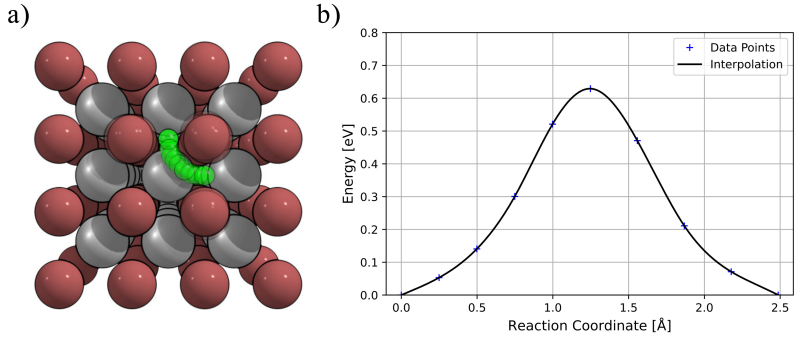

Figure 5.5: Calculated CI-NEB results for the H interstitial jump in the FeTi B2 phase: a) atomic view of the calculated minimum energy path for a hydrogen atom to diffuse from two nearest neighbors Fe_2Ti_4 octahedral sites. b) Potential energy variation along the minimum energy path referenced on the initial and final states.

In the available literature, some authors have empirically investigated the Arrhenius equation for hydrogen diffusion within the FeTi alloy and provided their found diffusion coefficients. Table 5.2 lists the available theoretical and empirical data in the literature.

Table 5.2: Available literature data of the Arrhenius coefficients for hydrogen diffusion within the FeTi-H system.

Phase	x_H	E_a [kJ/mol.H]	D_0 $[m^2/s]$	Reference
α-FeTi	-	60.71	-	This work
α-FeTi	-	59.82	-	[169]
α-FeTi	$\approx$0	47.86	$10.1 \cdot 10^{-8}$	[123]
α-FeTi	$\approx$0	46.41	$5.5 \cdot 10^{-8}$	[123]
β-FeTi	0.33	48.25	$7.2 \cdot 10^{-8}$	[170]
β-FeTi	0.33	31.84	$4.2 \cdot 10^{-11}$	[171]

As a first step, an Arrhenius-type equation was introduced to the model to represent the diffusivity of hydrogen within the FeTi-H system. The average value of the experimental D_0 and E_a coefficients from Arnold and Welter [123] was attributed solely as a function of temperature, $D_0 = 7.0{\times}10^4$ µm s^{-1}

and $E_a = 48.245\,\mathrm{kJ/mol\,H}$.

5.2 Phase-Field Simulations

Thus far, the incorporation of thermodynamic models for the α and β phases as well as the evaluation of chemical contributions to the interfacial energy in phase-field simulations have been discussed and examined. The following sections will delineate and validate these concepts through simulations.

5.2.1 Simulation of the interface equilibrium between α and β phases

In the KKS model, an analytical solution exists for the phase-field variables through an unidimensional equilibrium interface [83]. For the α and β steady-state equilibrium, they assume the form:

$$\eta_\beta^{ss}(x) = \frac{1}{2}\left[1 - \tanh\left(\frac{\sqrt{\omega}}{\sqrt{2}\kappa_\beta}x\right)\right], \tag{5.25}$$

and

$$x_H^{ss}(x) = h(\eta_\beta^{ss}(x))^{eq} x_H^\alpha + \left[1 - h(\eta_\beta^{ss}(x))^{eq} x_H^\beta\right]. \tag{5.26}$$

Here, the superscript ^{ss}, and ^{eq}, represent the values of the variables at steady-state and equilibrium, respectively.

To verify the implementation of the Gibbs energy thermodynamic models and the calculated chemical contribution to the interphase energy discussed in previous sections, a phase-field simulation of a flat/sharp interphase developing into the diffuse equilibrium interphase between β and α phases was performed until the steady-state was reached. The free energy density for the model followed the demonstration of Section 5.1.1, which was implemented in units of $\frac{\mathrm{nJ}}{\mu\mathrm{m}^3}$, as shown in Figure 5.3 and Figure 5.4.

Congruently, the parametrization of the interphase energy and thickness was performed following the concept presented in Section 5.1.2 to produce an interphase energy of 76 $\mathrm{mJ/m^2}$ and thickness of 1 nm. A three-dimensional simulation cell with dimensions of 10x1x1 nm in the Cartesian space $x-y-z$, respectively, and 500 finite elements along x were applied, resulting in $\Delta x = 0.02$ nm. As an initial step, the value for the L_β parameter was assumed arbitrarily to have unit values, while M_H was employed with the Arrhenius function described in Section 5.1.3.

The equilibrium temperature of 310 K and pressure of 997 091 Pa were held constant throughout the simulation. Initial conditions for both η and x_H phase-field variables were taken from step functions that equally divide

the volume cell (Ω) into two parts along x: $\eta_\beta = 1$ for $x < 0$ and $\eta_\beta = 0$ for $x \geq 0$, $x_H = 0.350351$ for $x < 0$ and $x_H = 0.046055$ for $x \geq 0$. These thermodynamic conditions reflect the para-equilibrium illustrated in Figure 5.1.

An initial time step of 1×10^{-5} was applied together with the time step with iteration adaptive as implemented in MOOSE [58], meaning that the time step is adjusted based on the number of required iterations needed for the solver to converge in the previous steps. Here growth and cutback factors of 1.5 and 0.5 were applied, respectively. The simulation was performed until the steady state was detected with a tolerance of 1×10^{-10}. Figure 5.6 illustrates the simulation's initial (t_0) and final (t_f) steps.

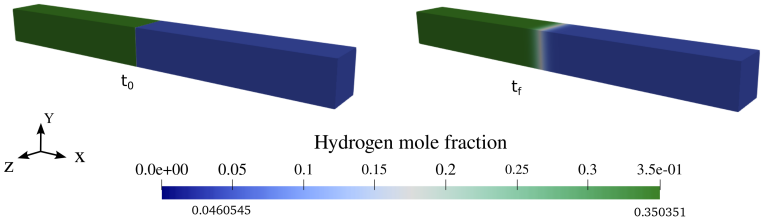

Figure 5.6: Hydrogen concentration distribution at initial step (t_0) and final step (t_f).

Figure 5.7 compares the simulated and analytical solution of the steady-state profile for the field variables η_β and x_H.

From Figure 5.7 the interphase thickness can be calculated by the difference of the x value for when $\eta_\beta = 0.9$ and $\eta_\beta = 0.1$, yielding the expected 1 nm thickness.

The interphase energy between the α and β phases was evaluated based on the total free energy difference between the initial and stationary states, and computed using the following expression:

$$\gamma_{\text{int}} = \frac{1}{A}\left(\int_{-\infty}^{\infty}\left[f_{loc} + \frac{\kappa_{\eta_\beta}}{2}\left(\mid \nabla\eta_\beta \mid\right)^2\right] \mathrm{d}\Omega - F^{eq}\right) \tag{5.27}$$

Where A represents the interphase area (i.e. the cross-section plane along the $y-z$ represented in Figure 5.6, in this case) and Ω is the domain of the simulation. The term F^{eq} stands for the thermodynamic bulk equilibrium between α and β phases, which can be derived from the well-known equilibrium condition [83].

$$F^{eq} = f_\alpha V\left(\frac{x_H^0 - {}^{eq}x_H^\beta}{{}^{eq}x_H^\alpha - {}^{eq}x_H^\beta}\right) + f_\beta V\left(\frac{{}^{eq}x_H^\beta - x_H^0}{{}^{eq}x_H^\alpha - {}^{eq}x_H^\beta}\right). \tag{5.28}$$

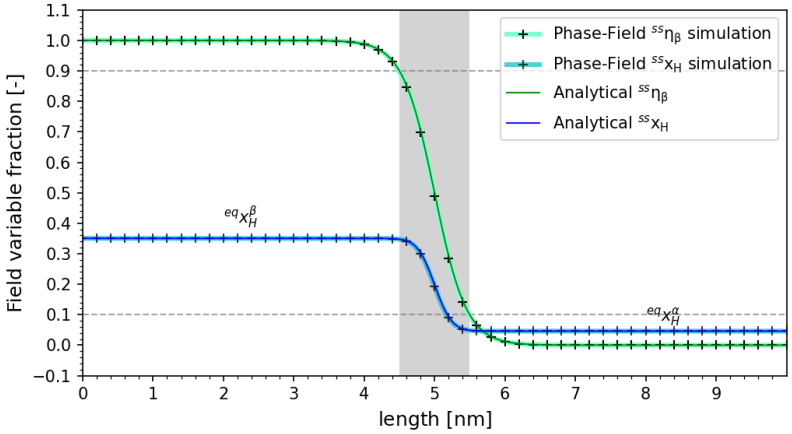

Figure 5.7: Comparison between the simulated and analytical solution for the steady state profile of η_β and x_H field variables. The gray patch illustrates the 1 nm interphase thickness expected from $\eta = 0.9$ to $\eta = 0.1$ ($\xi = 2.2$) at steady-state equilibrium. The black cross-markers were only plotted for every 0.2 nm.

Where V is the total volume of the simulation domain and x_H^0 the total solute fraction, which can be computed from the following expression:

$$x_H^0 = \frac{1}{V}\int_{-\infty}^{\infty} (x_H)\,\mathrm{d}\Omega. \tag{5.29}$$

The calculated interphase energy evolution over time is plotted in Figure 5.8.

Figure 5.8 illustrates the interphase energy evolution which is much more energetic at the initial stages due to the initial sharp interphase profile. Over time, the interphase profile smooths out at the pace that the interphase progresses reducing its energy until the system enters equilibrium. As expected, the interphase energy reaches the constant value of 76 mJ m^{-2} at stationary state.

5.2.2 Simulations of the β hydride growth from super-saturated α matrix

This section will demonstrate how the hydrogen supersaturation of the α phase matrix and its associated variation in chemical potential induces a

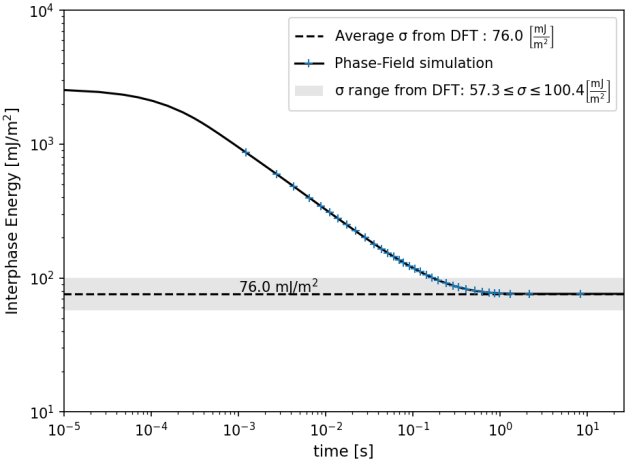

Figure 5.8: Simulation of the interphase energy evolution over time until steady-state is reached. The gray patch represents the interphase energy range calculated from DFT and the dashed line represents its average value of 76 mJ/m^2. Note that blue cross-markers were plotted for every 10 steps.

driving force for the β hydride formation and growth. The concepts are demonstrated theoretically and with phase-field simulations.

Thermodynamics of the hydride formation from supersaturated matrix

In general, driving forces exist in any transport phenomena, e.g., there will be an exchange of heat between two reservoirs if they have different temperatures. The heat flux stops when the difference in temperature goes to zero and the system enters thermal equilibrium. Analogously, a mass flow occurs in thermodynamic systems consisting of multiple elements. If there is a difference in the chemical potential of the elements within individual phases there will be a tendency for mass flow, consequently leading to phase transformation. These transformations are internal processes that minimize free energy by maximizing entropy. The most fundamental definition of driving force (D) relates the variation of entropy with respect to the variation of a general system's variable (ξ):

$$D = T\frac{\mathrm{d}S}{\mathrm{d}\xi}, \tag{5.30}$$

Since temperature is a positive quantity and $\mathrm{d}S \geq 0$ for a spontaneous process, if $D \leq 0$, the process does not spontaneously occur for any time. Figure 5.9 illustrates a complete thermodynamic analysis when considering the case of a supersaturated solution of hydrogen within the α parent phase with ${}^{mt}x_H^{\alpha} = 0.1$, showcasing the associated driving force for the β formation.

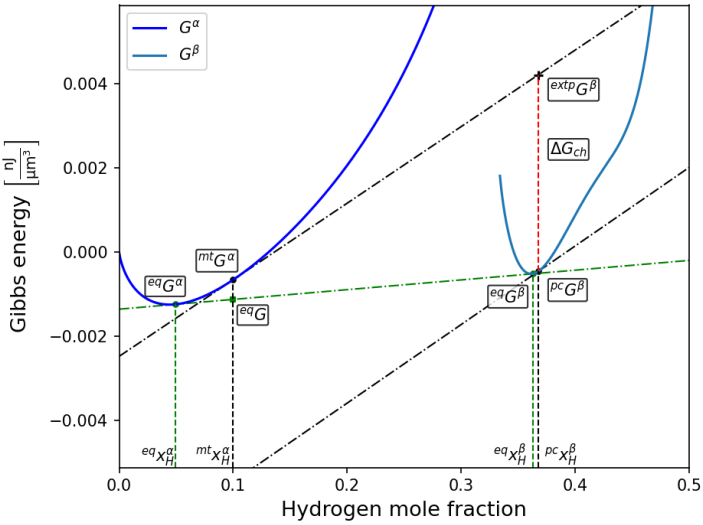

Figure 5.9: Illustration of the volumetric driving force for the β phase precipitation in a supersaturated hydrogen solution of $x_H = 0.1$ within the α parent matrix phase and its equilibrium state construction at 310 K under 997 091 Pa hydrogen partial pressure within the FeTi-H system.

Initially, the Gibbs energy of the matrix has a correspondent molar Gibbs energy (${}^{mt}G^{\alpha}$) which is not at the lowest possible energetic state for the system. The equilibrium composition of the α phase is represented in Figure 5.9 with a green point marked on the G^{α} curve. This composition relates to the state where the chemical potential of hydrogen is the same in each phase. Consequently, such a condition can be represented as a common tangent touching each Gibbs energy curve of the phases, shown as the green dash-dotted line in Figure 5.9.

The minimum Gibbs energy for the system ${}^{eq}G$ for an overall hydrogen mole fraction of $x_H = 0.1$ lies on this common tangent line at this composition. Therefore, the total decrease in free energy (ΔG_t) is associated with the completion of phase transformation and is given by the difference between the equilibrium Gibbs energy (${}^{eq}G$) and the energy of a supersaturated α

matrix ($^{mt}G^{\alpha}$):

$$\Delta G_t = {}^{eq}G - {}^{mt}G^{\alpha} \tag{5.31}$$

The value of ΔG_t is the total driving force for the transformation, however, it is not the driving force for nucleation. This is because the first nuclei to appear do not significantly change the α composition from $^{mt}x_H^{\alpha}$. Given a super-saturated solution within the α phase, the precipitation of the β phase ultimately occurs because of the positive driving force pushing the system to its lowest energy (or equilibrium) state.

Analogously, the driving force for this phenomenon is calculated as the distance between the tangent (or hyper-plane for a multicomponent system) to the Gibbs energy surface at the composition of the supersaturated parent phase and the parallel tangent to the precipitating phase [172]. These parallel tangent lines are represented in black dashed-dotted lines in Figure 5.9. Note that the hydrogen content within a firstly forming nucleate of a β phase precipitate ($^{pc}x_H^{\beta}$) within a supersaturated α matrix ($^{mt}x_H^{\alpha}$) is close to but not at equilibrium composition.

The extrapolation of the tangent line to G^{α} at $^{mt}x_H^{\alpha}$ to the $^{pc}x_H^{\beta}$ composition finds the $^{extp}G^{\beta}$ energy. This point characterizes the change in the chemical composition of the matrix crystal α without changing either its hydrogen chemical potential or crystal structure. Therefore, the difference in energy between $^{extp}G^{\beta}$ and $^{pc}G^{\beta}$ represents the potential governing a structural transformation from α to β at $^{pc}x_H^{\beta}$. For a phase transformation, the system's variable ξ is determined by the number of moles of new phase formed N^{β}. Applying constant temperature, pressure, and moles, i.e. $T\mathrm{d}S = G$, Equation 5.30 can be written as:

$$D = -\left(\frac{\partial G}{\partial N^{\beta}}\right)_{T,P,N} = -\Delta G_{ch}, \tag{5.32}$$

In the following, these concepts are utilized to demonstrate that the phase-field simulations performed in this work quantitatively agree with the predictions from the equilibrium thermodynamics and the classical nucleation theory.

The β growth from a flat ensemble

Similarly to Section 5.2.1 a three-dimensional simulation cell was constructed, here with dimensions of 20x1x1 nm. The Ω simulation cell was divided into 1000 finite elements along the x Cartesian coordinate, yielding $\Delta x = 0.02$ nm. The initial condition for the order parameters η_β and x_H was set as a step function with the para-equilibrium values of 1 and 0.350351 for x $<$ 5 nm

and 0 and 0.1 for x $\geq$ 5 nm. Note that the value of hydrogen mole fraction within the α phase region corresponds to a supersaturated state (as shown in Figure 5.9), consequently creating a driving force for the β phase to grow. Figure 5.10 shows the resulting simulation until steady-state.

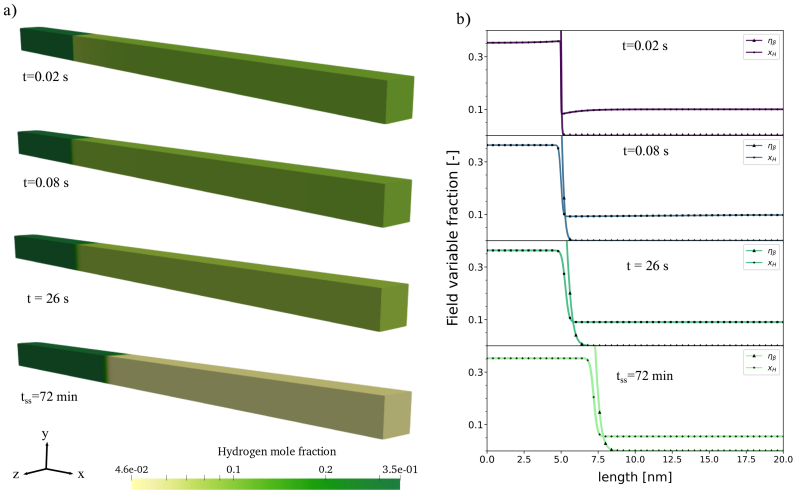

Figure 5.10: Simulation of the uni-dimensional growth of the β phase induced by a supersaturation of the α phase. a) Three-dimensional illustration of the hydrogen content evolution over time. b) Field variables plot over x Cartesian axis.

Figure 5.10 a) illustrates the three-dimensional image of the simulation volume (Ω) showing that the α phase is initially in a supersaturation state and as the simulation progresses, the concentration in the α region decreases, and the β phase fraction grows until the phases reach their bulk equilibrium composition and volume fraction at the steady state. Note that at the interface, at the first time step ($x_H \approx 0.1$ at $t = 0.02$), however, it can be seen that the concentration profile of hydrogen in the vicinity of the interphase region tends to its equilibrium composition in the α phase at the same time that within the β phase the concentration rises to meet the same chemical potential of the supersaturated α phase containing $x_H^\alpha = 0.1$, i.e. $\mu_H^\alpha(x_H^\alpha = 0.1) \Rightarrow \mu_H^\beta({}^{pc}x_H^\beta)$, as shown in Figure 5.9. This is expected by the imposition of the same chemical potential at the interphase as defined in the KKS model, shown with Equation 5.4.

Critical homogeneous nucleation size for the β phase

In this section the analytical solution for the classical nucleation theory (CTN) applied to the homogeneous nucleation scenario is compared against simulations to check further the correctness of the implementation of the Gibbs energy density of the phases and the chemical contribution to the interphase energy.

The theoretical idea behind CTN is that when a nucleate is formed, there will be a nucleation energy barrier resulting from the net change between two competing contributions: a volumetric contribution, related to the formation of a bulk phase, and an areal contribution, associated with the formation of an interphase (γ_{int}). The volumetric contribution tends to decrease the system's free energy due to the variation between the bulk Gibbs energy between an unstable matrix and the nucleate. The areal contribution increases the system's free energy by forming an interphase. In solids γ_{int} can vary widely depending on the coherency state and or the interface's orientation and should be summed over all interfaces of the nucleus $\sum \gamma^i_{\text{intint}} A^i$[156]. Ignoring the variation of γ_{int} and considering a spherical nucleate with radius of curvature r, the net change in Gibbs free energy can be described as follows:

$$\Delta G = -\frac{4}{3}\pi r^3 \Delta G_v + 4\pi r^2 \gamma_{\text{int}}, \tag{5.33}$$

where the term ΔG_v relates to the variation of Gibbs free energy density between the matrix and the forming particle, which is described as:

$$\Delta G_v = \frac{\Delta G_{ch}}{V_m^\beta} + \Delta G_{el}. \tag{5.34}$$

The term ΔG_{ch} represents the driving force associated with the chemical potential and the term ΔG_{el} is the elastic strain energy. The nucleation activation barrier thus corresponds to the saddle point of the net free energy change. This value is derived by the maximum of the ΔG curve associated with a critical radius, $\frac{\partial \Delta G}{\partial r} = 0$, resulting in:

$$r^* = \frac{2\gamma_{\text{int}}}{\Delta G_v}. \tag{5.35}$$

Applying Equation 5.35 in Equation 5.33, $\Delta G^* = \Delta G(r^*)$, the free energy barrier, or nucleation activation energy, can be found:

$$\Delta G^* = -\frac{4}{3}\pi \left(\frac{2\gamma_{\text{int}}}{\Delta G_v}\right)^3 \Delta G_v + 4\pi \left(\frac{2\gamma_{\text{int}}}{\Delta G_v}\right)^2 \gamma_{\text{int}} = \frac{16\pi {\gamma_{\text{int}}}^3}{3\Delta G_v^2}. \tag{5.36}$$

As an initial step, the elastic contribution to the volumetric Gibbs free energy is disregarded.

To solve the critical radius analytically the interphase energy between α and β phases and the driving force is required. For this purpose, the quantified interphase energy derived in Section 4.1.3 was directly employed in Equation 5.33, while the driving force was numerically solved as shown in Figure 5.9. Figure 5.11 shows the plot of the net change in Gibbs energy and its volumetric and areal contributions for the β phase nucleation.

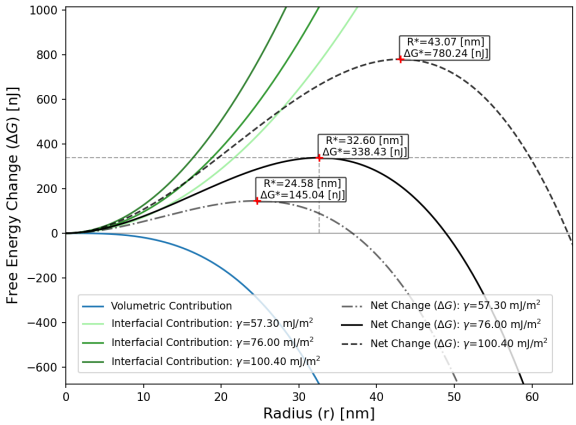

Figure 5.11: Analysis of the three-dimensional critical nuclei for the β phase precipitation from a supersaturated α matrix ($x_H^\alpha = 0.1$) considering the minimum, maximum and average value for the interphase energy quantified in Section 4.1.3.

For the assumed average value of the interphase energy of the 76 mJ m^{-2} and the supersaturated matrix α ($x_H^\alpha = 0.1$), the curvature radius of the critical nuclei of 32.6 nm is found. At the critical point, the volumetric and areal contributions are in an unstable equilibrium and any thermodynamic potential fluctuation within the material would induce a phase transformation. Suppose that the spherical β particle has a curvature radius smaller than the critical r^*. In that case, the interphase energy of the nuclei dominates and the system reduces its total free energy by the dissolution of the particle into the matrix. If $r > r^*$ the reduction of the system's energy is reduced by the growth of the β precipitate, which consumes the hydrogen content of the supersaturated α matrix until its equilibrium composition is reached and the driving force dissipated [173].

To validate these theoretical calculations, a two-dimensional analysis and simulation are suggested. Here, Equation 5.33, now accounting for a circular

particle within a two-dimensional area, is expressed as:

$$\Delta G = -\pi r^2 \Delta G_v + 2\pi r \gamma_{\text{int}}. \tag{5.37}$$

Differentiation of Equation 5.37 leads to:

$$r^* = \frac{\gamma_{\text{int}}}{\Delta G_v}, \tag{5.38}$$

and,

$$\Delta G^* = \frac{\pi \gamma_{\text{int}}^2}{\Delta G_v}. \tag{5.39}$$

The two-dimensional critical nuclei curvature radius is found as 16.3 nm. There is a simple factor of 2 between the three-dimensional and two-dimensional case, i.e. the critical radius of a two-dimensional nucleate is half that for the three-dimensional case. Figure 5.12 plots the full analysis for the two-dimensional case.

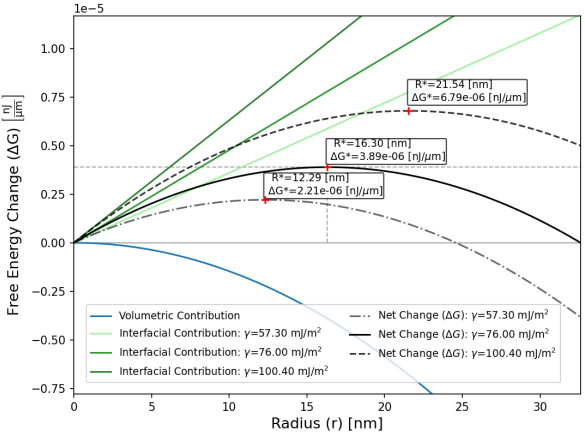

Figure 5.12: Analysis of the two-dimensional critical nuclei for the β phase precipitation from a supersaturated α matrix ($x_H^\alpha = 0.1$) considering the minimum, maximum and average value for the interphase energy quantified in Section 4.1.3.

As expected, the values for the critical radius are all half of those of the three-dimensional case, and the net change in energy is given per length.

For proof checking this concept a simulation of a supersaturated α with 0.1 hydrogen mole fraction containing an initial circular β phase particle with a radius smaller and bigger than the critical radius, 12.0 nm and 17.0 nm, respectively, was performed. For this simulation, the mesh adaptivity system that automatically refines or coarsens the mesh in regions of high or low estimated solution errors was applied to the η_β field variable, as implemented in MOOSE [58], with two cycles per step with a maximum h level of 2. Therefore, an overall initial mesh size of $\Delta x = \Delta y = 0.8$ nm was employed. Figure 5.13 illustrates the effect of mesh adaptivity after the interphase region is developed to its equilibrium profile.

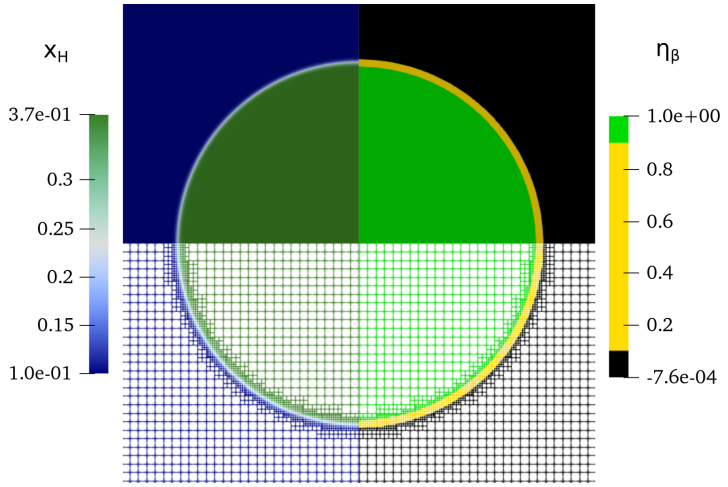

Figure 5.13: Illustration of the adapted mesh after the interphase region has developed its equilibrium profile on a two-dimensional simulation.

Afterwards these mesh adaptivity settings were used for simulations of the dissolution and growth of the particles 12.0 nm and 17.0 nm. The resulting simulations are shown in Figure 5.14.

From Figure 5.14 it is seen that for the initial particle size with r_0 =12.0 nm ($r_0 < r^*$) the particle starts shrinking, i.e. dissolves into the α matrix. As time passes, both the β particle and the α matrix become enriched in hydrogen. However, the overall composition of the simulation domain remains constant with negligible variations ($< 1 \times 10^{-8}$ mol H/µm^3). For this case, the β phase enriches in hydrogen to fulfill the imposition of the system having the same hydrogen chemical potential at the interphase, which comes from the KKS model. As shown in Figure 5.9, for an increasing supersaturation above ${}^{mt}x_H^\alpha$, the chemical potential of hydrogen in the α phase increases, i.e. $\frac{\partial^2 G^\alpha}{\partial x_H^2} > 0$, inducing the increase of hydrogen composition of the β phase,

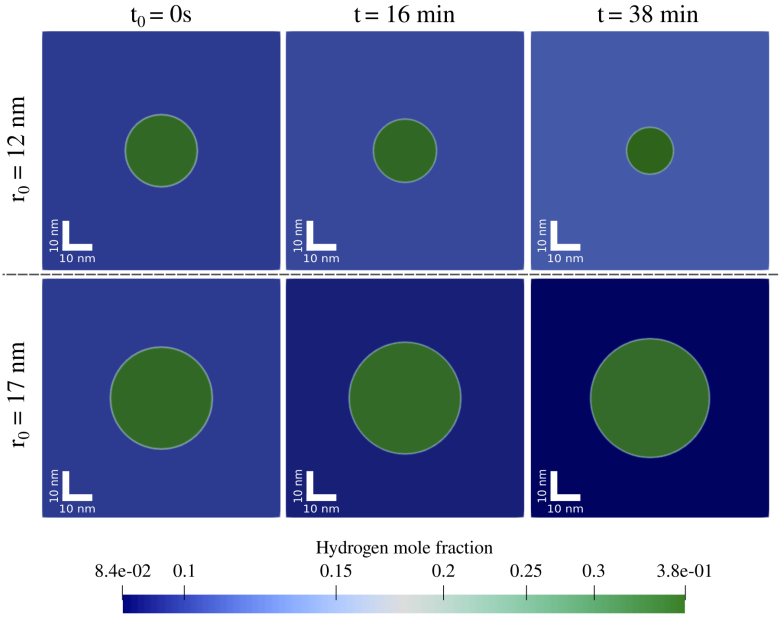

Figure 5.14: Simulation of two initial circular β phase particles within a α matrix with identical supersaturation state. The images use the same color range representing the hydrogen mole fraction in the simulation cell. The upper row illustrates the evolution in time for an initial particle with r =12.0 nm, while the bottom row shows the evolution of an initial particle with r =17.0 nm.

maintaining the correspondence in chemical potential. Even though for this simulation the driving force for the formation of β is increasing with time, the areal energy contribution dominates and a positive energetic feedback for the dissolution of the initial β particle perpetuates until the particle is completely dissolved. For an initial particle size with r_0 =17.0 nm ($r_0 > r^*$) the opposite occurs. As the critical curvature radius is greater than the critical one, the volumetric contribution is dominant, and the system reduces its free energy by growing the β phase fraction with the expense of reducing the supersaturation of the matrix. Both α and β phases compositions develop tending to reach their equilibrium compositions, ${}^{eq}x_H^{\alpha}$, and ${}^{eq}x_H^{\beta}$, respectively, at the steady-state, as shown it the bottom row of Figure 5.14.

5.2.3 Simulations of the FeTi alloy hydrogenantion

This section introduces a hydrogen flux ($\vec{J}_{\mathrm{H}}$) to the simulation domain, enabling the proper simulation of (de)hydrogenation processes.

The flux of hydrogen species in the Cahn-Hilliard equation, i.e. Equation 2.43, is given by:

$$\frac{\partial x_{\mathrm{H}}}{\partial t} = -\nabla \cdot \vec{J}_{\mathrm{H}}, \tag{5.40}$$

and

$$\vec{J}_{\mathrm{H}} = -M_{\mathrm{H}} \nabla \mu_{\mathrm{H}}. \tag{5.41}$$

The accumulation of the hydrogen species inside the domain Ω is given by the difference of the flowed species inwards and outwards Ω through its surface Γ. Since hydrogen is considered conserved, there is no production of extra species within the domain and therefore, the accumulation takes the form:

$$\frac{\partial x_{\mathrm{H}}}{\partial t} = -\oint_{\Gamma} \vec{J}_{\mathrm{H}} \cdot \hat{n}, \tag{5.42}$$

Note that Equation 5.42 describes the boundary condition shown in Equation C.19. Therefore, a hydrogen flux can be induced into the system if a chemical potential gradient is applied to part or the totality of Γ.

The Gibbs energy expression of the H_2 gas, as shown in Figure 5.15, may be used to quantify the variation of the chemical potential associated with an external hydrogen partial pressure applied to the system's boundaries.

With the Maxwell relation derived from the Gibbs energy, the volume can be expressed from:

$$V = \left(\frac{\partial G}{\partial P} \right)_T. \tag{5.43}$$

Using Equation 5.43, the Gibbs energy density (g) may be acquired by:

$$g = \frac{G}{V} = \frac{G}{\left(\frac{\partial G}{\partial P} \right)_T}. \tag{5.44}$$

Figure 5.16 compares the Gibbs energy density resulting from the ideal and Joubert's [13] models for the H_2 gas.

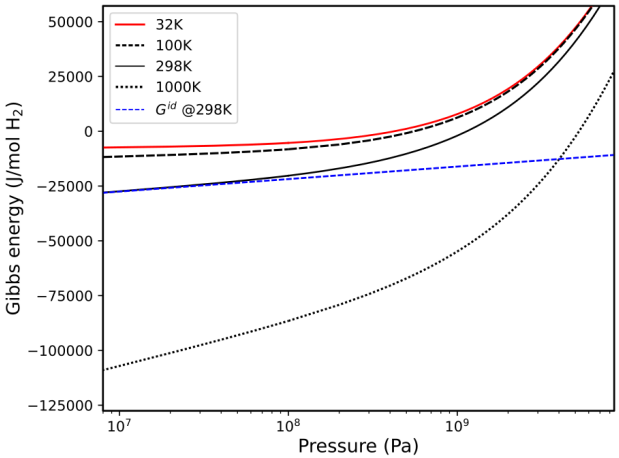

Figure 5.15: H_2 gas Gibbs energy over pressure at different temperatures compared to its ideal model (G^{id}) at room temperature 298 K.

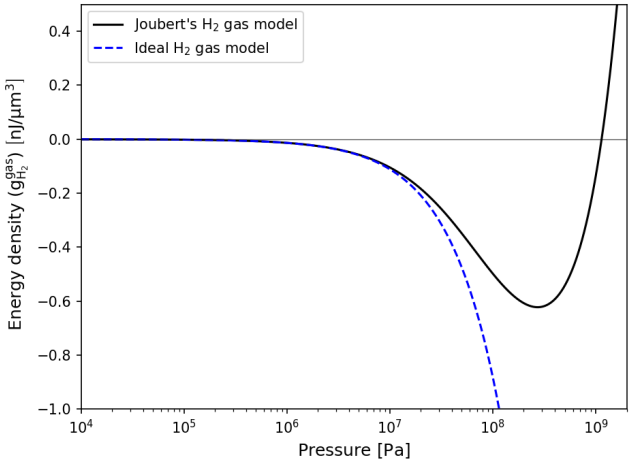

Figure 5.16: Gibbs energy density as a function of pressure using the ideal model (G^{id}) and Joubert's model for the H_2 gas at 298.15 K.

As the energy density deviates negligibly from the idea model at pressures below 1×10^7 Pa, the ideal model is employed to derive the following thermodynamic relations. As follows, applying Equation 5.44, the expression of the molar volume of the pure H_2 gas (${V_m}^{\mathrm{gas}}_{\mathrm{H_2}}$) is given by:

$$ {V_m}^{\mathrm{gas}}_{\mathrm{H_2}} = \left(\frac{\partial G^{\mathrm{gas}}_{\mathrm{H_2}}}{\partial P} \right)_T = \left(\frac{\partial \left(G^{\mathrm{gas}}_{\mathrm{H_2}} + RT \ln \frac{P}{P_0} \right)}{\partial P} \right)_T = \frac{RT}{P} \tag{5.45} $$

The Gibbs energy density of the H_2 gas ($g^{\mathrm{gas}}_{\mathrm{H_2}}$) is consequently obtained by dividing the H_2 end-member term of Equation 3.33 (expression for the pure H_2 gas) by Equation 5.45:

$$ g^{\mathrm{gas}}_{\mathrm{H_2}} = \frac{P\ G^{\mathrm{gas}}_{\mathrm{H_2}}}{RT} + P \ln\left(\frac{P}{P_0} \right) \tag{5.46} $$

.

Considering that the current system's temperature (T) and pressure (P) define the reference H_2 gas energy density state (${}^1g^{\mathrm{gas}}_{\mathrm{H_2}}$) and that a surplus of hydrogen partial pressure (P_s) is applied externally onto the system causing an over potential (${}^2g^{\mathrm{gas}}_{\mathrm{H_2}}$), the variation of the Gibbs energy density of hydrogen toward the solid is given by $\Delta g^{\mathrm{gas}}_{\mathrm{H_2}} = {}^1g^{\mathrm{gas}}_{\mathrm{H_2}} - {}^2g^{\mathrm{gas}}_{\mathrm{H_2}}$, and expressed by:

$$ \Delta g^{\mathrm{gas}}_{\mathrm{H_2}} = (P - P_s) \left[\frac{{}^0G^{\mathrm{gas}}_{\mathrm{H_2}}}{RT} - \ln P_0 \right] - P_s \ln(P_s) + P \ln(P) \tag{5.47} $$

Note that $\mathrm{Pa} \equiv \mathrm{J\,m^{-3}}$, and as expected, the pressure overpotential translates directly into a variation of the chemical potential.

Figure 5.17 shows the relationship between the surplus hydrogen partial pressure applied to the system and the associated variation of hydrogen chemical potential expected at the boundary.

Figure 5.17 identifies an external pressure for a given system and retrieves information on the H_2 chemical potential variation at the boundaries. In essence, the combination of Equation 5.47 and Equation 5.42 gives a quantitative perspective to track how an external hydrogen partial pressure applied to the boundaries of the simulation domain induces an over potential and consequently a hydrogen flux within the system. If $P_s = P$, the variation of hydrogen chemical potential $\Delta\mu_H = 0$, and no hydrogen flux is induced. However, if $P_s > P \therefore \Delta\mu_H > 0$, an induced hydrogen flux inwards the Ω simulation domain exists, and vice versa.

Figure 5.18 shows the simulation of the FeTi metal-hydride system when a surplus of pressure, i.e., $\Delta P = P_s - P$, of approximately 50 Pa, yielding

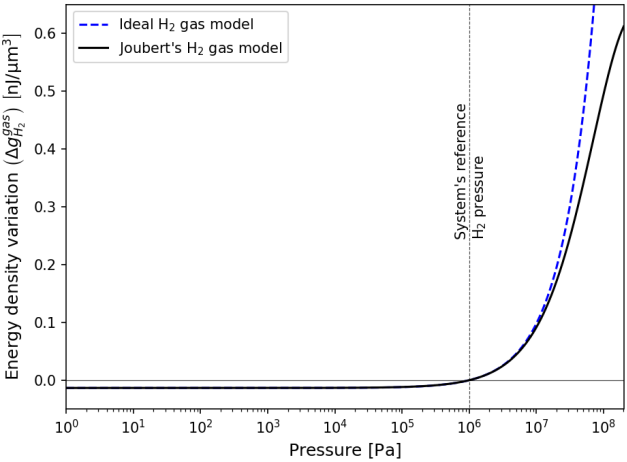

Figure 5.17: Gibbs energy density variation as a function of surplus hydrogen partial pressure considering that the system is at 310 K and 997 091 Pa. The solid black line and the dashed blue line represent the energy density variation using Joubert's model and the ideal model for the H_2 gas.

a variation of Gibbs energy density of 5×10^{-7} nJ µm^{-3}, is applied to the boundary in contact with an initial β hydride phase.

Note that an induced flux into the simulation domain exists just with an extremely low-pressure variation. This is possible because the system is internally in para-equilibrium, and any perturbation on the chemical potential acting on the α or β phase is sufficient to induce the system to develop. The volumetric β phase fraction is calculated at each step by

$$\eta_\beta^t = \frac{1}{V} \int_\Omega (\eta_\beta)\, \mathrm{d}\Omega, \tag{5.48}$$

and hydrogen mole fraction by

$$x_H^t = \frac{1}{V} \int_\Omega (x_H)\, \mathrm{d}\Omega. \tag{5.49}$$

Figure 5.19 shows the resulting evolution of these fractions during simulation of the induced flux, and illustrates the evolution of the β phase fraction and hydrogen mole fraction when submitted to a differential pressure of 50 Pa.

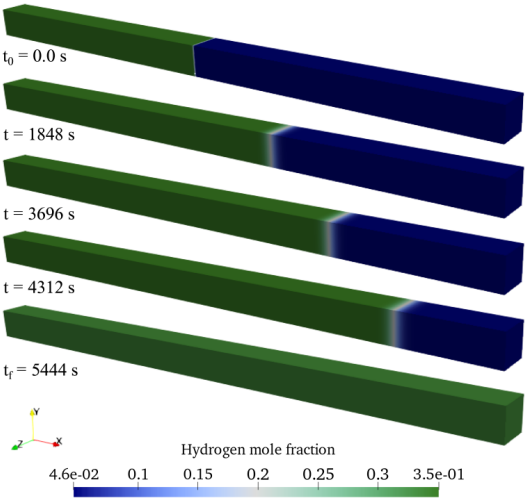

Figure 5.18: Simulation of the hydrogenation of the FeTi alloy with a surplus hydrogen partial pressure of $\Delta P = 500\,\text{Pa}$ at 310 K. The initial state of the system comprises a $\alpha - \beta - H_2$ equilibrium under 310 K and 997 091 Pa. The simulation progresses until the β phase dominates to the detriment of a α phase fraction reduction.

This opens up a crucial path for understanding the hydrogenation process kinetics in response to the applied pressure. The data provided allows for an assessment of the stability and performance of the material under these particular conditions, quantitatively reflecting the engineering variables associated with the application of the FeTi alloy for hydrogenation processes. A similar concept of overpotential-induced hydrogenation simulation developed in this section could be used in larger-scale simulation to compute PCI curves under dynamic conditions.

5.2.4 Simulations of spinodal decomposition of the β phase

The thermodynamic model of phase β developed in this work describes a miscibility gap that concerns the decomposition of phase β into two different phases named β_1 and β_2 with different hydrogen composition if the temperature is kept below a certain critical temperature (T_c). For these temperatures, the Gibbs energy of the β phase assumes a double well-shaped curve

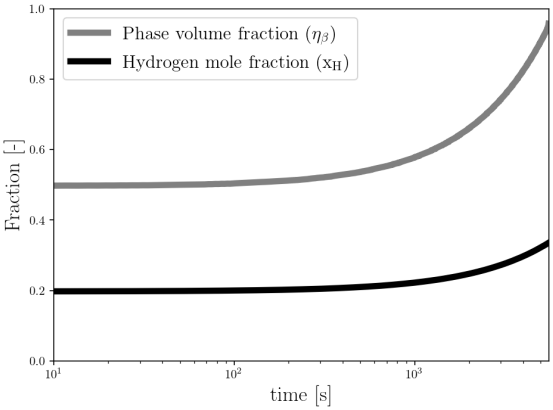

Figure 5.19: Simulation of the β phase fraction and hydrogen mole fraction evolution due to a surplus hydrogen partial pressure of $\Delta P = 50\,\text{Pa}$ at 310 K.

(see Figures 5.1 and 5.9 for instance). This characteristic is expressed within the equilibrium phase diagram of the temperature composition of the FeTi-H system, as shown in Figure 5.20, more specifically within the β phase region. Under these conditions, the phase is split into two determined equilibrium lines representing the internal equilibrium of the β phase, or in other words, the compositions at which the hydrogen chemical potential equalizes within the β phase itself.

Spinodal decomposition is a spontaneous kinetic phenomenon correlated with these thermodynamic features. It consists of the amplification of a natural compositional fluctuations within a homogeneous phase. Such transformation is generally observed when materials are subjected to quenching. As fluctuations of thermodynamic potentials are practically impossible to prevent, a homogeneous phase annealed within a miscibility gap becomes unstable regarding phase separation and decomposes into two different stable compositional regions.

A brief analysis of the miscibility gap within the β phase with respect to temperature is illustrated in Figure 5.21 a), and b). Figure 5.21 a) demonstrates that at internal thermodynamic equilibrium below 324 K, the phase β is more stable if it is decomposed into the phases β_1 and β_2. The stable fractions of each phase depend on temperature and composition and tend to be more pronounced as the temperature decreases. Figure 5.21 b) shows the equilibrium fraction of the spinodally decomposed β_1 and β_2 phases as a function of temperature for the nominal composition of 0.41 hydrogen mole fraction (correspondent to the composition value of T_c). The compositions of both β phases are stabilized with two distinct composition sets. The β_1 has a

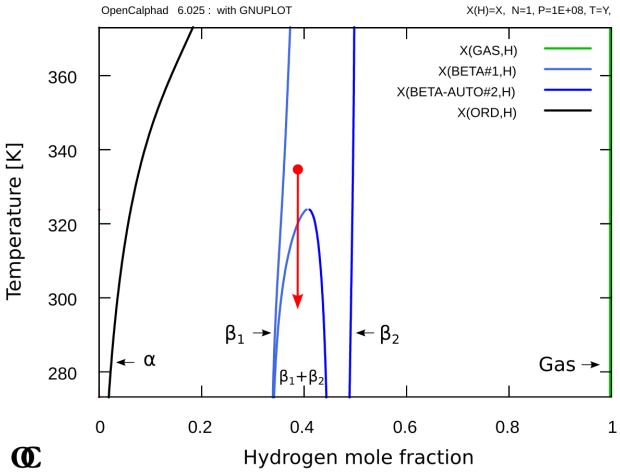

Figure 5.20: Calculated temperature-composition paraequilibrium phase diagram of the FeTi-H system. The red arrow indicates the simulation proposed in this section

lower solubility limit for hydrogen and tends to its stoichiometric composition (FeTiH) at low temperatures. The β_2 phase exhibits a higher concentration of hydrogen, and approaches the composition of the $(FeTi)_2H_3$ compound, with levels of hydrogen mole fraction around 0.43. Note that only the phase fractions of β_1 and β_2 are dependent on both temperature and composition; the internal equilibrium composition of these phases is only dependent on temperature. The simulation of such spinodal decomposition is proposed and shown in Figure 5.22. The simulation may be viewed as the quenching of a hydrogenated FeTi alloy with a hydrogen fraction of $x_H = 0.39$ from a temperature above T_c, which would consist of a homogeneous phase β, to 300 K, which is below T_c. This process is shown with a red arrow superimposed on the temperature-composition equilibrium phase diagram in Figure 5.20.

For this simulation, the domain was initiated with a random distribution of the hydrogen composition within the miscibility gap between $x_H = 0.35$ and $x_H = 0.43$. Periodic boundary conditions were applied to all of the two-dimensional 100 nm x 100 nm simulation domain. The adaptive mesh was not enforced and the finite elements were defined with $\Delta x = \Delta y = 0.667$ nm.

Figure 5.22 shows that maintaining the kinetic parameters for diffusion in the α phase, a clear spinodally decomposed two-phase microstructure is

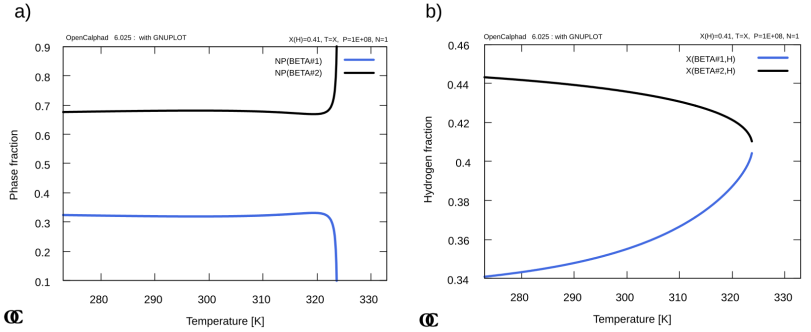

Figure 5.21: Analysis of the thermodynamics of β phase spinodal decomposition for the nominal composition of 0.41 hydrogen mole fraction over temperature. a) evolution of the β_1 and β_2 hydrogen content; b) evolution of phase fraction of the β_1 and β_2 phases

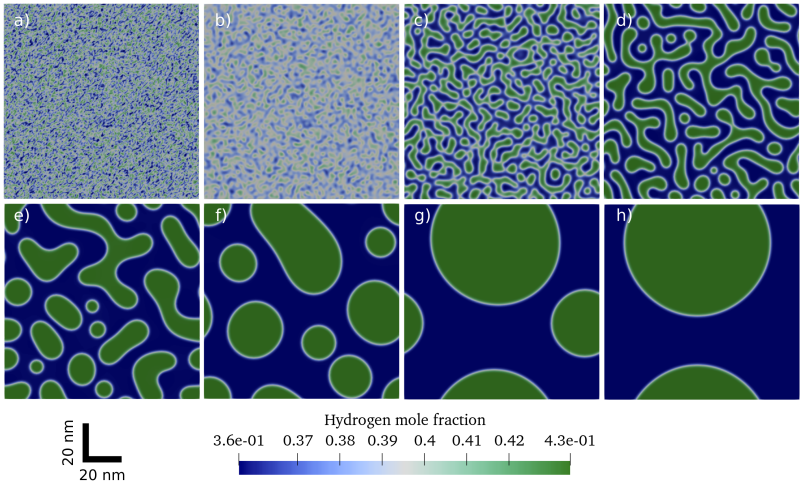

Figure 5.22: Snapshots of the simulation of the β phase spinodal decomposition at 300 K. a) 0.000s or initial state; b) 0.001s; c) 0.050s; d) 0.500s; e) 5.000s; f) 50.000s; g) 500.000s; and h) 5000.000s or steady state.

obtained in fractions of seconds. Moreover, the compositions of the β_1 and β_2 phase regions were the same as that calculated at 300 K in Figure 5.20, further confirming that the Gibbs energy for the β phase is well implemented

within the phase field model.

The potential benefit of using this β phase model with a miscibility gap in practical applications consists of the possibility of capturing limiting or threshold levels of combined external engineering thermodynamic potentials (e.g. temperature, pressure and strain) that trigger the formation of the β_2 phase. As discussed in Section 3.2.5, the β_2 phase may be interpreted as a precursor metastable phase from which the γ phase nucleates. Because the γ phase is potentially a more stable phase within the FeTi-H system, it could be the reason for the observed trapped hydrogen within the material, which decreases its potential as a reversible hydrogen storage material. Thus, this model potentially allows for understanding the thermodynamic conditions that can prevent the phases detrimental to the alloy's reversible properties and may indicate operational parameters that promote the full hydrogenation reversibility for hydrogen storage applications.

5.2.5 Simulations of coupled micromechanics for phase transformation

This section presents examples of the coupling of micromechanics with phase transformation demonstrated in Section 2.4.3 and Section 4.2.2. For an initial circular embedding of β particles in a matrix α in the $x - y$ Cartesian plane, the function $B(\vec{n})$ for the full coherence case produces a habit plane perpendicular to $[0\,1\,0]$ (see Figure 4.9 for reference) as shown in Figure 5.23.

Figure 5.23 shows that the minimum elastic energy represented by the vector n_0 occurs in the $[1\,0\,0]_\beta$ direction. Consequently, as discussed in more detail in Section 4.2.2, the expected habit plane that would evolve during a simulation along the plane $(0\,0\,1)_\beta$ should be perpendicular to the n_0 direction, i.e. the plane $(1\,0\,0)_\beta$.

As a preliminary validation, a simulation adhering to these parameters is suggested. In this simulation, a two-dimensional domain Ω with dimensions of 200x200 nm in the $x - y$ plane was constructed. As initial conditions, a circular particle β with a radius of 25 nm is centralized in Ω. Unlike previous simulations, the temperature was set at 333 K to avoid the occasional first-order thermodynamic transition of β into the β_2 phase. The pressure was set following the calculated plateau pressure for this temperature condition, as seen in Figure 3.20. Zero Dirichlet boundary conditions were enforced for all displacement variables perpendicular to the boundaries of Ω, i.e., no volumetric change of Ω was ensured. Both the time step and mesh adaptive were employed. Figure 5.24 shows the resulting simulation.

As the β phase is formed causing a high volumetric expansion, enforcing constrained displacement at the boundaries should effectively play against the dissipation of the associated elastic energy, inducing the β phase to dissolve into the matrix. In Figure 5.24 it can be quantitatively observed that the α matrix increases in hydrogen content and consequently the volume fraction of β decreases, as indicated at least qualitatively.

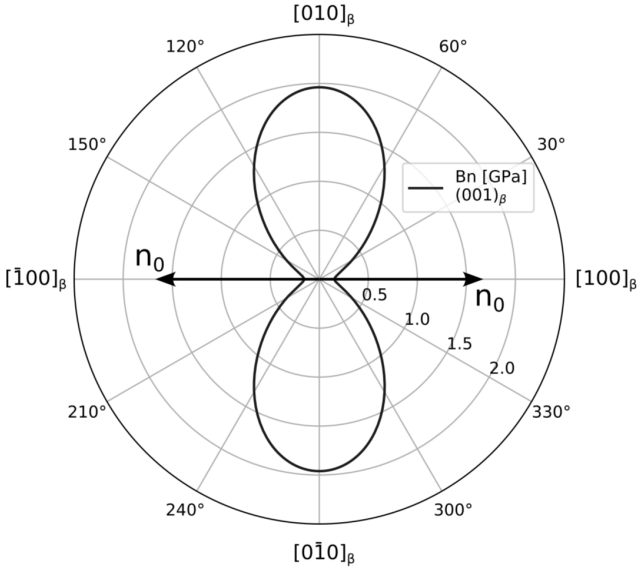

Figure 5.23: Polar plot of the $B(\vec{n})$ function calculated on the $(0\,0\,1)_\beta$ plane. Black arrows represent the direction that minimizes the function $(B(\vec{n}_0))$ in the $x-y$ Cartesian plane.

Moreover, the particle evolves in a transient transformation that approaches the minimization of the free energy of the system composed of the Gibbs energy densities of the phases, the homogeneous chemical contribution to the interphase energy, and the elastic energy. The only inhomogeneous property associated with the free energy of the simulation cell is the elastic energy and, therefore, is the only contribution that causes the variation of the morphology of the β particle.

In this two-dimensional simulation on the $x-y$ plane, the phase field simulation confirms the prediction of the micromechanic analysis as the β particle evolves following the habit plane $(1\,0\,0)_\beta$ predicted in Figure 5.24.

To demonstrate a three-dimensional visualization, Figure 5.25 presents the initial stage of a spherical particle within a α phase matrix after the very resolved first step of $t \approx 1\times10^{-6}$ s. The volume of the simulation domain Ω was set with dimensions of 200x200x200 nm in the $x-y-z$ Cartesian coordinates. Volume variation was constrained by imposing constant (Dirichlet) zero displacement boundary conditions to displacement variables perpendicular to

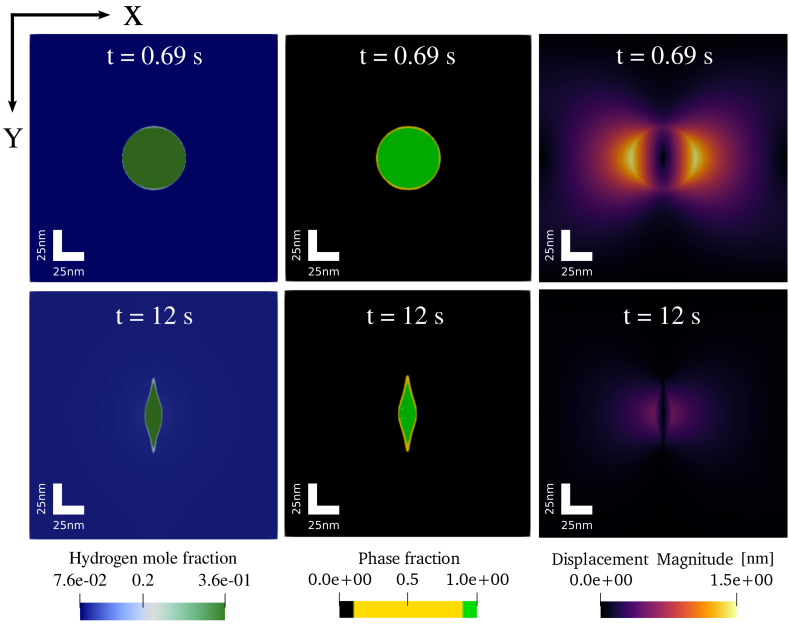

Figure 5.24: Simulation of a circular β particle on the $x-y$ plane for constrained boundary displacement. Top row: simulation stage at 0.69 s; bottom row: simulation stage after 12 s.

the surface boundary plane. The effects of the stress-free transformation strain presented in Section 4.2.2 can be observed in Figure 5.25.

In Figure 5.25 a) it is evident that the highest displacement magnitude occurs along the x direction. A better quantitative visualization of displacement in the Cartesian sections $x-z$, $y-z$, and $x-y$ illustrated in Figure 5.25 is shown in Figure 5.26 a), b) and c), respectively.

Note that the $x-z$ plane presents the lowest maximal displacement value, while displacements develop at its minimum along the z direction. The displacement along x is clearly dominant. Furthermore, the magnitude of displacement is a directly proportional function of the precipitate fraction within Ω and is expected to be more intense for a larger volume of precipitate β.

Figure 5.27 illustrates the monitored morphological evolution of the initial circular precipitate across the three orthogonal planes depicted in Figure 5.26 through a two-dimensional computer simulation. These simulations were conducted by rotating the material properties of the system relative to the

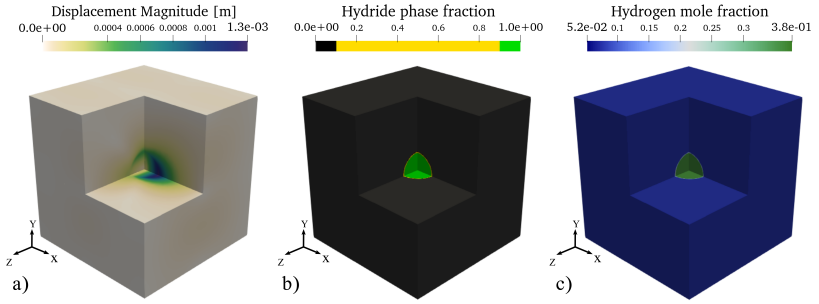

Figure 5.25: First resolved step of a volumetric simulation of an initial spherical β particle within a α matrix. a) displacement magnitude in µm; b) order parameter η_β, representing the phase fraction of β; c) hydrogen mole fraction.

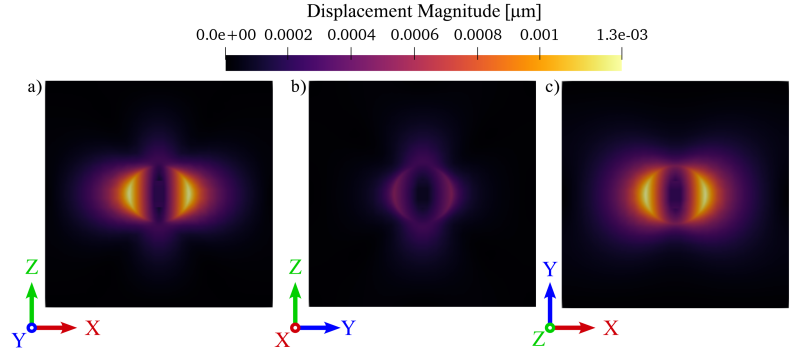

Figure 5.26: Displacement magnitude on the plane sections. a) $x-z$, b) $y-z$, and c) $x-y$.

fixed Cartesian space $x-y-z$. Specifically, the elasticity stiffness tensors $\mathbb{C}^{\alpha}_{ijkl}$ and $\mathbb{C}^{\beta}_{ijkl}$, together with the stress-free transformation strain ϵ^{SFTS}_{ij}, were adjusted so that the $x-y$ plane was reoriented to align with $x-z$ and $y-z$, as demonstrated in Figure 5.27 a) and Figure 5.27 b).

A principal characteristic of the morphological evolution, as illustrated in Figure 5.27, is that for any simulation involving the x axis, the particle tends to elongate, aligning its morphology following the habit plane $(1\,0\,0)_\beta$. As the inhomogeneous elasticity of the α and β phase is not so pronounced, the elevated value of the stress-free strain ε_{11} (see Equation 4.38 for reference) can be interpreted as the predominant factor influencing the phase morphol-

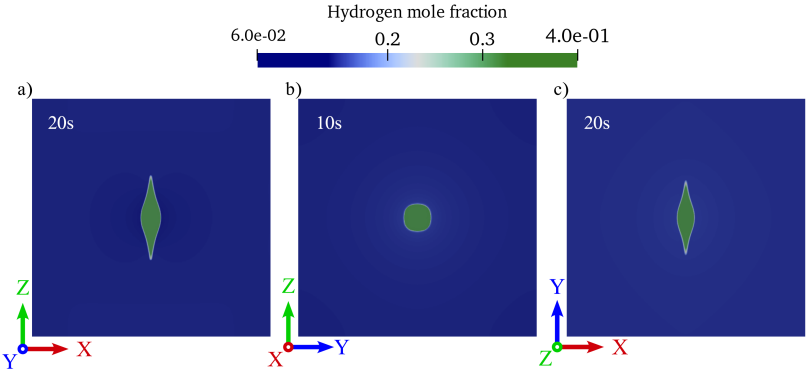

Figure 5.27: Evolved hydrogen mole fraction for all the Cartesian planes. a) In $x-z$ after 20 s, b) In $y-z$ after 10 s , and c) In $x-y$ after 20 s.

ogy evolution. In contrast to these planes, the morphology of the particle simulated along the $y-z$ plane manifests distinct morphology, with the β precipitate transitioning from a circular to a more squared configuration, and no preferential direction is observed. The simulation result indicates that a three-dimensional phase-field simulation would produce an almost plate-shaped β phase. It is worth mentioning that the simulation performed along the $y-z$ presented faster kinetics for the precipitate dissolution in the α matrix and was completely dissolved already after 20 s physical time. In contrast, along the $x-z$ and $x-y$ planes, the precipitate continued to develop its morphology at this point. However, in all cases, the precipitate was fully dissolved by the end of each simulation.

6 Summary and Outlook

This chapter summarizes the dissertation and outlines potential directions for further development of the presented findings and models.

6.1 Summary of the dissertation

In this doctoral thesis, a quantitative-based phase-field model for the simulation of the hydrogenation of a two-phase FeTi-H system is developed. The model comprises integrated multi-physical properties of the solid and gas phases obtained in their majority from theoretical quantum mechanical calculations and by computational thermodynamic assessments informed by a mix of theoretical analysis and experimental measurements. The major contributions of this work are as follows.

1. DFT settings that ensure precise computational determination of various properties of crystal structures within the FeTi-H system, along with their emergent characteristics — such as lattice parameters, equilibrium bulk volume, elastic constants, activation energy barrier for hydrogen diffusion, formation and reaction energies, interfacial energy, and surface energies — have been identified.
2. The comprehensive thermodynamic model of the FeTi-H system was successfully developed. The computation of the bulk phase equilibria accurately yields solubility limits and invariants of phase transformation in the full operational temperature and hydrogen pressure ranges. The comprehension of equilibrium types and their correlation with structural variants of hydride phases within the system has been significantly enhanced. Furthermore, the thermodynamic model assessed in this work employs the state of the art model for H_2 gas, and is analytically congruent with existing models for the equimolar body-centred cubic phase in the Fe-Ti system. This congruence facilitates near-seamless integration into the comprehensive Fe-Ti-H system and allows for its extension to other multi-component systems.
3. A new generalizable approach for analysing the interphase properties between metal-hydride systems is developed. The framework not only

reduces the computational demand for quantifying interfaces, but also combines these accurate DFT calculated properties with fundamental thermodynamics of surfaces and interfaces and micromechanical analysis. The framework was applied to the FeTi-H system, from which several outcomes were obtained: surface energies of the hydrides were quantitatively calculated, demonstrating that the hydrogenation of the metal and hydride surfaces is stabilized when capped with hydrogen. The interplay between chemical and coherency elastic strain energy contributions of the metal-hydride interfacial energy was demonstrated showing that a coherent, mixed coherent state governs the morphology of FeTiH-β precipitates in an homogeneous FeTi-α matrix.

4. A quantitative-based phase field model for the FeTi-H system was developed. The model properly incorporates realistic thermodynamic functionals assessed with Calphad method, as well as the chemical and inhomogeneous elastic strain energy of the interface. The hydrogen mobility is combined with the structural and chemical parameters allowing for a realistic temporal simulation of the diffusion-controlled phase transformations. Furthermore, a rigorously quantitative approach was demonstrated for hydrogen flux induced by overpotential, predicated on the variation in Gibbs energy density of H_2 gas as a boundary condition. This methodology allows for precise control of temporal dependencies related to hydrogen gas temperature and pressure, relevant to practical usage scenarios. Ultimately, all elastic anisotropic effects arising from the integrated chemo-mechanical interactions between the FeTi-α and FeTiH-β phases were meticulously incorporated into the model. These effects were rigorously validated through fundamental simulations to ascertain the robustness of the integrated model parameters against theoretical predictions.

6.2 Future perspectives

Further proposed investigations based on the current model

The present doctoral work provides a general multi-scale computational approach for quantitatively modeling microstructure evolution in inhomogeneous metal-hydride systems, which was primarily applied to the FeTi-H system. The developed phase-field model includes accurate fundamental quantitative properties and sets the basis for further comprehensive improvement of the FeTi hydrogenation model. The provided model may already be employed to investigate several phenomena, which is listed below as an indication of the future simulations capable of supporting answering interesting scientific questions:

1. Identify the effect of arbitrary applied strain onto the system on the kinetics of hydrogenation and dehydrogenation. These can be inferred,

for instance by the kinetics of the hydride phase formation and dissolution, respectively.

2. Identify the directionality of the strain and stresses resulting from the formation of the hydrides and their effect on the kinetics of multiple precipitates interactions in monocrystal α matrix.
3. Assess the variation of hydrogen energy density associated with variations in temperature and hydrogen partial pressure necessary to hydrogenate the system when mechanics are involved. This analysis would elucidate the contribution of mircromechanics of the precipitates on the hysteresis effect observed in experimental PCI curves, allowing for a better comprehension of the operational conditions for hydrogenation.
4. Simulate the hydrogenation properties under several time-dependent thermodynamic conditions in order to identify mechanisms that could lead the β phase to transform into β_2

Further proposed extension of the current model

The efforts for further improving the provided model can be distinguished in two main categories, those related to the expansion for multi-chemical dependencies, and those related to multi-structural dependencies.

Among others, the following list indicates the key next steps to further develop the model in relation to the chemical dependencies:

1. The thermodynamic model of the FeTi-H system isoplethal section can be incorporated into the full ternary Fe-Ti-H system. The end-members thermodynamic model parameters arising from the expansion of the FeTi-H models into the Fe-Ti-H system can be evaluated from DFT calculations.
2. Evaluate the mobility of metallic elements within all the phases of the system. The assessed mobilities, in its best, would comprise structure, temperature, and chemical dependencies. These dependencies would allow not only for simulating local segregation of the metallic atoms and their impact on the hydrogenation of the FeTi-H system but also help on evaluating the degradation of the material during its long-term application. This analysis would be possible, for example, by simulating the disproportionation of the hydride into other intermetallic phases, e.g. the C14 Laves phase and titanium hydride that are more stable than the ternary hydrides. As FeTi primary potential application is related to stationary storage, evaluating the disproportionation of the material is highly desired.
3. Expand the thermodynamic model of the phases to include new elements of interest. The expansion of the thermodynamic models for multi-component systems is crucial for evaluating the influence of new elements on the thermo-kinetic properties of hydrogenation. A multi-component thermodynamic model is essential for studying, for example, the feasibility of using recycled materials and raw materials with

lower purity for hydrogen storage application. Furthermore, these assessments could be used for computational high-throughput (at its best with use of machine learning algorithms) to optimize compositions that provide best thermodynamic properties for reversible hydrogenation.

When it comes to structural improvements, the following list could be explored:

1. The phase-field model can be expanded to comprise muitiple precipitate orientations. This is achieved by including multiple order parameters for each crystiline orientation of the β phase. This could improve the simulation of the precipitation interaction and the influence of the inhomogeneous elasticity emerging from the interaction of these precipitates with themselves and the matrix α.
2. The phase-field model can be expanded to comprise polycrystalline α matrix. This can be achieved by including new set of order parameters for the α phase related to its crystalline orientation in the simulation domain. To accomplish this, the inhomogeneous elasticity model for the matrix should be rotated accordingly, and the interfacial energy between the grains should be quantitatively characterized, possibly with DFT. This model can then be applied to study the coarsening kinetics of precipitates in the presence of grain boundaries. The elastic fields generated by grain boundaries would affect diffusion kinetics. The grain boundary density would have a net contribution on the diffusion-controled processes, thereby affecting the hydrogenation kinetics. In addition, the ripening kinetics between precipitates across the grain boundary can be investigated, and the precipitate evolution kinetics of multiple precipitates in polycrystals can be studied.

Appendices

A Quantum Mechanics

A.1 Investigation of DFT settings

For the DFT settings analysis, the basic exchange-correlation functionals `PW91`, `PBE`, and `PBESol` were employed. To address the possible strong electronic correlations of the localized orbitals, an on-site Hubbard U correction [174, 175, 176] was included as an additional parameter for each of these basic functionals. For the Hubbard analysis, U values were set to 4.0 eV for Ti and 4.3 eV for Fe. Additionally, long-range dispersive (van der Waals) interactions for `PBE` and `PBESol` were also explored by incorporating the DFT-D3 correction method with Becke-Johnson damping [177, 178].

As a first step, the DFT settings were converged over **k**-point spacing. For this purpose, an initial `ENCUT=700` was employed, and the values of **k**-point spacing were varied using values of 0.5, 0.4, 0.3, 0.2, 0.15, 0.1, 0.08, and 0.06. The optimal value for **k**-point spacing was selected as that less refined value performing with a variation not exceeding 0.001 eV/atom in comparison with that of the most refined calculation using `kspacing = 0.06`). Ultimately, the optimal value was found as `kspacing = 0.2`.

Subsequently, the selected **k**-point spacing was maintained throughout all calculations while scanning the `ENCUT` value from 250 eV to 700 eV with steps of 50 eV. An additional value of `ENCUT=520` was also tested for comparison with the literature, which often uses this value as a standard. Figure A.1 and Figure A.2 illustrate the results for the cubic α and orthorhombic β phases, respectively.

As shown in Figure A.1 and Figure A.2, the value of `ENCUT=500` is demonstrated to be sufficient to produce a negligible variation with respect to the most refined run using `ENCUT=700`. This value was therefore kept constant throughout all the calculations in this study.

For each exchange-correlation functional used in this study, the energy vs. volume variation data points were fitted to the Birch–Murnaghan equation of state. The cell shape and ion positions were relaxed for each selected volume of the α and β compounds, employing `ISIF=4` within VASP for this purpose. The equilibrium volumes (V_0) of the compounds were determined by minimizing the fitted Birch–Murnaghan curve. Based on these equilib-

rium volumes, the compounds were generated, and additional DFT runs were performed with refined settings for energy convergence, with residual atomic forces less than 5×10^{-6} eV·Å^{-1} and energy tolerance of 1×10^{-8} eV.

In addition, the bulk moduli (B_0) and their derivatives with respect to pressure ($\partial B_0/\partial P$) are determined using the fitted Birch–Murnaghan curve. The comparison of the performance of each exchange-correlation functional employed in this study to calculate the bulk properties of the compounds α and β is presented in Figures A.3 and A.4, respectively. These figures include a comparison with experimental data from the literature.

Based on the analysis of the bulk properties presented in Figures A.3 and A.4, three DFT settings to further investigate the synergetic properties between the α and β phases were selected. The choice of `PW91`, `PBE`, and `PBESol + U` was made because, in the ground state, the volume of the compounds should be smaller and their moduli are expected to be higher than those measured under room conditions. Table A.1 displays the lattice parameters resulting from the bulk optimization using these DFT settings.

Table A.1: Calculated lattice parameters for the cubic, and tetrahedral α, and orthorhombic β phases using different DFT settings. The superscripts ^{c}, ^{t}, and ^{o}, refer to the cubic, tetrahedral, and orthorhombic lattice parameters, respectively.

XC-functional	a^c_α [Å]	a^t_α [Å]	c^t_α [Å]	a^o_β [Å]	b^o_β [Å]	c^o_β [Å]
`PW91`	2.953	4.176	2.953	4.559	4.264	2.903
`PBE`	2.954	4.179	2.954	4.543	4.271	2.918
`PBESol + U`	2.968	4.197	2.968	4.569	4.235	2.932

The ground state energy of the H_2 molecule was calculated using the same settings and utilized to calculate the reaction energy of hydrogen absorption in the ground state. The results are shown in Table A.2

Table A.2: Calculated energy of absorption (ΔE_{abs} [kJ/mol.H_2]) using different exchange-correlation functionals.

XC-functional	ΔE_{abs} kJ/mol.H_2
`PW91`	−24.9
`PBE`	−20.9
`PBESol + U`	−17.8

The computed value of ΔE_{abs} with `PW91` is found as -24.94 mol.H_2. This value falls within the range of the reaction enthalpy for the formation of β hydrides during FeTi hydrogen absorption, which is reported between -22.8 and -27.4 kJ/mol.H_2 as summarized by Dematteis *et al.* [35]. These

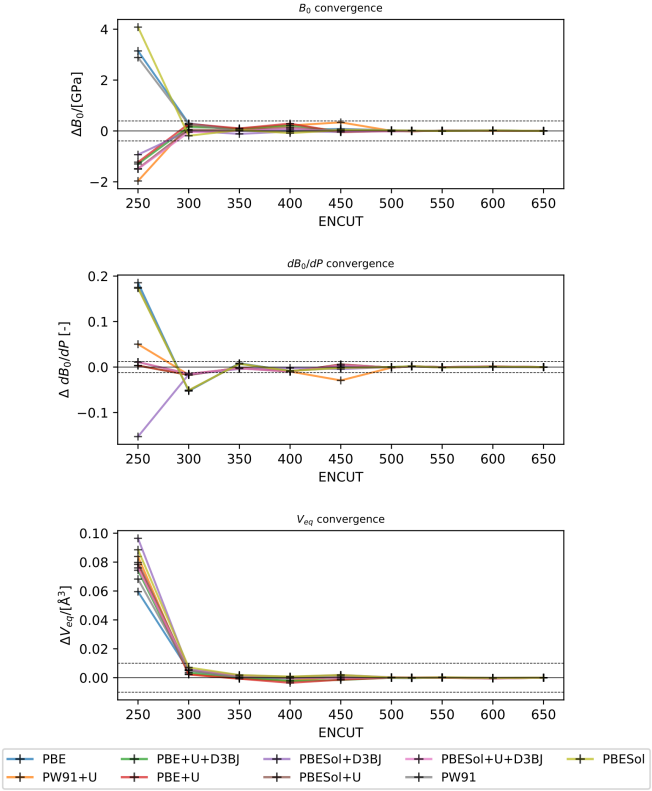

Figure A.1: ENCUT value convergence test performed for the cubic α phase with respect to a refined run of `ENCUT=700` and `kspacing = 0.2`.

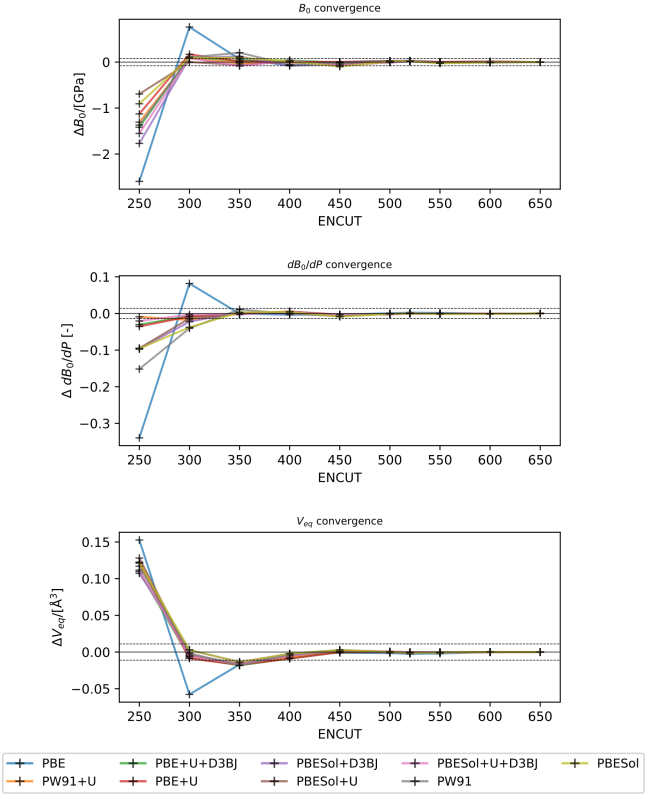

Figure A.2: ENCUT value convergence test performed for the orthorhombic β phase with respect to a refined run of `ENCUT=700` and `kspacing = 0.2`.

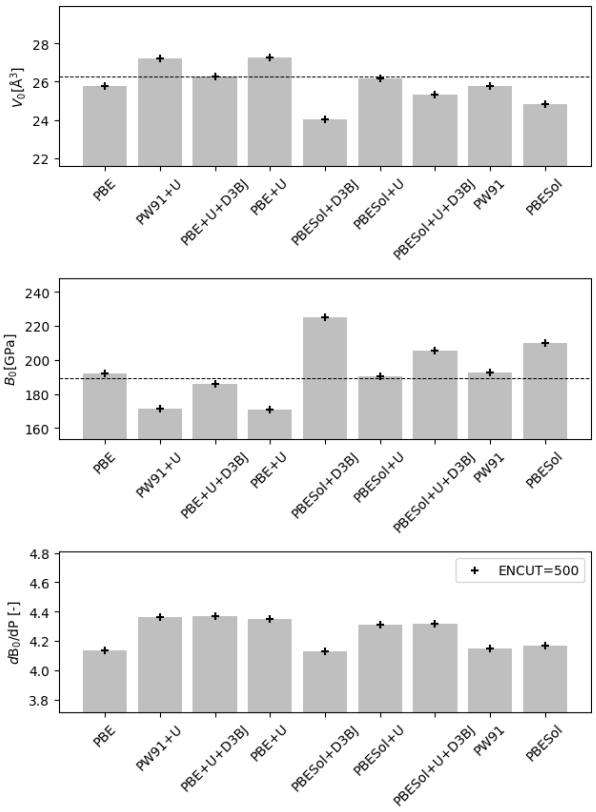

Figure A.3: Equilibrium volume (V_0 Å^3), bulk modulus (B_0 [GPa]) and its partial derivative in respect to pressure ($\partial B_0/\partial P$ [-]) using different DFT exchange-correlation functional for the cubic α phase. The dashed lines correspond to experimental values from the literature [145].

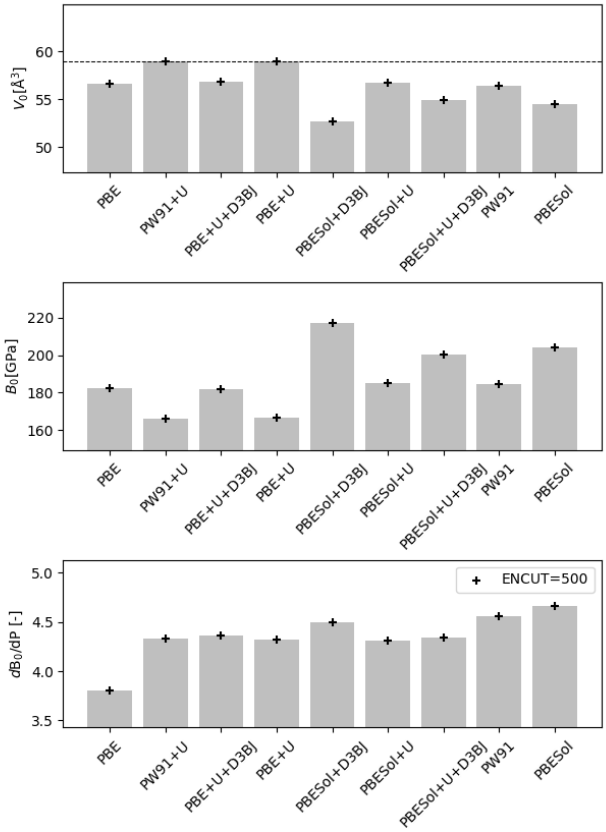

Figure A.4: Equilibrium volume (V_0 Å^3]), bulk modulus (B_0 [GPa]) and its partial derivative in respect to pressure ($\partial B_0/\partial P$ [-]) using different DFT exchange-correlation functional for the orthorhombic β phase. The dashed line corresponds to the experimental value from the literature [134] measured for the analogous FeTiD-β deuteride.

results suggest that the PW91 functional provides a consistent representation of emerging properties between metal and hydride in the FeTi system and supports its suitability for quantifying the chemical contribution to the interphase-boundary energy in this study.

The three selected functionals are employed to compute the elastic stiffness tensor ($\mathbb{C}_{ijkl}$) of the tetrahedral α and orthorhombic β phases, shown in Table A.3 and Table A.4, respectively.

Table A.3: Calculated elastic constants (in GPa) in Voigt notation for the tetrahedral α phase.

	XC-functional		
Elastic constants	PW91	PBE	PBESol + U
c_{11}	306.0	310.0	371.4
c_{22}	306.0	310.0	371.4
c_{33}	379.5	385.0	388.3
c_{44}	148.3	151.0	142.9
c_{55}	75.0	78.5	106.0
c_{66}	75.0	78.5	106.0
c_{12}	165.0	162.7	121.3
c_{13}	106.5	103.0	88.6
c_{23}	106.5	103.0	88.6

Table A.4: Calculated elastic constants (in GPa) in Voigt notation for the tetrahedral β phase.

	XC-functional		
Elastic constants	PW91	PBE	PBESol + U
c_{11}	313.0	314.6	340.6
c_{22}	302.2	302.7	332.3
c_{33}	360.0	353.1	374.1
c_{44}	86.3	87.0	59.4
c_{55}	63.4	66.5	121.9
c_{66}	74.5	75.4	64.8
c_{12}	173.3	173.7	148.3
c_{13}	82.8	82.8	89.4
c_{23}	99.6	95.0	86.8

For each functional used, stress-free transformation strain matrices were constructed using the lattice parameters obtained for the tetrahedral α and orthorhombic β phases. This information was combined with their respective

C_{ijkl} values to calculate the $B(\vec{n})$ function. The resulting $B(\vec{n})$ surface for computations with the three selected functionals is displayed in Figure A.5.

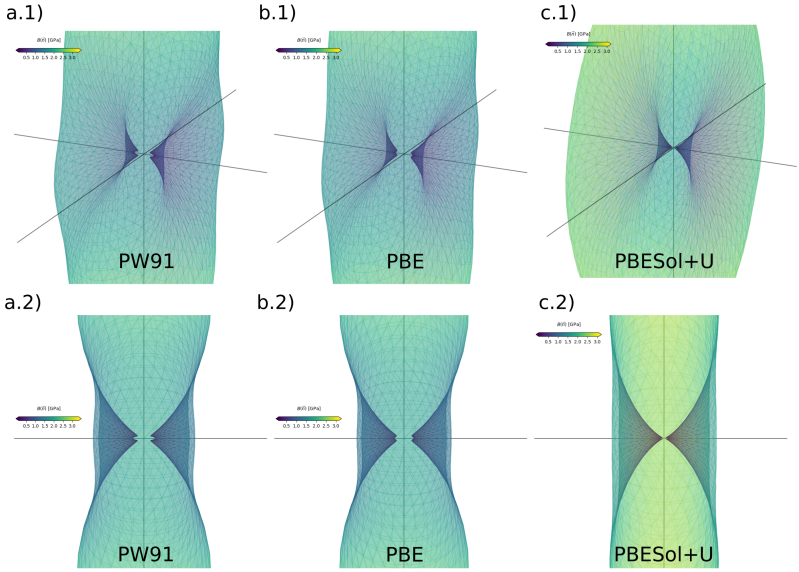

Figure A.5: Illustration of the calculated $B(\vec{n})$ function using the simple average α and β phases elastic stiffness tensor ($\mathbb{C}_{ijkl}$) and stress-free transformation strain computed with results obtained when using: a.1) and a.2) `PW91`; b.1) and b.2) `PBE`; c.1) and c.2) `PBESol +U`, from diagonal and $[0\,1\,0]_\beta$ perspective, respectively.

The minimum vector $\vec{n}_0$ was determined through numerical minimization. For all three employed functionals, it was found that $\vec{n}_0$ is parallel to the $(0\,1\,0)_\beta$ plane. To facilitate comparison, the $\vec{n}_0$ vector that forms the smallest positive angle (Θ [°]) with respect to the $(0\,0\,1)_\beta$ plane was selected. The results for the different exchange-correlation functionals are presented in Table A.5.

The Khachaturyan-Shatalov microelasticity theory assumes a homogeneous elastic modulus between the parent and precipitate phases. Figure A.5 displays the $B(\vec{n})$ function surface when employing the simple average elastic stiffness tensor ($\mathbb{C}_{ijkl}$) for the α and β phases. However, to explore the boundaries of our approach, the $B(\vec{n})$ function was also calculated using the individual $\mathbb{C}_{ijkl}$ values for the α and β phases. Table A.5 compares the angle (Θ) using these assumptions for the selected exchange-correlation functionals employed. It is worth noting that, especially for the `PW91` functional,

the choice between the homogeneous $\mathbb{C}_{ijkl}$ values derived from the simple average, the α phase, or the β phase has minimal impact on the orientation of the coherent habit plane. This suggests that the small "bump" curve observed around the $\pm[0\,1\,0]_\beta$ directions, leading to the inclination of the habit plane at an angle Θ, is likely an inherent characteristic of the FeTi metal-hydride system rather than a result of approximations or assumptions in these exchange-correlation functionals. Furthermore, these findings also support the justification for using average lattice parameters in the construction of interface slabs and average bulk moduli in the micromechanics analysis conducted in this study.

Table A.5: Calculated habit plane orientation angle (Θ) in respect to the $(0\,0\,1)_\beta$ plane using different DFT settings (note that all $\vec{n}_0$ were found parallel to the $(0\,1\,0)_\beta$ plane).

XC-functional	$\mathbb{C}_{ijkl}$ from:	Θ [°]
PW91	avrg(α, β)	19.43
	α	19.43
	β	19.43
PBE	avrg(α, β)	15.35
	α	17.38
	β	15.34
PBESol + U	avrg(α, β)	17.38
	α	17.38
	β	19.43

Calculated DFT Reaction Enthalpies

The calculated reaction energies for the permutation of hydrogen in all possible interstitial sites of the β and γ phase structures, as referred in Section 3.2.3 are presented in Figure A.6, and Figure A.7, respectively.

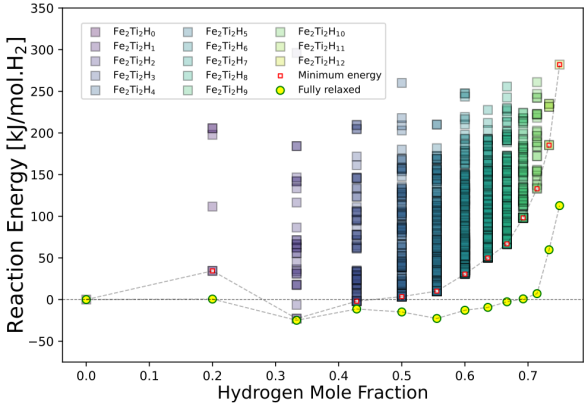

Figure A.6: DFT ground-state reaction energies (hydrogen absorption) of the compounds with β crystal structures obtained by hydrogen-vacancy permutations in the octahedral sites.

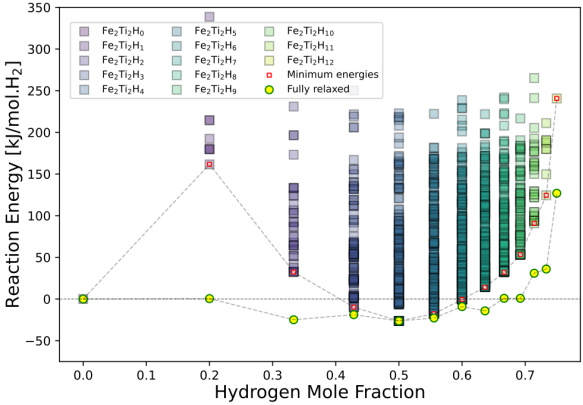

Figure A.7: DFT ground-state reaction energies (hydrogen absorption) of the compounds with γ crystal structures obtained by hydrogen-vacancy permutations in the octahedral sites.

Surface and interface slab models

In this section, the illustrations of each interface slab model and their associated strained surface slab models that were used to calculate the chemical contribution of the interface energy presented in Section 4.1.3 are shown in Figure A.8 to Figure A.14.

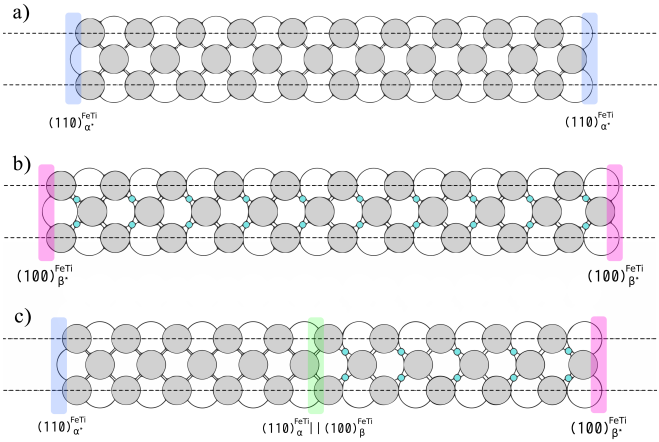

Figure A.8: Illustration of the slab structures of the interface slab and its reference strained slabs. a) $(1\,1\,0)^{FeTi}_{\alpha^*}$, b) $(1\,0\,0)^{FeTi}_{\beta^*}$, and c) $(1\,1\,0)^{FeTi}_{\alpha} \parallel (1\,0\,0)^{FeTi}_{\beta}$ slab.

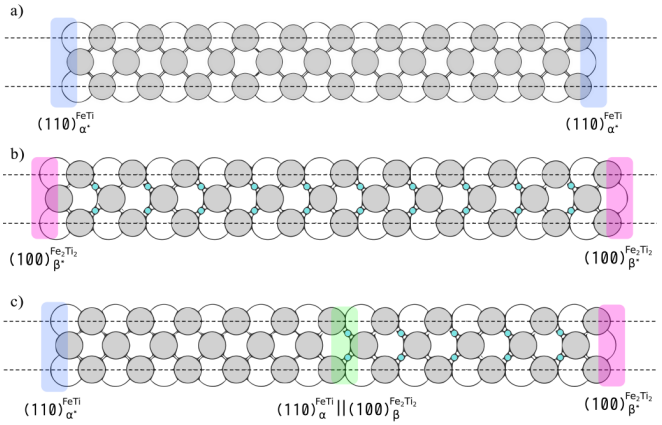

Figure A.9: Illustration of the slab structures of the interface slab and its reference strained slabs. a) $(1\,1\,0)^{\mathrm{FeTi}}_{\alpha^*}$, b) $(1\,0\,0)^{\mathrm{Fe_2Ti_2}}_{\beta^*}$, and c) $(1\,1\,0)^{\mathrm{FeTi}}_{\alpha} \parallel (1\,0\,0)^{\mathrm{Fe_2Ti_2}}_{\beta}$.

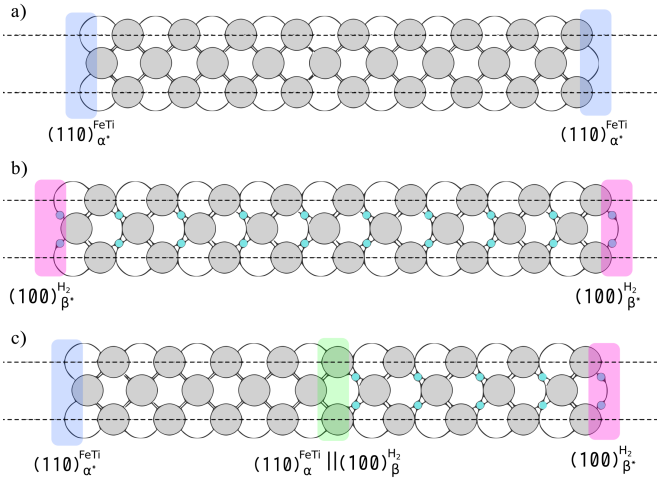

Figure A.10: Illustration of the slab structures of the interface slab and its reference strained slabs. a) $(1\,1\,0)^{\mathrm{FeTi}}_{\alpha^*}$, b) $(1\,0\,0)^{\mathrm{H_2}}_{\beta^*}$, and c) $(1\,1\,0)^{\mathrm{FeTi}}_{\alpha} \parallel (1\,0\,0)^{\mathrm{H_2}}_{\beta}$.

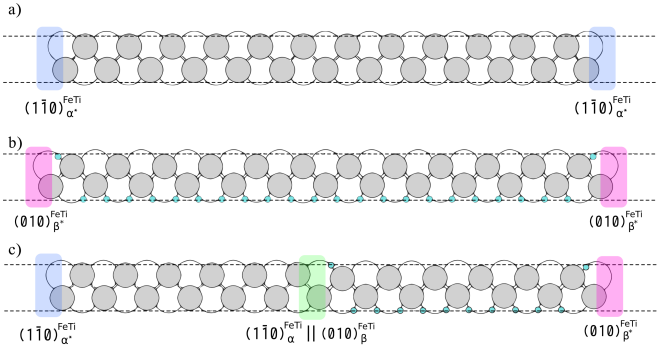

Figure A.11: Illustration of the slab structures of the interface slab and its reference strained slabs. a) $(1\,\bar{1}\,0)^{\mathrm{FeTi}}_{\alpha^*}$, b) $(0\,1\,0)^{\mathrm{H_2}}_{\beta^*}$, and c) $(1\,\bar{1}\,0)^{\mathrm{FeTi}}_{\alpha} \parallel (0\,1\,0)^{\mathrm{H_2}}_{\beta}$.

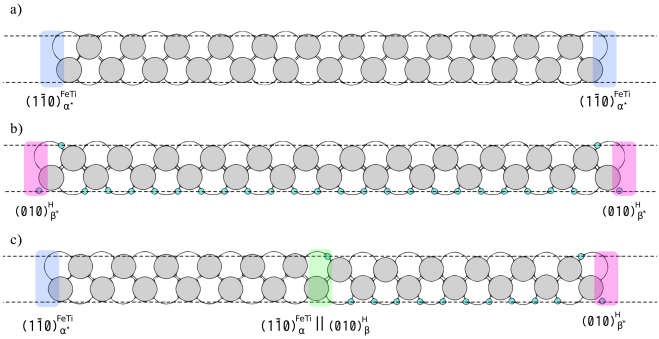

Figure A.12: llustration of the slab structures of the interface slab and its reference strained slabs. a) $(1\,\bar{1}\,0)^{\mathrm{FeTi}}_{\alpha^*}$, b) $(0\,1\,0)^{\mathrm{H}}_{\beta^*}$, and c)$(1\,\bar{1}\,0)^{\mathrm{FeTi}}_{\alpha} \parallel (0\,1\,0)^{\mathrm{H}}_{\beta}$.

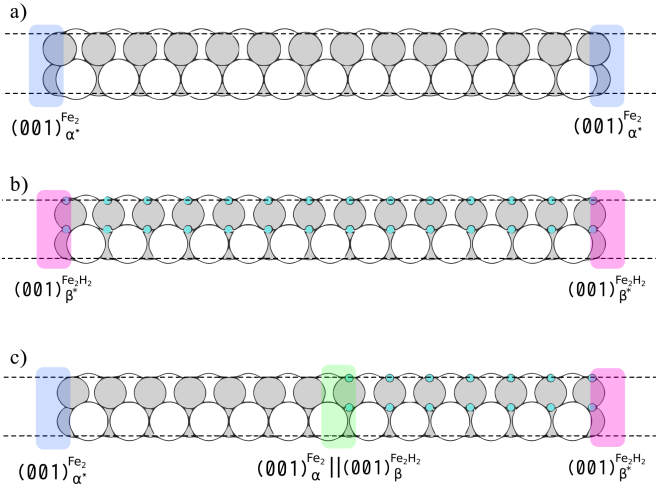

Figure A.13: Illustration of the slab structures of the interface slab and its reference strained slabs. a) $(0\,0\,1)^{\mathrm{Fe_2}}_{\alpha^*}$, b) $(0\,0\,1)^{\mathrm{Fe_2H_2}}_{\beta^*}$, and c) $(0\,0\,1)^{\mathrm{Fe_2}}_{\alpha} \parallel (0\,0\,1)^{\mathrm{Fe_2H_2}}_{\beta}$.

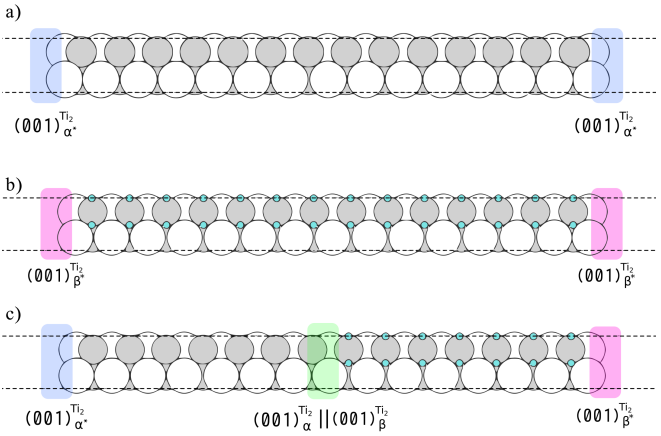

Figure A.14: Illustration of the slab structures of the interface slab and its reference strained slabs. a) $(0\,0\,1)^{\mathrm{Ti_2}}_{\alpha^*}$, b) $(0\,0\,1)^{\mathrm{Ti_2}}_{\beta^*}$, and c) $(0\,0\,1)^{\mathrm{Ti_2}}_{\alpha} \parallel (0\,0\,1)^{\mathrm{Ti_2}}_{\beta}$.

B Thermodynamics

B.1 Useful Gibbs Energy Relations

The chemical potential of component i in solutions is given by the partial Gibbs energy for the component i:

$$\mu_i = \left(\frac{\partial G}{\partial N_i}\right)_{T,p,N_{j\neq i}}. \tag{B.1}$$

Since the most used phase models yield expressions for the molar quantity of the Gibbs energy, it is useful to transform Eq. B.1 with respect to mole fractions of components:

$$G_i = G_m + \left(\frac{\partial G}{\partial x_i}\right)_{T,p,x_k} - \sum_j x_j \left(\frac{\partial G}{\partial x_i}\right)_{T,p,x_l} \qquad (k \neq i, l \neq j). \tag{B.2}$$

The second derivatives of the Gibbs energy are usually used when calculating the thermodynamic factor in diffusion problems and also for computing the stability function. The second derivative of the Gibbs energy with respect to mole fractions is given by:

$$\Omega_{ij} = \left(\frac{\partial G_m}{\partial x_i \partial x_j}\right)_{T,p,x_k} \qquad (k \neq i, k \neq j). \tag{B.3}$$

The molar Gibbs energy of mixing in a generic phase ϕ ($^{\text{mix}}G^{\phi}_{\text{m}}$) is defined as:

$$^{\text{mix}}G^{\phi}_{\text{m}} = G^{\phi}_{\text{m}} - \sum_i^n x_i^0 G_i^{\phi} \tag{B.4}$$

From the relation $G = H - TS$, the entropy of mixing is given by:

$$S^{\phi}_{\text{mix}} = -\left(\frac{\partial G^{\phi}_{\text{mix}}}{\partial T}\right)_{p,N_i}, \tag{B.5}$$

and the enthalpy of mixing by:

$$H^{\phi}_{\mathrm{mix}} = G^{\phi}_{\mathrm{mix}} - T\left(\frac{\partial G^{\phi}_{\mathrm{mix}}}{\partial T}\right)_{p,N_i} . \tag{B.6}$$

C Phase-Fields

C.1 FEM solutions for phase-field problems

In order to address the phase-field model through the Finite Element Method (FEM), it is imperative to discretize the system of partial differential equations (PDEs) within a spatial mesh. By employing the *Galerkin* method, the solutions to these PDEs are approximated using analytical representations known as *shape functions*, which are typically polynomials that can be integrated in a piecewise and continuous manner. Numerous methodologies exist to obtain solutions via FEM; however, the *Galerkin* approach is particularly advantageous for multiphysics applications due to its purely numerical nature, which ensures its efficacy irrespective of the underlying physical phenomena. Consequently, this section delineates a step-by-step derivation of the equations to be resolved using FEM.

C.1.1 Theorems useful for solving the phase-field problems

In the process of converting the phase-field equations into their *weak form*, the application of the **Divergence Theorem** and the **Product Rule** are frequently requested. These mathematical tools are particularly important for delineating boundary conditions and reducing differential complications. Therefore, these principles are provided in this section for consultation.

Divergence Theorem

According to the divergence theorem, the integral over a volume (Ω) of the divergence of a vector field, where Ω is enclosed by a surface Γ, is equivalent to the flux of the vector field across the surface Γ when projected onto its outward-pointing normal.

$$\int_{\Omega} \nabla F \, \mathrm{d}\Omega = \oint_{\Gamma} F \cdot \hat{n} \, \mathrm{d}\Gamma. \tag{C.1}$$

Product rule

When combined with the divergence theorem, the product rule for a scalar a multiplied by a vector $\mathbf{b}$ helps to lower the order of derivatives in an expression.

$$\nabla(a\mathbf{b}) = \nabla a \cdot \mathbf{b} + a\nabla \cdot \mathbf{b}. \tag{C.2}$$

Rearrange the terms (and observe that this is applicable for both a vector $\mathbf{a}$ and a scalar b as well)

$$\begin{aligned} -\nabla a \cdot \mathbf{b} &= a\nabla \cdot \mathbf{b} - \nabla(a\mathbf{b}) \\ -\nabla \cdot \mathbf{a}b &= \mathbf{a} \cdot \nabla b - \nabla(\mathbf{a}b). \end{aligned} \tag{C.3}$$

C.1.2 Constructing residuals

The Method of Mean Weighted Residuals posits that the solutions to PDEs can be well represented by a limited series of test functions, indicated as ψ. This method involves modifying the strong form of a PDE so that all terms are consolidated on one side of the equation, thus setting the equation to zero. By multiplying the terms by a test function ψ, this approach creates what is known as the *residual* ($\mathscr{R}_v$). The purpose of the method is to identify the variable v that satisfies $\mathscr{R}_v = 0$.

Applying this concept to the Allen-Cahn equation (Equation 2.42):

$$\frac{\partial \eta_j}{\partial t} + L_j \frac{\partial f_{loc}}{\partial \eta_j} - L_j \nabla \cdot (\kappa_j \nabla \eta_j) = 0. \tag{C.4}$$

In the sequence, the test function is multiplied by each term and integrated with respect to the problem domain Ω.

$$\int_\Omega \psi \frac{\partial \eta_i}{\partial t} + \int_\Omega L_j \left(\psi \frac{\partial f_{loc}}{\partial \eta_j} \right) - \int_\Omega L_j \psi \nabla \cdot (\kappa_j \nabla \eta_j) = 0. \tag{C.5}$$

The relationship derived from Equation C.3,

$$\nabla \cdot \mathbf{a}b = -\mathbf{a} \cdot \nabla b + \nabla(\mathbf{a}b), \tag{C.6}$$

is applied to the $-\int_\Omega L_j \psi \nabla \cdot (\kappa_j \nabla \eta_j)$ term, where the vector $\mathbf{a} \equiv \kappa_j \nabla \eta_j$ and $b \equiv L_j \psi$, obtaining:

$$-\int_\Omega \kappa_j \nabla \eta_j \cdot \nabla \left(L_j \psi \right) + \int_\Omega \nabla \left(\kappa_j \nabla \eta_j L_j \psi \right). \tag{C.7}$$

The divergence theorem (Equation C.1) is then applied to the second term to lower the derivative order, with the expense of generating a surface integral:

$$-\int_{\Omega} \kappa_j \nabla\eta_j \cdot \nabla\left(L_j\psi\right) + \oint_{\Gamma} \kappa_j \nabla\eta_j L_j\psi. \tag{C.8}$$

The *residual* of the non-conserved field variable represented by the order parameter η_j is then obtained as:

$$\begin{aligned}\mathscr{R}_{\eta_j} = &\int_{\Omega} \psi\frac{\partial\eta_i}{\partial t} + \int_{\Omega} L_j\left(\psi\frac{\partial f_{loc}}{\partial\eta_j}\right) \\ &+ \int_{\Omega} \kappa_j\nabla\eta_j \cdot \nabla\left(L_j\psi\right) - \oint_{\Gamma} \kappa_j\nabla\eta_j L_j\psi\cdot\hat{n}.\end{aligned} \tag{C.9}$$

Note that the last term is an integral along the volume's surface normal $\hat{n}$ to that surface's domain $\Gamma = \partial\Omega$. This term represents the boundary condition of the η_j order parameter, required to solve the problem. The Equation C.9 is the final *residual* expression for the Allen-Cahn equation solved to η_j given in the *weak* form.

To include the additional elastic term to the Allen-Cahn formulation, the second term of Equation C.9 is modified by adding the variation of elastic energy E^{el} term to the free energy density.

$$\begin{aligned}\mathscr{R}_{\eta_j} = &\int_{\Omega} \psi\frac{\partial\eta_i}{\partial t} + \int_{\Omega} L_j\left[\psi\left(\frac{\partial f_{loc}}{\partial\eta_j} + \frac{\partial E^{el}}{\partial\eta_j}\right)\right] \\ &+ \int_{\Omega} \kappa_j\nabla\eta_j \cdot \nabla\left(L_j\psi\right) - \oint_{\Gamma} \kappa_j\nabla\eta_j L_j\psi\cdot\hat{n}.\end{aligned} \tag{C.10}$$

An additional displacement variable (u) must be determined when including mechanics within the Allen-Cahn equation. For solving for u, the balance of linear momentum, Equation C.11:

$$\nabla\cdot\sigma = 0, \tag{C.11}$$

is computed following the same procedure of multiplying by the test function and integrating over the domain Ω, yielding

$$\int_{\Omega} \psi\left(\nabla\cdot\sigma\right) = 0. \tag{C.12}$$

Now, using the identity

$$\nabla\cdot\left(\mathbf{A}^{\intercal}\cdot\mathbf{b}\right) = \mathbf{b}\cdot\left(\nabla\cdot\mathbf{A}\right) + \mathbf{A} : \left(\nabla\mathbf{b}\right), \tag{C.13}$$

and noting that $\sigma = \sigma^{\intercal}$, due to the conservation of angular momentum,

$$\int_{\Omega} \psi \cdot (\nabla \cdot \sigma) = \int_{\Omega} \nabla \cdot (\sigma \cdot \psi) - \int_{\Omega} \sigma : (\nabla \psi) \,. \tag{C.14}$$

Applying the divergence theorem to convert the first term to surface integral, the *residual* related to the displacements u is found:

$$\mathscr{R}_u = \oint_{\Gamma} \hat{n} \cdot (\sigma \cdot \psi) - \int_{\Omega} \sigma : (\nabla \psi) \,. \tag{C.15}$$

To construct the residual for the conserved field variable represented by the order parameter c_i, the same concept is applied to the Cahn-Hilliard equation. From this point, two new *residuals* are attributed $\mathscr{R}_{\mu_i}$ and $\mathscr{R}_{c_i}$. To find their expression, the same concept is applied, i.e., the equations are equalized to zero and the Product Rule combined with the Divergence Theorem is employed when necessary to obtain the weak form of the partial differential equations. As follows, the Equation 2.44 becomes:

$$\frac{\partial c_i}{\partial t} - \nabla \cdot M_i \nabla \mu_i = 0. \tag{C.16}$$

Integrating on the volume domain Ω and multiplying by the test function, the *residual* $\mathscr{R}_{\mu_i}$ is written as:

$$\mathscr{R}_{\mu_i} = \int_{\Omega} \frac{\partial c_i}{\partial t} \psi - \int_{\Omega} \nabla \cdot M_i \nabla \mu_i \psi. \tag{C.17}$$

The vector $\mathbf{a} \equiv M_i \nabla \mu_i$ and $b \equiv \psi$ are identified and the product rule is applied, so that:

$$\mathscr{R}_{\mu_i} = \int_{\Omega} \frac{\partial c_i}{\partial t} \psi + \int_{\Omega} M_i \nabla \mu_i \cdot \nabla \psi - \int_{\Omega} \nabla \left(M_i \nabla \mu_i \psi \right) \tag{C.18}$$

and the divergence theorem applied to the right-most term, becoming:

$$\mathscr{R}_{\mu_i} = \int_{\Omega} \frac{\partial c_i}{\partial t} \psi + \int_{\Omega} M_i \nabla \mu_i \cdot \nabla \psi - \oint_{\Gamma} M_i \nabla \mu_i \psi \cdot \hat{n}. \tag{C.19}$$

The concept is again applied to obtain the *residual* of the conserved compositional order parameter $\mathscr{R}_{c_i}$. The Equation 2.45, is reorganized to:

$$\frac{\partial f_{loc}}{\partial c_i} - \mu_i - \nabla \cdot (\kappa_i \nabla c_i) = 0 \tag{C.20}$$

and each term is integrated on the volume domain Ω and multiplied by the test function, defining the *residual* $\mathscr{R}_{c_i}$:

$$\mathscr{R}_{c_i} = \int_\Omega \left(\frac{\partial f_{loc}}{\partial c_i} - \mu_i \right) \psi - \int_\Omega \nabla \cdot (\kappa_i \nabla c_i)\, \psi. \tag{C.21}$$

The product rule is then employed by defining $\mathbf{a} \equiv \kappa_i \nabla c_i$ and $b = \psi$, obtaining:

$$\mathscr{R}_{c_i} = \int_\Omega \left(\frac{\partial f_{loc}}{\partial c_i} - \mu_i \right) \psi + \int_\Omega \kappa_i \nabla c_i \cdot \nabla \psi - \int_\Omega \nabla \cdot (\kappa_i \nabla c_i \psi)\,, \tag{C.22}$$

and finally, the divergence theorem is used to lower the derivative order and obtain a surface integral in Γ, allowing for boundary conditions for the compositional order parameter:

$$\mathscr{R}_{c_i} = \int_\Omega \left(\frac{\partial f_{loc}}{\partial c_i} - \mu_i \right) \psi + \int_\Omega \kappa_i \nabla c_i \cdot \nabla \psi - \oint_\Gamma \kappa_i \nabla c_i \psi \cdot \hat{n}. \tag{C.23}$$

D Supplementary Material

D.1 `POSCAR` files

The `POSCAR` files utilized in this work can be found online. The link to the Supplementary Material is retrieved by scanning the QR code below.

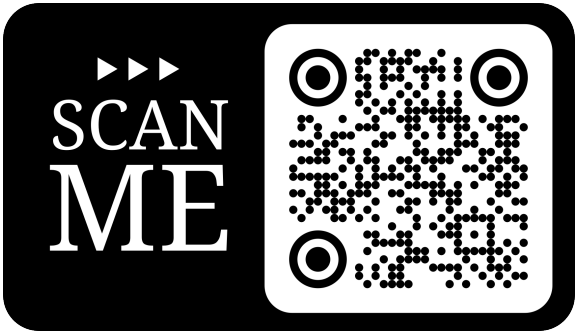

Bibliography

[1] Jos Delbeke, Artur Runge-Metzger, Yvon Slingenberg, and Jake Werksman. *The Paris Agreement*, chapter Towards a Climate-Neutral Europe: Curbing the Trend, pages 24–45. Routledge, London, 2019.

[2] European Green Deal – Climate Action.

[3] Claudio Pistidda. Solid-state hydrogen storage for a decarbonized society. *Hydrogen*, 2(4):428–443, 2021.

[4] Gregorio Marbán and Teresa Valdés-Solís. Towards the hydrogen economy? *International Journal of Hydrogen Energy*, 32(12):1625–1637, 2007.

[5] Andreas Züttel. Materials for hydrogen storage. *Materials Today*, 6(9):24–33, 2003.

[6] Kazukiyo Okano, Akiteru Maruta, and Kazunari Sasaki. *Future Technological Directions*, pages 117–119. Springer Japan, Tokyo, 2016.

[7] Charles W. Hamilton, R. Tom Baker, Anne Staubitz, and Ian Manners. B–N compounds for chemical hydrogen storage. *Chem. Soc. Rev.*, 38:279–293, 2009.

[8] Gregor Hoogers, editor. *Fuel Cell Technology Handbook*. CRC Press, Boca Raton, 1st edition, 2002. First published 2002, eBook published 27 September 2002.

[9] Strahinja Zecevic, Edward M. Patton, and Parviz Parhami. Carbon–air fuel cell without a reforming process. *Carbon*, 42(10):1983–1993, 2004.

[10] Morgan D. Hayes, Hongwei Xin, Hong Li, Timothy A. Shepherd, and John P. Stinn. Electricity and Fuel Use of Aviary-Laying Hen Houses in the Midwestern United States. 30(2):259–266, 2014.

[11] R. S. Irani. Hydrogen Storage: High-Pressure Gas Containment. *MRS Bulletin*, 27(9):680–682, 2002.

[12] S.M Aceves, J Martinez-Frias, and O Garcia-Villazana. Analytical and experimental evaluation of insulated pressure vessels for cryogenic hydrogen storage. *International Journal of Hydrogen Energy*, 25(11):1075–1085, 2000.

[13] J. M. Joubert. A Calphad-type equation of state for hydrogen gas and its application to the assessment of Rh-H system. *International Journal of Hydrogen Energy*, 35(5):2104–2111, 2010.

[14] Sunita Satyapal, John Petrovic, Carole Read, George Thomas, and Grace Ordaz. The U.S. Department of Energy's National Hydrogen Storage Project: Progress towards meeting hydrogen-powered vehicle requirements. *Catalysis Today*, 120(3):246–256, 2007. Proceedings of the Korea Conference on Innovative Science and Technology (KCIST-2005):Frontiers in Hydrogen Storage Materials and Technology.

[15] Manfred Klell. *Storage of Hydrogen in the Pure Form*, chapter 1, pages 1–37. John Wiley Sons, Ltd, 2010.

[16] R. Wiswall. *Hydrogen storage in metals*, pages 201–242. Springer Berlin Heidelberg, Berlin, Heidelberg, 1978.

[17] N.N. Greenwood and A. Earnshaw. *Chemistry of the Elements*, chapter 27 - Nickel, Palladium and Platinum, pages 1144–1172. Butterworth-Heinemann, Oxford, second edition, 1997.

[18] W.M. Mueller, J.P. Blackledge, and G.G. Libowitz. *Metal Hydrides*. Academic Press, 2013.

[19] Michael Hirscher. *Handbook of Hydrogen Storage: New Materials for Future Energy Storage*, volume 41. 2016.

[20] Helmut Buchner. *Energiespeicherung in Metallhydriden*, volume 1. 1982.

[21] Darren P Broom. *Hydrogen Storage Materials: The Characterization of Their Storage Properties*. Springer Science & Business Media, 2011.

[22] Kazunari Sasaki, Hai-Wen Li, Akari Hayashi, Junichiro Yamabe, Teppei Ogura, Hai-Wen Li, Akari Hayashi, Junichiro Yamabe, Teppei Ogura, and Stephen M. Lyth. *Hydrogen Energy Engineering: A Japanese Perspective*. 2016.

[23] Yuh Fukai. *The Metal-Hydrogen System: Basic Bulk Properties*, pages 9–53. Springer, Berlin, 2005.

[24] Martin Dornheim. Thermodynamics of metal hydrides: Tailoring reaction enthalpies of hydrogen storage materials. In Juan Carlos Moreno-Pirajan, editor, *Thermodynamics*, chapter 33. IntechOpen, Rijeka, 2011.

[25] J.-M. Joubert and S. Thiébaut. Thermodynamic assessment of the Pd–H–D–T system. *Journal of Nuclear Materials*, 395(1):79–88, 2009.

[26] J. D. Clewley, T. Curran, Ted B. Flanagan, and W. A. Oates. Thermodynamic properties of hydrogen and deuterium dissolved in palladium at low concentrations over a wide temperature range. *J. Chem. Soc., Faraday Trans. 1*, 69:449–458, 1973.

[27] E. Wicke and G. H. Nernst. Zustandsdiagramm und thermodynamisches Verhalten der Systeme Pd/H2 und Pd/D2 bei normalen Temperaturen; H/D-Trenneffekte. *Berichte der Bunsengesellschaft für physikalische Chemie*, 68(3):224–235, 1964.

[28] H. Frieske and E. Wicke. Magnetic Susceptibility and Equilibrium Diagram of PdH. *Berichte der Bunsengesellschaft für physikalische Chemie*, 77(1):48–52, 1973.

[29] Ted B. Flanagan, W. Luo, and J.D. Clewley. Calorimetric enthalpies of absorption and desorption of protium and deuterium by palladium. *Journal of the Less Common Metals*, 172-174:42–55, 1991.

[30] T. B. Flanagan and W. A. Oates. Some thermodynamic aspects of metal hydrogen systems. *Journal of Alloys and Compounds*, 404-406:16–23, 2005.

[31] W.A. Oates and Ted B. Flanagan. On the origin of increasing hydrogen pressures in the two solid phase regions of intermetallic compound-hydrogen systems. *Scripta Metallurgica*, 17(8):983–986, 1983.

[32] R. B. Schwarz and A. G. Khachaturyan. Thermodynamics of Open Two-Phase Systems with Coherent Interfaces. *Phys. Rev. Lett.*, 74:2523–2526, 1995.

[33] R.B. Schwarz and A.G. Khachaturyan. Thermodynamics of open two-phase systems with coherent interfaces: Application to metal–hydrogen systems. *Acta Materialia*, 54(2):313–323, 2006.

[34] R. B. Schwarz, A. K. Khachaturyan, A. Caro, M. I. Baskes, and E. Martinez. Coherent phase decomposition in the Pd–H system. *Journal of Materials Science*, 55(11):4864–4882, 2020.

[35] Erika M. Dematteis, Nicola Berti, Fermin Cuevas, Michel Latroche, and Marcello Baricco. Substitutional effects in TiFe for hydrogen storage: A comprehensive review. *Materials Advances*, 2(8):2524–2560, 2021.

[36] Ronald Griessen and Thomas Riesterer. *Heat of formation models*, pages 219–284. Springer Berlin Heidelberg, Berlin, Heidelberg, 1988.

[37] R. Griessen and A. Driessen. Heat of formation and band structure of binary and ternary metal hydrides. *Phys. Rev. B*, 30:4372–4381, Oct 1984.

[38] Andrii Lys, Julien O. Fadonougbo, Mohammad Faisal, Jin-Yoo Suh, Young-Su Lee, Jae-Hyeok Shim, Jihye Park, and Young Whan Cho. Enhancing the Hydrogen Storage Properties of A_xB_y Intermetallic Compounds by Partial Substitution: A Short Review. *Hydrogen*, 1(1):38–63, 2020.

[39] Yuanyuan Shang, Zhifeng Lei, Ebert Alvares, Sebastiano Garroni, Ting Chen, Roberto Dore, Mauro Rustici, Stefano Enzo, Alexander Schökel,

Yunzhu Shi, Paul Jerabek, Zhaoping Lu, Thomas Klassen, and Claudio Pistidda. Ultra-lightweight compositionally complex alloys with large ambient-temperature hydrogen storage capacity. *Materials Today*, 67:113–126, 2023.

[40] Peter Hannappel, Ebert Alvares, Felix Heubner, Claudio Pistidda, Paul Jerabek, and Thomas Weißgärber. Thermodynamic assessment of the ceh and ceni5 h system. *Calphad*, 85:102701, 2024.

[41] D. Chandra. 12 - Intermetallics for hydrogen storage. In Gavin Walker, editor, *Solid-State Hydrogen Storage*, Woodhead Publishing Series in Electronic and Optical Materials, pages 315–356. Woodhead Publishing, 2008.

[42] HyCARE focuses on large-scale, solid-state hydrogen storage. *Fuel Cells Bulletin*, 2:11, 2019.

[43] https://www.gknhydrogen.com/product, GKN Hydrogen.

[44] David Michael Dreistadt, Thi-Thu Le, Giovanni Capurso, José M. Bellosta von Colbe, Archa Santhosh, Claudio Pistidda, Nico Scharnagl, Henry Ovri, Chiara Milanese, Paul Jerabek, Thomas Klassen, and Julian Jepsen. An effective activation method for industrially produced TiFeMn powder for hydrogen storage. *Journal of Alloys and Compounds*, 919:165847, 2022.

[45] A. Kinaci and M. K. Aydinol. Ab Initio Investigation of FeTi–H System. *International Journal of Hydrogen Energy*, 32(13):2466–2474, 2007.

[46] A. Izanlou and M. K. Aydinol. An Ab Initio Study of Dissociative Adsorption of H_2 on FeTi Surfaces. *International Journal of Hydrogen Energy*, 35(4):1681–1692, 2010.

[47] A. V. Bakulin, S. S. Kulkov, S. E. Kulkova, S. Hocker, and S. Schmauder. Influence of Substitutional Impurities on Hydrogen Diffusion in B2-TiFe Alloy. *International Journal of Hydrogen Energy*, 39(23):12213–12220, 2014.

[48] Jee Yun Jung, Young-Su Lee, Jin-Yoo Suh, Joo-Youl Huh, and Young Whan Cho. Tailoring the Equilibrium Hydrogen Pressure of TiFe via Vanadium Substitution. *Journal of Alloys and Compounds*, 854:157263, 2021.

[49] Hayoung Kim, ShinYoung Kang, Ji Yeong Lee, Tae Wook Heo, Brandon C. Wood, Jae-Hyeok Shim, Young Whan Cho, Do Hyang Kim, Jin-Yoo Suh, and Young-Su Lee. A new perspective on the initial hydrogenation of $TiFe_{0.9}M_{0.1}$ (M = V, Cr, Fe, Co, Ni) alloys gained from surface oxide analyses and nucleation energetics. *Applied Surface Science*, 610:155443, 2023.

[50] Archa Santhosh, ShinYoung Kang, Nathan Keilbart, Brandon C. Wood, Thomas Klassen, Paul Jerabek, and Martin Dornheim. Influence of near-surface oxide layers on TiFe hydrogenation: mechanistic insights and implications for hydrogen storage applications. *Journal of Materials Chemistry A*, pages –, 2023.

[51] G. Kresse and J. Hafner. *Ab initio* molecular dynamics for liquid metals. *Physical Review B*, 47(1):558–561, 1993.

[52] G. Kresse and J. Furthmüller. Efficient iterative schemes for *ab initio* total-energy calculations using a plane-wave basis set. *Physical Review B*, 54:11169–11186, 1996.

[53] G. Kresse and J. Furthmüller. Efficiency of ab-initio total energy calculations for metals and semiconductors using a plane-wave basis set. *Computational Materials Science*, 6(1):15–50, 1996.

[54] G. Kresse and D. Joubert. From ultrasoft pseudopotentials to the projector augmented-wave method. *Physical Review B*, 59(3):1758–1775, 1999.

[55] Bo Sundman, Ursula R. Kattner, Mauro Palumbo, and Suzana G. Fries. OpenCalphad - a free thermodynamic software. *Integrating Materials and Manufacturing Innovation*, 4:1–15, 2015.

[56] Richard Otis and Zi-Kui Liu. pycalphad: CALPHAD-based Computational Thermodynamics in Python. *Journal of Open Research Software*, 2017.

[57] Brandon Bocklund, Richard Otis, Aleksei Egorov, Abdulmonem Obaied, Irina Roslyakova, and Zi Kui Liu. ESPEI for efficient thermodynamic database development, modification, and uncertainty quantification: Application to Cu-Mg. *MRS Communications*, 9(2):618–627, 2019.

[58] Alexander D. Lindsay, Derek R. Gaston, Cody J. Permann, Jason M. Miller, David Andrš, Andrew E. Slaughter, Fande Kong, Joshua Hansel, Robert W. Carlsen, Casey Icenhour, Logan Harbour, Guillaume L. Giudicelli, Roy H. Stogner, Peter German, Jacob Badger, Sudipta Biswas, Leora Chapuis, Christopher Green, Jason Hales, Tianchen Hu, Wen Jiang, Yeon Sang Jung, Christopher Matthews, Yinbin Miao, April Novak, John W. Peterson, Zachary M. Prince, Andrea Rovinelli, Sebastian Schunert, Daniel Schwen, Benjamin W. Spencer, Swetha Veeraraghavan, Antonio Recuero, Dewen Yushu, Yaqi Wang, Andy Wilkins, and Christopher Wong. 2.0 - MOOSE: Enabling massively parallel multiphysics simulation. *SoftwareX*, 20:101202, 2022.

[59] Frank Jensen. *Introduction to Computational Chemistry*. John Wiley & Sons, 3rd edition, 2016.

[60] P. Hohenberg and W. Kohn. Inhomogeneous Electron Gas. *Physical Review Journal Archive*, 136:B864–B871, 1964.

[61] W. Kohn and L. J. Sham. Self-Consistent Equations Including Exchange and Correlation Effects. *Physical Review Journal Archive*, 140:A1133–A1138, 1965.

[62] D. M. Ceperley and B. J. Alder. Ground State of the Electron Gas by a Stochastic Method. *Physical Review Letters*, 45:566–569, 1980.

[63] Mardirossian Narbe and Head-Gordon Martin. Thirty years of density functional theory in computational chemistry: an overview and extensive assessment of 200 density functionals. *Molecular Physics*, 115(19):2315–2372, 2017.

[64] Richard M. Martin. *Electronic Structure: Basic Theory and Practical Methods*. Cambridge University Press, 2 edition, 2020.

[65] John P. Perdew, J. A. Chevary, S. H. Vosko, Koblar A. Jackson, Mark R. Pederson, D. J. Singh, and Carlos Fiolhais. Atoms, Molecules, Solids, and Surfaces: Applications of the Generalized Gradient Approximation for Exchange and Correlation. *Physical Review B*, 46(11):6671–6687, 1992.

[66] Kieron Burke, John P. Perdew, and Yue Wang. Derivation of a Generalized Gradient Approximation: The PW91 Density Functional. *Electronic Density Functional Theory*, pages 81–111, 1998.

[67] John P. Perdew, Kieron Burke, and Matthias Ernzerhof. Generalized Gradient Approximation Made Simple. *Physical Review Letters*, 77:3865–3868, 1996.

[68] John P. Perdew, Adrienn Ruzsinszky, Gábor I. Csonka, Oleg A. Vydrov, Gustavo E. Scuseria, Lucian A. Constantin, Xiaolan Zhou, and Kieron Burke. Restoring the Density-Gradient Expansion for Exchange in Solids and Surfaces. *Physical Review Letters*, 100(13):136406, 2008.

[69] Marvin L. Cohen. The pseudopotential panacea. *Physics Today*, 32(7):40–47, 1979.

[70] Marvin L. Cohen. Pseudopotentials and Total Energy Calculations. *Physica Scripta*, 1982(T1):5, 1982.

[71] D. R. Hamann, M. Schlüter, and C. Chiang. Norm-Conserving Pseudopotentials. *Physical Review Letters*, 43:1494–1497, 1979.

[72] P. E. Blöchl. Projector augmented-wave method. *Physical Review B*, 50:17953–17979, 1994.

[73] Bo Sundman, Ursula R. Kattner, Christophe Sigli, Matthias Stratmann, Romain Le Tellier, Mauro Palumbo, and Suzana G. Fries. The OpenCalphad thermodynamic software interface. *Computational Materials Science*, 125:188–196, 2016.

[74] Bo Sundman, Nathalie Dupin, and Bengt Hallstedt. Algorithms useful for calculating multi-component equilibria, phase diagrams and other kinds of diagrams. *Calphad*, 75:102330, 2021.

[75] Hans Leo Lukas, Suzana G. Fries, and Bo Sundman. *Computational Thermodynamics: The Calphad Method*. Cambridge University Press, 2007.

[76] Mats Hillert. The compound energy formalism. *Journal of Alloys and Compounds*, 320(2):161–176, 2001. Materials Constitution and Thermochemistry. Examples of Methods, Measurements and Applications. In Memoriam Alan Prince.

[77] Otto Redlich and A. T. Kister. Algebraic Representation of Thermodynamic Properties and the Classification of Solutions. *Industrial & Engineering Chemistry*, 40(2):345–348, 1948.

[78] Muggianu, Yves-Marie and Gambino, Michèle and Bros, Jean-Pierre. Enthalpies de formation des alliages liquides bismuth-étain-gallium à 723 k. Choix d'une représentation analytique des grandeurs d'excès intégrales et partielles de mélange. *Journal de Chimie Physique*, 72:83–88, 1975.

[79] John W. Cahn and John E. Hilliard. Free Energy of a Nonuniform System. I. Interfacial Free Energy. *The Journal of Chemical Physics*, 28(2):258–267, 2004.

[80] John W Cahn. On spinodal decomposition. *Acta Metallurgica*, 9(9):795–801, 1961.

[81] M. Allen Sam and W. Cahn John. Ground state structures in ordered binary alloys with second neighbor interactions. *Acta Metallurgica*, 20(3):423–433, 1972.

[82] Samuel M. Allen and John W. Cahn. A correction to the ground state of FCC binary ordered alloys with first and second neighbor pairwise interactions. *Scripta Metallurgica*, 7(12):1261–1264, 1973.

[83] Seong Gyoon Kim, Won Tae Kim, and Toshio Suzuki. Phase-field model for binary alloys. *Physical Review E*, 60:7186–7197, 1999.

[84] Long-Qing Chen and Shenyang Hu. *Phase-Field Method Applied to Strain-Dominated Microstructure Evolution during Solid-State Phase Transformations*, chapter 11, pages 271–296. John Wiley Sons, Ltd, 2004.

[85] S.Y. Hu and L.Q. Chen. A phase-field model for evolving microstructures with strong elastic inhomogeneity. *Acta Materialia*, 49(11):1879–1890, 2001.

[86] S.B. Biner and S.Y. Hu. Simulation of damage evolution in composites: A phase-field model. *Acta Materialia*, 57(7):2088–2097, 2009.

[87] M.P. Gururajan and T.A. Abinandanan. Phase field study of precipitate rafting under a uniaxial stress. *Acta Materialia*, 55(15):5015–5026, 2007.

[88] Armen Gurgenovich Khachaturian. Theory of structural transformations in solids. *John Wiley & Sons Inc*, 1983.

[89] Shusuke Ukita, Hiroshi Ohtani, and Mitsuhiro Hasebe. Thermodynamic analysis of the Ti-H and Zr-H binary phase diagrams. *Nippon Kinzoku Gakkaishi/Journal of the Japan Institute of Metals*, 71(9):721–729, 2007.

[90] M. Zinkevich, N. Mattern, A. Handstein, and O. Gutfleisch. Thermodynamics of Fe-Sm, Fe-H, and H-Sm systems and its application to the hydrogen-disproportionation-desorption-recombination (HDDR) process for the system $Fe_{17}Sm_2$-H_2. *Journal of Alloys and Compounds*, 339(1-2):118–139, 2002.

[91] V.E. Antonov, I.T. Belash, E.G Ponyatovskii, V.G. Thiessen, and V.I Shiryaev. Magnetization of Iron Hydride. *Physica Status Solidi A*, 65(1):K43–K48, 1981.

[92] G W Wille and J W Davis. Hydrogen in Titanium Alloys. Technical report, McDonnell Douglas Astronautics Co., St. Louis, MO (USA), 1981.

[93] A. San-Martin and F. D. Manchester. The H-Ti (Hydrogen-Titanium) system. *Bulletin of Alloy Phase Diagrams*, 8(1):30–42, 1987.

[94] M. Arita, K. Shimizu, and Y. Ichinose. Thermodynamics of the Ti-H system. *Metallurgical Transactions A*, 13(8):1329–1336, 1982.

[95] Larry Kaufman and Harvey Nesor. Coupled phase diagrams and thermochemical data for transition metal binary systems — I. *Calphad*, 2(1):55–80, 1978.

[96] Ortrud Kubaschewski von Goldbeck. *Fe-Ti Iron-Titanium*, pages 152–156. Springer Berlin Heidelberg, Berlin, Heidelberg, 1982.

[97] Joanne L. Murray. The FeTi (Iron-Titanium) system. *Bulletin of Alloy Phase Diagrams*, 2(1):320–334, 1981.

[98] Joanne L. Murray. *Phase diagrams of binary titanium alloys*. Monograph series on alloy phase diagrams. ASM International Metals Park, Ohio, Metals Park, Ohio, 1987.

[99] A T Dinsdale, T G Chart, and Putland E H. NPL Report DMA (A) 96. Technical report, 1985.

[100] K.C. Hari Kumar, Wollants Patrick, and L. Delaey. Thermodynamic reassessment and calculation of Fe-Ti phase diagram. *Calphad*, 18(2):223–234, 1994.

[101] L. F. S. Dumitrescu, M. Hillert, and N. Sounders. Comparison of Fe-Ti assessments. *Journal of Phase Equilibria*, 19(5):441, 1998.

[102] Kumar K. C. Hari, L. Dumitrescu, Bo Sundman, and Patrick Wollants. Thermodynamic assessment of the Fe-Ti system with special emphasis on the modeling of the FeTi (B2) phase [C]. In *Proceedings of the Calphad XXVIII Conference*, page 95. INPG Grenoble, 1999.

[103] A. R. Miedema, F. R. de Boer, and R. Boom. Model predictions for the enthalpy of formation of transition metal alloys. *Calphad*, 1(4):341–359, 1977.

[104] Cacciamani Gabriele, De Keyzer Jozefien, Ferro Riccardo, E. Klotz Ulrich, Lacaze Jacques, and Wollants Patrick. Critical evaluation of the Fe-Ni, Fe-Ti and Fe-Ni-Ti alloy systems. *Intermetallics*, 14(10 - 11):1312–1325, 2006.

[105] Cuiping Guo, Changrong Li, Xiang Zheng, and Zhenmin Du. Thermodynamic modeling of the Fe–Ti–V system. *Calphad*, 38:155–160, 2012.

[106] Hong Bo, Jiang Wang, Liliana Duarte, Christian Leinenbach, Li Bin Liu, Hua Shan Liu, and Zhan Peng Jin. Thermodynamic re-assessment of Fe-Ti binary system. *Transactions of Nonferrous Metals Society of China (English Edition)*, 22(9):2204–2211, 2012.

[107] K. Santhy and K.C. Hari Kumar. Thermodynamic modelling of magnetic laves phase in Fe–Ti system using first principle method. *Intermetallics*, 128:106978, 2021.

[108] Mario J. Kriegel, Marius H. Wetzel, Olga Fabrichnaya, and David Rafaja. Binary Ti–Fe system. Part II: Modelling of pressure-dependent phase stabilities. *Calphad*, 76:102383, 2022.

[109] Mats Hillert and Magnus Jarl. A model for alloying in ferromagnetic metals. *Calphad*, 2(3):227–238, 1978.

[110] Adolf Sieverts. Zur Kenntnis der Okklusion und Diffusion von Gasen durch Metalle. *Zeitschrift für Physikalische Chemie*, 60U(1):129–201, 1907.

[111] R. Checchetto, G. Trettel, and A. Miotello. Sievert-type apparatus for the study of hydrogen storage in solids. *Measurement Science and Technology*, 15(1):127, 2003.

[112] Pascal Tessier. *Hydrogen Storage in Metastable Fe-Ti*. PhD thesis, McGill University, 1995.

[113] J. J. Reilly and R. H. Wiswall. Formation and properties of iron titanium hydride. *Inorganic Chemistry*, 13(1):218–222, 1974.

[114] H. Wenzl and E. Lebsanft. Phase diagram and thermodynamic parameters of the quasibinary interstitial alloy $Fe_{0.5}Ti_{0.5}H_x$ in equilibrium with hydrogen gas. *Journal of Physics F: Metal Physics*, 10(10):2147–2156, 1980.

[115] Kazusuke Yamanaka, Hiroshi Saito, and Mayumi Someno. Hydride Formation of Intermetallic Compounds of Titanium-iron, -Cobalt, -Nickel and -Copper. *Nippon Kagaku Kaishi (Journal of The Chemical Society of Japan, Chemistry and Industrial Chemistry)*, (8):1267–1272, 1975.

[116] G. K. Sujan, Zengxi Pan, Huijun Li, Daniel Liang, and Nazmul Alam. An overview on TiFe intermetallic for solid-state hydrogen storage: microstructure, hydrogenation and fabrication processes. *Critical Reviews in Solid State and Materials Sciences*, 45(5):410–427, 2020.

[117] F. Reidinger, J. F. Lynch, and J. J. Reilly. An x-ray diffraction examination of the FeTi-H_2 system. *Journal of Physics F: Metal Physics*, 12(3):L49–L55, 1982.

[118] P. D. Goodell, G. D. Sandrock, and E. L. Huston. Kinetic and Dynamic Aspects of Rechargeable Metal Hydrides. *Journal of the Less Common Metals*, 73(1):135–142, 1980.

[119] W. Schäfer, G. Will, and T. Schober. Neutron and electron diffraction of the FeTi-D(H)-γ phase. *Materials Research Bulletin*, 15(5):627–634, 1980.

[120] T. Schober and W. Schaefer. Transmission electron microscopy neutron diffraction studies of FeTi-H(D). *Journal of the Less Common Metals*, 74(1):23–31, 1980.

[121] P. Fischer, W. Hälg, L. Schlapbach, F. Stucki, and A. F. Andresen. Deuterium storage in FeTi. Measurement of desorption isotherms and structural studies by means of neutron diffraction. *Materials Research Bulletin*, 13(9):931–946, 1978.

[122] G Xiang, X Luo, T Cao, A Zhang, and H Yu. Atomic Diffusion and Crystal Structure Evolution at the Fe-Ti Interface: Molecular Dynamics Simulations. *Materials*, 15(18), 2022.

[123] G. Arnold and J. M. Welter. Diffusivity of hydrogen and deuterium at low concentration in $Fe_{0.5}Ti_{0.5}$. *Metallurgical Transactions A*, 14(8):1573–1577, 1983.

[124] R.C. Bowman, A. Attalla, G.C. Carter, and Y. Chabre. NMR Studies of Hydrogen Relaxation and Diffusion in $TiFeH_x$ and $TiFe_{1-y}Mn_yH_x$. In A. F. Andresen and A. J. Maeland, editors, *Hydrides for Energy Storage*, pages 97–118. Pergamon, 1978.

[125] James J. Reilly and Richard H. Wiswall. Hydrogen storage and purification systems III. [Pressure-temperature composition relationships]. Technical Report 21, Brookhaven National Lab., Upton, N.Y. (USA), BNL-21322, 1976.

[126] E. Lebsanft. *Das System TiFeH(D) - Strukturen, Phasendiagramm, Thermodynamik, Diffusion des Wasserstoffs in TiFeH und Methoden der Präparation.* PhD thesis, Kernforschungsanlage Jülich, 1978.

[127] J. Schefer, P. Fischer, W. Hälg, F. Stucki, L. Schlapbach, and A. F. Andresen. Structural phase transitions of FeTi-deuterides. *Materials Research Bulletin*, 14(10):1281–1294, 1979.

[128] T. Schober. The iron-titanium - hydrogen system: A transmission electron microscope (TEM) study. *Scripta Metallurgica*, 13(2):107–112, 1979.

[129] Naruki Endo, Hiroyuki Saitoh, Akihiko Machida, and Yoshinori Katayama. Formation of BCC TiFe hydride under high hydrogen pressure. *International Journal of Hydrogen Energy*, 38(16):6726–6729, 2013.

[130] P Thompson, F Reidinger, J J Reilly, L M Corliss, and J M Hastings. Neutron diffraction study of -iron titanium deuteride. *Journal of Physics F: Metal Physics*, 10(2):L57, 1980.

[131] J. R.G. da Silva, S. W. Stafford, and Rex B. McLellan. The thermodynamics of the hydrogen-iron system. *Journal of the Less Common Metals*, 49:407–420, 1976.

[132] D. E. Jiang and Emily A. Carter. Diffusion of interstitial hydrogen into and through bcc Fe from first principles. *Physical Review B*, 70(6):064102, 2004.

[133] F. H. Beck. Effect of Hydrogen on the Mechanical Properties of titanium and its Alloys. NASA Contractor Report NASA-CR-134796, 1975.

[134] P. Thompson, M. A. Pick, F. Reidinger, L. M. Corliss, J. M. Hastings, and J. J. Reilly. Neutron diffraction study of β iron titanium deuteride. *Journal of Physics F: Metal Physics*, 8(4):L75–L80, 1978.

[135] P. Thompson, J. J. Reilly, F. Reidinger, J. M. Hastings, and L. M. Corliss. Neutron diffraction study of gamma iron titanium deuteride. *Journal of Physics F: Metal Physics*, 9(4):L61–L66, 1979.

[136] P. Thompson, F. Reidinger, J. J. Reilly, L. M. Corliss, and J. M. Hastings. Neutron diffraction study of α-iron titanium deuteride. *Journal of Physics F: Metal Physics*, 10(2):L57–L59, 1980.

[137] Jr. William D. Callister and David G. Rethwisch. *Materials Science and Engineering: An Introduction*. Wiley, Hoboken, NJ, 10th edition, 2018. Includes bibliographical references and index.

[138] D. G. Westlake. Application of a geometric model to the hydrides of FeTi. *Journal of Materials Science*, 19(1):316–326, 1984.

[139] Zhi Sheng Nong, Jing Chuan Zhu, Xia Wei Yang, Yong Cao, Zhong Hong Lai, and Yong Liu. First-principles study of hydrogen storage and diffusion in B2 FeTi alloy. *Computational Materials Science*, 81:517–523, 2014.

[140] W. Schäfer, E. Lebsanft, and A. Bläsius. Investigation of TiFe Deuteride Structures by Means of Neutron Powder Diffraction and the Mössbauer Effect. *Zeitschrift für Physikalische Chemie*, 115:201–212, 1979.

[141] P. Fischer, J. Schefer, K. Yvon, L. Schlapbach, and T. Riesterer. Orthorhombic structure of γ-TiFeD$_{\approx 2}$. *Journal of the Less Common Metals*, 129:39–45, 1987.

[142] P. Thompson, J. J. Reilly, and J. M. Hastings. The application of the Rietveld method to a highly strained material with microtwins: TiFeD$_{1.9}$. *Journal of Applied Crystallography*, 22:256–260, 1989.

[143] Anubhav Jain, Shyue Ping Ong, Geoffroy Hautier, Wei Chen, William Davidson Richards, Stephen Dacek, Shreyas Cholia, Dan Gunter, David Skinner, Gerbrand Ceder, and Kristin A. Persson. Commentary: The Materials Project: A materials genome approach to accelerating materials innovation. *APL Materials*, 1:011002, 2013.

[144] Francis Birch. Finite Elastic Strain of Cubic Crystals. *Physical Review Journals Archive*, 71(11):809–824.

[145] U. Buchenau, H. R. Schober, J. M. Welter, G. Arnold, and R. Wagner. Lattice dynamics of Fe$_{0.5}$Ti$_{0.5}$. *Physical Review B*, 27(2):955–962, 1983.

[146] Ki-Hyun Kim, Jae-Hyeok Shim, and Byeong-Joo Lee. Effect of alloying elements (Al, Co, Fe, Ni) on the solubility of hydrogen in vanadium: A thermodynamic calculation. *International Journal of Hydrogen Energy*, 37(9):7836–7847, 2012. 7th Petite Workshop on the Defect Chemical Nature of Energy Materials, 14-17 March 2011, Storaas, Kongsberg, Norway.

[147] Liu Zi-Kui and J. Ågren. On the transition from local equilibrium to paraequilibrium during the growth of ferrite in Fe-Mn-C austenite. *Acta Metallurgica*, 37(12):3157–3163, 1989.

[148] A.T. Dinsdale. SGTE data for pure elements. *Calphad*, 15(4):317–425, 1991.

[149] M Chase. *NIST-JANAF Thermochemical Tables, Monograph 9 (Part I and Part II)*. Published by the American Chemical Society and American Institute of Physics, 4$^{\text{th}}$ edition, 1998.

[150] Xueyou Zhang, Bo Wang, Yanzhou Ji, Fei Xue, Yi Wang, Long-Qing Chen, and Ce-Wen Nan. First-principles calculations of domain wall energies of prototypical ferroelectric perovskites. *Acta Materialia*, 242:118351, 2023.

[151] L. Martin, G. Vallverdu, H. Martinez, F. Le Cras, and I. Baraille. First principles calculations of solid-solid interfaces: An application to conversion materials for lithium-ion batteries. *Journal of Materials Chemistry*, 22(41):22063–22071, 2012.

[152] L. M. Liu, S. Q. Wang, and H. Q. Ye. First-principles study of metal/nitride polar interfaces: Ti/TiN. *Surface and Interface Analysis*, 35(10):835–841, 2003.

[153] Zbigniew Łodziana. Surface Properties of $LaNi_5$ and TiFe—Future Opportunities of Theoretical Research in Hydrides. *Frontiers in Energy Research*, 9(October):1–9, 2021.

[154] Juarez L.F. Da Silva, Catherine Stampfl, and Matthias Scheffler. Converged properties of clean metal surfaces by all-electron first-principles calculations. *Surface Science*, 600(3):703–715, 2006.

[155] W. Liu, J. C. Li, W. T. Zheng, and Q. Jiang. NiAl (110) Cr (110) interface: A density functional theory study. *Physical Review B - Condensed Matter and Materials Physics*, 73(20):1–7, 2006.

[156] David A. Porter, Kenneth E. Easterling, and Mohamed Y. Sherif. *Phase transformations in metals and alloys, third edition*. 2009.

[157] A. Christensen and Emily A. Carter. Adhesion of ultrathin ZrO2(111) films on Ni(111) from first principles. *Journal of Chemical Physics*, 114(13):5816–5831, 2001.

[158] Daniel Scheiber, Werner Eßl, Johann Strutzenberger, Frank Goodwin, Jürgen Spitaler, and Georg Reiss. Morphology of fe2al5 particles and the interface to wc coating in the context of hot-dip galvanizing: An ab initio study. *Journal of Alloys and Compounds*, 824:153854, 2020.

[159] Silvia Leitner, Daniel Scheiber, Thomas Dengg, Jürgen Spitaler, Thomas Antretter, and Werner Ecker. Analysis of shape, orientation and interface properties of Mo_2C precipitates in Fe using ab-initio and finite element method calculations. *Acta Materialia*, 204:116478, 2021.

[160] Andre Costa e Silva. Importance of Interfacial Energy in Precipitation Modeling Using Computational Thermodynamics Techniques. In *TMS 2015 144th Annual Meeting & Exhibitio*, pages 1409–1416, Cham, 2016. Springer International Publishing.

[161] R. Shi, N. Ma, and Y. Wang. Predicting equilibrium shape of precipitates as function of coherency state. *Acta Materialia*, 60(10):4172–4184, 2012.

[162] Tae Wook Heo, Kimberly B. Colas, Arthur T. Motta, and Long Qing Chen. A phase-field model for hydride formation in polycrystalline metals: Application to δ-hydride in zirconium alloys. *Acta Materialia*, 181:262–277, 2019.

[163] Tae Wook Heo, Ming Tang, Long Qing Chen, and Brandon C. Wood. Defects, Entropy, and the Stabilization of Alternative Phase Boundary Orientations in Battery Electrode Particles. *Advanced Energy Materials*, 6(6), 2016.

[164] Daniel A. Cogswell and Martin Z. Bazant. Coherency strain and the kinetics of phase separation in $LiFePO_4$ nanoparticles. *ACS Nano*, 6(3):2215–2225, 2012.

[165] Changle Li, Song Lu, Sergiy Divinski, and Levente Vitos. Theoretical and experimental grain boundary energies in body-centered cubic metals. *Acta Materialia*, 255:119074, 2023.

[166] Jingliang Wang, Georg K H Madsen, and Ralf Drautz. Grain boundaries in bcc-Fe: a density-functional theory and tight-binding study. *Modelling and Simulation in Materials Science and Engineering*, 26(2):025008, jan 2018.

[167] Graeme Henkelman and Hannes Jónsson. Improved tangent estimate in the nudged elastic band method for finding minimum energy paths and saddle points. *Journal of Chemical Physics*, 113(22):9978–9985, 2000.

[168] Graeme Henkelman, Blas P. Uberuaga, and Hannes Jónsson. Climbing image nudged elastic band method for finding saddle points and minimum energy paths. *Journal of Chemical Physics*, 113(22):9901–9904, 2000.

[169] S. E. Kulkova, A. V. Bakulin, and L. S. Chumakova. Diffusion Properties of Hydrogen in B2-TiFe. *Physical Mesomechanics*, 25(5):424–431, 2022.

[170] E. Lebsanft, D. Richter, and J. Töpler. Investigation of the hydrogen diffusion in FeTiHx by means of quasielastic neutron scattering. *Journal of Physics F: Metal Physics*, 9(6):1057–1064, 1979.

[171] Robert C. Bowman and Wayne E. Tadlock. Hydrogen diffusion in β-phase titanium iron hydride. *Solid State Communications*, 32(4):313–318, 1979.

[172] Mats Hillert. Application of Gibbs energy-composition diagrams. *Lectures on the Theory of Phase Transformations, TMS, Warrendale, PA*, pages 1–33, 1999.

[173] John Ågren and Qing Chen. Simplified Growth Model for Multicomponent Systems - Inclusion of PARA and NPLE Conditions. *Journal of Phase Equilibria and Diffusion*, 43(6):738–744, 2022.

[174] Vladimir I. Anisimov, Jan Zaanen, and Ole K. Andersen. Band theory and Mott insulators: Hubbard U instead of Stoner I. *Physical Review B*, 44(3):943–954, 1991.

[175] S. Dudarev and G. Botton. Electron-energy-loss spectra and the structural stability of nickel oxide: An LSDA+U study. *Physical Review B*, 57(3):1505–1509, 1998.

[176] O. Bengone, M. Alouani, P. Blöchl, and J. Hugel. Implementation of the projector augmented-wave LDA+U method: Application to the electronic structure of NiO. *Physical Review B*, 62:16392–16401, 2000.

[177] Stefan Grimme, Jens Antony, Stephan Ehrlich, and Helge Krieg. A consistent and accurate ab initio parametrization of density functional dispersion correction (DFT-D) for the 94 elements H-Pu. *Journal of Chemical Physics*, 132(15):154104, 2010.

[178] Stefan Grimme, Stephan Ehrlich, and Lars Goerigk. Effect of the damping function in dispersion corrected density functional theory. *Journal of Computational Chemistry*, 32(7):1456–1465, 2011.

Acknowledgements

From the moment of our conception, we start interacting with our surroundings. These interactions, often called experiences, build our culture, shape our knowledge, model our brains, and naturally and interactively teach us the optimum way of dealing with the most adverse conditions that the universe occasionally presents. This evolving process is a simple manifestation of thermodynamics: imagine babies in a bedroom; they will naturally "mess" around, interacting with one another and with the items they encounter, disorganizing the room and maximizing the surrounding entropy. It is therefore the role of grown-ups, the parents, and the teachers to actively transfer their own energy to reduce that local high-entropy state, serving as an example to that learning brain of how to keep things organized—even though it will cost some instant energy—the barrier must be overcome to produce a durable and sustained environment that is pleasant for the next use, comfortable for the next "learning". At this pace, the collective of individuals produces goods for their peers, enhances the quality of life for their neighbors, and ultimately, society emerges. We do not choose where we will be born, and if our philosophy convinces us that the universe is deterministic, we may even consider that we do not choose with whom we will interact. From this perspective, we navigate through time as one of the infinite and scattered tiny parts of the universe that hold the consciousness of its existence.

In this context, I feel extremely fortunate to be part of it and to have been able to interact with so many amazing individuals. The foundation of all this is, of course, my family: my mom, Marinalva Correia Macedo, and my father, Valter Daniel Alvares, who provided me with all the conditions to "keep the room organized", to learn how to interact, deal with situations, and plan actions wisely. Without their support, life would surely be intractable, and I am so lucky to have them and to be able to express my gratitude. My partner, Mariana Asahi, has been fluctuating through this universe with me, and among all the adventures we face, she has always been there, sharing her genuine love and contributing to my personal growth. Through my love for her, I have learned how to understand the greatness of the universe, to be resilient, to be grateful for the small, wonderful things in this world, and I feel endless gratitude for having met her. Similarly, my brother, Matheus Daniel C. Alvares, joined my life when I was twelve and has since strengthened my

understanding of being an example, someone of trust and inspiration. I am so proud of him, and I am grateful to him for teaching me the meaning of brotherhood.

Next, I must mention the people whom I have personally met and from whom I have somehow retained parts as ideas that are always in my mind when it comes to technical, scientific, or philosophical thinking. Anyone can steal anything from you, but knowledge is something they cannot take. This phrase, apart from the great example it came with, was one of the foundational phrases my father ever told me. The way you talk to people matters, and you want to be the person who will be missed when you leave the room. This has come to me through my mom, and I envy her for how good she is at it. I honestly would like to be ten percent of how loved she is wherever she goes. The idea of trying to leave a mark on this planet, as we acknowledge our finitude, came from a metaphor by my Physics teacher, Anderson Antunes, in high school. His cleverness and intelligence, along having his similar background, inspired me and showed me that learning physics was both interesting and possible.

In the academic area, I was very fortunate to learn from Prof. Claudemiro Bolfarini, Prof. Walter Botta, and Prof. André Costa e Silva. They taught me the foundations of metallurgy, thermodynamics, and materials physics; they trusted me from the beginning and opened doors that I will never forget, for which I will always be grateful. My mentors, Dr. Olena Danilova, Dr. Johannes Preußner, and Prof. Guilherme Zepon, deserve my gratitude for their guidance, discussions, and technical and professional development during my master's work. Of course, I will always be grateful to the people composing the workgroup on which this thesis is based: Prof. Martin Dornheim, Dr. Paul Jerabek, Dr. Tae Wook Heo, Prof. Claudio Pistidda, Prof. Thomas Klassen, and Prof. Anna Garden, who trusted me and encouraged me to engage with this project, providing me with the foundations and guidance to accomplish, discover, and deploy new ideas. I should also mention that at the start of this work, I was fortunate to maintain contact with Prof. Bo Sundman. What a pleasure it was to interact with such a knowledgeable and experienced person. He unintentionally showed me that humility is part of being at the top in a field. Prof. Kai Sellschopp truly helped me with computational chemistry during his post-doc in our group. I can tell that we became more than colleagues; we shared the deepest conversations during lunch, discussions at work, conferences, and life in Hamburg. It was truly an honor to have met you.

The colleagues from the USA–what an honor it was to have been hosted by them and to have learned so much in such a short period of time! Thanks a lot for engaging with me: Dr. Bo Wang, Dr. Andrew Rowberg, Dr. Shiyoung Kang, Dr. Younggil Song, Dr. Brandon Bocklund, M.Sc. Richmond Odufisan. All the colleagues who shared the office in our remarkable building 59 of Helmholtz-Zentrum Hereon, and who went through all those scary moments during Covid time, you helped me in many aspects, including scientific discussion, partnership, and technical support: Dr. Archa Santhosh, Dr.

Yuanyuan Shang, Dr. Karimi Fahim, Dr. Thi Thu Le, Dr. André Neves, Dr. Gökham Gizer, Dr. Ingo Scheider, Ing. Oliver Metz; and of course our research visitors who enrich our group: Dr. Phutthimet Thongtan, Dr. Gabriele Scarpati, M.Sc. Roberto Doré, M.Sc. Lekshimi Dinachandran, M.Sc. Sara Paraboschi, M.Sc. Giorgia Pollini.

To finalize the risky task of naming people, I want to collectively mention my friends from the República Guaxinim during my university years, as well as my childhood friends. They have had such a strong impact on me when I reflect back, and I am truly grateful for the life lessons we have shared. Special thanks to Gustavo Santos, whom I have known for at least 20 years, who shares similar tastes in most things in life and who helped with the cover image of this work. There are numerous people who came and, although silent, left their mark. I am grateful to anyone who believed it was worth spending their energy on me. I hope to give something back by presenting this "encapsulated" piece of knowledge as a thesis. It is the written outcome of a long process of interaction that, fortunately, and in some way by chance, emerged from a vast ocean of possible alternatives. Among all the people who have ever lived, I am grateful to have been born at exactly this small fraction of time, in this specific location, to interact with you. Now, this piece will eventually be integrated into our best artificial intelligence technology and constitute a small block on our progress shelf. I hope this contribution will be useful for the other bits of this universe, ourselves, who will use it to enhance the experience shared collectively by us.

The intermetallic alloy FeTi is regarded as a promising storage material for solid-state hydrogen storage: cost-effective, safe, and operable under near-ambient conditions. However, a consistent multiscale model capable of describung the various atomic, thermodynamic, and microstructural processes involved in FeTi hydrogenation has so far been elusive. This dissertation presents, for the first time, an integrated computational model based on density functional theory (DFT), CALPHAD, and phase-field methodology that quantitatively describes the hydrogenation of FeTi. Starting from First-Principles calculations, thermodynamic properties, interfacial energies, and elastic effects are determined with high accuracy and incorporated into mesoscale simulations. The resulting model accurately reproduces experimental isotherms, explains the formation and stability of the occurring hydride phases, and enables realistic predictions of microstructural evolution during hydrogen uptake. Thus, this work provides a foundation for the digital design and computational optimization of FeTi-based hydrogen storage materials.

P. Jerabek

Logos Verlag Berlin

ISBN 978-3-8325-6050-8